

LASER SPACE RELAY COMMUNICATION
EXPERIMENT — MODULATOR TECHNOLOGY

February 1973

Principal Investigator..... F.E. Goodwin
Modulator Technology..... J.E. Kiefer
Coating Development..... A. Braunstein
Modulator Driver Development.. J.H. Lange, Jr.

Prepared Under Contract NAS 1-10894

By
HUGHES RESEARCH LABORATORIES
3011 Malibu Canyon Road
Malibu, California 90265

For
NATIONAL AERONAUTICS AND SPACE ADMINISTRATION

"Page missing from available version"

ABSTRACT

This report presents the results of a contractual program to develop the modulator technology necessary for a 10.6 μm laser communication system using cadmium telluride as the modulator material.

The program consisted of the following tasks:

1. The growth of cadmium telluride crystals of sufficient size and purity and with the necessary optical properties for use as laser modulator rods.
2. Develop a low-loss antireflection coating for the cadmium telluride rods.
3. Design and build a modulator capable of 300 MHz modulation.
4. Develop a modulator driver capable of a data rate of 300 Mbits/sec, 12 W rms output power, and 40 percent efficiency.
5. Assemble and test the modulator system.

All design goals were met and the system was built and tested.

"Page missing from available version"

TABLE OF CONTENTS

1.	INTRODUCTION AND SUMMARY	1
1.1	Introduction	1
1.2	Summary.	2
1.3	Conclusions and Recommendations.	7
2.	DATA MODULATOR	9
2.1	Theory of Coupling Modulation.	9
2.2	Design of the Data Modulator	15
2.3	Laser/Modulator Integration.	24
2.4	Mechanical Description	28
2.5	Modulator Temperature Controller	32
2.6	Data Modulator Performance Tests	33
3.	CADMIUM TELLURIDE MATERIAL DEVELOPMENT	45
3.1	Summary of Results	45
3.2	Cadmium Telluride Crystal Growth	47
3.3	Cadmium Telluride Crystal Evaluation	62
4.	COATING DEVELOPMENT.	81
4.1	Task Goals and Results	81
4.2	Design of Antireflection Coatings.	82
4.3	Antireflection Coatings for CdTe and ZnSe.	85
4.4	Experimental Coating Results for CdTe.	86
5.	MODULATOR DRIVER DEVELOPMENT	91
5.1	Modulator Driver Requirements and Review of State of the Art	91
5.2	Goals and Technical Approach of the Modulator Driver Development Task.	94
5.3	Evaluation of ENI Amplifier.	94

5.4	Wideband Power Splitter/Combiner Techniques	104
5.5	Breadboard Amplifier Design and Performance Data	104
6.	V-BAND MODULATOR EXPERIMENT.	121
6.1	V-Band Modulator Configuration	121
6.2	V-Band Dielectric Loss Measurements.	126
6.3	V-Band Modulator Tests	129
7.	COMMUNICATION DEMONSTRATION TESTS.	133
7.1	Communication Tests Using Direct Detection.	134
7.2	Communication Tests Using Coherent Detection.	143
	REFERENCES	151
	Appendix A — Intracavity CdTe Modulators For CO ₂ Lasers.	A-1
	Appendix B — Frequency Response of Intra- cavity Laser Coupling Modulation.	B-1
	Appendix C — Calculations for Direct and Coherent Detection Techniques	C-1
	Appendix D — Wideband Power Splitter/Combiner Techniques.	D-1

LIST OF ILLUSTRATIONS

<u>Figure</u>		<u>Page</u>
2-1	Coupling Modulation Geometry.	10
2-2	CW Power Output Versus Γ_0 for Typical Coupling Modulator.	14
2-3	Laser Cavity Configuration for Intra- Cavity Coupling Modulation.	16
2-4	Modulator Optical Configuration	16
2-5	Achievable λ/d Ratios	18
2-6	Modulator Driver Equivalent Circuit	19
2-7	Theoretical Modulated Output Power as a Function of Coupling C_m and Retardation Γ_m	22
2-8	Exploded View of Metal-Ceramic Discharge Tube.	23
2-9	Laser Cavity Assembly	25
2-10	Coupling Modulation	27
2-11	Theoretical Laser Output Power Versus Mirror Coupling for Internal Modulator Loss Equal to 0, 0.01, and 0.05	29
2-12	Effect of Internal Modulator Loss on Laser Output.	29
2-13	Section Drawing of Assembled Modulator/ Laser Interface	30
2-14	Data Modulator During Assembly	30
2-15	Data Modulation During Assembly Showing Printed Circuit Heating Elements.	31
2-16	Assembled Data Modulator.	31
2-17	Oven Performance.	34
2-18	Transient Response of Oven, 1.25°C Overshoot	34

<u>Figure</u>		<u>Page</u>
2-19	Optical Transmission Through Oven During Warmup.	35
2-20	Transmission During 1-Hour Test	35
2-21	Laser Performance With Modulator and Lens in Cavity.	38
2-22	Estimated Performance of Laser With Optimized Lens and Modulator.	39
2-23	Theoretical Static (dc) Coupling Factors for Three Modulator Rods.	42
2-24	Block Diagram of Data Modulator Performance Test Setup	42
2-25	Predicted (Curve) and Measured (Points) Output Power From Laser as a Function of Driving Voltage.	44
3-1	Expanded Phase Diagram of CdTe.	48
3-2	Dependence of CdTe Melting Point on Cd Pressure	50
3-3	Preparation and Purification of CdTe.	53
3-4	Schematic of Apparatus for Crystal Growth.	57
3-5	Modified Bridgman Growth Furnace.	57
3-6	CdTe Sample 226, 5 cm Diameter Ingot.	58
3-7	Transmission Spectrum of CdTe Sample Before and After Heat Treatment	61
3-8	CdTe Pressure-Temperature Equilibrium Relationships	63
3-9	Electro-Optic Evaluation Apparatus Diagram	66
3-10	Electro-Optic Evaluation Apparatus.	66
3-11	Typical Transient Thermal Response for Temperature Independent Absorption.	69

<u>Figure</u>		<u>Page</u>
3-12	Laser Calorimeter Schematic	69
3-13	Laser Calorimeter	70
3-14	Optical Calorimeter	71
3-15	Infrared Transmission of As-Grown CdTe For Oxygen Contamination Evaluation	76
3-16	Indium and Oxygen Doped Samples After First Heat Treat.	78
3-17	Indium and Oxygen Doped Samples After Second Heat Treat	78
3-18	Apparent Voids in Oxygen Doped CdTe	79
4-1	Double Layer Antireflection Coating Design Diagram for ZnSe	84
4-2	CdTe 250 HT No. 5 BaF ₂ /ZnS Antireflection Coating Both Sides.	89
5-1	Transmitted Sideband Power as a Function of Modulator Driving Power.	93
5-2	Block Diagram of ENI 406L Amplifier	97
5-3	Amplifier Frequency Response Measured With Tunable Frequency Source	97
5-4	Second, Third, and Fourth Harmonics as a Function of Input Level for 1 MHz Fixed Source.	98
5-5	Fifth and Sixth Harmonics as a Function of Input Level for 1 MHz Fixed Source	98
5-6	Saturation Characteristics, Output Power Versus Input Power.	99
5-7	Pulse Response for Unsaturated Output and Saturated Output.	100
5-8	Phase Shift Versus Frequency.	102
5-9	Group Delay Versus Frequency.	103

<u>Figure</u>		<u>Page</u>
5-10	Block Diagram of Balanced Driver Using Two Power Amplifier Stages.	108
5-11	Circuit Diagram of Pre-Driver	109
5-12	Circuit Diagram of Power Amplifier.	110
5-13	Four-To-One Stepdown Transmission Line Transformer.	113
5-14	One-To-Nine Stepup Transmission Line Transformer	115
5-15	Hybrid Power Divider.	115
5-16	Waveform of Driver With a 10 ns Pulse and 20 MHz Square Wave, Used as Signal Source.	118
5-17	Pre-Driver and Driver Configuration	119
6-1	V-Band Power (P_{uW}) Versus Laser Circulating Power for 1 mW of 1-Sideband Modulated Output Power.	123
6-2	Configuration of V-Band Modulator Experiment.	125
6-3	V-Band Modulator Test Fixture and Rod	125
6-4	V-Band VSWR Versus Frequency.	127
6-5	V-Band VSWR Versus Frequency.	127
6-6	V-Band Reflection Versus Frequency.	128
6-7	Ideal V-Band Modulator Experiment Test Setup	130
7-1	Setup for Communication Tests Using Direct Detection.	135
7-2	Swept Frequency Response.	136
7-3	Frequency Response of System.	137
7-4	Swept Frequency Response Using 7904 Oscilloscope With 500 MHz Response.	138

<u>Figure</u>		<u>Page</u>
7-5	Signal Waveform 240 MB/sec, 1024 Bit PSW, 7904 Scope.	139
7-6	Eye Patterns for 240 MB/sec Signal.	141
7-7	Baseband Spectrum of Digital Signal	142
7-8	Test Setup for Communication Tests Using Coherent Detection.	144
7-9	Homodyne Tests.	146
7-10	Heterodyne Spectrum at 300 MHz.	148
7-11	Heterodyne Tests.	149

SECTION 1

INTRODUCTION AND SUMMARY

1.1 INTRODUCTION

Low altitude satellites currently are being designed to gather large amounts of data in the form of earth imagery, e.g., ERTS and Nimbus, which must be relayed to earth stations. These data may be stored and dumped to a single ground station, relayed to multiple ground stations, or relayed to ground in real time via a synchronous satellite. The method of store and dump has been in use for some time, but it is severely limited in information capacity. The relay mode, while simple in concept, is very difficult to implement. A wideband real-time link over a distance of 22,000 miles requires high performance equipment, for example, a 6 GHz microwave link would require a 30 ft diameter transmitter on the sensor satellite and an 18 ft antenna on the synchronous satellite. A comparison of laser and microwave systems for this application clearly favors the laser in size, weight, and efficiency. The $10.6\text{ }\mu\text{m}$ CO_2 laser heterodyne system, for example, could do the job with a 5 in. transmitter and receiver antenna for equal transmitter powers.

The Laser Space Relay Communication Experiment was conceived as a means to evaluate the concept of wideband optical communication between satellites and from satellite to ground, specifically for a $10.6\text{ }\mu\text{m}$ CO_2 laser system using coherent detection.

The $10.6\text{ }\mu\text{m}$ laser communication concept is especially attractive for the space relay application for several reasons. The high efficiency of the laser transmitter source, near 10%, with the near-ideal detection sensitivity of coherent optical detection, gives a system margin greater than any other laser system combination. Further, the wavelength of $10\text{ }\mu\text{m}$ is an optimum for obtaining maximum optical antenna gain for modest sized optics and modest state of the art pointing requirements.

The disadvantages of the 10.6 μm concept are: the difficult modulation of the laser signal, the need for a tunable local oscillator to track Doppler shift generated by an orbiting spacecraft, and the need for cooling the detector. The present program was aimed at advancing the state of the art of 10 μm modulator technology, to develop a data modulator to modulate the laser signal, and to investigate one method of making a tunable local oscillator by modulating the local oscillator. These accomplishments would remove two disadvantages of the 10 μm concept.

1.2 SUMMARY

At the beginning of the present program, the technology for wide-band modulation of 10.6 μm laser radiation was limited by inferior electro-optic material and inadequate electronic drivers. The modulator material used prior to this time was gallium arsenide, suitable for use in an external traveling wave modulator but only marginally acceptable for use in an intracavity modulator because of high optical loss. Another limitation was the insufficient driving voltage and poor efficiency of modulator driver amplifiers. A peak voltage of only 20 V was obtainable from the best available transistor, and operation of the transistor above 300 MHz was marginal. The requirements for a fully modulated 10 μm signal appeared beyond reach; either a traveling wave modulator 1 meter in length, or an intracavity modulator using gallium arsenide would require a 200 V driving voltage.

The goals of the program thus were aimed at advancing the state of the art of 10 μm modulator technology. The technical approach was to attack the problem broadly: investigate new techniques of modulation, particularly intracavity modulation; investigate new materials, such as cadmium telluride; investigate new coatings to minimize loss; and investigate new electronic techniques for obtaining higher driving voltages and driver efficiencies. The program plan was thus centered around the following tasks:

- Data modulator (intracavity coupling) demonstration
- Cadmium telluride material development

- Coating development
- Modulator driver development
- V-band modulator experiment (tunable LO)
- Modulator tests
- Communication demonstration.

At the onset of the program, the use of cadmium telluride as an electro-optic material for intracavity modulation of CO₂ lasers was demonstrated (Appendixes A and B). It was shown that the intracavity modulator required significantly less driving voltage, but that its performance was strongly influenced by the absorption loss in the material and the reflective and absorption loss of the coatings. Calculations of modulator performance showed that with sufficiently low modulator loss and coating quality, a CO₂ laser could be modulated with about 12 W driving power at a bandwidth of 300 MHz. Thus, the program goals were set at developing an intracavity coupling modulator and driver combination that would satisfy the minimum requirements for a space relay laser transmitter subsystem. These were to provide the equivalent of 1 W of 100% modulated signal power with a total prime power requirement of 30 W for the laser and 30 W for the modulator driver.

1.2.1 Achievements

1.2.1.1 Data Modulator

The goals of this task were to design and build an efficient coupling modulator capable of modulating at rates in excess of 300 MB/sec. Since the modulator performance is proportional to the length-to-thickness ratio of the rod, the design approach was to maximize this ratio. The use of a lens in combination with the modulator rod permitted much higher ratios for a given crystal length. A ratio of 35 was set as the design goal. This value was selected because it was the optimum value for a modulator rod of 4-cm length, a length that was considered practical to reliably achieve.

A length/diameter ratio of 28 was achieved with rod No. 8 and a ratio of 23 with rod No. 7. Both of these rods performed as predicted and each demonstrates highly efficient modulation. Rod No. 7 produced the equivalent of 0.6 W of 100% modulated optical power with 50 V drive, and rod No. 8 produced 0.75 W with the same driving voltage. These measurements were made on a laser having approximately 35 W of circulating power. The lens which focused the energy down on the modulator rod was made of cadmium telluride. Both the lens and the rod are AR coated.

1.2.1.2 Cadmium Telluride Material Development

Initial production of cadmium telluride crystals resulted in poor crystallinity. Although the loss and strength properties of the material were acceptable, in general the largest single crystal obtained during the first 6 months was the order of an inch in length. Several modulator rods were fabricated, electroded, and coated.

The electrical properties of these first modulator crystals were seriously damaged during the coating process, resulting in a delay of the program schedule. After careful evaluation, it was learned that improved process control of the substrate temperature during the coating process prevented damage of the crystals. At about the same time, larger crystals were obtained from boules grown in a larger furnace. New modulator rods were fabricated from the larger crystals and new coatings applied. Four new modulator rods were fabricated and two were assembled into modulators.

In the final analysis, the results exceeded the goals of the program. Crystals larger than 5 cm were produced. A heat-treating process was developed that minimizes optical loss at $10\text{ }\mu\text{m}$. One recent sample showed an absorption of only 0.00089 cm^{-1} . Further, the cadmium telluride crystal growth technology including phase equilibrium considerations, descriptions of the modified Bridgman technique and the thermal annealing technique have been developed.

1.2.1.3 Coating Development

The goals of the coating development task were to produce antireflection coatings for cadmium telluride with less than 1% total absorption and reflection loss. At the beginning of the program, the technique of reliably applying coatings to CdTe had not yet been developed. However, with the conclusion of the program, excellent AR and high-reflectivity coatings are now available for CdTe. Reflection loss of 0.25% and absorption loss of 0.2% have been achieved, giving a total AR coating loss of less than 1%. The final modulator rods and lenses operating in the laser, whose losses include scatter, birefringence, and aberrations as well as absorption and reflection, show a total loss for all causes at 1.7% for the modulator rods and 1.8% for the lenses. Allowing 0.8% for a typical material loss for a 4 cm crystal, each coating is responsible for less than 0.5% loss. These results exceed the goals by a substantial margin and are largely responsible for the fine performance of the modulator in the laser cavity.

1.2.1.4 Modulator Driver Development

This task was limited to less than 10% of the total program effort. For this reason, the technical approach was limited in scope to two stages of effort: evaluation of a commercial wideband amplifier and construction of a breadboard circuit based on the commercial amplifier in an effort to improve its basic efficiency, output voltage, and risetime. The following results were achieved:

- a. Efficiency of the commercial amplifier was 8%. The efficiency of the breadboard was measured at 33%.
- b. The output voltage of the commercial amplifier was 22 V into a 50Ω load. A transformer improved this to 66 V into a modulator load. The breadboard amplifier can deliver 50 V into a 50Ω load without the need of a transformer.
- c. The commercial amplifier has a risetime of 3 nsec. The breadboard has a risetime of 1.5 nsec.

The results of the task show that the amplifier concept is suitable for driving the data modulator at data rates even greater than 300 MBit/sec and at efficiencies suitable to provide 10 W driving power to the modulator with 30 W prime power.

1.2.1.5 V-Band Experiment

During the performance of these tests, the V-band modulator rod was broken in handling and the tunable local oscillator experiment could not be completed. However, another rod was fabricated from residual material and two important tests were conducted on this rod; the first was to use the rod inside the laser cavity having a circulating power of about 40 W, and the second was a measurement of modulation retardation when the modulator was driven with a V-band source. The success of the first experiment illustrates that the modulator material losses and coating losses are sufficiently low that to permit the device to be included inside a laser cavity. The success of the second verifies that the performance predicted by the analysis is achievable. These factors can be used to predict an impressive 0.8 mW of tunable LO power with a V-band driving power of 100 mW.

1.2.1.6 Communication Demonstration Test

Intracavity coupling modulation can produce a type of modulation called double sideband suppressed carrier modulation. A coherent, or phase-locked receiver is required to retrieve the information (product detection). In the case of a 10.6 μm coherent receiver, two types of product detection are possible. One is optical homodyne and the other is optical heterodyne with electronic. In the communication demonstration tests conducted during this program, both types of coherent detection were demonstrated for a digital modulation rate of 240 Mbit/sec. These tests prove the validity of the system concept for wideband digital communication using the CO_2 laser.

The validity of the system concept for efficient, wide band, digital modulation and detection of $10.6\text{ }\mu\text{m}$ energy has been shown and the proof of technology needed for serious planning for applications in space data relay communications is given in this report.

Intracavity modulation, requiring extremely low loss modulator material and virtually perfect coatings has been demonstrated. Although the V-band experiment was not completed, there is greater reason now to believe that the technique is viable for a tunable local oscillator than when the program began. Further, the importance of the V-band experiment is reduced because of recent progress with high pressure waveguide lasers with greater tuning range.

It is the conclusion of this report that the success achieved in the development of this concept is largely due to the superior material and coatings. This fact justifies the part of the program effort extended to these tasks, and raises the question of what proportion of future effort should be applied to more fundamental material and coating development. At the present, we are still severely limited in size and quantity of crystals. We have been fortunate for concurrent high power window development programs, but these programs have diminished because the importance of cadmium telluride material as a $10.6\text{ }\mu\text{m}$ window material has decreased in favor of the halides. Now, the only justification for further development of cadmium telluride is for its electro-optic properties. It is hoped that this report will support this justification.

Further device development will surely result in improved performance of the data modulator. Longer crystals will permit larger l/d ratios. Improved polarizers will permit a near 100% improvement in modulator efficiency. Utilizing the intracavity modulator in a waveguide laser opens the possibility of even greater improvements in modulating efficiency.

Material development and device development therefore share about equally in recommended further effort. There is no doubt that such effort will yield more efficient, lighter weight, more reliable modulator components for 10.6 μm laser communication systems.

SECTION 2

DATA MODULATOR

2.1 THEORY OF COUPLING MODULATION

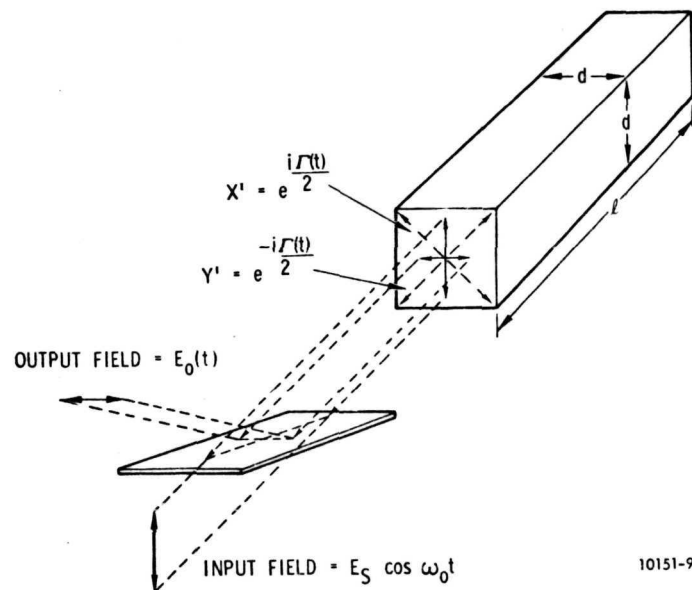
The wavelength dependence of the electro-optic effect makes modulation at the 10.6 μm wavelength more difficult than the shorter optical wavelengths. Long traveling wave modulator structures have been used to achieve effective modulation at this wavelength, but these structures are not practical for flight hardware. Placing a shorter modulator in the laser cavity enhances the modulation efficiency because of the higher level of circulating optical power in the device. Although intracavity modulators have been demonstrated at both 3.39 μm and 10.6 μm , their usefulness depends critically on the quality of the modulator material and the coatings. These effects are discussed in this section and the detail technologies are discussed in Sections 3 and 4.

Two types of intracavity modulators have been investigated previously, intracavity FM and coupling modulation. The modulator developed on this program uses the coupling modulation format to achieve maximum bandwidth capability. The geometry of coupling modulation is depicted in Fig. 2-1.

$\Gamma(t)$ is the relative retardation for a single pass through the modulator. The effective retardation is $2\Gamma(t)$, since the energy transverses the modulator twice before it is coupled out. The field coupled from the laser is

$$E_o(t) = kE_o \sin \omega_o t \sin \Gamma(t)$$

where k is the coupling factor of the output polarizer. If we assume the modulation is sinusoidal at frequency ω_m with a peak amplitude of Γ_m , the expression for the field coupled from the laser will expand



10151-9

Fig. 2-1. Coupling Modulation Geometry.

into a Bessel series. Appendix C contains the detailed computations of these expansions for the optical field, the coherent detected signal power, and the direct detected signal power. Tables C-I and C-II of Appendix C list the carrier and first three sidebands of the above signals. These tables are simplified and reproduced in Table 2-I for the purpose of discussion and interpretation.

2.1.1 Optical Field

The optical field terms are written in Table 2-I with arbitrary dc retardation so that a carrier term may be generated if desired, or set to zero if desired. For example, if it is desired to use direct detection, then a carrier term is required, and a dc bias must be applied. Of particular interest, however, is double sideband suppressed carrier modulation (DSBSC), where the carrier is provided by the laser local oscillator. For this case, the optical field consists of no carrier and no even harmonics, but only the odd harmonics.

2.1.2 Coherent Detection of DSBSC Signal

The DSBSC signal of the modulated laser output has an optical spectrum similar to that shown in Table 2-I where the dc retardation Γ_0 is set to zero. Note that both the carrier term and the second harmonic term go to zero. At the receiver detector, the local oscillator laser is added in phase with the resultant fundamental signal vector giving product demodulation of the signal. The first and the odd harmonic terms are demodulated, and the total harmonic distortion is mainly the third order term. For a typical value of $\Gamma_m = 0.06$, the third harmonic distortion is 0.015%.

2.1.3 Direct Detection of Amplitude Modulated Signal

Setting a dc bias on the modulator should provide sufficient carrier to produce the equivalent of amplitude modulation of the signal. This

TABLE 2 - I
Optical And Electronic Signal Spectrum

Frequency of Carrier and Sidebands	Optical Field Amplitude Spectrum		DSBSC Spectrum
	$\sqrt{2}E_o$ Scale Factor, $\Gamma_o \neq 0$	$\sqrt{2}E_o$ $\Gamma_o = 0$ DSBSC	
ω_c	$\sin(\Gamma_o)J_0(\Gamma_m) \sin(\omega_c t + \beta_o + G)$	0	<p>Electronic Current Spectrum of Direct Detection AM Signal $\Gamma_o = 0.13$ $\Gamma_m = 0.06$</p>
$\omega_c - \omega_m$	$\cos(\Gamma_o)J_1(\Gamma_m) \cos[(\omega_c - \omega_m)t + \beta_o + G]$	$J_1(\Gamma_m) \cos[(\omega_c - \omega_m)t + \beta_o + G]$	
$\omega_c + \omega_m$	$-\cos(\Gamma_o)J_1(\Gamma_m) \cos[(\omega_c + \omega_m)t + \beta_o + G]$	$-J_1(\Gamma_m) \cos[(\omega_c + \omega_m)t + \beta_o + G]$	
$\omega_c - 2\omega_m$	$\sin(\Gamma_o)J_2(\Gamma_m) \sin[(\omega_c - 2\omega_m)t + \beta_o + G]$	0	
$\omega_c + 2\omega_m$	$\sin(\Gamma_o)J_2(\Gamma_m) \sin[(\omega_c + 2\omega_m)t + \beta_o + G]$	0	
$\omega_c - 3\omega_m$	$\cos(\Gamma_o)J_3(\Gamma_m) \cos[(\omega_c - 3\omega_m)t + \beta_o + G]$	$J_3(\Gamma_m) \cos[(\omega_c - 3\omega_m)t + \beta_o + G]$	
$\omega_c + 3\omega_m$	$-\cos(\Gamma_o)J_3(\Gamma_m) \cos[(\omega_c + 3\omega_m)t + \beta_o + G]$	$-J_3(\Gamma_m) \cos[(\omega_c + 3\omega_m)t + \beta_o + G]$	
Electronic (Detected) Current Spectrum*			<p>Electronic Current Spectrum of Coherent Detection of DSBSC Signal $\Gamma_o = 0$, $\Gamma_m = 0.06$</p>
dc Term	$\frac{E_o^2}{2} [1 - 0.040] \approx 0.015 E_o^2$	Coherent Detection of DSBSC, $\Gamma_m = 0.06$	
ω_m	$E_o^2 (0.25) J_1(0.12) \approx 0.015 E_o^2$	$\frac{E_o^2}{2} [1 - J_0(2\Gamma_m)] + \frac{E_c^2}{2} \approx \frac{E_c^2}{2}$	
$2\omega_m$	$E_o^2 [0.940] J_2(0.12) \approx 0.0017 E_o^2$	$2\sqrt{2} E_o E_c \cos(\Delta) J_1(\Gamma_m) = 0.084 E_o E_c$	
$3\omega_m$	$E_o^2 [0.25] J_3(0.12) \approx 0.0000046 E_o^2$	$E_o^2 J_2(2\Gamma_m) \approx 0$	

* Current $i = \eta e / h\nu \cdot$ optical power.

type of modulation can be detected by direct detection. In order to compute the minimum necessary dc bias for this type of modulation and detection, we set the dc carrier power equal to the first sideband power and solve for

$$[1 - \cos(2\Gamma_o)J_o(2\Gamma_m)] = \sin(2\Gamma_o)J_1(2\Gamma_m)$$

$$\sim [1 - \cos(2\Gamma_o)] = \sin(2\Gamma_o)\Gamma_m$$

For a value of $\Gamma_m = 0.06$, $\Gamma_o \geq 0.13$. The second harmonic distortion is

$$\frac{\cos(2\Gamma_o)J_2(2\Gamma_m)}{\sin(2\Gamma_o)J_1(2\Gamma_m)} = \frac{0.96}{0.26} \left(\frac{\Gamma_m}{2} \right) = 1.84\Gamma_m = 0.110$$

and the third harmonic distortion is

$$\frac{\sin(2\Gamma_o)J_3(2\Gamma_m)}{\sin(2\Gamma_o)J_1(2\Gamma_m)} = \frac{\Gamma_m^2}{6} = 0.0006.$$

Choosing a larger value of Γ_o will help reduce the second harmonic distortion; however, Γ_o cannot be made arbitrarily large since the laser will cease to lase when the value of the coupling coefficient equals the gain of the tube. The optimum operating point for the lasers used in these experiments has been determined experimentally. From Fig. 2-2, the point of maximum linearity appears when $\Gamma_o = 0.5$. The second harmonic distortion is about 2% and the third is about 0.04%.

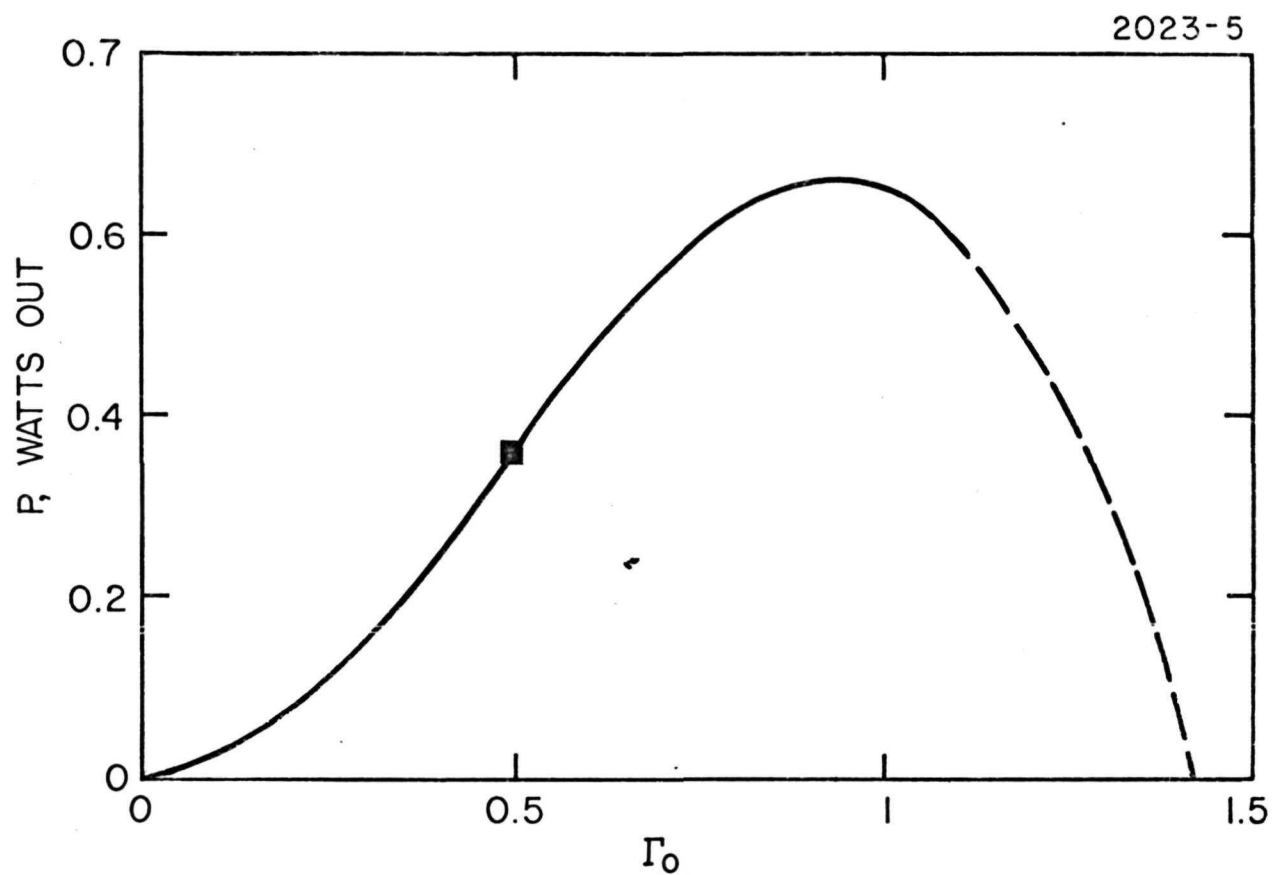


Fig. 2-2. CW Power Output Versus Γ_0 for Typical Coupling Modulator.

2.2 DESIGN OF THE DATA MODULATOR

2.2.1 Optimization to Achieve Efficient Performance

Efficient modulation is obtained using high length-to-height ratios (ℓ/d) and high drive voltages. To achieve the maximum ℓ/d ratio, it is necessary to establish accurately the crystal and optical geometry. This requires a lens in the cavity, as shown in Fig. 2-3. The lens reduces the beam diameter, providing high ℓ/d ratios in crystals of a given length. (Typical crystal lengths are limited to 5 cm or less because of manufacturing techniques.) The use of a high quality CdTe lens introduces additional loss into the cavity, but this loss is primarily due to the antireflective coatings since the material loss in a thin lens is not significant. Figure 2-4 defines the parameters that must be examined to determine the achievable ℓ/d ratios. (All spot sizes are defined as the diameter to the $1/e^2$ intensity points on the gaussian profile.)

According to Kaminow and Turner¹, the illuminated volume within a modulator is a minimum when the confocal parameter² is equal to L , the equivalent single-pass modulator length. For this case, the spot size at the reflective surface, $2\omega_o$, the spot size at the modulator entrance surface, $2\omega_s$, and the safety factor, S , are, respectively,

$$2\omega_o = (2\lambda L/\pi n)^{1/2} = (4\lambda \ell/\pi n)^{1/2} \quad L = 2\ell$$

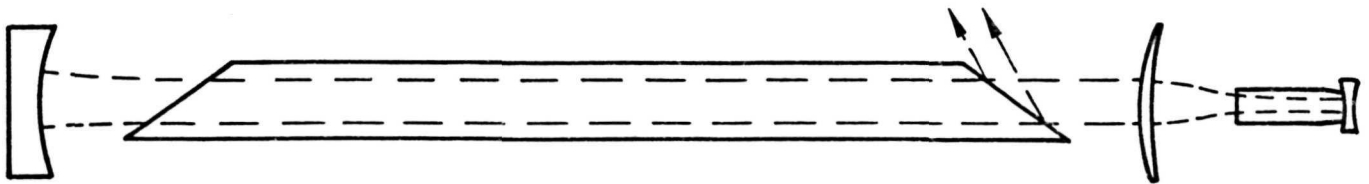
$$2\omega_s = 2\sqrt{2}\omega_o = (8\lambda \ell/\pi n)^{1/2}$$

$$S = d/2\omega_s$$

Let $R = \ell/d$. Then,

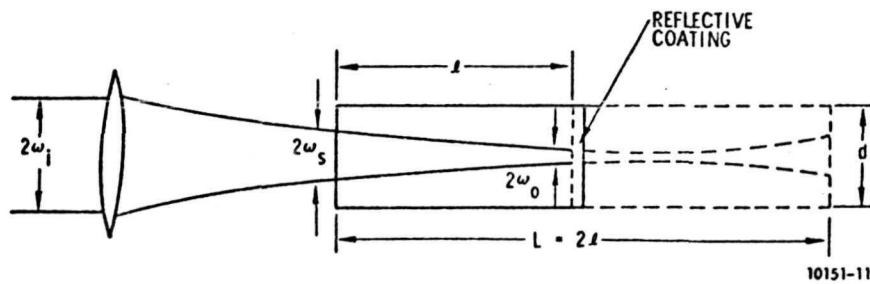
$$d = 8RS^2\lambda/\pi n$$

$$\ell = Rd$$



10151-10

Fig. 2-3. Laser Cavity Configuration for Intra-Cavity Coupling Modulation.



10151-11

Fig. 2-4. Modulator Optical Configuration.

A safety factor of 1.5 will cause a truncation loss of about 1%, assuming a gaussian beam. For alignment tolerance, a safety factor of 2 is the minimum practical value. The variation of ℓ and d for this safety factor is shown in Fig. 2-5 as a function of the ℓ/d ratio. For example, with the limitation of a single crystal length of 5 cm, the maximum achievable ℓ/d ratio is 35 with a crystal height of 1.43 mm.

2.2.2 Lens Design

Table 2-II contains the selected lens radii for matching 3, 4, and 5 cm modulators. To make the necessary calculations, it was assumed that the cavity optical length is 45 cm, the curved mirror radius is 1.0 m, and the lens material is CdTe.

TABLE 2-II

Selected Lens Radii for Matching 3-, 4-, and 5-cm Modulators

Modulator Length (cm)		Lens Radii (cm)		Focal Length (cm)	Lens Spacing (cm)	Overall Length (cm)
Nominal	Optimum	R1 (convex)	R2 (concave)			
3	2.93	6.75	14.23	7.72	6.30	9.05
4	3.94	8.35	18.57	9.12	7.12	11.10
5	4.96	8.35	16.12	10.36	7.76	12.75

T787

The lens radii, selected from available test plates, were selected to minimize spherical aberration. The design results in a meniscus lens. The last two columns of Table 2-II show the required spacing between the modulator and lens, and the overall length of the combination. In all cases this length exceeds the available space

between the laser tube and the end of the Invar cavity; thus the modulator and oven must extend beyond the end of the test cavity.

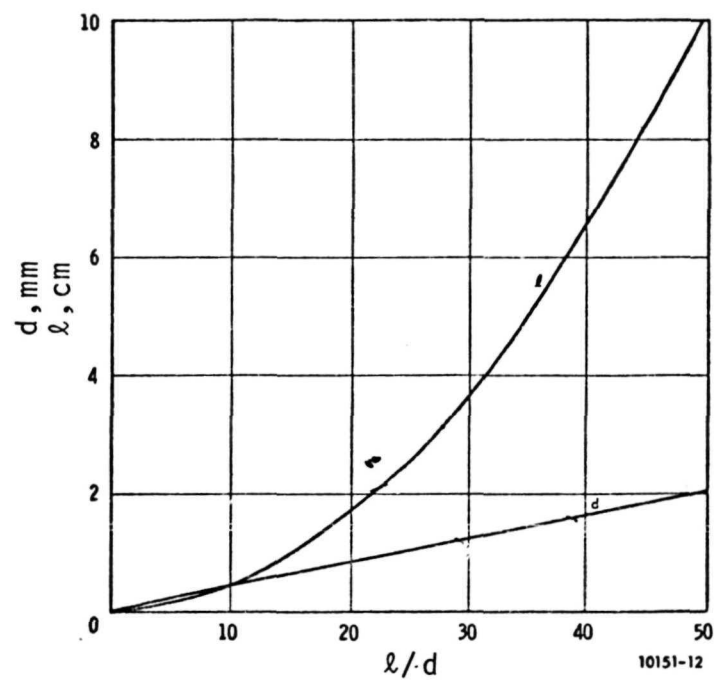


Fig. 2-5. Achievable l/d Ratios.

2.2.3 Modulator Driver Power

If a class A amplifier is designed to provide the required voltage across the capacitive modulator over a specified bandwidth, the equivalent circuit shown in Fig. 2-6 can be used; where C_s is driver and stray capacity, C_m is the modulator capacity and R is the equivalent shunt resistance (ideally the output impedance of the amplifier). For this circuit

$$V(t) = i(t)R$$

$$f_m = 1/2\pi R(\ell C_s + C_m),$$

where f_m is the maximum modulation frequency, 150 MHz for this system. Assuming a sinusoidal input drive,

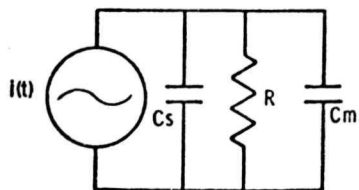
$$P = 2\pi f_m (C)V^2, \quad C = C_s + C_m$$

where V is the rms output voltage across the modulator.

From electro-optic theory,

$$V_{rms} = \frac{V_\pi}{\pi} \frac{d}{\ell} \frac{\Gamma_m}{\sqrt{2}}$$

where V_π is the basic halfwave voltage for CdTe (44,000 volts), V_{rms} is the rms voltage applied to the crystal, ℓ/d is the ratio of length-to-thickness of the modulator rod, and Γ_m is the peak modulator



10151-13

Fig. 2-6.
Modulator Driver
Equivalent Circuit.

retardation. Using this expression, the power necessary to drive the modulator is

$$P_{\text{mod}} = \frac{\omega_m C}{2} \left[\frac{V_\pi}{\pi} \frac{d}{\ell} \frac{\Gamma_m}{\Gamma_m} \right]^2 .$$

2.2.4 Modulated Laser Output Power

Coupling modulator output power depends critically upon the value of circulating power incident on the modulator in the cavity. To compute the power in the first sidebands, note is made of the optical spectrum of the DSBSC signal in Table 2-I.

$$E_{-1} = \sqrt{2} E_o J_1(\Gamma_m) \cos [(\omega_c - \omega_m)t]$$

$$E_{+1} = -\sqrt{2} E_o J_1(\Gamma_m) \cos [(\omega_c + \omega_m)t]$$

The circulating power P_c , time averaged, is $E_o^2/2$ and the sideband power coupled out of the laser is

$$P_t = \frac{(E_{-1})^2 + (E_{+1})^2}{2} = \frac{2[\sqrt{2} E_o J_1(\Gamma_m)]^2}{2} = 4 \left(\frac{E_o^2}{2} \right) [J_1(\Gamma_m)]^2$$

$$P_t = P_c \Gamma_m^2$$

Finally, since the Brewster window is not perfectly efficient in coupling out the modulated power, the actual power transmitted is

$$P_t = k P_c \Gamma_m^2$$

Figure 2-7 is a plot of the modulated laser output power as a function of coupling factor C_m and retardation Γ_m , for various values of laser circulating power. Finally, the amount of transmitted power can be equated directly to the modulator driving power

$$P_t = 2kP_c P_{\text{mod}} \frac{1}{\omega_m C} \left(\frac{\pi \ell}{V\pi d} \right)^2$$

Assumptions for values of P_c , ω_m , C , ℓ , and d will give a direct relation for the required modulator driving power. These are explored in more detail in Section V.

2.2.5 Laser Design

Since the performance of the laser modulator critically depends on the laser itself, some detail will be given on the actual design of the laser discharge tube and cavity.

2.2.5.1 Discharge Tube

The laser plasma tube is of metal ceramic design with beryllia bore sections, Kovar anodes, and cadmium telluride Brewster windows. The active discharge region is 25 cm plus the cathode region, and the bore is 5 mm diameter. Heat is removed conductively through aluminum clamps, which also serve as mechanical support for the discharge tube. Figure 2-8 shows an exploded view of the tube and an assembled view. In the assembled view, the mounting clamps are shown mounted to a water-cooled base plate. Essential design parameters for the discharge tube and laser cavity design are as follows:

Bore diameter	5 mm
Discharge length	25 cm
Total pressure	30 Torr

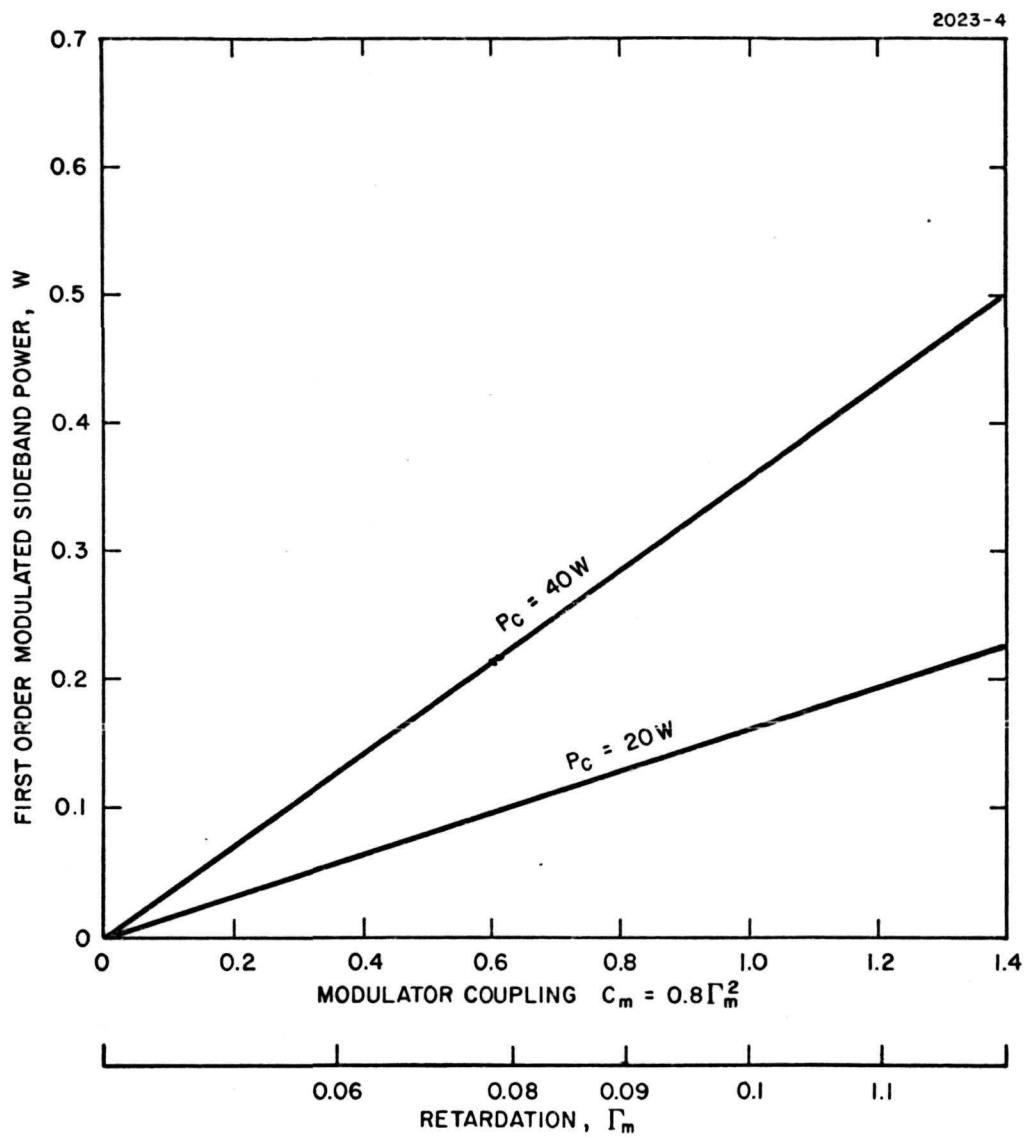


Fig. 2-7. Theoretical Modulated Output Power as a Function of Coupling C_m and Retardation Γ_m . ($k = 0.8$ for germanium Brewster plate).

M7825

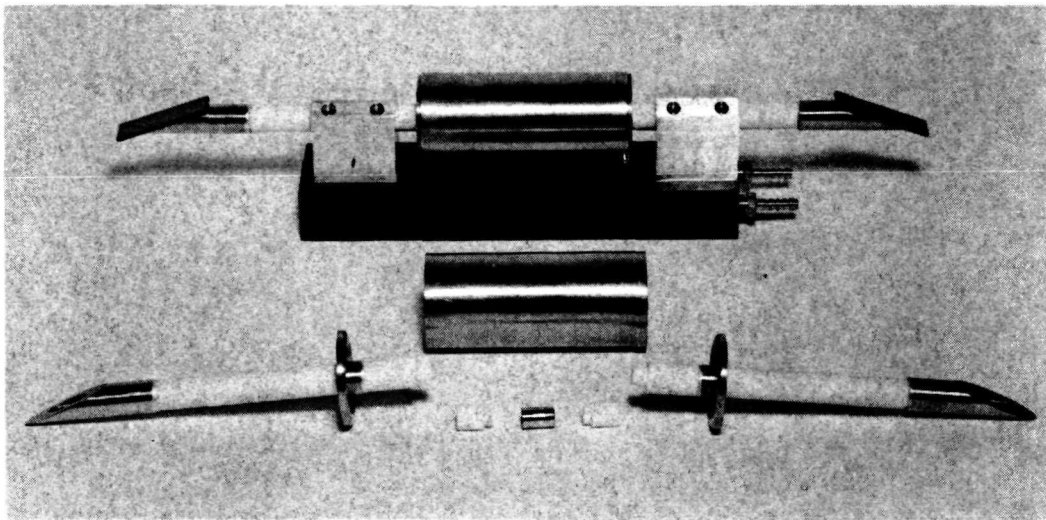


Fig. 2-8. Exploded View of Metal-Ceramic Discharge Tube.

Xe:CO ₂ :N ₂ :He	1:7:7:15
Small signal gain	1.3 dB
Net gain (less cavity losses)	1.1
Saturation flux	250 W/cm ²
Optimum power out	2.7 W
Fresnel No.	1.47
Cavity length	40 cm

The volume of the discharge tube, including bore volume and cathode volume, is 130 cm³. Typical lifetime of this tube is about 250 hours. Thus, to extend the lifetime, a ballast tank (of about 1 liter volume) is added to the discharge tube. This ballast tank extends the useful life of the tube to 2000 hours or more.

2.2.5.2 Laser Cavity

Figure 2-9 shows an assembled laser cavity including the Invar cavity, mirror mounts, ballast tank, and base plate for cooling the discharge tube. Although this photo shows a conventional mirror in place of the modulator, the modulator port and folding mirror can be seen on top of the unit.

2.3 LASER/MODULATOR INTEGRATION

Since the modulator serves as one of the mirrors of the laser cavity, the modulator becomes an integral part of the laser. Further, the high l/d ratio requires that a lens accompany the modulator; thus the lens becomes an integral part of the modulator. The lens and modulator rod taken together simulate the laser mirror.

The modulator may be oriented so applied voltage produces only phase shift of the optical energy, which in turn produces frequency modulation of the light. For this FM mode of operation, the modulator first-surface is coated with an AR coating and the second or output

M 8205

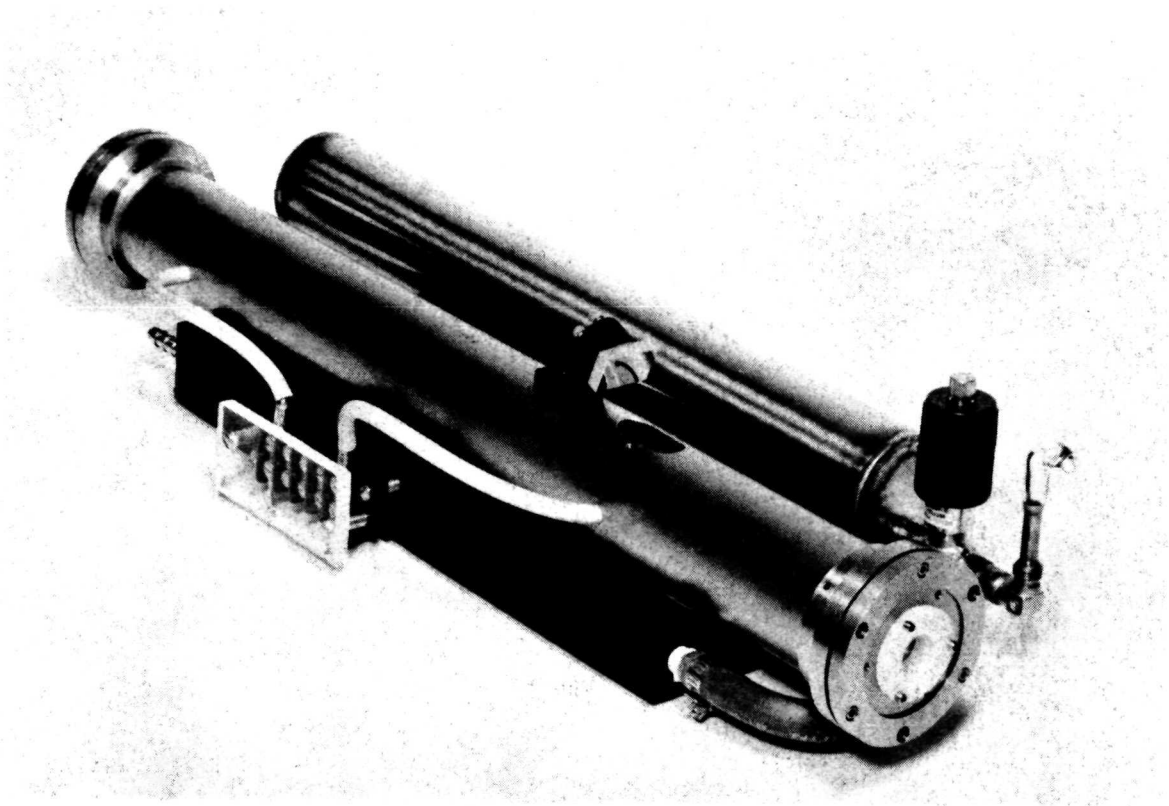


Fig. 2-9. Laser Cavity Assembly.

surface is coated with a partially transmitting mirror, about 10%. For coupling modulation, the crystal produces birefringence in the cavity, which rotates the plane of polarization of the energy in the cavity, so that energy is coupled out of the cavity off the Brewster window. For coupling modulation, the second-surface mirror of the modulator is high reflectivity with zero transmittance.

The performance of the modulator is a function of the circulating power in the laser cavity. Conversely, the circulating optical power in the laser cavity is a strong function of the modulator losses and other cavity losses. This interdependence can be expressed by (Ref. 2, Appendix A)

$$P_c = \frac{\pi A I_s}{2} \frac{(1 - \alpha_c)^{1/2} \left[g_o L + \frac{1}{2} \ln(1 - \alpha_c)(1 - \alpha_f) \right]}{\left[(1 - \alpha_c)^{1/2} + (1 - \alpha_f)^{1/2} \right] \left[1 - (1 - \alpha_c)^{1/2} (1 - \alpha_f)^{1/2} \right]}$$

where

P_c is the optical power incident on the modulator

A is the cross sectional area of the beam

I_s is the saturation intensity

α_c is the loss of the curved mirror and cavity diffraction losses

α_f is the combined loss of the modulator material α_m , modulator mirror α_2 , modulator coupling C_m , and output mirror coupling C_o

g_o is the small signal gain per unit length

L is the length of the discharge

For the FM case, the power output taken through the modulator mirror P_{of} is then (see Fig. 2-10)

$$P_{of} = (1 - \alpha_m - \alpha_2) P_c C_o$$

where C_o is the output coupling through the transmission mirror.

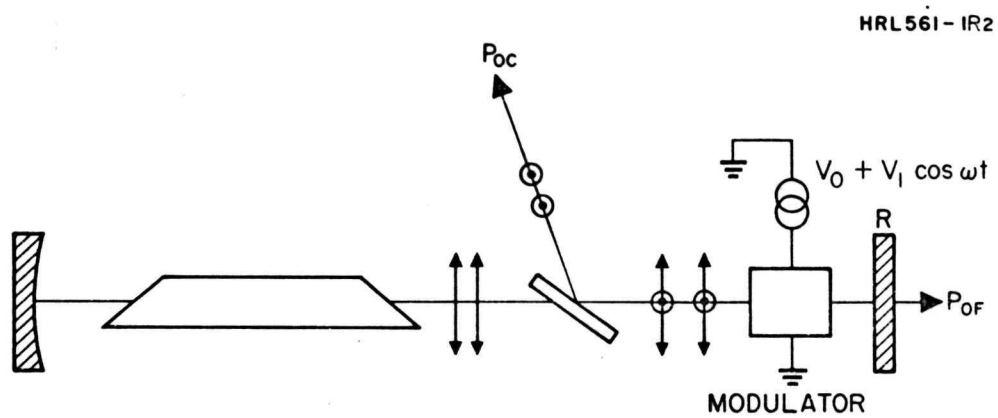


Fig. 2-10. Coupling Modulation.

and the coupled power P_{oc} for coupling modulation is

$$P_{oc} = (1 - 2\alpha_m - \alpha_2 - C_o)P_c C_m.$$

where C_m is the modulator coupling.

Figure 2-11 is a plot of laser output power as a function of output mirror coupling for the FM case. Three values of modulator loss are assumed. Figure 2-12 is a plot of the ratio of the output power of the laser with modulator to that with no modulator as a function of modulator loss for three values of mirror transmission.

2.4 MECHANICAL DESCRIPTION

Figure 2-13 shows a section drawing of the assembled modulator laser interface. The main parts of the modulator are identified. During the assembly, the modulator rod is first bonded to the electrodes. Figure 2-14 shows a rod assembly bonded to lead electrodes for an optical FM modulator where acoustic damping is important. Metallized ceramic sections form the electrodes for the coupling modulator where wide bandwidth is required.

The bonded modulator rod/electrode assembly is placed on a block of beryllia (BeO), and another block of beryllia is placed over the assembly. These sections then are tightly bolted together. The crystal does not suffer mechanical strain, however, since the electrodes are slightly wider than the rod.

The next phase of the assembly is shown in Fig. 2-15. Heating elements are bonded to the beryllia block assembly and connections made to the modulator electrodes, heater element, and thermistor. The fiberglass support mount is then placed around the beryllia block and the unit is slid into the modulator housing cylinder. A threaded cap flange holds the entire unit together. The final assembled modulator is shown in Fig. 2-16.

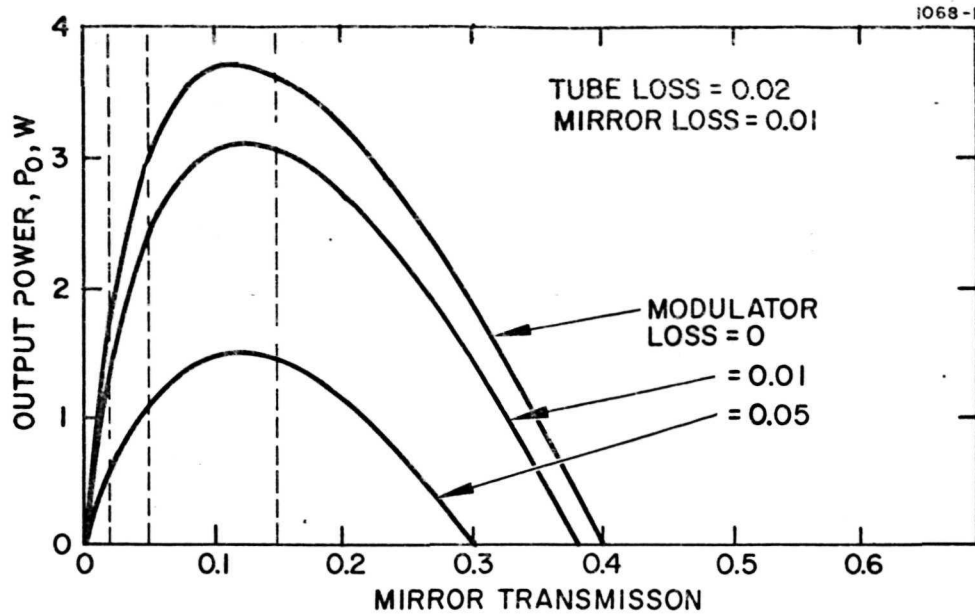


Fig. 2-11. Theoretical Laser Output Power Versus Mirror Coupling For Internal Modulator Loss Equal to 0, 0.01, and 0.05.

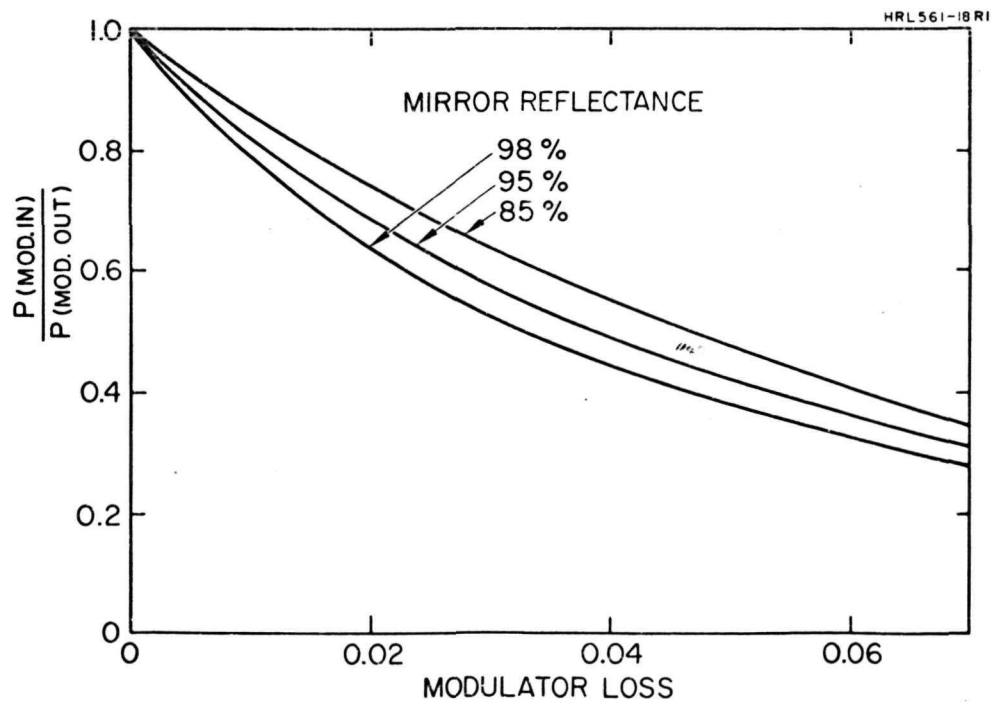


Fig. 2-12. Effect of Internal Modulator Loss on Laser Output.

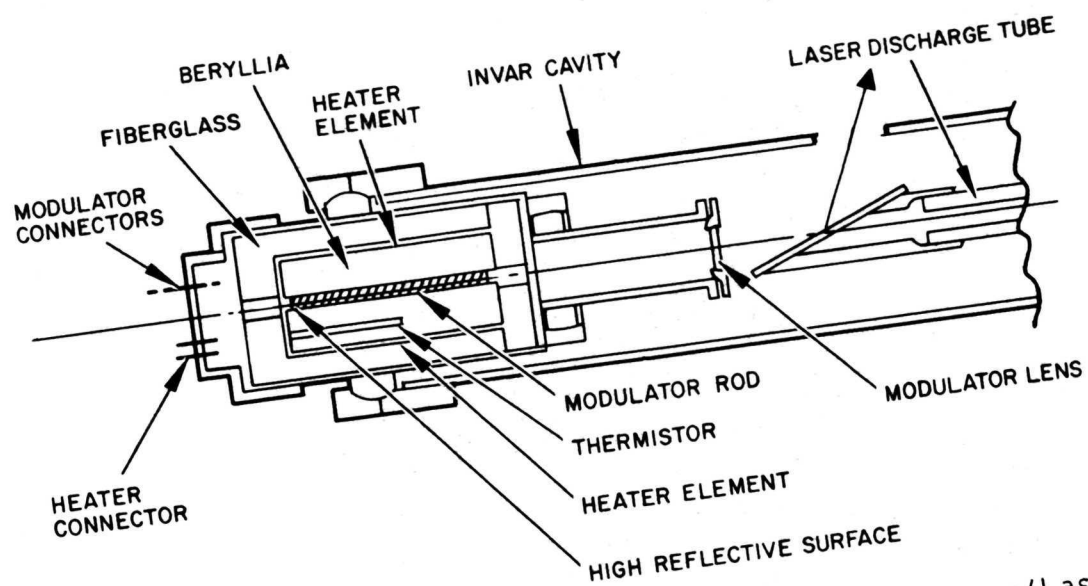


Fig. 2-13. Section Drawing of Assembled Modulator/Laser Interface.

M8814

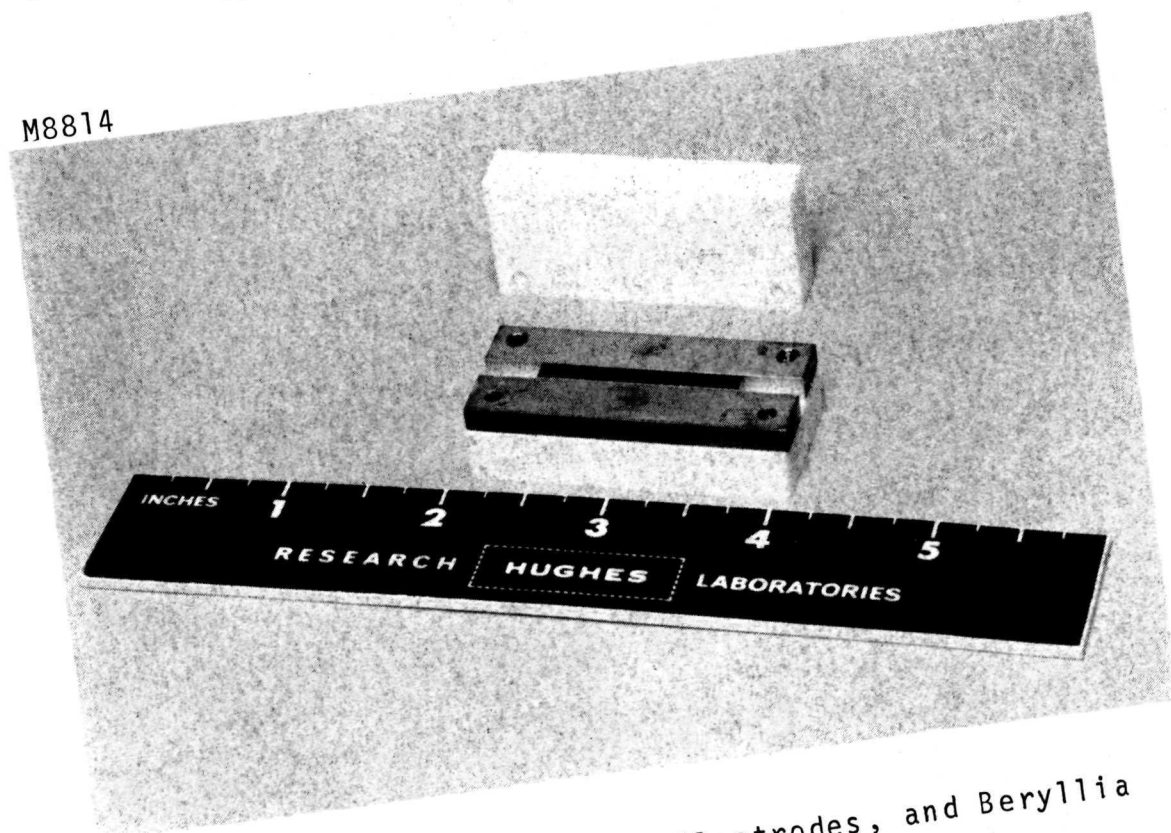


Fig. 2-14. Modulator Rod, Electrodes, and Beryllia Blocks.

M8999

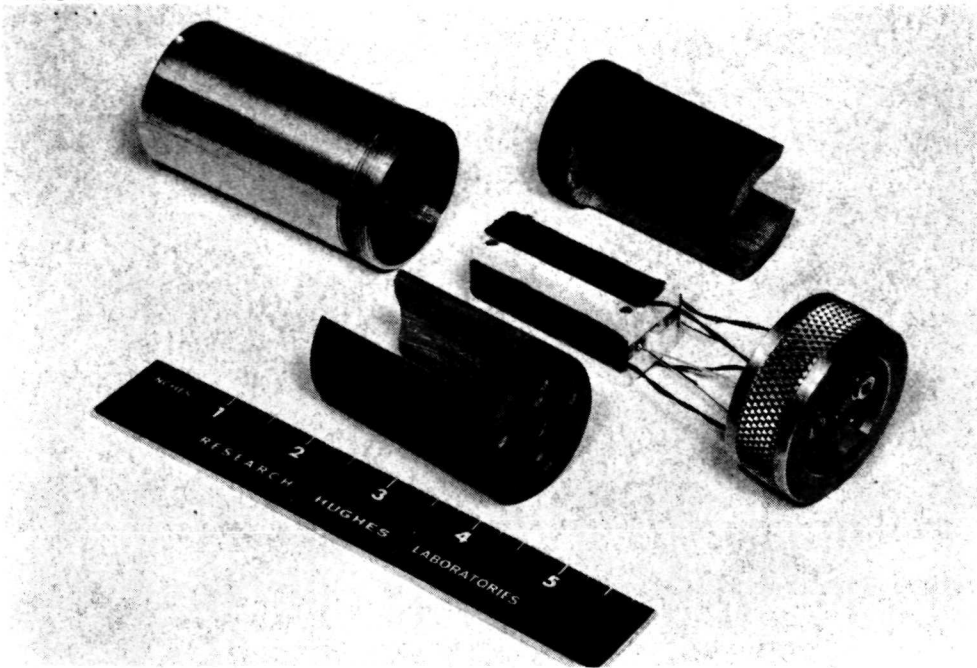


Fig. 2-15. Data Modulator During Assembly Showing Printed Circuit Heating Elements.

M9109

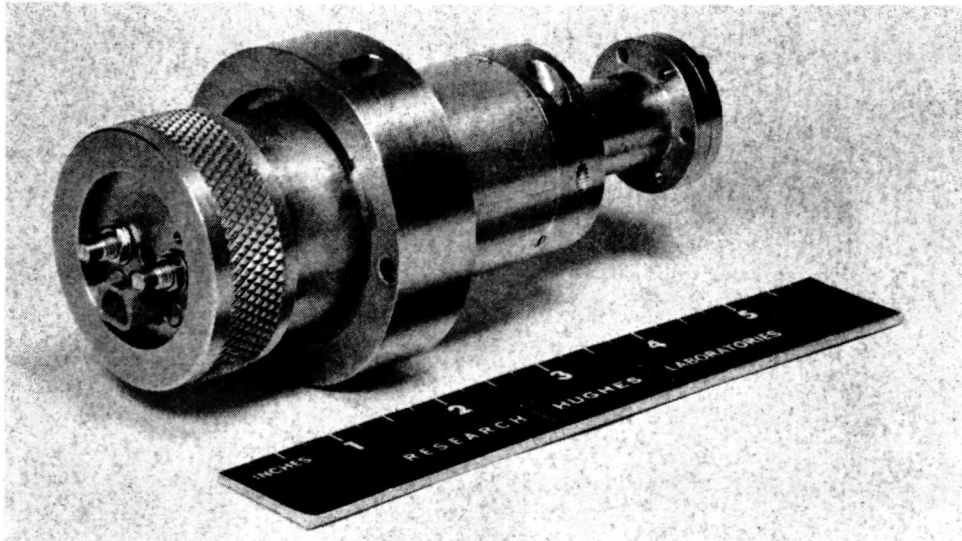


Fig. 2-16. Assembled Data Modulator.

2.5 MODULATOR TEMPERATURE CONTROLLER

Since the modulator crystal is several centimeters in length, it introduces a temperature-dependent phase shift on the order of 1 wavelength per degree centigrade temperature change of the crystal. The modulator temperature, therefore, must be regulated to some fraction of a degree centigrade.

The refractive index of CdTe varies as a function of temperature of the crystal by

$$\frac{1}{n} \frac{dn}{dT} = 4.4 \pm 0.3 \times 10^{-5} \text{ } ^\circ\text{C}^{-1}.$$

The resultant phase shift in the material of length l is

$$\delta\Phi = 11.3 \text{ } l\delta T \text{ for CdTe.}$$

The length of the modulator crystal is ~ 4 cm. Thus, a phase shift of $\delta\Phi \geq 0.4$ wavelengths occurs for every degree change in the CdTe temperature.

The electronic frequency stabilization of the laser oscillator will have the capacity to follow variations in the optical length of the cavity to at least 1.5 wavelengths. This requires that the modulator be stabilized to within about 0.5 wavelengths. The required temperature stabilization of the modulator is then

$$(\delta T)_{\max} = \pm 0.63^\circ\text{C}.$$

The laser modulator with its damping structure is enclosed in a 1 in. square BeO assembly with a thermistor temperature sensing element imbedded in the BeO, and a printed circuit heating element bonded to the outside (see Fig. 2-15). The temperature of the structure is easily regulated to maintain the required $\pm 0.63^\circ\text{C}$. A bread-board version of this oven structure was fabricated and tested to prove

the design. Performance of the oven under laboratory conditions exceeded the required performance by more than an order of magnitude. Data from these engineering design tests are given in Figs. 2-17 through 2-20.

Figure 2-17 illustrates oven performance over a period of approximately 20 min; the temperature of the oven was monitored with a thermocouple mounted within the structure. During this test, the temperature was lowered after a period of about 12 min to demonstrate the response of the oven. The temperature stability was $\pm 0.03^{\circ}\text{C}$ after 5 min and $\pm 0.012^{\circ}\text{C}$ after 10 min. Transient response is shown in Fig. 2-18, with a maximum temperature overshoot of 1.25°C .

To assure that the modulator crystal temperature remains constant, a CO_2 beam was transmitted through the uncoated CdTe crystal, and the amplitude of the energy was monitored. Since the crystal is not coated in these tests, interference between the two end faces of the crystal causes the amplitude to cycle each time the optical distance between faces changes by $\lambda/2$. Figure 2-19 shows the oven performance during warmup over a period of 30 min; Fig. 2-20 is a 1 hour run and during that time the oven power was interrupted for 10 sec. The oven maintained the optical length of the crystal within $\lambda/60$ during this run (except during the power interruption), implying a temperature change of less than 0.04°C .

The selection of the electronic proportional controller for the modulator temperature control was based on simplicity, reliability, and operational performance. The unit selected is Model 70, manufactured by RFL Industries, Boonton, New Jersey. This unit has been packaged in a control box to accompany the data modulator.

2.6 DATA MODULATOR PERFORMANCE TESTS

During the selection of the final modulator configuration, a number of steps were taken to verify the optimization and performance according to theory. The rod used for the data modulator was selected from four available rods. For the purposes of identification, the data associated with each rod are listed as follows:

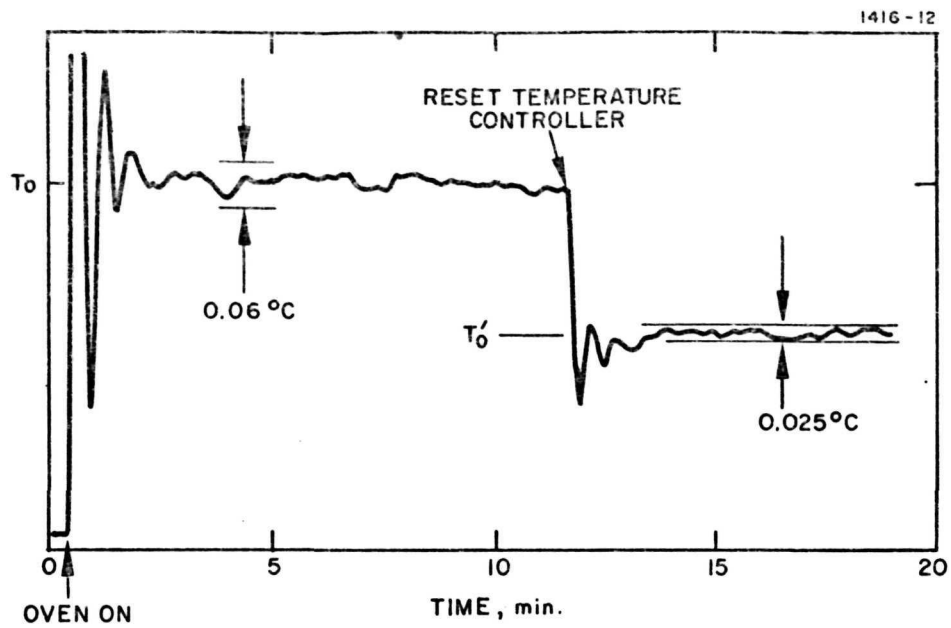


Fig. 2-17. Oven Performance.

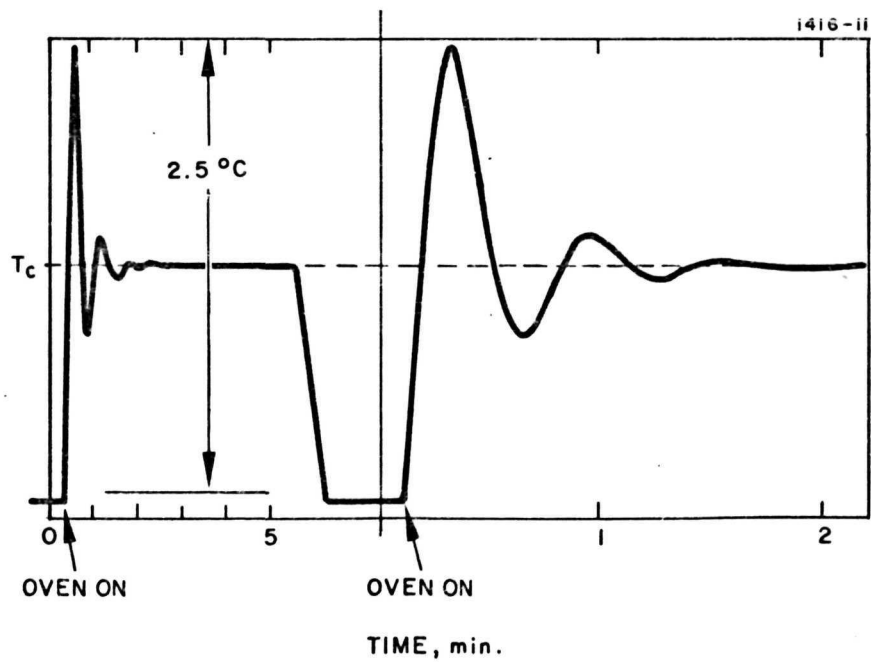


Fig. 2-18. Transient Response of Oven, 1.25°C Overshoot.

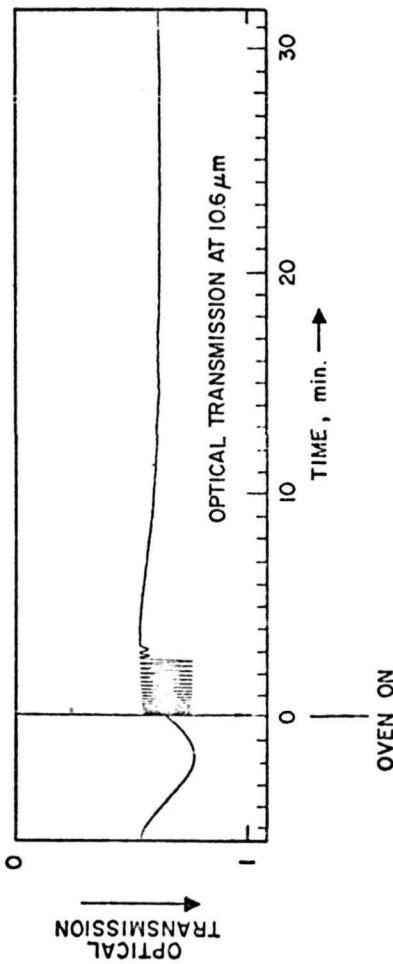
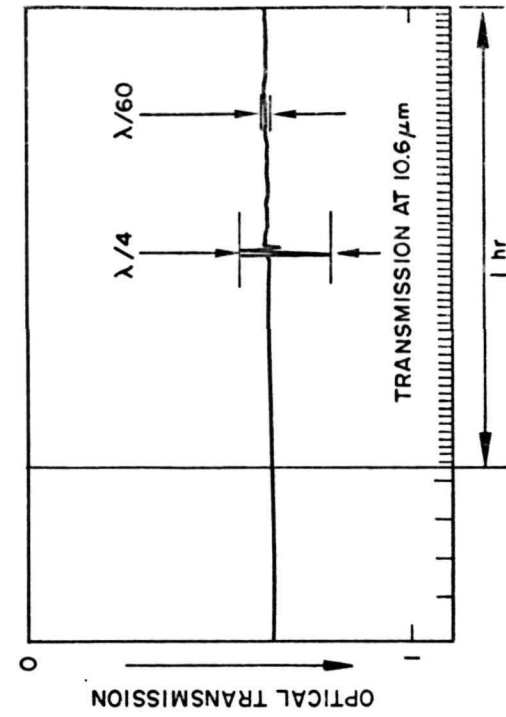
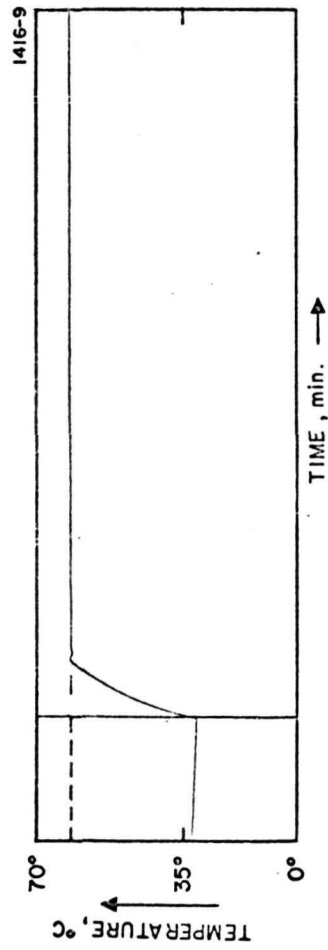
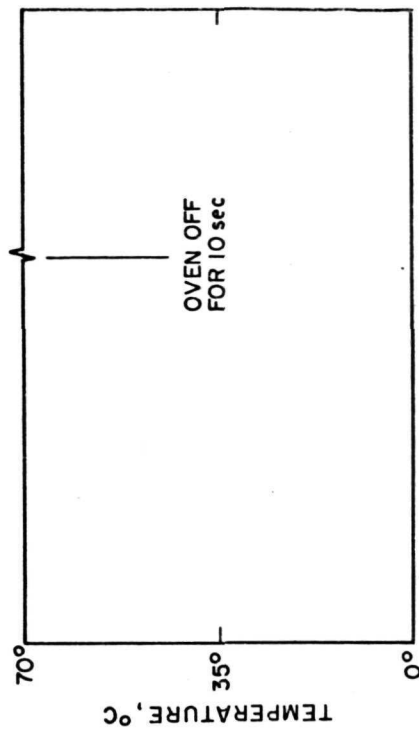


Fig. 2-19. Optical Transmission Through Oven During Warmup.

Fig. 2-20. Transmission During 1-Hour Test.

<u>Rod Number</u>	<u>Length</u>	<u>Thickness</u>	<u>l/d</u>	<u>Total Loss</u>	<u>Reflectance</u>	<u>Absorption</u>
5	4.8 cm	3 x 3 mm	16	~2 %	0.0064	0.008
6	4.3	3 x 3 mm	14.5	~2 %	0.0064	0.008
7	3.5	1.5 x 1.5	23	~2 %	0.0064	0.008
8	3.5	1.25 x 1.25	28	~2 %	0.0064	0.008
Lens	-	-	-	~2.8 %	0.0064	0.016
V-band	2.8	1.7 x 1.7		~2 %	0.0064	0.008

Each of these rods was AR coated on both ends; the above reflectance values refer to the percent of incident power reflected from one surface. The values for absorption are calculated from the total loss less the reflectance losses.

2.6.1 Laser Performance with Modulator in Cavity

As pointed out in Section 2.2, the performance of the laser is critically related to the losses in the cavity, particularly those related to the modulator rod and lens. These losses take the form of scatter, absorption, reflection, spherical aberration in the case of the lens, and diffraction. The measurement of losses in the rods listed above were made with a power meter and therefore do not take into account losses due to aberration or scatter. In order to determine the total effective loss, a series of measurements were made with modulator rods, lenses and combinations thereof located in a laser cavity. The performance of the laser was measured with a conventional flat mirror and also with the other intracavity elements.

The gain of the laser was measured to be 33% for a current of 0.015 A and a gain of 25% for a current of 0.010 A. The laser was tested with a standard partially transmitting germanium mirror, having a transmission of 6% and a reflectance of 92.5%. The absorption of loss of the mirror is 1.5%.

Using the relation between circulating power in a cavity, P_c , saturation power P_s , laser gain $g_0 L$, and losses α given in Section 2.3, the ratio of circulating power to saturation power can be written

$$\frac{P_c}{P_s} = \frac{1}{2} \frac{(1 - a) \left[g_o L + \frac{1}{2} \ln(1 - a) \right]}{\left[1 + (1 - a)^{1/2} \right] \left[1 - (1 - a)^{1/2} \right]}$$

where a in the equation is the total two way loss in the lens, modulator, and output mirror, $a = c_o + 2a_m + 2a_l$; c_o is the output coupling of the end mirror, a_m is the single pass loss in the modulator and a_l is the single pass loss in the lens. The above equation is plotted in Fig. 2-21 showing two curves, one for a tube gain of 33% and one for a gain of 25%.

The performance of the laser under the various conditions is given as follows:

<u>Tube Current</u>	<u>Laser Power Out</u>	<u>Configuration</u>
0.010 A	2.8 W	6% mirror
0.010 A	1.6 W	6% mirror + lens
0.010 A	1.1 W	6% mirror + lens + modulator rods 5, 6, 7

The points shown in Fig. 2-21 represent the above performance data when plotted. From these data, the effective two way losses of the lens and the modulator rods can be estimated. These values are

<u>Element</u>	<u>Two Way Loss</u>	<u>One Way Loss</u>
CdTe Lens	3.4%	1.7%
Modulator	3.6%	1.8%

The values of circulating power for the experimental points are 47 W, 27 W and 16.7 W respectively.

Since the 7.5% loss introduced by the output mirror in these tests can be eliminated in the final modulator configuration, this curve can be used to estimate the circulating power for such a modulator plus lens combination. Figure 2-22 shows the curve for the laser operating at 0.015 A tube current. This value was chosen as an optimistic performance of a new tube at 0.010 A. The measured performance

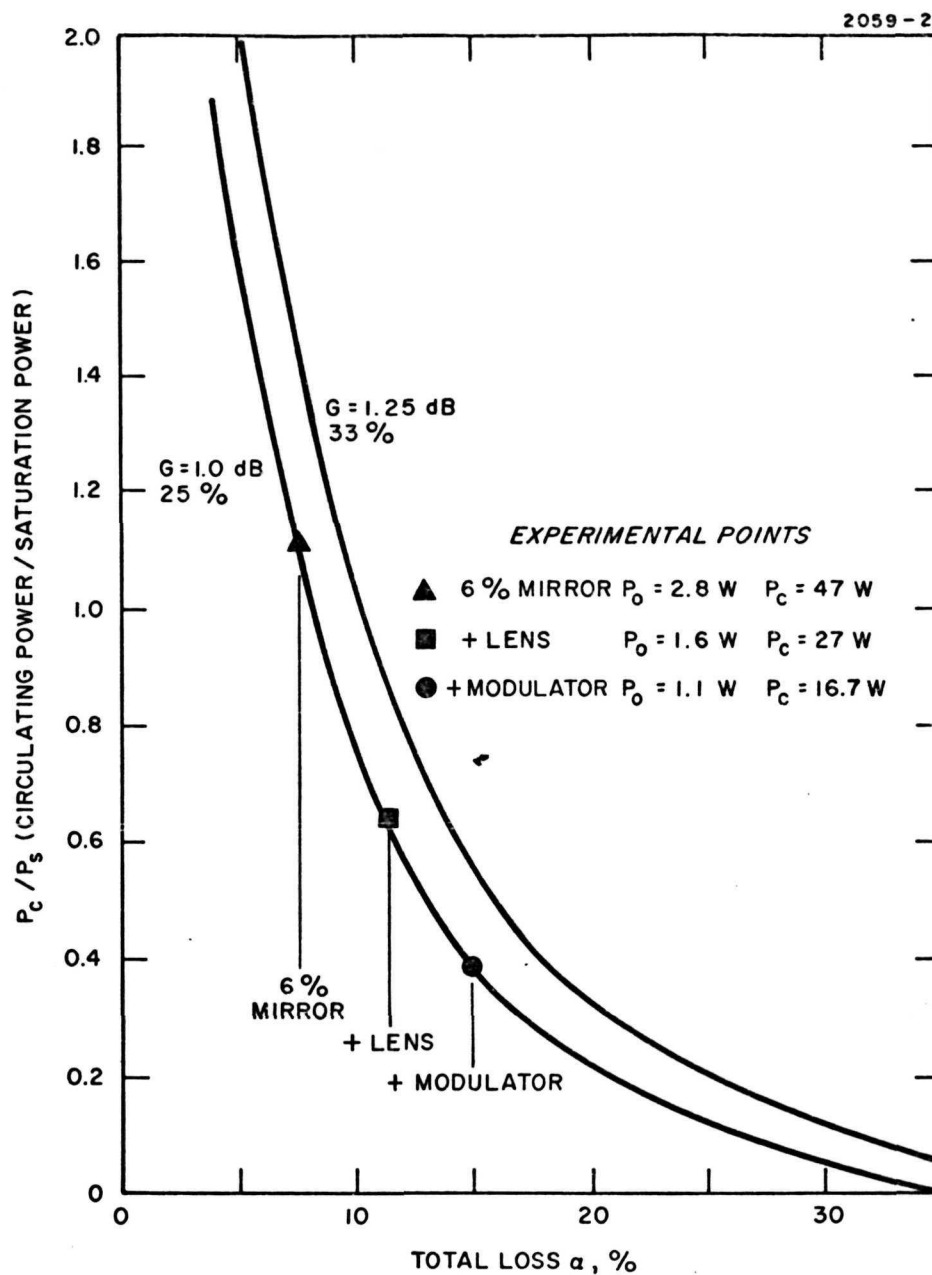


Fig. 2-21. Laser Performance With Modulator and Lens in Cavity.

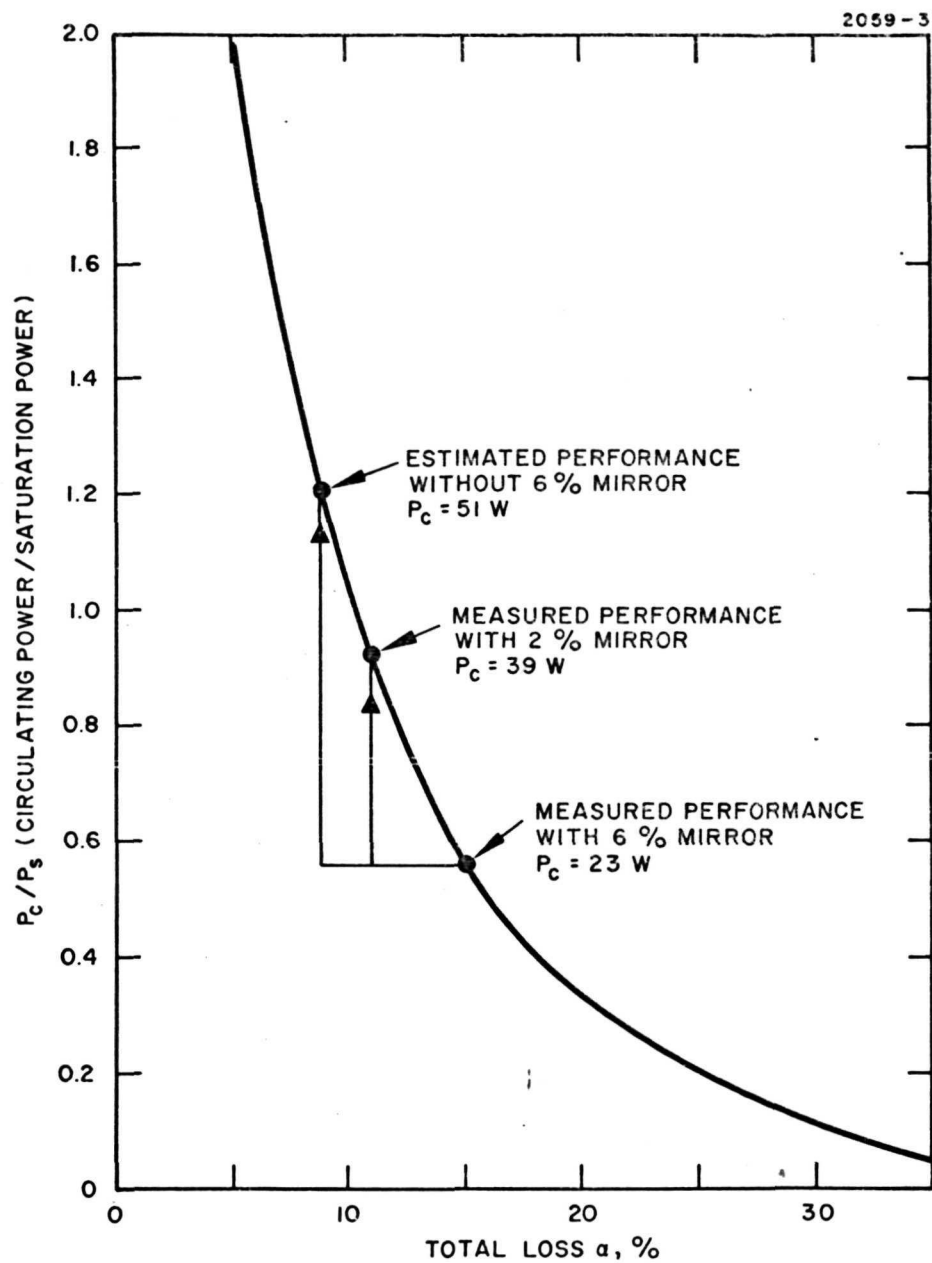


Fig. 2-22. Estimated Performance of Laser With Optimized Lens and Modulator.

shows a circulating power of 23 W. Eliminating the 6% loss due to the output mirror moves the point higher on the curve. The calculated circulating power for these conditions is $P_c = 51$ W.

Alignment of the laser, lens, and modulator in the cavity is relatively easy provided the end mirror of the cavity is partially transmitting.

Modulator rod No. 5 was coated with an antireflection coating and a germanium 98% mirror placed at the end of the rod in the modulator structure. This arrangement permits sampling the laser circulating power during alignment and during measurements. Using the 98% output reflector, the operating point is somewhat lower than the optimistic point shown in Fig. 2-22, giving an estimated circulating power of about 39 W.

2.6.2 Measurement of Modulator Retardation

a. dc Term

The retardation Γ of the modulator is related to the applied voltage by $\Gamma = \Gamma_o + \Gamma_m \sin \omega_m t = \pi/V_\pi \ell/d(V_o + V_m \sin \omega_m t)$. The optical output of the laser is related to the dynamic retardation as shown in Appendix C. For the purposes of measurement, a sinusoidal modulation voltage is assumed and the coupled output power for the dc and first harmonic terms is

$$\begin{aligned} \text{dc term } P_{dc} &= kP_c \left\{ \frac{1}{2} 1 - \cos(2\Gamma_o) J_0(2\Gamma_m) \right\} \\ \omega_m \text{ term } P_\omega &= kP_c \left\{ \text{sinc}(2\Gamma_o) J_1(2\Gamma_m) \sin \omega_m t \right\} \end{aligned}$$

The optical power which is rotated by the modulator is coupled out of the cavity by the Brewster window of the laser. For these lasers, the windows are cadmium telluride having a refractive index of $n = 2.67$.

The percentage of optical power coupled out is calculated to be 57% times the amount rotated, or

$$\begin{aligned} \text{dc term } P_{\text{dc}}/P_c &\cong 0.284 \left[1 - \cos\left(\frac{2\pi}{V_\pi}\right) V_o \right] \\ \omega_m \text{ term } P_w/P_c &\cong 0.57 \left[\sin\left(\frac{2\pi}{V_\pi}\right) V_o \right] \left[\frac{\pi}{V_\pi} V_m \right]. \end{aligned}$$

In order to evaluate the dc term, we assume V_m is zero and plot the coupling coefficient for the three modulator rods of interest as shown in Fig. 2-23. A block diagram of the data modulator performance test setup is shown in Fig. 2-24.

Experimental measurements of the dc coupling factor with the application of dc voltage have not yielded the predicted results. The actual amount of optical power coupled out with the application of 1000 V dc is in the order of a few milliwatts. These results were the same for several crystals. Efforts to reconcile these results with past dc tests are currently being considered. Because of risk of damage to the crystals due to electrical breakdown, the dc tests have been limited to 1 kV dc.

The dynamic coupling factor, or ω_m term, is zero when there is no dc bias. The use of the modulator as an AM modulator however, depends upon having a given amount of bias. Since the application of dc does not provide this, the dc bias must be provided by a fixed birefringence. Usually, there is some optical leakage flux from the residual birefringence in the modulator rod and it is practical to use this leakage in lieu of the dc-induced birefringence. In fact, a value of equivalent Γ_s may be calculated from the static birefringence

$$\begin{aligned} \frac{P_{\text{leakage}}}{P_c} &= 0.284 \left[1 - \cos 2\Gamma_s \right] \\ \Gamma_s &= \frac{1}{2} \cos^{-1} \left\{ 1 - 3.5 \frac{P_{\text{leakage}}}{P_c} \right\}. \end{aligned}$$

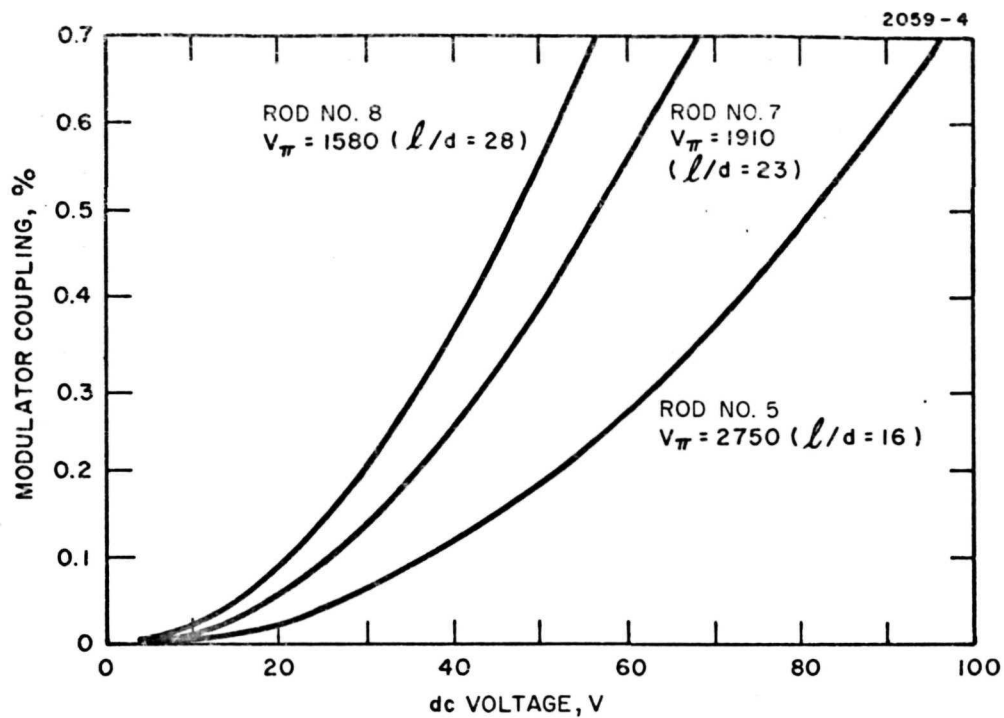


Fig. 2-23. Theoretical Static (dc) Coupling Factors for Three Modulator Rods.

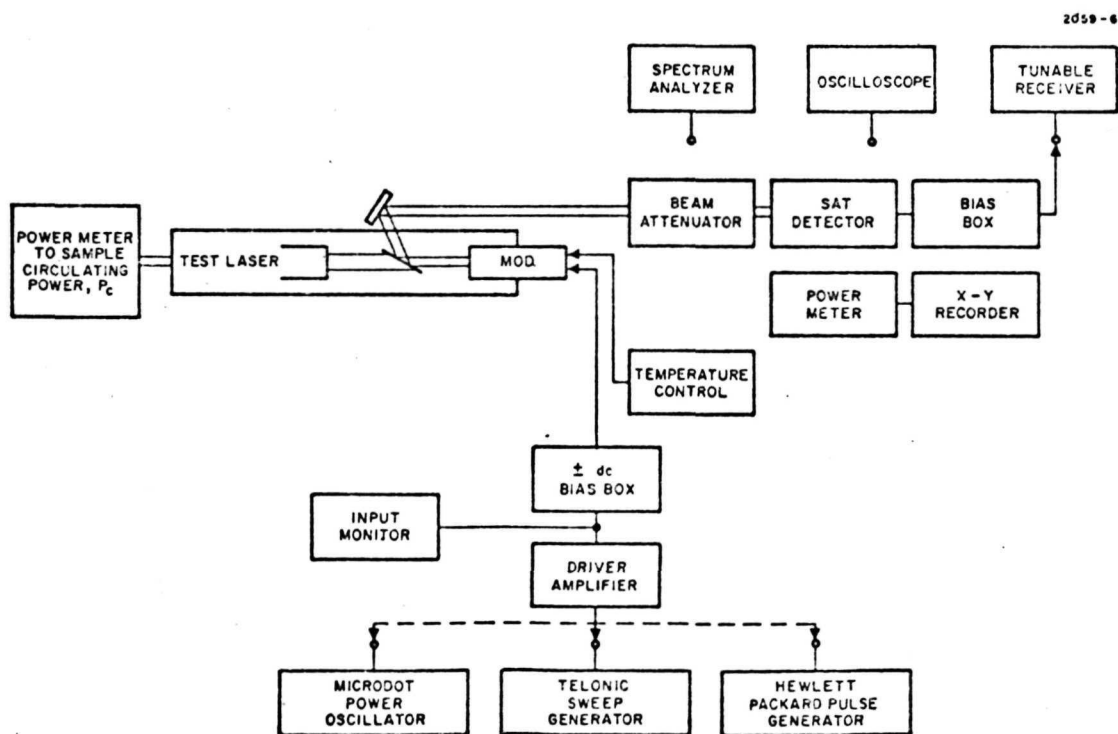


Fig. 2-24. Block Diagram of Data Modulator Performance Test Setup.

A typical value of leakage power is 0.020 W giving a value for Γ_s of 4.7×10^{-3} . This amount of leakage is equivalent to 4.1 V of dc bias.

b. ac Term or Dynamic Retardation

Section 2.2.4 showed that the modulated output power of a coupling modulator in the first sidebands is

$$P_t = kP_c \Gamma_m^2 .$$

It can also be shown that the total power coupled out of the device is

$$P_t = \frac{E_o^2}{2} \left[1 - J_0(2\Gamma_m) - 2J_2(2\Gamma_m)(\cos 2\omega_m t) + \dots \right]$$

which, to a first approximation, reduces to the same value. Expanding this expression for modulator rod No. 7, we have

$$P_t = 1.07 \times 10^{-6} V_{rms}^2$$

where the circulating power in the laser is measured at 35 W, the l/d ratio of the modulator rod is measured at 23. The curve in Figure 2-25 shows the theoretical power output from the laser Brewster window as a function of rms driving voltage. The points in the figure represent the actual measured output power using an optical power meter. The measured performance of the coupling modulator closely follows the predicted performance, except for lower voltages where the leakage power of about 15 mW is added to the measured power and at the higher voltages the circulating power in the laser cavity begins to fall off.

For a driving voltage of 50 V, the measured circulating power was reduced to about 30 W.

The close agreement of the data points and the predicted curve demonstrate the dynamic retardation of the coupling modulator. Further, a coupled power of 0.3 W DSBSC power represents an equivalent of 0.6 W of 100% modulated carrier. These values meet the practical objectives for wideband modulation of a CO₂ laser for the laser space relay communication experiment.

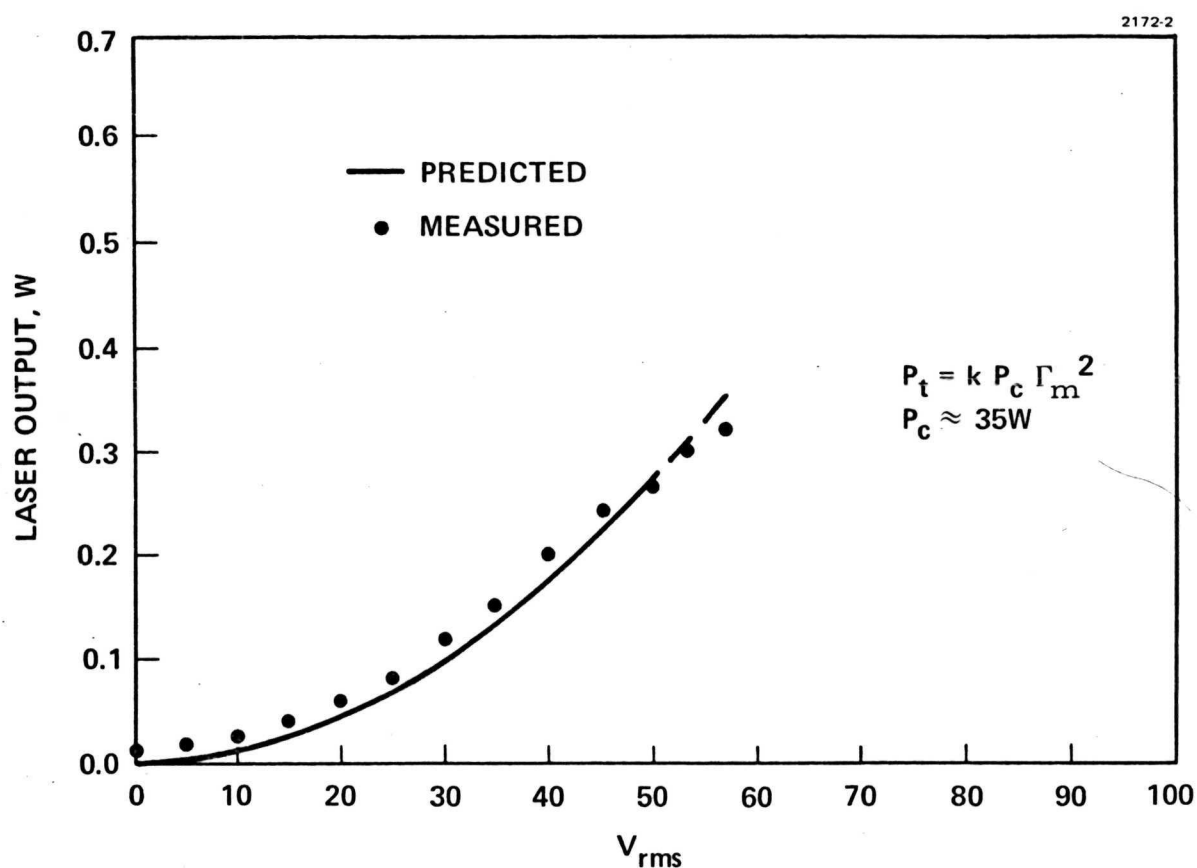


Fig. 2-25. Predicted (Curve) And Measured (Points) Output Power From Laser as a Function of Driving Voltage.

SECTION 3

CADMIUM TELLURIDE MATERIAL DEVELOPMENT

3.1 SUMMARY OF RESULTS

At the beginning of the present program, cadmium telluride had been produced in sample quantities and had been sufficiently evaluated to show that the material had superior electro-optic properties for the modulation of 10.6 μm light. The electro-optic coefficient is a factor of two greater than that of gallium arsenide. Absorption loss measurements showed that its loss properties were significantly less than those of GaAs. A single crystal rod of 3 cm length had been produced. Since the full capabilities of 10.6 μm CO_2 lasers in communication systems could be realized only by improvements in electro-optic devices, a great portion of the effort from the present program was devoted to the development and refinement of the material. The goal was to produce a minimum of 20 boules of the material aimed at achieving improved crystallinity, lower loss, and improved strength of the single crystals for use in developing modulators. These ambitious goals were met with severe problems; as with any new semiconductor material, the art of producing the material is learned slowly.

Parallel efforts in cadmium telluride material development were supported by ONR under Contract N00014-70-C-0303, and AFML under Contract F33615-71-C11778. The ONR contract was related to the development of CdTe for modulators, whereas the AF contract was for the development of high power windows for 10.6 μm . To meet the needs of the above programs, as well as the present program, a substantial increase in the production capability was needed. Several new furnaces were developed to meet these needs.

Initial production resulted in crystals of poor crystallinity. Although the loss and strength properties of the material were acceptable, in general the largest single crystal obtained during the first

six months of production was the order of an inch in length. Several modulator rods were fabricated, electroded, and coated.

The electrical properties of the modulator crystals were seriously altered during the coating process. After careful evaluation, it was learned that improved process control of the substrate temperature during the coating process eliminated alteration of the crystal electronic properties. At about the same time, larger crystals were being obtained from the furnaces. New modulator rods were fabricated from larger crystals, new coatings applied, and finally the rods were assembled into modulators. The problems with the material development resulted in inevitable delays, which forced the experimental portion of the program to be extended.

The results and achievements of the material development program, in the final analysis, exceeded the goals by a substantial margin. Modulator crystals greater than 5 cm were produced. A heat treating process was developed that minimizes loss of the material at 10.6 μm . One recent sample showed an absorption of 0.00089 cm^{-1} .

As one of the requirements of the program, samples of each of the boules grown for the present program were sent to Langley Research Center for low temperature spectral analysis. The principle results of the low temperature measurements was that most samples were exceptionally free of impurities. Oxygen and aluminum doped samples were also examined with the intention of correlating these impurities with the spectral properties of the samples. However, the results of these analyses were inconclusive. In one case, iron was definitely identified as an impurity, although its presence did not have noticeable effect on the gross absorption properties.

The following sections give a detailed account of the cadmium telluride crystal growth technology including phase equilibrium considerations, description of the modified Bridgman technique, and the thermal annealing technique. One section is exclusively devoted to crystal evaluation techniques.

3.2 CADMIUM TELLURIDE CRYSTAL GROWTH

3.2.1 Phase Equilibrium Considerations

Cadmium telluride tends to undergo stoichiometric variations³ in the growth and cooling procedure; these variations are factors in the determination of what the electrical properties, especially conductivity and type of conduction, will be.

A look at an expanded phase diagram in the region of interest, i.e., the existence region (Fig. 3-1), shows that the maximum melting point of cadmium telluride is not the stoichiometric composition; the composition of the maximum melting point varies with the constituent pressure above the melt. If a certain vapor pressure of the component (e.g., Cd) is maintained above the melt, the system has a tendency to grow at the composition corresponding to the applied vapor pressure. As solidification proceeds, the segregation process tends to make the melt more and more concentrated with regard to the component present in excess. However, as this occurs the liquid is no longer in equilibrium with the vapor; a reaction between vapor and melt sets in until equilibrium is again reached. The end result is dependent on the rate at which the composition changes as a consequence of the segregation, compared with the rate at which atoms are transferred between the melt and the vapor. A steady state eventually will be reached in which the crystals will attain a composition between the maximum melting composition (e.g., A for $P_{Cd} = 0.8$ in Fig. 3-1) and the stoichiometric composition.

In the modified Bridgman technique these conditions (e.g., composition, component overpressure) can be altered to produce CdTe that is stoichiometric, cadmium-rich, or tellurium-rich.

The modified Bridgman technique was developed⁴ primarily to grow high resistivity material for optical modulators, gamma detectors, and infrared windows. High resistivity material is readily obtained when deep levels in the band are filled with electrons from donor impurities. The addition of a donor to the melt causes the entire

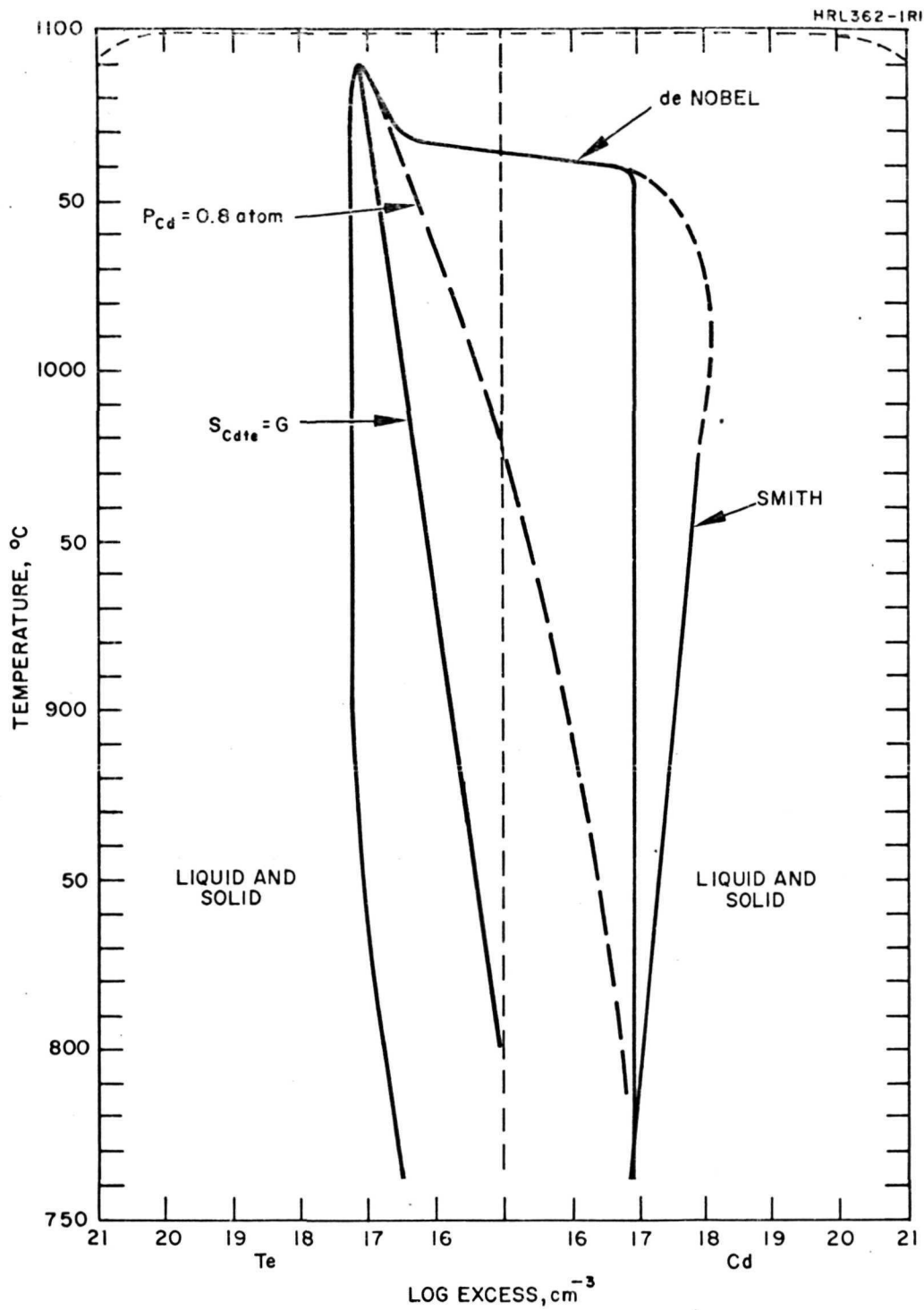


Fig. 3-1. Expanded Phase Diagram of CdTe.

tellurium-rich side of the phase diagram (Fig. 3-2) to yield high resistivity material when rapidly cooled (quenched) to room temperature from elevated temperatures as indicated in the diagram. Obviously, if the material is slowly cooled, it will move into the low resistivity region to the right of the line in Fig. 3-2, which represents the amount of indium dopant in the crystal. By proper selection of the quench point, high resistivity CdTe is obtained over a range of conditions making extremely critical control of pressure, quench temperature, or donor (e.g., indium) concentration unnecessary. Typical results of this process are shown in Table 3-1. In addition, slowly cooled material (low ρ) within certain size limits, may be thermally annealed after growth and subsequently quenched to yield high resistivity material.

TABLE 3-1

Resistivity as a Function of Growth Conditions

Ingot	Resistivity, Ω -cm	Indium, cm^{-3}	Atmosphere	Pressure, atm
21	10^7	2.4×10^{17}	Cd	1
22	10^7	2.5×10^{17}	Cd	1
24	10^7	2.5×10^{17}	Cd	1
25	10^7	5×10^{17}	Cd	1
01	10^5	1.9×10^{18}	Cd	2.1
37	$10^8 - 10^9$	2.5×10^{17}	Te	0.84
38	10^7	2.5×10^{17}	Te	0.84
35	10^8	1.7×10^{17}	Te	0.5

T182

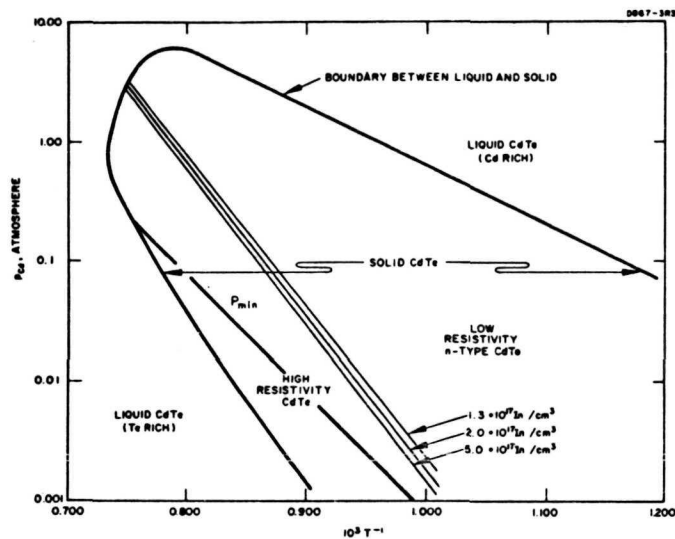
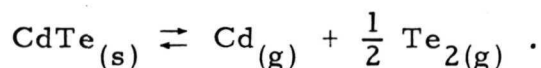


Fig. 3-2. Dependence of CdTe Melting Point on Cd Pressure.

3.2.2 Cadmium Telluride Purification and Preparation Techniques

Purification of the starting material is a very important part of the crystal growing process. Many methods for obtaining pure CdTe have been reported, but much of the early work which involved purification of the elemental constituents by sublimation and zone refining was necessary because high purity cadmium and tellurium could not be obtained commercially. This is no longer the case; the elements can now be obtained with a minimum purity of 99.9999%. Zone refining the compound is not an efficient means of obtaining high purity crystals because the segregation coefficients of most impurities in CdTe are about 0.5 and that of aluminum is actually greater than one. When impurity segregation coefficients are close to unity, many zone passes are necessary to reach a given purity level, and the time required intensifies the problem of contamination by the container. For these reasons, purification of the compound by sublimation was chosen as the most promising technique.

Purification by sublimation is more rapid than zone refining, and less chance of container contamination exists because no melt is involved and the temperatures are low. In addition, the compound recombines stoichiometrically³ according to the equation



Therefore, any excess cadmium or tellurium can be segregated because the vapor pressures of cadmium and tellurium are much higher than that of CdTe.

Purification by sublimation is based on a distribution equilibrium between the solid and gas phases. Impurities that are nonvolatile will be effectively segregated, and those that are volatile will be in equilibrium with the sublimate and condensate. Starting with the purest cadmium and tellurium available (at least 99.9999%), the components are reacted to form the compound CdTe and then sublimed to purify it. This is a one-step process which takes place in a closed evacuated

tube (Fig. 3-3). Starting with cadmium and tellurium, near-stoichiometric amounts are placed in a long quartz tube which has been cleaned in electronic grade HF-HNO₃, washed in deionized water, and coated with pyrolytic carbon. The deionized wash consists of a closed system of circulating deionized water which continuously passes through a deionizer. After the tube is loaded, it is sealed off under a vacuum of 10⁻⁷ Torr.

The tube is initially lowered partially into the furnace until the heat is sufficient to start the reaction of cadmium and tellurium. The reaction is exothermic and proceeds rapidly. When the reaction stops, the tube is then lowered completely into the furnace and withdrawn at 0.25 in./hour.

There is no attempt to clean the material mechanically or chemically. This method reduces contamination by minimizing handling. In addition, the CdTe sublimate is heated in the sublimation tube under a hydrogen atmosphere at 800°C. This is done to remove any oxides, thereby preventing removal of the pyrolytic carbon coating by oxidation. In addition, the material is prevented from sticking to the tube through the reaction of silica with the oxide. It is important that the material does not come in contact with the fused silica container, because the container has been found to be a source of contamination. A direct correlation has been found between the impurities in the fused silica tubes and the impurities in CdTe crystals. Consequently, synthetic quartz, which has the lowest impurity content of any available tubing, is used to grow the single crystals.

3.2.3 Modified Bridgman Technique

The optimum growth conditions for producing high quality, large, single crystals of CdTe are determined by rate of growth, growth temperature, temperature gradient, and rate of cooling of the ingot.

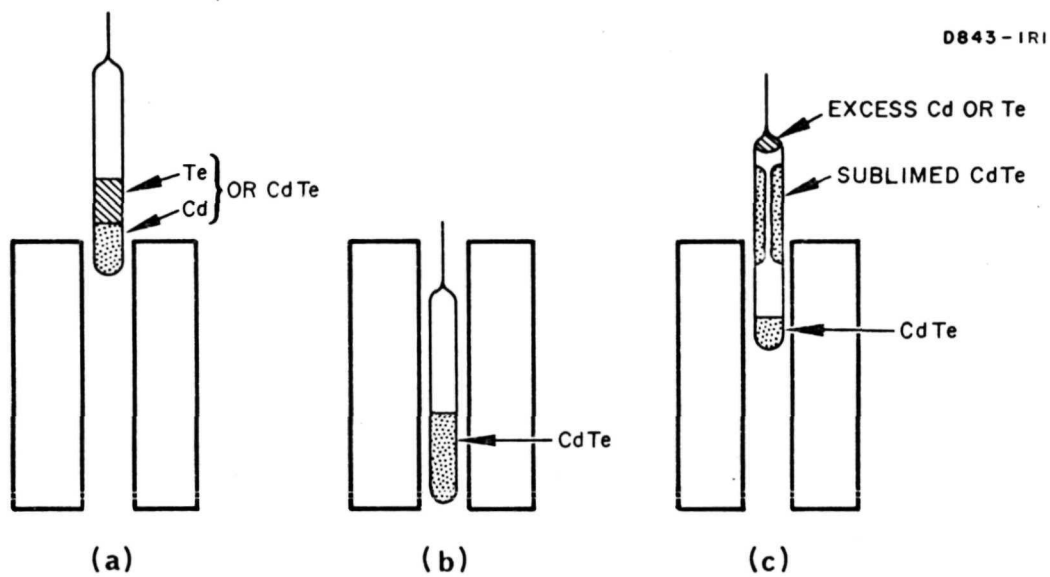


Fig. 3-3. Preparation and Purification of CdTe.

The following general conditions for crystal growth by the modified Bridgman technique have been determined as a result of numerous investigations:

- A sharp temperature gradient in the growth zone is necessary for an axial flow of heat. Crystals grown through a shallow gradient are invariably polycrystalline. We currently use a gradient at the melting point of CdTe of $20^{\circ}\text{C}/\text{cm}$.
- A flat axial profile is required to minimize the radial flow of heat and thermal convection in the melt.
- A slow growth rate is necessary to avoid rapid cooling of the surface, which would result in a concave solid-liquid interface in the direction of growth. (A convex interface in the direction of growth is considered ideal.) The thermal conductivity is the dominant factor determining growth rate. Thus, for materials having low thermal conductivity, the growth rate must be slow. For CdTe, a concave shape was obtained for growth speeds much greater than 0.20 in. /hour. In addition, at speeds much greater than 0.20 in. /hour, the dislocation density increases rapidly. If the crystals are grown very slowly to minimize the dislocation density, the seeds which form initially propagate linearly through the crystal along the growth axis. The speed is then too slow for the fastest growing crystal plane to dominate. As a result, an optimum speed of 0.10 to 0.20 in. /hour is used.
- Crystals of approximately 1-in. diameter minimize radial temperature fluctuations across the ingot because of their large mass.
- The crystal must be rotated if the furnace is not symmetrical. Rotation will smooth out the asymmetry of the furnace and minimize radial fluctuations.
- The solid-liquid interface can become concave if the melt temperature is run well above the melting point of the material. A temperature of 5 to 10°C above the melting point is ideal.

- The pressure of one of the components above the melt as used in the modified Bridgman technique also affects the crystallinity. In particular, when the cadmium pressure was much above or below 1 atm, the crystallinity degenerated.
- Six different geometric configurations of quartz crucibles have been tested to determine whether the different methods of crystal nucleation and slopes of the tube had any effect on the crystallinity of the material. Recently one showed a particular advantage for the growth of CdTe.

Because CdTe readily dissociates at high temperatures, growth from the melt requires a closed system. Although an ordinary Bridgman method of growth in a closed system can be used, there is little control over the electrical parameters and composition of the crystal. If the melt is off stoichiometry, the composition of the melt changes continuously as solidification takes place, thus changing the composition and resistivity of the solid as it grows.

Crystal growth of CdTe was pursued by the modified Bridgman technique. The main advantage of this technique is that the composition of the melt can be controlled. It also offers the advantages of uniformity of ingot size and greater uniformity of impurities in the direction transverse to the direction of growth. The growth tube is elongated (Fig. 3-4) so that cadmium or tellurium can be placed in a reservoir high in the tube, where vapor pressure can be controlled by a second furnace operating significantly below the temperature of the crystal furnace. Crystals of CdTe can be grown stoichiometrically, cadmium-rich, or tellurium-rich, by changing the pressure of one of the components. In practice, the Modified Bridgman tubes, made of synthetic quartz, are cleaned and coated with pyrolytic carbon. The sublimate is loaded into the tube and hydrogen is treated at 800°C to remove the oxides. Cadmium is placed within the reservoir of the tube, the tube is sealed under a vacuum of 10^{-8} Torr, and lowered through the crystal growth furnace. When CdTe is prepared at specified temperatures, with appropriate overpressures of its components and with $10^{17}/\text{cm}^3$ indium atoms or other suitable n-type dopants, the

resulting material is high resistivity. The region specifying these conditions is presented in Fig. 3-2. As shown in the figure, indium-doped CdTe grown at a pressure of 1 atm should have high resistivity if it is quenched rapidly to room temperature from a temperature of 900°C or higher. Since the ultimate resistivity is also influenced by quench rate, profile of the lower furnace, and rate of crystal growth, these factors must be controlled to optimize the as-grown crystal.

The platinum-wound modified Bridgman furnaces which satisfy the temperature profile conditions shown in Fig. 3-4 are illustrated in Fig. 3-5. A portion of typical boules of single crystal CdTe grown in this equipment is shown in Fig. 3-6.

Several modifications of the modified Bridgman technique were accomplished during the course of this study, which added to improved materials for use as modulators.

The crucible, which was developed for the growth of large ingots (5-cm diameter) of CdTe and which would yield the largest single crystals, consisted of an inner crucible of high purity synthetic fused silica (Suprasil) clad on the outside with regular fused silica (Amersil) and has a total wall thickness of approximately 1 mm. This is necessary because of the lower softening point of the synthetic fused silica (below the usually quoted 1200°C) because of the high OH content residual from the hydrothermal growth process. The softening point of synthetic quartz containers was variable and frequently observed to be close to the melting point of CdTe. The synthetic fused silica is significantly purer than the other grades, and therefore is necessary as an internal liner close to the melt (separated by a pyrolytic carbon layer). The thin wall has been proved to be required for maximum single crystal yield because of the greater ease of heat removal. In addition, a large conductive metal heat sink on the nose of the crystal greatly assists in the axial removal of heat; this was incorporated into the lowering mechanism of the growth furnace apparatus. Growth parameters including lowering rate and thermal gradient were adjusted to yield maximum monocrystallinity. Most runs were slowly cooled and allowed to run out of the bottom of the furnace before removal.

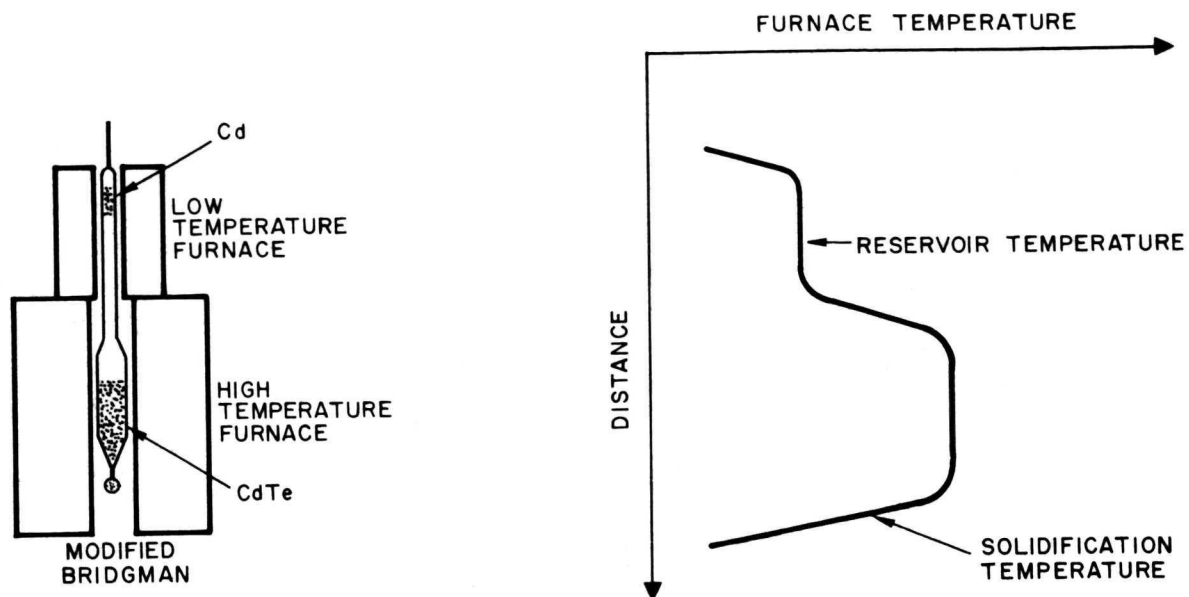


Fig. 3-4. Schematic of Apparatus for Crystal Growth.

M7848

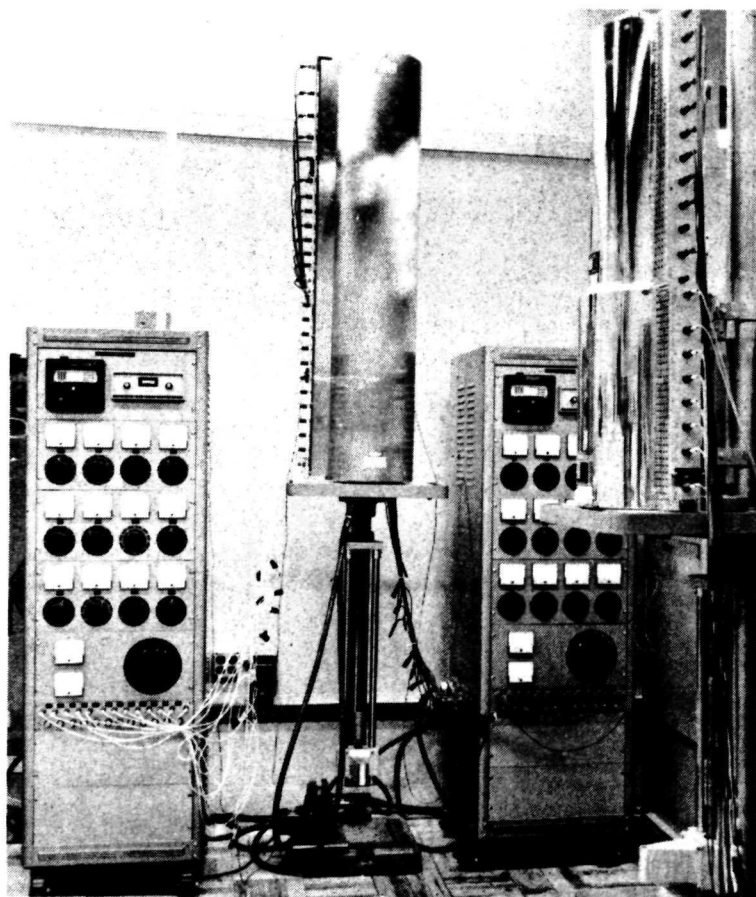


Fig. 3-5.
Modified Bridgman
Growth Furnace.

1843-4

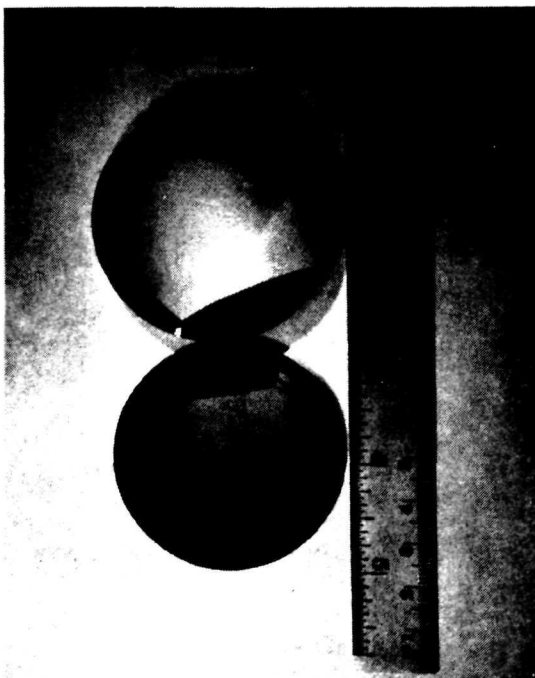
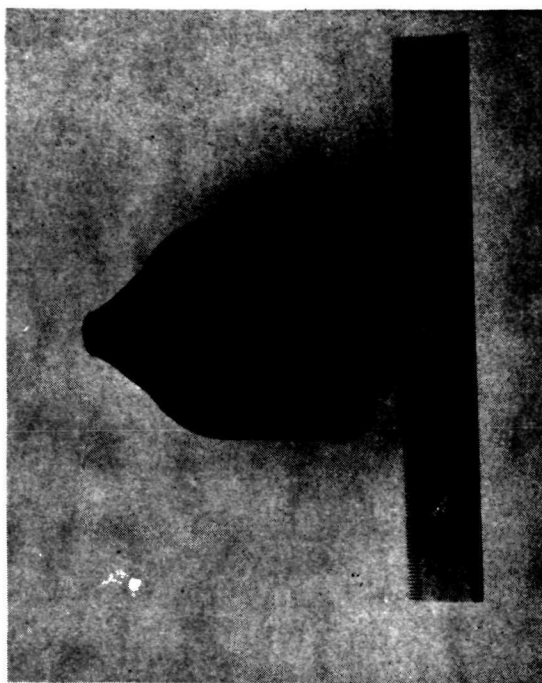
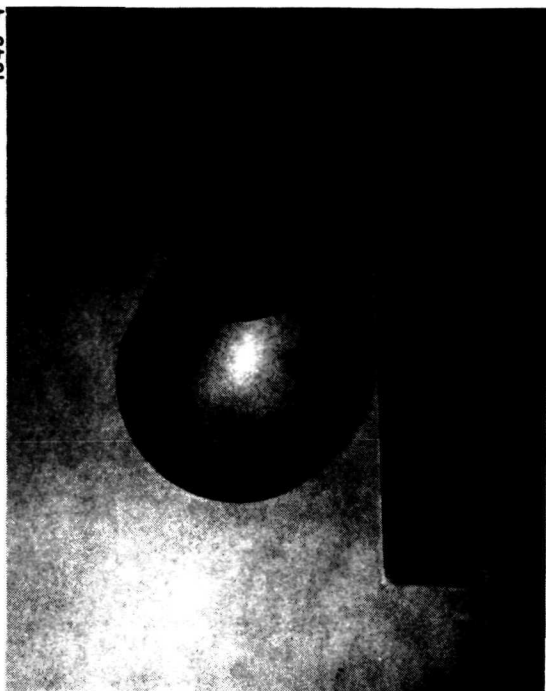


Fig. 3-6. CdTe Sample 226, 5 cm Diameter Ingot.

Although this technique yielded some of the largest single crystals of CdTe yet reported (see Fig. 3-6), problems persisted that resulted in cracking of the ampoule before sufficiently low temperatures were achieved and sometimes resulted in explosion. In addition, slowly cooled crystals required longer annealing times. Too often, single crystals of large sizes showed extensive cracking. Several causes observed for these results were (1) keying of the CdTe or cadmium coating (deposited over the ingot after or during solidification) to the walls of the crucible where the carbon coating was porous or somehow removed, (2) differential contraction (expansion) of a solidified ingot that sets in a sharp thermal gradient, and (3) deposition of large amounts of metallic cadmium onto the ingot by condensation of the excess cadmium from above. At the present time, large single crystals can be grown from which modulator rods as long as 5 cm x 5 mm x 5 mm can be cut. However, the problems have not yet been entirely solved.

3.2.4 Thermal Annealing

In the process of quenching under an atmosphere of one of the components, it is assumed that the atomic positions of vacancies and foreign atoms remain unchanged while the electrons and holes are free to redistribute themselves over the energy levels in the crystal. Consequently, quenching under a high cadmium pressure would introduce cadmium interstitials as the dominant donor. As the cadmium pressure is lowered, the concentration of cadmium interstitials decreases and the donor impurity (indium) becomes the dominant electron supplier. Further reduction in cadmium vapor pressure eventually results in a tellurium-rich crystal in which the dominant defects are cadmium vacancies rather than interstitials. The cadmium vacancy is an electron acceptor. When enough of these have been introduced so all the electrons from the donor impurity are captured in the quenching process, the n-type region of conductivity ends. The imperfections that trap electrons are thought to be cadmium vacancies with a single negative electrical charge (V'_{Cd}).

As the cadmium pressure is lowered further, the V''_{Cd} (cadmium vacancy with effective charge of -2) functions as a trap for the holes during the quenching process. The ionization energy of these V''_{Cd} levels is too large to give appreciable conduction at room temperature. It is not clear whether these deep-lying energy levels consist of a double negatively charged cadmium vacancy or associates of cadmium vacancies with donors³; however, the result is that the transition from n- to p-type material takes place over a wide range of atmospheres in which the crystal has an extremely high resistance. The pressure range yielding low resistivity p-type conductivity is never reached.

If the cooling takes place slowly or if the quench occurs at too low a temperature, vacancies are able to diffuse away and the deep acceptor centers are not present; the Fermi level is no longer pinned near the center of the forbidden energy zone, and the lower resistivity material is formed. This is in good agreement with the phase diagram (Fig. 3-2) which shows, for example, that indium doped CdTe grown at a pressure of 1 atmosphere should have high resistivity if it is quenched rapidly from 1000°C to room temperature. The temperature range from which a crystal may be quenched to room temperature and have high resistivity, i. e., no free carrier absorption, has an upper limit that is the melting point of CdTe at the cadmium pressure being used (the left boundary of the solidus region in Fig. 3-2 and a lower limit determined by the shallow donor concentration in the crystal (one of the diagonal lines corresponding to different indium concentrations in Fig. 3-2).

Typical optical transmission curves before and after the thermal anneal procedure are shown in Fig. 3-7.

When the ingot size was increased to a 5-cm diameter and the total weight of CdTe exceeded 500 grams, we observed that quenching became impossible because of the large mass and relatively poor thermal conductivity of the material. A technique was initiated that involved slowly cooling the crystal with accompanying lowering of the

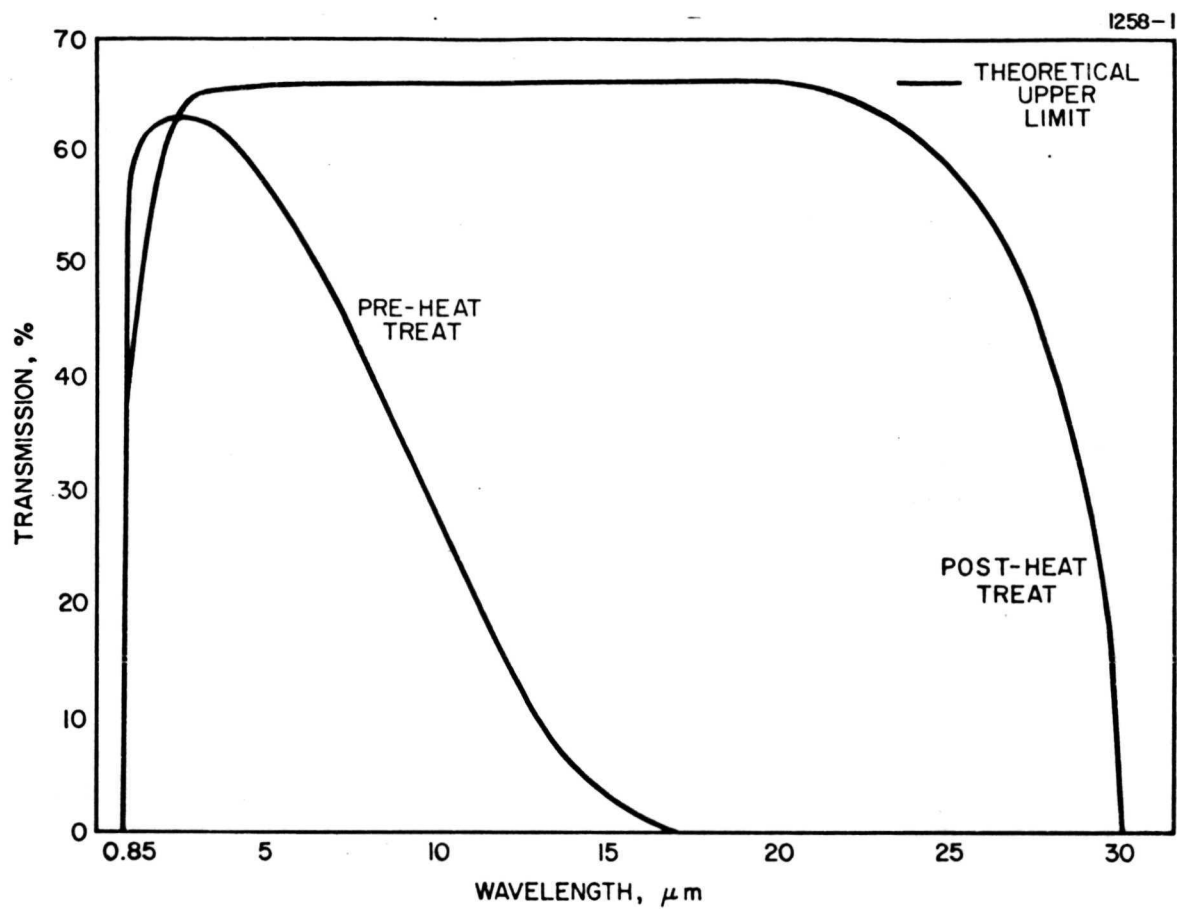


Fig. 3-7. Transmission Spectrum of CdTe Sample Before and After Heat Treatment.

overpressure as illustrated by the dotted line in Fig. 3-8, * remaining in the high resistivity region to a temperature where diffusion processes become sluggish. This annealing procedure can also assist in reducing any thermal strain that may have been present due to growth conditions; certainly it cannot introduce any additional strain in the ingot. This technique is still in the experimental stage and, as such, is not entirely reproducible. Initially, excellent results have been obtained. At the present time, however, modulator rods are cut from the ingots and heat treated by the standard quench technique.

3.3 CADMIUM TELLURIDE CRYSTAL EVALUATION

3.3.1 Measurement of Electro-Optic Coefficient

The most efficient means of measuring the electro-optic coefficient of a material such as CdTe utilizes a sample of the material in the form of a rectangular bar with the end faces and two opposing sides parallel to crystalline (110) planes. The end faces are optically polished to allow passage of a light beam, and the (110) plane sides are electroded to provide for the electric driving field across the crystal.

In its simplest form, the measurement is made by allowing the polarized output beam of a suitable laser to pass axially through the sample, through a crossed analyzer, and onto a detector where the intensity of the transmitted light can be measured. A known dc voltage is then applied to the crystal, and the intensity of the transmitted light is measured as a function of the applied voltage. When an element with birefringence Γ radians is placed between crossed polarizers with the

*The circle designated with number 1 is the area of thermal anneal used both prior to quenching or subsequent to slow cooling techniques.

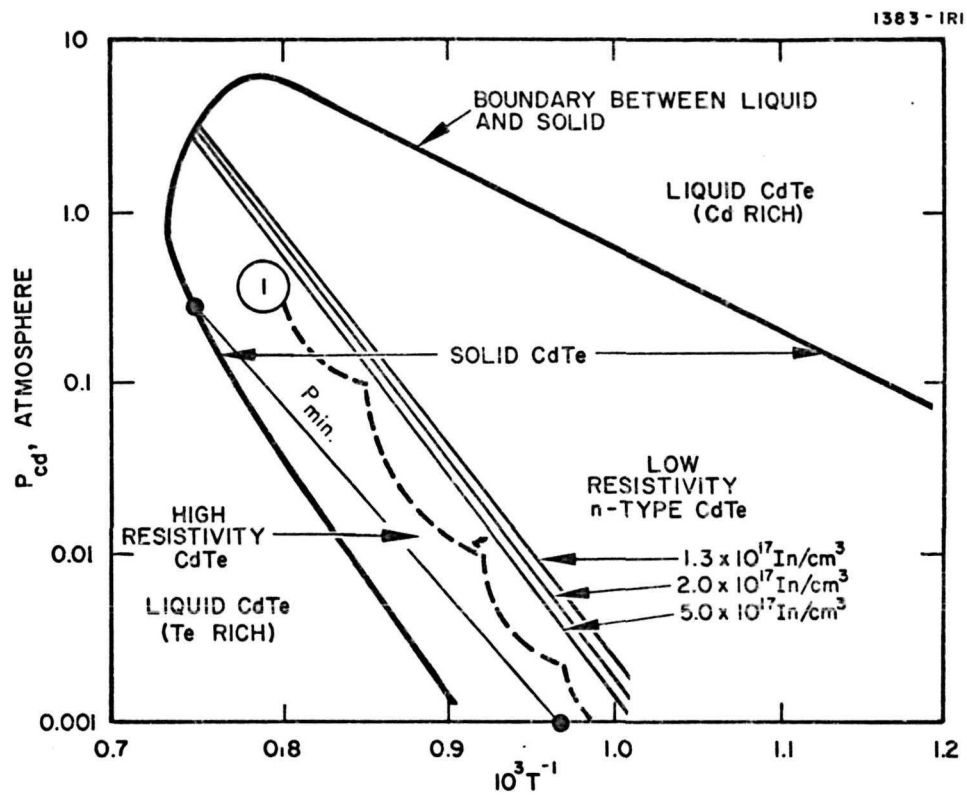


Fig. 3-8. CdTe Pressure-Temperature Equilibrium Relationships.

induced axes of the element $\pi/4$ from the polarizer axes, the ratio of transmitted to incident light intensity is given by

$$I/I_o = \sin^2 (\Gamma/2) \quad (1)$$

For this crystalline orientation, the birefringence or phase retardation as a function of driving voltage V is

$$\Gamma = \frac{2\pi}{\lambda} n_o^3 r_{41} \left(\frac{\ell}{d} \right) V \text{ radians}, \quad (2)$$

where λ is the free space wavelength of the incident radiation, n_o is the refractive index, r_{41} is the electro-optic coefficient, ℓ is the length, and d is the thickness of the sample. Combining the two equations and solving for r_{41} ,

$$r_{41} = \frac{\lambda}{2\pi n_o^3} \frac{1}{V} \left(\frac{d}{\ell} \right) \sin^{-1} 2 \sqrt{\frac{I}{I_o}}, \quad (3)$$

which yields the unclamped electro-optic coefficient.

To measure r_{41} with an ac signal (e.g., to find the clamped or high-frequency value of r_{41}), a quarter-wave plate with axes parallel to the induced axes of the sample is placed in series optically with the sample, and a sinusoidal signal with peak voltage V_o and frequency F_m is applied to the sample. The above equations are then modified as follows.

$$I/I_o = \sin^2 \left(\frac{\Gamma}{2} + \frac{\pi}{4} \right) = \frac{1}{2} \sin (1 + \Gamma) \quad (4)$$

$$\Gamma = \frac{2\pi}{\lambda} n_o^3 r_{41} \left(\frac{\ell}{d} \right) V_o \sin (2\pi F_m t) \quad (5)$$

Thus,

$$\left. \frac{I}{I_o} \right|_{\max} - \left. \frac{I}{I_o} \right|_{\min} = \sin \left[\frac{2\pi}{\lambda} n_o^3 r_{41} \left(\frac{\ell}{d} \right) V_o \right] , \quad (6)$$

or for small signals

$$r_{41} \sim \frac{\Delta I}{I_o} \frac{\lambda}{2\pi n_o^3 V_o} \left(\frac{d}{\ell} \right) , \quad (7)$$

The apparatus for these measurements is illustrated schematically in Fig. 3-9 and a photograph of our test station is shown in Fig. 3-10.

3.3.2 Optical Absorption Measurements

The calorimetric technique is the most common method of measuring the optical absorption coefficient of materials at 10.6 μm . Basically, this method involves radiating a sample of the material to be measured with a known amount of energy from a CO_2 laser and measuring the resultant temperature rise of the sample. From the mass and specific heat of the material and the power absorbed, the absorption coefficient of the material may then be calculated.

The power absorbed in a medium of length ℓ and having nominally plane, parallel faces, is given by

$$P_a = \frac{(1-R)(1-e^{-\alpha\ell})}{(1-Re^{-\alpha\ell})} P_i , \quad (8)$$

where R is the reflection coefficient at normal incidence, P_i is the normally incident power, and α is the absorption coefficient. For the product $(\alpha\ell)$ much less than unity, the relation for the power absorbed simplifies to

$$P_a \approx \alpha\ell P_i , \quad (9)$$

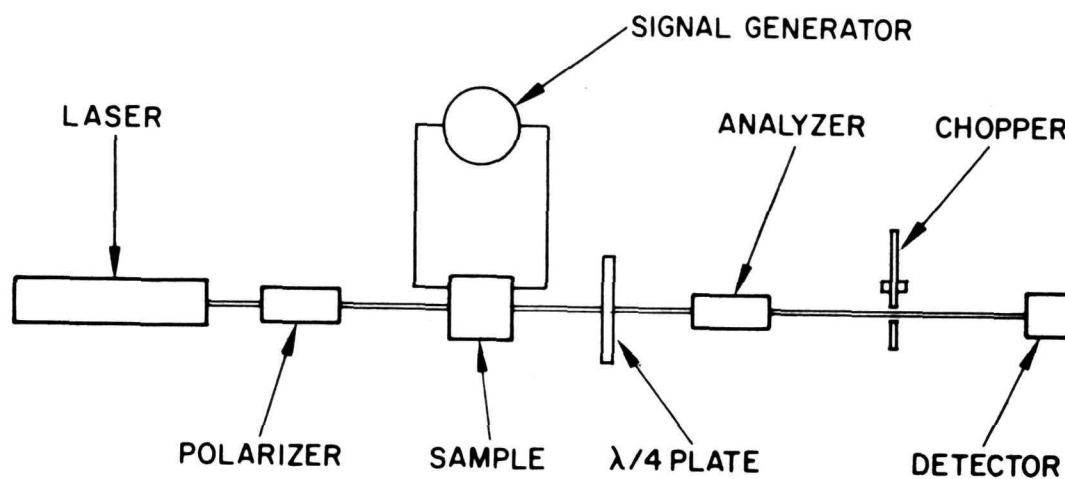


Fig. 3-9. Electro-Optic Evaluation Apparatus Diagram.

M 7319

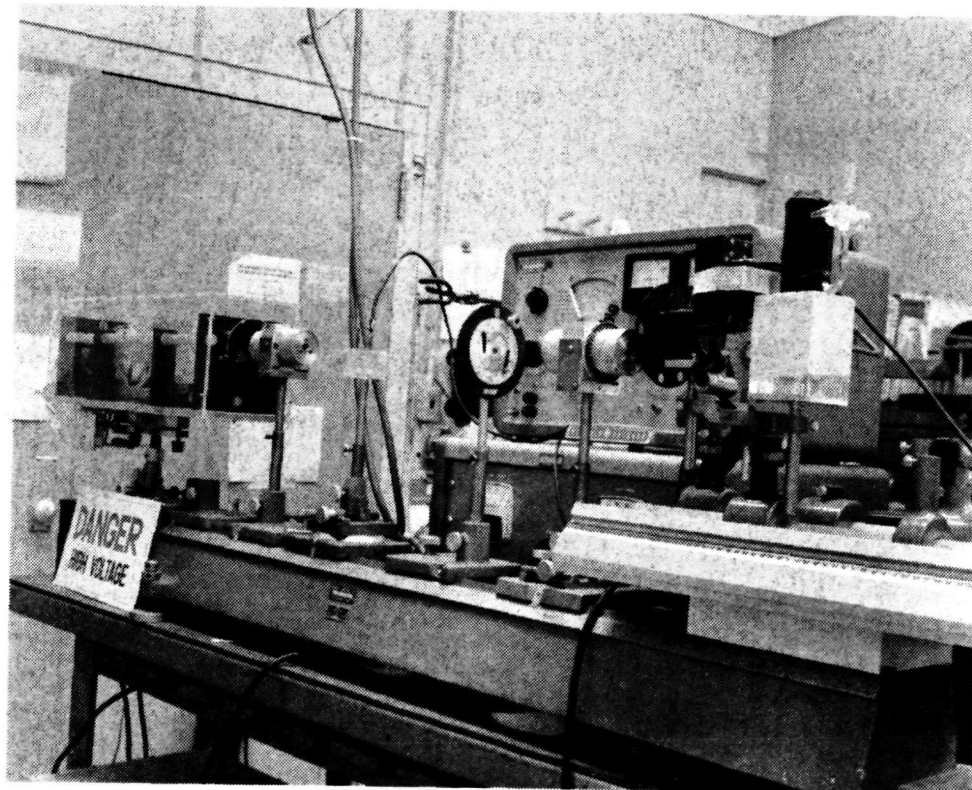


Fig. 3-10. Electro-Optic Evaluation Apparatus.

independent of the reflection coefficient. The power absorbed is found calorimetrically by analysis of the sample's transient thermal response to the incident power.

Consider a sample having no constraints on the temperature at its boundaries and subject to heat losses to the environment alone. The heat losses increase as the temperature difference ΔT between the sample and the environment increases. The rate of heat loss P_L at a specific temperature difference ($\Delta T = \Delta$) is given by

$$P_L \Big|_{\Delta T = \Delta} = -C_p M \frac{d(\Delta T)}{dt} \Big|_{\Delta T = \Delta}, \quad (10)$$

where C_p is the sample heat capacity, M the sample mass, and $d(\Delta T)/dt$ the instantaneous change in sample temperature with respect to time.

If power is incident on a sample, its temperature rise is influenced by the absorbed power and also by the power lost to the environment. The instantaneous change in sample temperature at $\Delta T = \Delta$ in this case is given by

$$\frac{d(\Delta T)}{dt} \Big|_{\substack{\Delta T = \Delta \\ P_i \neq 0}} = \frac{1}{C_p M} (P_a - P_L) \Big|_{\Delta T = \Delta}. \quad (11)$$

Combining eqs. (9), (10), and (11), and solving for α results in the relation,

$$\alpha(\Delta T) \Big|_{\Delta T = \Delta} = \frac{C_p M}{\ell P_i} \left[\frac{d(\Delta T)}{dt} \Big|_{\substack{\Delta T = \Delta \\ P_i \neq 0}} - \frac{d(\Delta T)}{dt} \Big|_{\Delta T = \Delta} \right]. \quad (12)$$

Equation (12) implies that the absorption coefficient α , which may be temperature dependent, can be found experimentally by analysis of transient thermal response of a sample during and after laser irradiation. A typical transient response of a sample having temperature

independent absorption is shown in Fig. 3-11. The sample is initially at equilibrium with the environment ($\Delta T=0$). During laser irradiation, the slope

$$\left. \frac{d(\Delta T)}{dt} \right|_{\substack{\Delta T=\Delta \\ P_i \neq 0}} \quad (13)$$

is measured at a particular departure from equilibrium $\Delta T = \Delta$. As the sample returns to equilibrium, the slope

$$\left. \frac{d(\Delta T)}{dt} \right|_{\Delta T=\Delta} \quad (14)$$

is measured at the same departure from equilibrium. The absorption coefficient is found by substitution of these values into eq. (12).

The calorimeter is illustrated schematically in Fig. 3-12 and a photograph of the actual device using a CO_2 laser as the source is shown in Fig. 3-13. We have used both CO_2 (10.6 μm) and Nd:YAG (1.06 μm) as source illuminators for this calorimeter. A close-up view of the sample holder is shown in Fig. 3-14.

3.3.3 Modulator-Related Properties of CdTe

Several of the important modulator-related properties of modified Bridgman-grown CdTe have been measured. The properties measured at Hughes Research Laboratories include the refractive index, hardness, the electro-optic coefficient, the optical absorption coefficient, the loss tangent at 1 GHz, the specific heat, and the temperature coefficient of the refractive index. The value given for thermal conductivity was determined on our sample from a commercial source using the Colora Thermoconductometer.* Values of the properties measured

* Measurement performed by Ablestik Adhesive Company, Gardena, California.

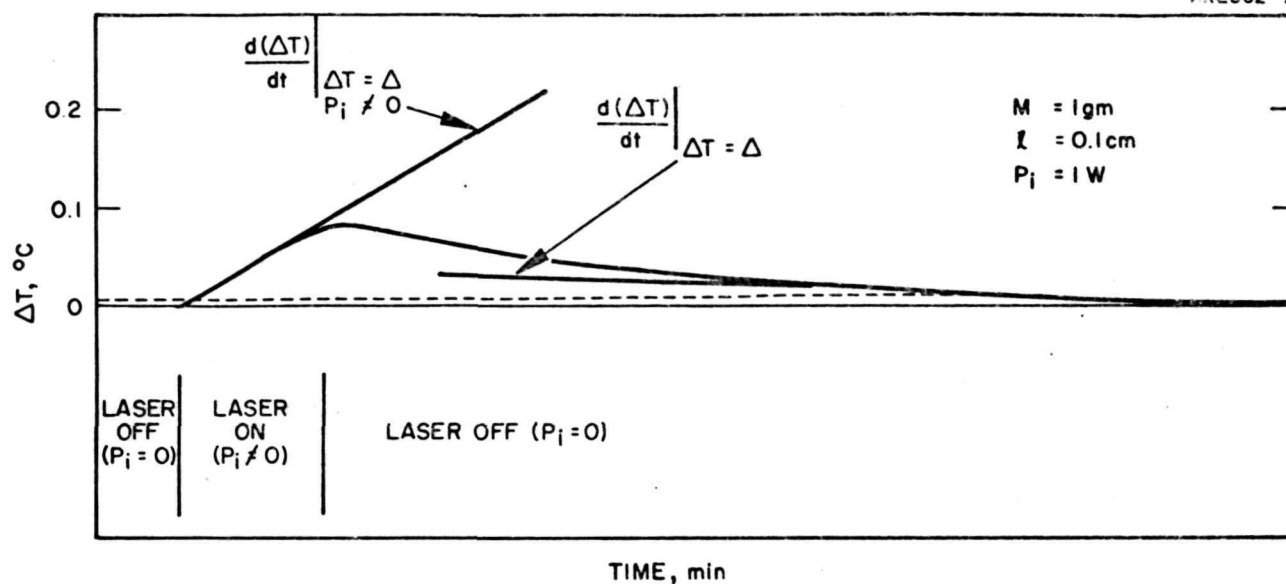


Fig. 3-11. Typical Transient Thermal Response for Temperature Independent Absorption.

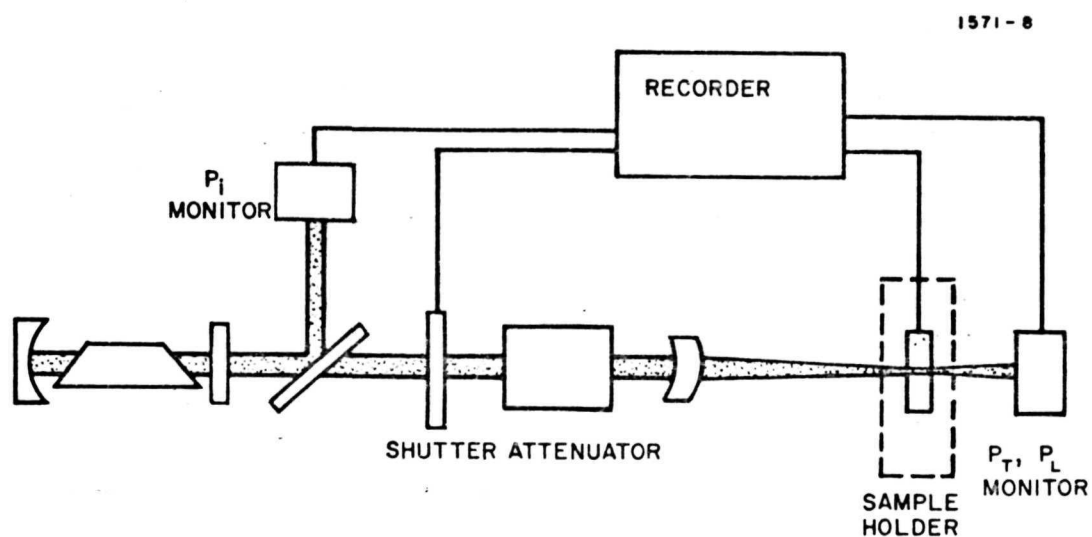


Fig. 3-12. Laser Calorimeter Schematic.

M8593

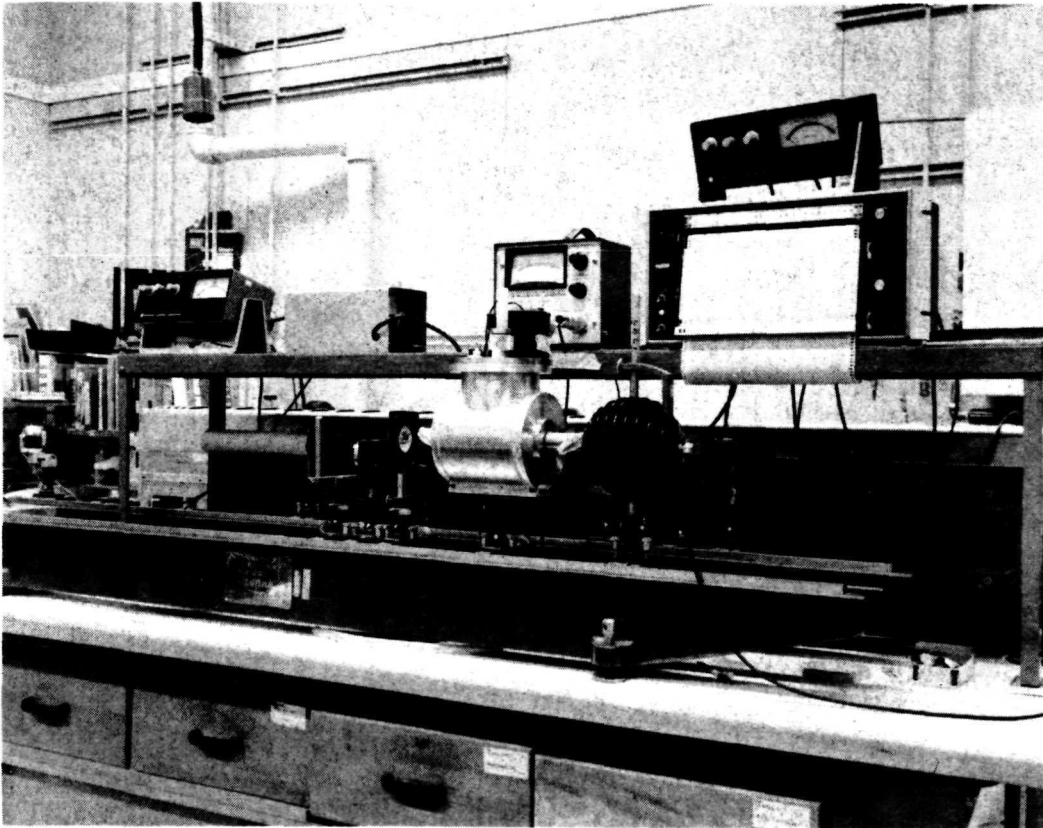


Fig. 3-13. Laser Calorimeter.

M8592

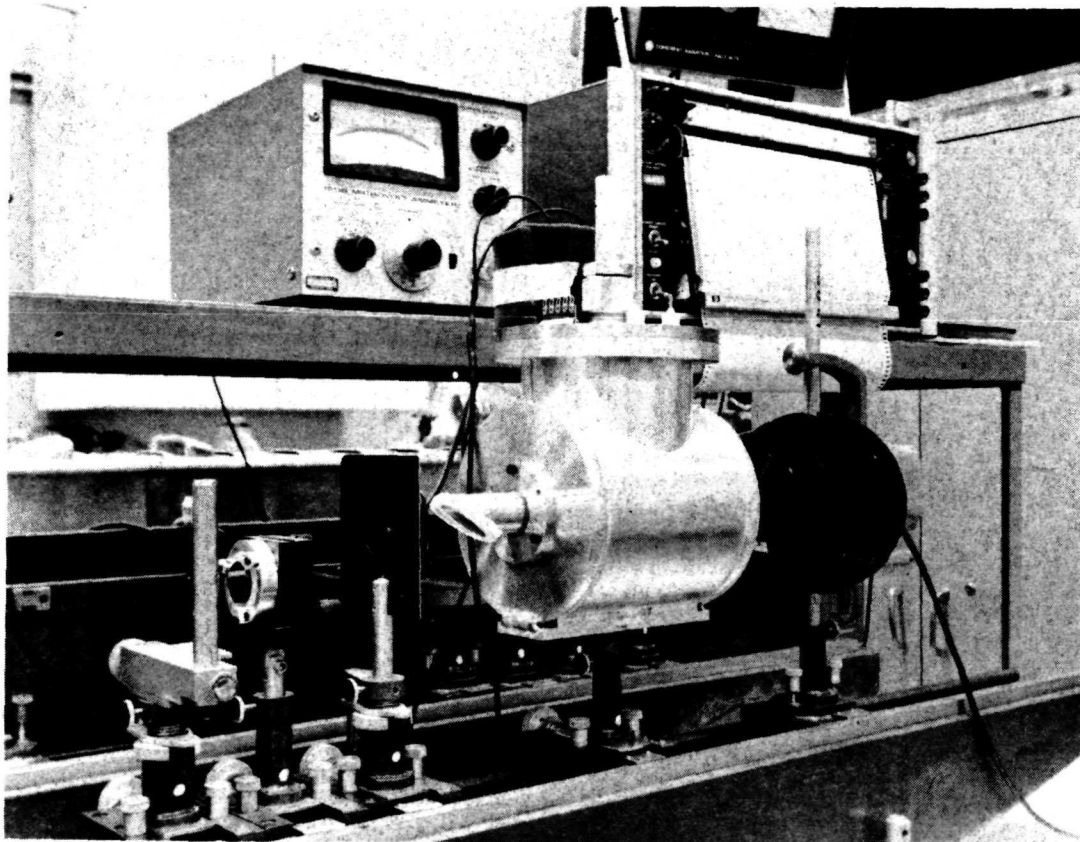


Fig. 3-14. Optical Calorimeter.

are given in Table 3-II. For completeness, the values of other important properties from the literature are also included. Where applicable, the values given correspond to data taken at 10.6 μm . Results of the absorption measurements on thermally annealed samples show the lowest value for single crystal material to be $\alpha = 0.0015 \text{ cm}^{-1}$. Actual bulk values may be less than this measured value as discussed in recent work, as by Shiozawa, *et al.*⁵ Currently, single crystal CdTe averages 0.002 to 0.003 cm^{-1} . The method of measurement of α , the absorption coefficient is discussed in a previous section.

TABLE 3-II
CdTe Properties

Clamped (high frequency) electro-optic characteristic $n_o^3 r_{41}$	$10 \pm 1 \times 10^{-11} \text{ m/V}$
Halfwave voltage $V_\pi \cdot \ell/d$ (10.6 μm)	53 kV
Dielectric constant ϵ/ϵ_o	10
Resistivity	$>10^7 \Omega \cdot \text{cm}$
Loss tangent (1 GHz)	$<10^{-2}$
Refractive index n_o	2.67
Transmission range	1 to 25 μm
Optical absorption coefficient	0.0015 to 0.003 cm^{-1}
Thermal conductivity	0.0093 $\text{cal} (\text{sec} \cdot \text{cm} \cdot ^\circ\text{C})^{-1} 120^\circ\text{C}$
Temperature coefficient of the refractive index $(1/n) dn/dt$	$4.4 \times 10^{-5} ^\circ\text{C}^{-1}$
Linear coefficient of thermal expansion	$5.5 \times 10^{-6} ^\circ\text{C}^{-1}$
Hardness	
Moh	2.8
Knoop	47 to 53

T668

3.3.4 Oxygen Contamination Studies

In the investigation of the limiting mechanisms of the absorption coefficient of CdTe, a number of factors, including impurity content, have been analyzed.* However, analysis of impurity content by mass spectrographic and emission spectrographic techniques failed to show any meaningful correlation between impurity levels and the measured absorption coefficient. Even for variations in oxygen content — a contaminant of great suspect for limiting the absorption coefficient — ranging from 0.4 to 22 ppma, no significant deterioration of α (absorption coefficient) was observed (see Table 3-III). To determine the role of oxygen as a deleterious impurity to optical transmission at 10.6 μm , we undertook a series of experiments using CdO to dope ingots with known concentrations of oxygen. Although the degree of solubility (segregation coefficient) is unknown for oxygen in CdTe, the concentrations introduced into the melt were 0, 100, 1000, and 10,000 ppma oxygen; 10 ppma oxygen was not used since data indicated little difference could be shown between intentionally doped samples at that level and unintentionally doped ones, i.e., not specifically added oxygen impurity. Crystals were grown, both only oxygen doped and oxygen plus indium doped (2×10^{17} In atoms/cc). Indium is used as the usual dopant to ensure high resistivity, hence good quality after the heat treatment procedure. The ingots were grown by a Bridgman technique, and after being cut and polished were optically evaluated. The results of the investigation are summarized in Table 3-IV. The data contain few conclusions. Samples that were not indium-doped showed poor optical transmission but no free carrier absorption (see Fig. 3-15) and could not be further treated in any way. In this figure, samples are designated according to the oxygen concentration of the starting materials, i.e., 0 = no intentional oxygen doping, 1 = 100 ppma,

*This investigation was supported by the Air Force Materials Laboratory under contract F33615-71-C-1778.

TABLE 3-III

Oxide Impurity Study of CdTe Crystals

ppma Oxygen ^(a)	(b) cm^{-1}	$\rho, \Omega\text{-cm}$	Sample
0.4	0.008	6×10^8	214
0.6	0.7	0.99	219 ^(c)
0.9	0.010	6×10^8	208
1.1	0.002	$> 10^7$	176
2.5	0.010	---	191
6.6	---	2.0	204 ^(c)
22.0	0.007	4×10^2	212
<p>(a) Mass spectrographic analysis performed by Bell and Howell, Pasadena, California.</p> <p>(b) Calorimetric absorption coefficient measurement made at HRL.</p> <p>(c) Free carrier absorption.</p>			

T669

TABLE 3-IV
CdTe Samples Oxygen and Indium^(a) Doped

Sample	Oxygen, ppma	10.6 μ m Transmission I_T/I_o , %		
		As Grown	First Heat Treatment	Second Heat Treatment
1-0	0	0	63	56
1-1	100	0	10	24
1-2	1000	0	5	50
1-3	10,000	0	2	17
2-0	0	0	56	--
2-1	100	0	42	--
2-2	1000	0	52	--
2-3	10,000	0	54	--
3-0-N ^(b)	0	57	--	--
3-0-T ^(b)	0	51	--	--
1-1-N ^(c)	100	0	60	--
1-1-T ^(d)	100	0	64	--
<p>(a) Indium doping $\approx 2 \times 10^{17}$ atoms/cc.</p> <p>(b) Control sample, no indium doping.</p> <p>(c) Absorption coefficient, $\alpha = 0.116 \text{ cm}^{-1}$.</p> <p>(d) $\alpha = 0.016 \text{ cm}^{-1}$.</p>				

T670

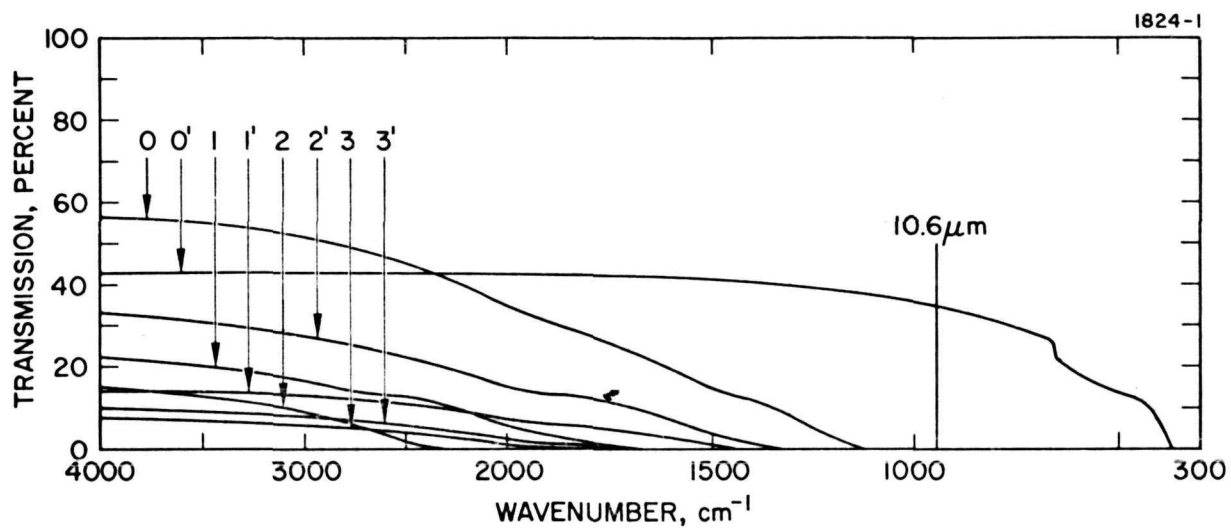


Fig. 3-15. Infrared Transmission of As-Grown CdTe For Oxygen Contamination Evaluation.

2 = 1000 ppma, and 3 = 10,000 ppma oxygen. Data are shown for two different samples, one designated by prime that contains no indium. Both oxygen and indium doped samples initially showed no transmission at 10.6 μm and were subsequently subjected to thermal anneal. After heat treatment, a sample with no intentional oxygen doping showed a 63% transmission using a calibrated laser beam. Increasing concentrations showed decreasing transmission but the range was so low that the accuracy of the results is questionable. The spectrophotometer traces taken after one heat treatment (see Fig. 3-16) indicate the possibility of residual free carrier absorption in some of the doped samples. However, a second cut of samples showed nominal transmission using a 10.6- μm laser beam following a first heat treatment. A second heat treatment (see Fig. 3-17) showed essentially a lack of free carrier absorption in all samples, but extremely poor transmission. The main result of the oxygen study was to show that oxygen contamination at these high levels has extremely deleterious effects on the structural quality of the crystal. Crystals become very brittle and polishing causes excessive pitting of the surfaces. These effects are exhibited by extreme variations in optical transmission caused by scattering. The general crystal bulk was filled with voids (see Fig. 3-18) and the crystal had a very black appearance similar to soft coal.

The second heat treatment, although carried out under an overpressure of Cd, seemed to have been deleterious to all samples (including undoped or unintentionally doped samples), which may be a result of the existence of an oxygen partial pressure in transmission of these samples after processing. As anticipated, there are general evidences of variations in oxygen content from nose to tail with the tail of some ingots appearing to have higher transmission and higher resistivity than the nose. However, we feel that an insufficient number of samples was studied and conditions were not adequately reproducible to draw any additional conclusions. Great amounts of oxygen contamination (>100 ppma) obviously must be avoided for high quality optical material as required for the infrared modulator application.

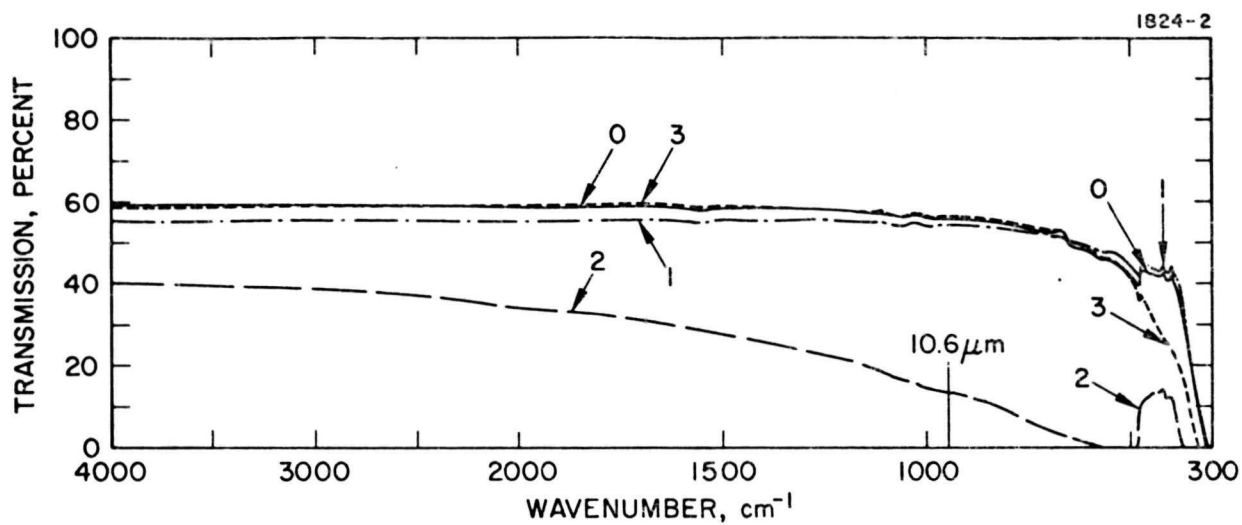


Fig. 3-16. Indium and Oxygen Doped Samples After First Heat Treat.

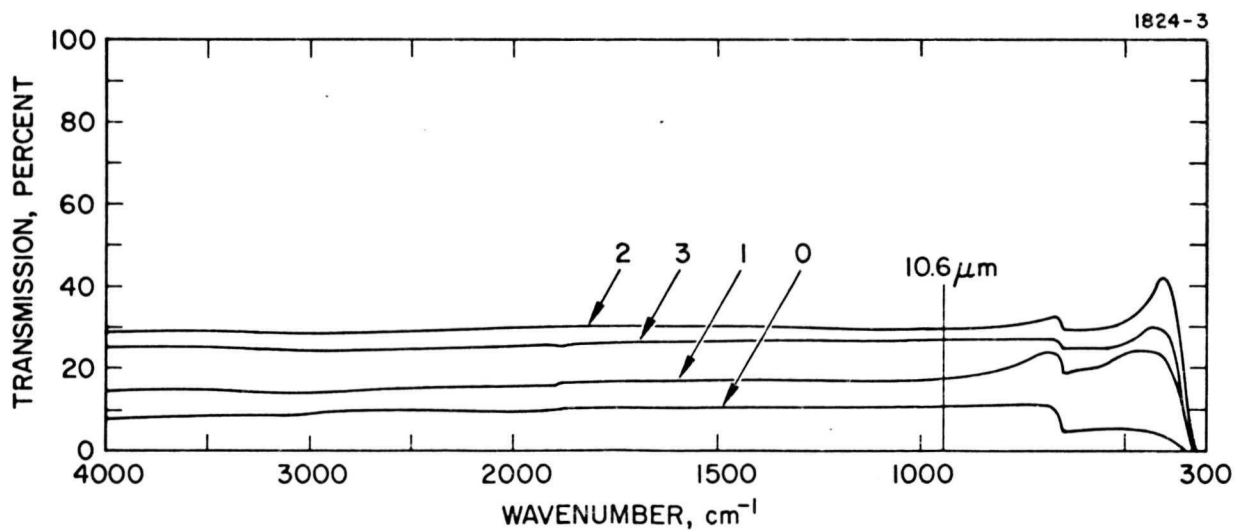
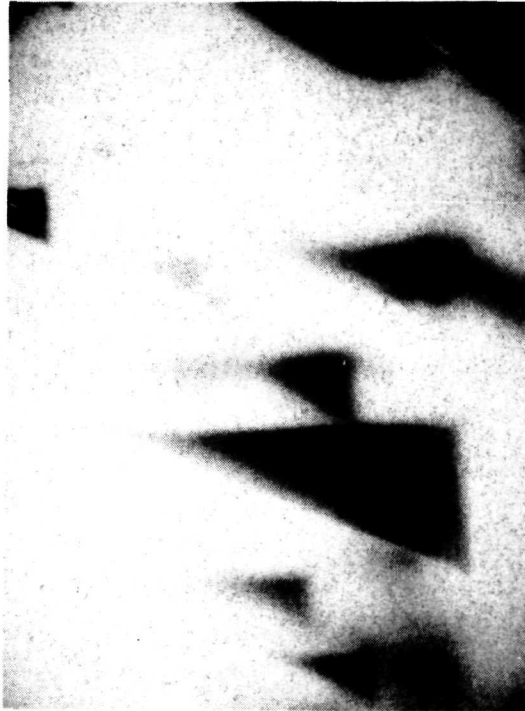


Fig. 3-17. Indium and Oxygen Doped Samples After Second Heat Treat.

M8973



60x

Fig. 3-18.
Apparent Voids in Oxygen Doped
CdTe.

"Page missing from available version"

SECTION 4

COATING DEVELOPMENT

4.1 TASK GOALS AND RESULTS

The need for high quality coatings for the modulator rod and associated optics, such as a lens, arises from the deleterious effect that losses have on the laser performance. The seriousness of intracavity losses on the laser performance is shown in Section 2.3.

The goals of the coating development task were to produce antireflection coatings for cadmium telluride with less than 1% total absorption and reflection loss. At the beginning of the program, the technique of applying coatings to CdTe had not yet been achieved. Experience on gallium arsenide was generally favorable, yet cadmium telluride showed some anomalous surface effects which indicated that the gallium arsenide experience was not applicable.

The approach to development of the coating was to simultaneously procure experimental coatings from qualified vendors and to develop the technique independently in our own laboratory. An agreement was reached with OCLI whereby they produced coatings at their own expense and sent them to us for evaluation in our laboratory. Another vendor provided experimental coatings on a best-efforts cash basis. The results of these efforts were that our own coatings and the OCLI coatings were comparable, whereas the other vendor's coatings were of lesser quality.

The results of this task are that excellent AR and high reflectivity coatings have been produced for CdTe. Typical reflection loss of 0.25% and absorption loss of 0.2% have been achieved, giving a total AR coating loss of less than 1/2%.

The following discussion gives theoretical considerations related to the design of antireflection coatings for CdTe and the experimental results obtained from this development work. Finally, reflection and loss data for actual modulator coatings is included.

4.2 DESIGN OF ANTIREFLECTION COATINGS

Antireflection coatings can range from a simple single layer having virtually zero reflectance at 1 wavelength to a multilayer system of twenty or more layers having virtually zero reflectance over a wavelength range of several octaves. The type used in any particular application will depend on a variety of factors including the substrate material, the wavelength region, the required performance, and the cost.

For design of coatings and for tutorial purposes, most reference works assume that the substrates and materials used for coating are completely transparent (i. e., $k = 0$, where k = absorption index or extinction coefficient of the material) in the spectral region in which the reduction of surface reflectance is to be obtained. Cox and Hass⁶ and H. A. Macleod⁷ used this assumption and have presented detailed designs and discussions of antireflection coatings for optical surfaces using single layer, double layer, and multilayer coatings. Therefore, this section will not include any detailed discussion of the derivation of these designs since they are treated in an excellent manner in the above works, although material and design information for 10.6 μm are not included in those references. However, design data incorporated in this section do consider the factor of absorption in film materials, because at the present technological stage of coating application methods, the high power 10.6 μm laser flux to which the coatings will be subjected makes the inclusion of absorption considerations in the designs mandatory.

Practical coatings are generally restricted to one-or two-layer designs with occasional use of a three-layer coating. This is particularly true at 10.6 μm where the large physical thicknesses required in the layers causes problems in the realization of a given design. Single-layer coatings are limited in usefulness since one obtains a zero of reflectance only when the refractive index of the coating material is equal to the square root of the substrate index. When this condition cannot be met, two or more layers must be used to obtain a true zero of reflectance using available materials.

When two layers are used in the coating design, the added freedom permits one to choose many different combinations of refractive indices and layer thicknesses to produce a zero of reflectance at a prescribed wavelength. The basis for choice of a particular design to pursue experimentally then becomes criteria such as the minimization of absorption and the minimization of differential strains which might lead to poor adherence. In the work reported here, minimization of absorption has been the prime criterion in making the choice of designs.

An important aid to designing two-layer antireflection coatings is a diagram such as that shown in Figure 4-1 for ZnSe (see Ref. 6 for more details). Every point in the shaded regions of the diagram represents a pair of refractive index values for the coating materials which will produce a zero of reflectance on the given substrate. Points outside the shaded regions, but close to them, will yield low reflectance, but not zero. The corresponding thicknesses are then calculated from a pair of design equations. The final step is to calculate the $10.6\text{ }\mu\text{m}$ absorption expected for each coating design based on either measured absorption indices for the individual film materials or best guesses where no measurements are available.

The remainder of this section contains some illustrative coating design information for KCl, CdTe, and ZnSe. This information is strictly theoretical in nature, and there are many factors that contribute to the actual performance of a coating that are not included in the theory leading to the design thicknesses and absorption values. Therefore, the optimum experimental thicknesses need not be the same as the theoretical ones (although they are usually expected to be close) and the absorptions need not be as low as the theoretical predictions. Some of these problems are discussed further in the section on experimental results.

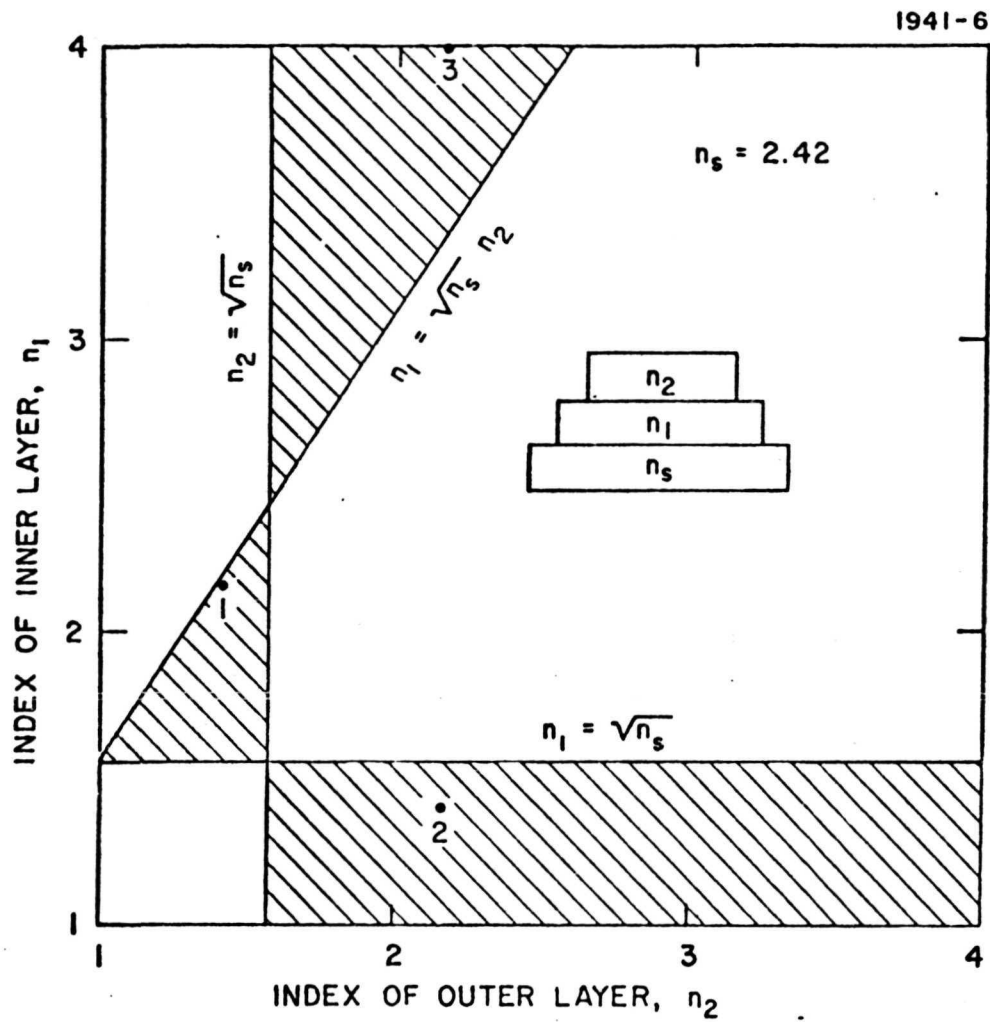


Fig. 4-1. Double Layer Antireflection Coating Design Diagram for ZnSe.

4.3 ANTIREFLECTION COATINGS FOR CdTe AND ZnSe

In the case of these semiconductor materials, their high refractive indices relative to that of the low index halides provide new options in coating design. Single layers are theoretically feasible if zero reflectance is not required. Also, double-layer coatings are possible with refractive index values in all three regions of the design diagram. In particular, one may now choose double-layer coatings from the rectangular region of the diagram where the index of the first layer is less than the square root of the substrate index and the index of the second layer is greater than the square root of the substrate index. These coatings have important properties which are described below.

The design diagram for ZnSe is shown in Fig. 4-1; the diagram for CdTe would be similar. The three numbered points on the diagram correspond to the identifying numbers in Table 4-I, which contains design data for these three coatings as well as for a ThF_4 single layer. At each point the two-layer solution which minimizes absorption and coating thickness has been chosen for inclusion in the table.

A comparison of the solutions labeled 1 and 2 illustrates the advantages of the solution in the rectangular region of the design diagram (No. 2). They both utilize the same materials to produce a zero of reflectance at $10.6 \mu\text{m}$, but in opposite order. For solution 2, which has the order BaF_2/ZnS , the required coating thicknesses are much less than for solution 1 (which is important at long wavelengths), and the predicted absorption is less than half that for solution 1. Another important advantage of solution 2 is that the water-sensitive low index fluoride is not exposed to the environment; the outer semiconductor layer protects it.

Solution 3 in Fig. 4-1 and Table 4-I (Ge/ZnS) is included because the Ge/ZnS combination represents an important pair of materials which is widely used in commercial infrared optical coatings. The use of germanium may be prohibited at high power levels because of the danger of thermal runaway, but a Ge/ZnS antireflection coating for ZnSe may still be usable for low power applications.

TABLE 4-I

Theoretical Designs for Antireflection Coatings on ZnSe

No. on Design Diagram	Coating Materials		Layer Optical Thicknesses, Wavelengths		Absorption Per Coated Surface, %
	Layer 1	Layer 2	Layer 1	Layer 2	
-	ThF ₄		0.250	-	0.023 (R = 0.13%)
1	ZnS	BaF ₂	0.222	0.241	0.142
2	BaF ₂	ZnS	0.138	0.059	0.066
3	Ge	ZnS	0.116	0.303	0.043
10.6 μ m Optical Constants					
	ZnSe	ThF ₄	BaF ₂	ZnS	Ge
n	2.42	1.5	1.395	2.16	4.0
k	-	1×10^{-4}	5×10^{-4}	2×10^{-4}	2.5×10^{-5}

T729

Table 4-II contains design information for some typical coatings on CdTe. Again one sees the striking improvement in performance and reduction in layer thicknesses that can be obtained with coating designs from the rectangular region of the design diagram (compare ZnS/BaF₂ with BaF₂/ZnS). The ThF₄ single layer and the ZnS/ThF₄ and BaF₂/ZnS double layers have been studied experimentally; results are reported in 4.4.

4.4 EXPERIMENTAL COATING RESULTS FOR CdTe

The three different antireflection coatings that have been studied on CdTe windows are ThF₄ single layers, and ZnS/ThF₄ and BaF₂/ZnS double layers. The dominant experimental fact is that for all three of these coatings the theoretical design data do not match

TABLE 4-II

Theoretical Designs for Antireflection Coatings on CdTe

Coating Materials		Layer Optical Thicknesses, Wavelengths		Absorption Per Coated Surface, %
Layer 1	Layer 2	Layer 1	Layer 2	
ThF ₄	-	0.250	-	0.024 (R = 0.73%)
ZnS	ThF ₄	0.133	0.207	0.034
ZnS	BaF ₂	0.185	0.212	0.127
BaF ₂	ZnS	0.119	0.076	0.058
Note: 10.6 μ m optical constants: same as Table III for coating materials, n = 2.67 for CdTe				

T730

the experimental results. For the ThF₄ single layer of 1/4-wavelength thickness, reflectances below 4.5% could not be achieved (theoretical prediction 0.73%), whereas for the double layers minimum reflectance is realized for layer thicknesses relatively far from the theoretical ones. The reasons for these discrepancies are not known, but they are believed to be a result of surface effects on the CdTe. ZnSe, which might be expected to have surface properties like those of CdTe, should be watched for similar effects.

Table 4-III shows results to date for the three coatings studied on CdTe. The coatings were deposited in a conventional diffusion pumped vacuum system with liquid nitrogen trapping onto CdTe surfaces heated to 150°C. The ZnS source was a vitreous carbon crucible with a tungsten pancake filament, the BaF₂ source was a heavy Mo boat, ThF₄ was deposited using both types of source with no apparent difference in performance.

TABLE 4-III

Experimental Antireflection Coating Results on CdTe Windows

Coating Design	Theoretical Optical Thicknesses (Wavelengths)	Theoretical Reflectance (%)	Experimental Reflectance (%)	Theoretical 10.6 μm absorption per surface (%)	Experimental 10.6 μm absorption per surface (%)
ThF_4	0.250	0.73	4.5-5	0.024	not measured
ZnS/ThF_4	0.133/0.207	0	0.15-0.25	0.034	0.25-0.50
BaF_2/ZnS	0.119/0.076	0	0.15-0.30	0.058	0.06-0.25

T733

The ThF_4 single layers were monitored with a 10.6 μm CO_2 laser so the optical thickness is known to be 1/4-wavelength at 10.6 μm in all cases. Physical thicknesses were measured interferometrically to confirm the assumed value of 1.50 for the ThF_4 refractive index at 10.6 μm . The minimum reflectance achieved with these 1/4-wavelength layers was consistently in the range from 4.5 to 5.0% in conflict with the theoretical prediction of 0.73%.

The ZnS/ThF_4 double layers were also monitored with a CO_2 laser. In this case it was found that, using the theoretical design thicknesses, the reflectance at the minimum was between 1 and 1.5%. The thicknesses were then adjusted empirically to obtain minimum values in the range 0.15 to 0.25%. The final prescription arrived at for the deposition was as follows: deposit ZnS until the original CdTe reflectance of 20.7% is reduced to 10.3%, deposit ThF_4 until a minimum is reached. The theoretical stopping point for the first layer is 13.9%.

The BaF_2/ZnS double layers were monitored with a He-Ne laser at 6328 Å. The theoretical design thicknesses require deposition of 2.1 wavelengths of BaF_2 and 1.4 wavelengths of ZnS at 6328 Å taking account of the known dispersion in the two materials. The use of these thicknesses produced a reflectance of 1.1% on the CdTe windows. When the thicknesses were empirically adjusted to 1.75 wavelengths at 6328 Å

for both layers, reflectances in the range 0.15 to 0.3% were consistently obtained. Translated to $10.6\text{ }\mu\text{m}$, these results imply that minimum reflectance is occurring at optical thicknesses of 0.100 wavelengths and 0.090 wavelengths for BaF_2 and ZnS , respectively, whereas the theoretical values are 0.119 and 0.076 wavelengths. Figure 4-2 shows the spectral response measured from 2.5 to $22\text{ }\mu\text{m}$ for a 2 in. diameter CdTe window antireflection coated with the empirically adjusted BaF_2/ZnS design along with a theoretical curve calculated from the data shown on the figure. The reflectance at $10.6\text{ }\mu\text{m}$ was also measured with a CO_2 laser; it was found to be quite uniform with an average of 0.73% (two coated surfaces) across the face of the window. The $10.6\text{ }\mu\text{m}$ absorption measured calorimetrically at the center of the window was 0.25% per coated surface.

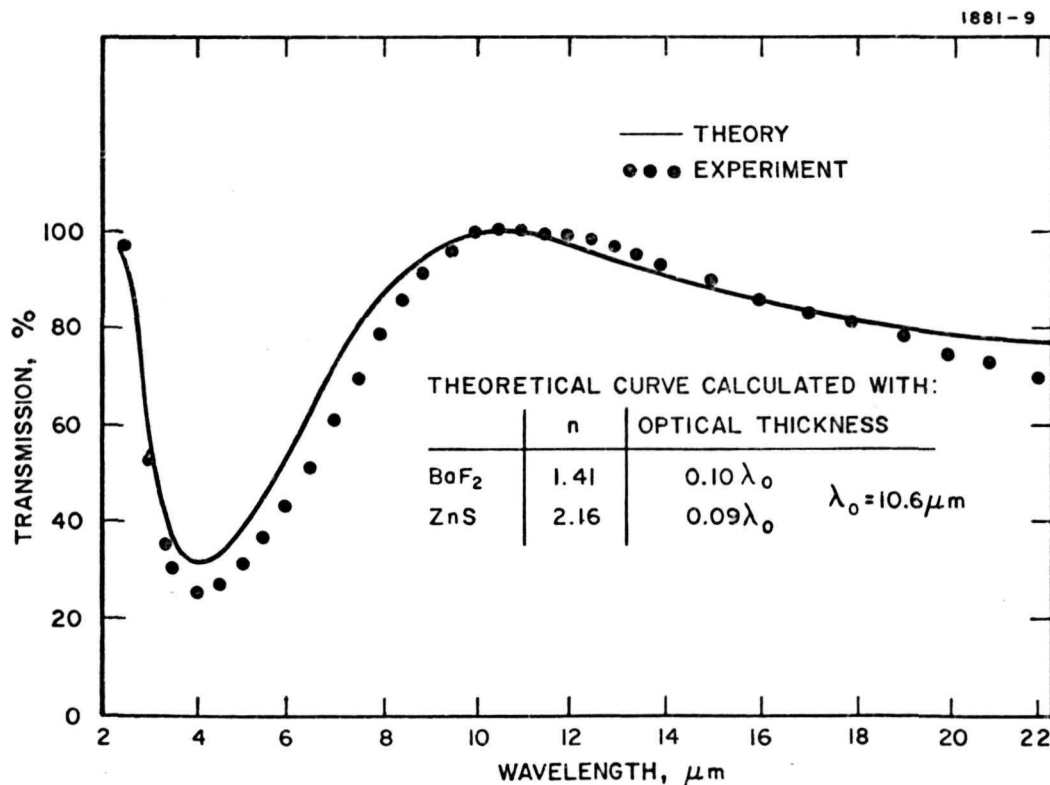


Fig. 4-2. CdTe 250 HT No. 5 BaF_2/ZnS Antireflection Coating Both Sides.

"Page missing from available version"

SECTION 5

MODULATOR DRIVER DEVELOPMENT

5.1 MODULATOR DRIVER REQUIREMENTS AND REVIEW OF STATE OF THE ART

5.1.1 Driver Requirements

The level of the modulator driving power required to drive a modulator is a function of several parameters including the capacitance of the device, the frequency of operation, and the level of voltage required. Section 2.2 derives an expression for the transmitted power from the laser

$$P_t = 2k P_c P_{\text{mod}} \frac{1}{\omega_m C} \left(\frac{\pi \ell}{V_{\pi} d} \right)^2$$

which can be rewritten as

$$P_{\text{mod}} = \frac{\omega C}{2k P_c} \left(\frac{V_{\pi} d}{\pi \ell} \right)^2 P_t$$

where ω_m is the maximum modulation frequency
 C is the capacitance of the modulator
 P_c is the circulating power in the laser
 ℓ is the length of the modulator rod
 d is the height of the modulator rod
 P_t is the required transmitted sideband power.

Many of the parameters were arbitrarily fixed to arrive at a power goal for the modulator driver. It was assumed that an ℓ/d ratio for the modulator of 35 was not unreasonable. It was also assumed that a

circulating power P_c of 40 W was not unreasonable. Figure 5-1 shows a plot of the transmitted sideband power as a function of modulator driving power for circulating power levels of 20 W and 40 W. A design goal of 12 W was set to provide 0.5 W of first order sideband signal power. This amount of power is equivalent to 1 W of 100% modulated AM signal power in terms of detection information signal-to-noise ratio.

5.1.2 Review of State of the Art

Two types of electronic drivers were considered for development in this task. The first type consisted of an extension of the state of the art of conventional solid state transistor driver amplifiers. The second type was an entirely new concept in electronic devices known as electron-beam semiconductor (EBS) devices.

Conventional transistor driver amplifiers having large gain-bandwidth products are limited in the amount of voltage the device can handle. The best available rf transistors have a maximum collector voltage of 28 V. Even a high power rf transistor is not of much use for driving an electro-optic modulator where voltages of more than 100 V peak are required. Thus, a transistor driver for such a modulator must utilize some sort of voltage transformer. At the beginning of the present task, one commercial solid state amplifier attracted our attention because it utilized a unique feature to achieve high power wideband amplification. This was achieved by summing the power from several low level stages in a hybrid transformer. For this technique, the power and bandwidth are not limited by the transistor, but rather by the transformer. With the aid of a 1:9 impedance step-up transformer, the commercially available amplifier appeared to approach our modulator driver power goals and bandwidth, although the efficiency was not high enough.

The EBS amplifier, on the other hand, showed promise of exceeding our goals in efficiency, rise time, bandwidth, and power by very large margins. However, the lifetime of the semiconductor target

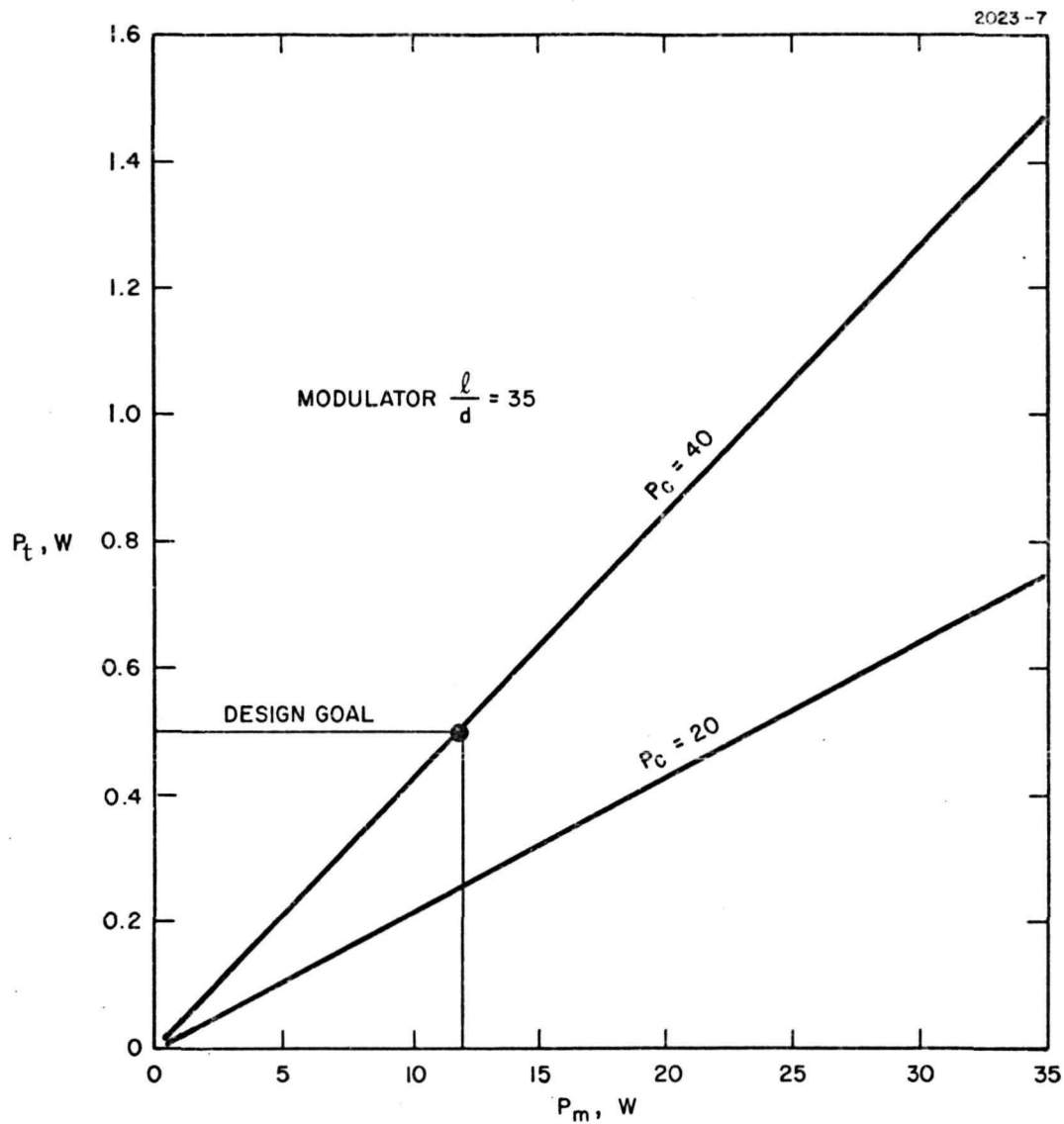


Fig. 5-1. Transmitted Sideband Power as a Function of Modulator Driving Power (Establishing Design Goals for Modulator Driver).

is limited to a few hundred hours. Research and development on semiconductor targets was clearly beyond the scope of the present task. During the course of the present program, development of EBS devices has continued at Watkins Johnson Company. Although the target reliability has been improved from hundreds to a few thousand hours, the lifetime still appears to be the limiting factor of that type of device.

5.2 GOALS AND TECHNICAL APPROACH OF THE MODULATOR DRIVER DEVELOPMENT TASK

The prime power available to supply the modulator driver amplifier on a spacecraft is limited to about 30W. The value of 30 W was derived by considering about 100 W total power available for the wideband space relay transmitter system. The amount of prime power supplied to the electronics and gimbal system, the laser transmitter discharge tube, and the modulator driver, is divided about evenly for an optimized system. Under this assumption, the design goal for the modulator driver was 12 W, imposing an amplifier efficiency goal of 40%.

The task effort was limited to about 10% of the total program effort. For this reason, the technical approach was conservative and extremely limited in scope. The task consisted of two stages of effort:

- Purchase and evaluate a commercially available amplifier that uses hybrid coupling to sum the outputs of a number of low power amplifier stages. Determine fundamental limitations of bandwidth and efficiency.
- Build a breadboard circuit based on the commercial amplifier in an effort to improve its basic efficiency, output voltage, and risetime.

5.3 EVALUATION OF ENI AMPLIFIER

A commercially available wideband solid state amplifier having a bandwidth of 250 MHz and an output of 10 W was purchased on the contract for evaluation. This particular amplifier, manufactured by Electronic Navigation Industries, Inc. (Model 406 L), combines

the outputs of eight 1.5-W amplifiers in a hybrid coupler to give 10 W of rated output. This unique feature allows this amplifier to overcome the limitations of single-ended transistor amplifiers. However, the efficiency of the amplifier is less than 8%, far short of the target 40% desired for space applications. Because it is a linear class A amplifier, considerable steady state bias power is used. For digital signals, the linearity normally associated with class A amplifiers may be traded off for more efficient operation, such as class B.

5.3.1 Characteristics of 406L Amplifier

Briefly, the device operates in reasonable agreement with published specifications and is a good wideband power amplifier. The measured risetimes (3 nanoseconds) does not agree with the 250-MHz upper cutoff frequency for a simple model. However, measurement of the group delay shows a sharp increase for frequencies above 100 MHz. Thus, although the amplifier is broadband to 250 MHz, the group delay frequency dependence above 100 MHz limits its use as a pulse amplifier.

Evaluation data for the measured characteristics of the amplifier are listed in the following figures and tables:

Fig. 5-2, Block Diagram of ENI 406L Amplifier.

Table 5-1, Summary of Measured Characteristics.

Fig. 5-3, Amplifier Frequency Response Measured with Tunable Frequency Source.

Fig. 5-4, Second, Third, and Fourth Harmonics as a Function of Input Level for 1-MHz Fixed Source.

Fig. 5-5, Fifth and Sixth Harmonics as a Function of Input Level for 1-MHz Fixed Source.

Fig. 5-6, Saturation Characteristics, Output Power vs. Input Power.

Fig. 5-7, Pulse Response for Unsaturated Output and Saturated Output.

Fig. 5-8, Phase Shift vs. Frequency.

Fig. 5-9, Group Delay vs. Frequency.

TABLE 5-1

Measured ENI 406L Amplifier Characteristics

Gain:	43 dB
Bandwidth:	100 kHz - 270 MHz
Noise Figure:	10 dB (measured from 30 to 200 MHz)
Harmonic Distortion:	40 dB or more down from the fundamental for linear operation
Efficiency:	Typically 8.3%
Linearity:	Gain is linear to +35 dBm output. The amplifier is compressed 1 dB at +36.7 dBm output
Intermodulation Distortion:	The third-order intercept point is +42 dBm
Pulse Risetime:	3 nsec with $\pm 10\%$ overshoot and ringing for a 0.5-nsec input pulse risetime
Pulse Droop:	50% in 500 nsec - corresponds to a 160 kHz lower band edge
Group Delay:	Essentially constant from 5 MHz to 100 MHz

T788

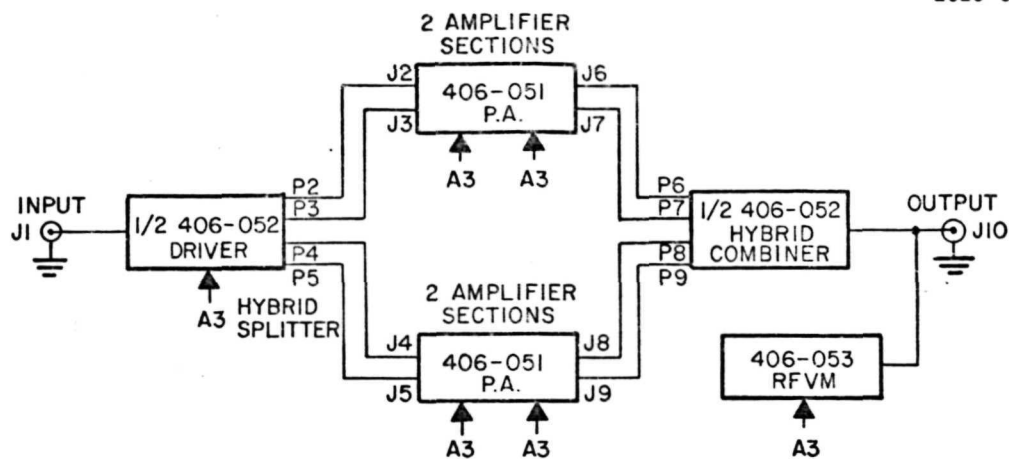


Fig. 5-2. Block Diagram of ENI 406L Amplifier.

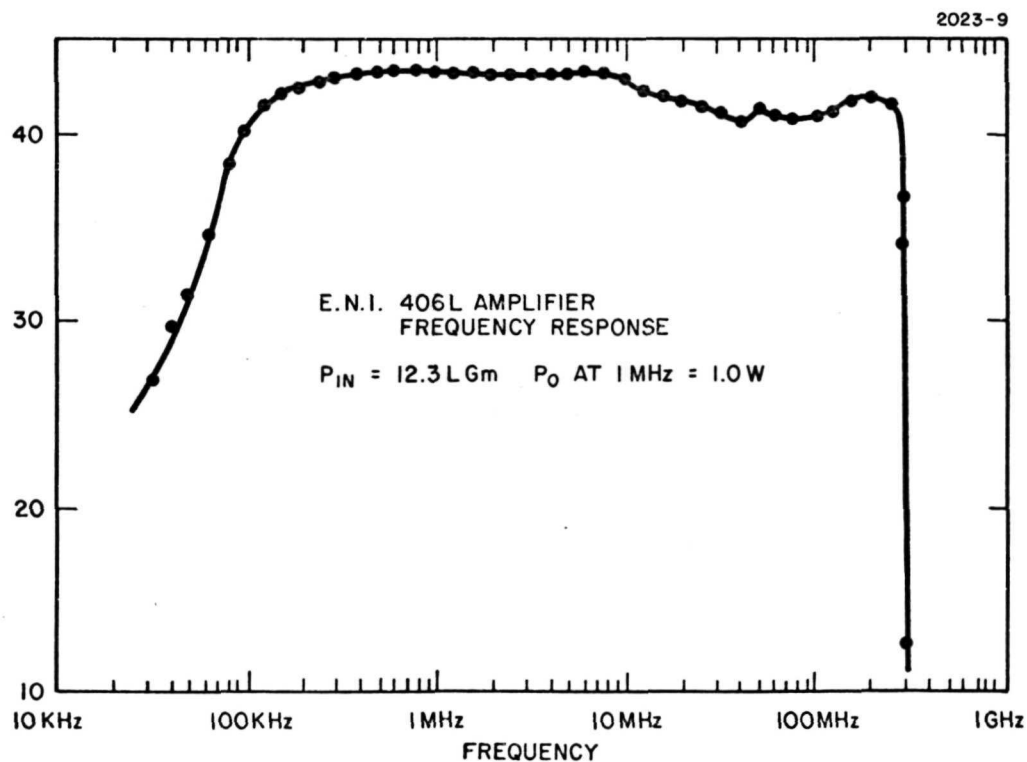


Fig. 5-3. Amplifier Frequency Response Measured With Tunable Frequency Source.

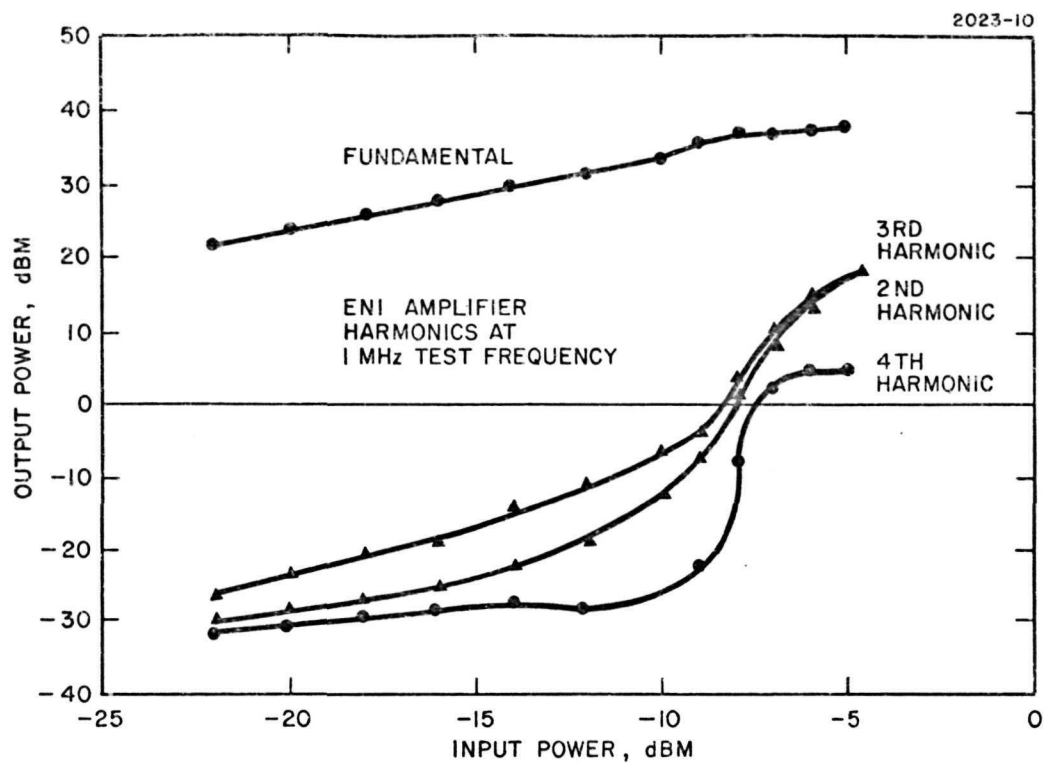


Fig. 5-4. Second, Third, and Fourth Harmonics as a Function of Input Level for 1 MHz Fixed Source.

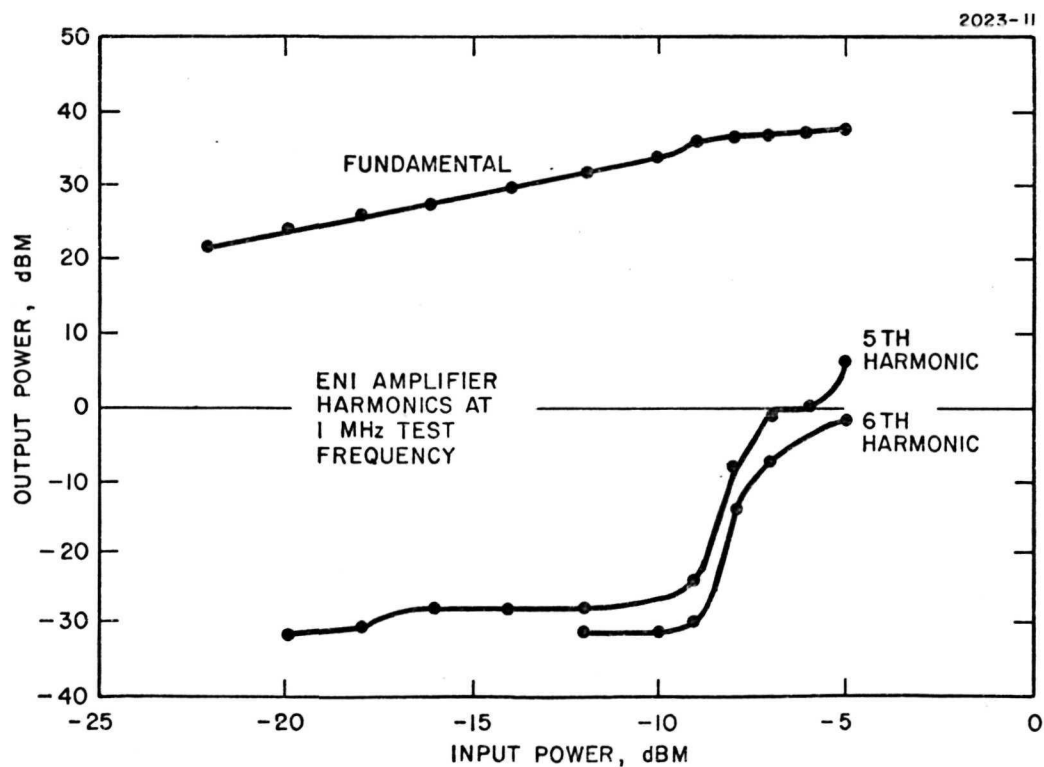


Fig. 5-5. Fifth and Sixth Harmonics as a Function of Input Level for 1 MHz Fixed Source.

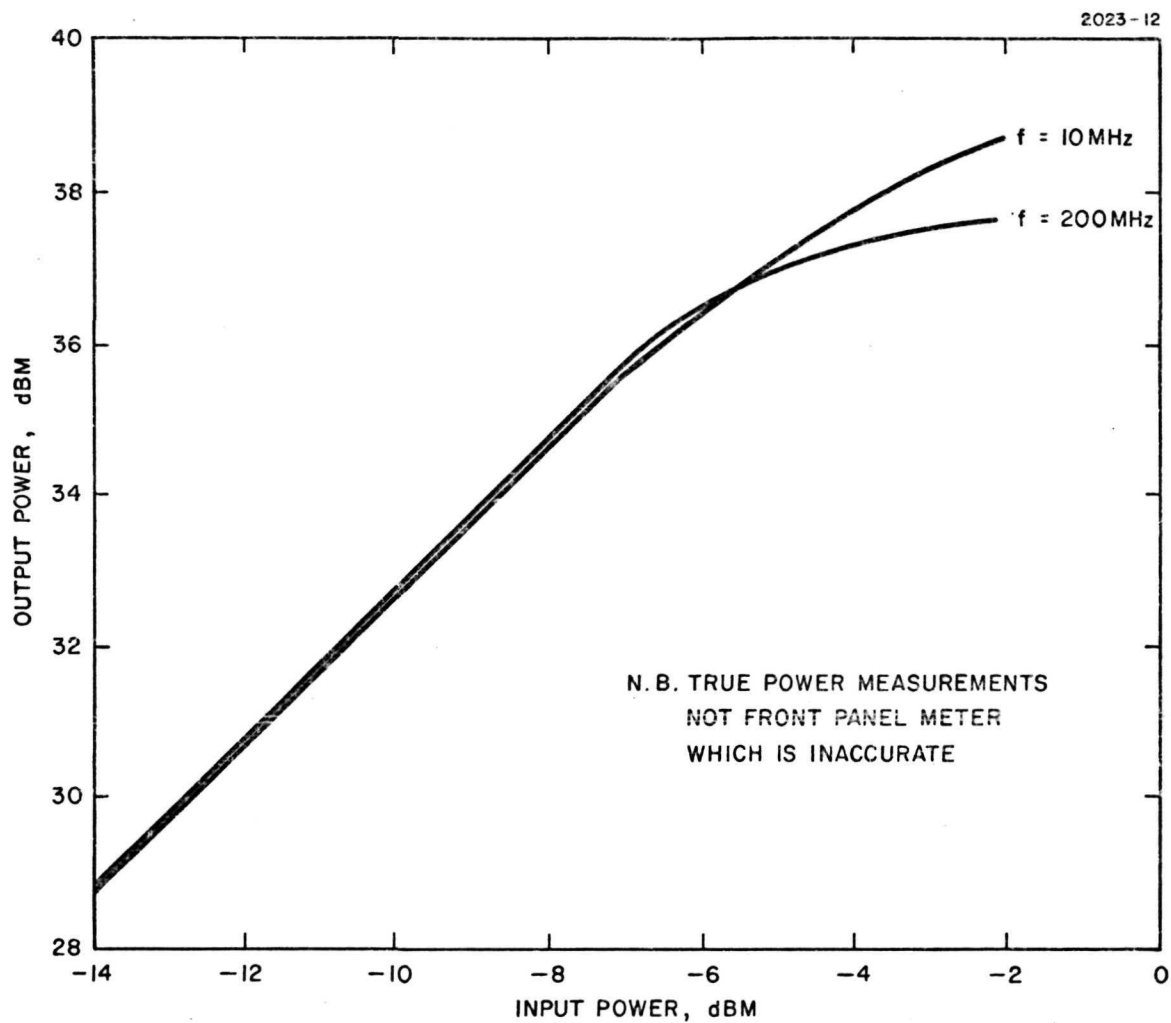


Fig. 5-6. Saturation Characteristics, Output Power Versus Input Power.

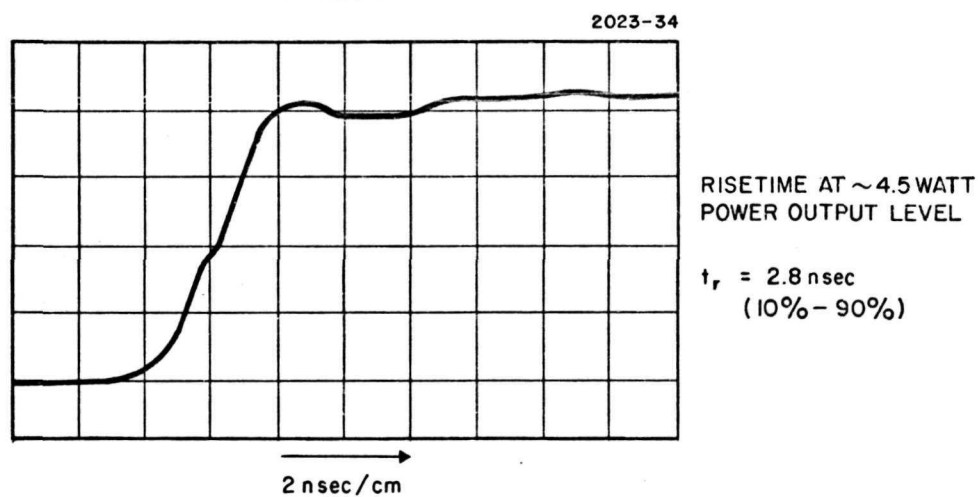
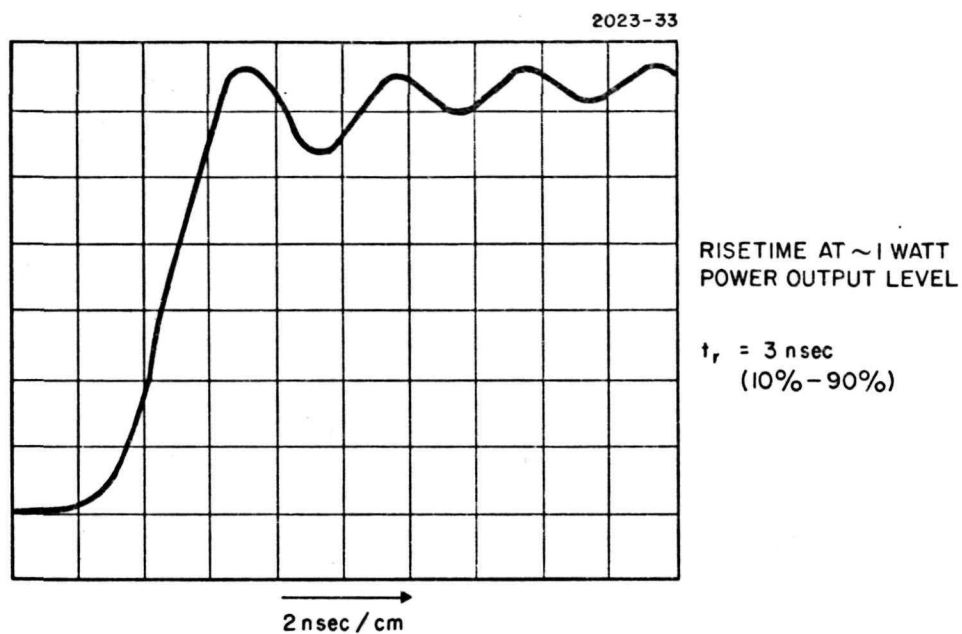
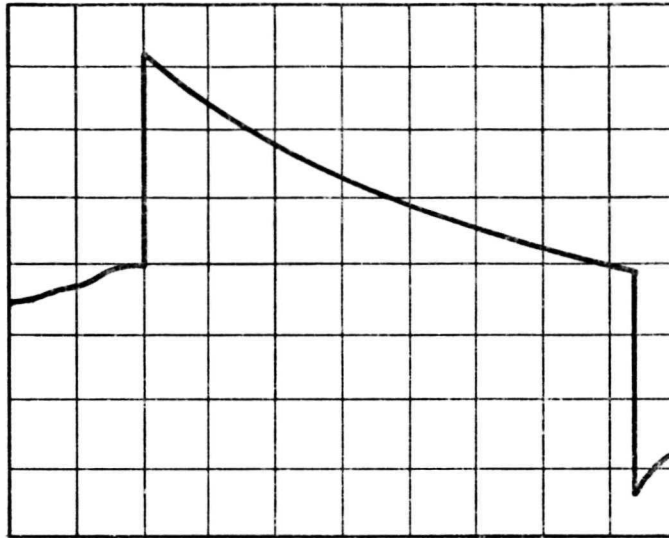


Fig. 5-7. Pulse Response for Unsaturated Output and Saturated Output.

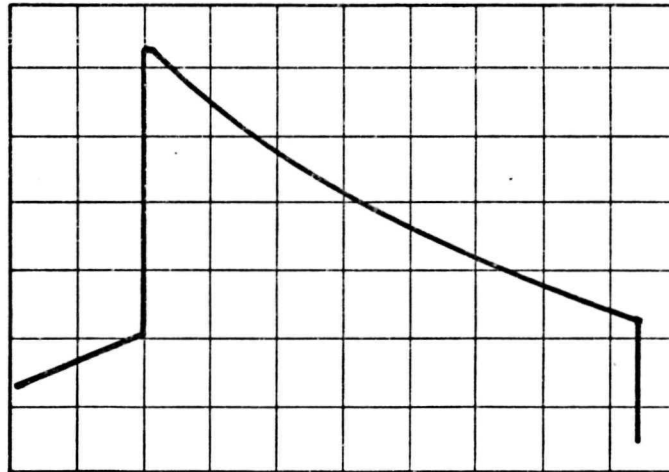
2023-35



PULSE DROP AT
~1 WATT POWER LEVEL

200 nsec / cm

2023-36



PULSE DROP AT
~4.5 WATT POWER LEVEL

200 nsec / cm

Fig. 5-7. (Continued).

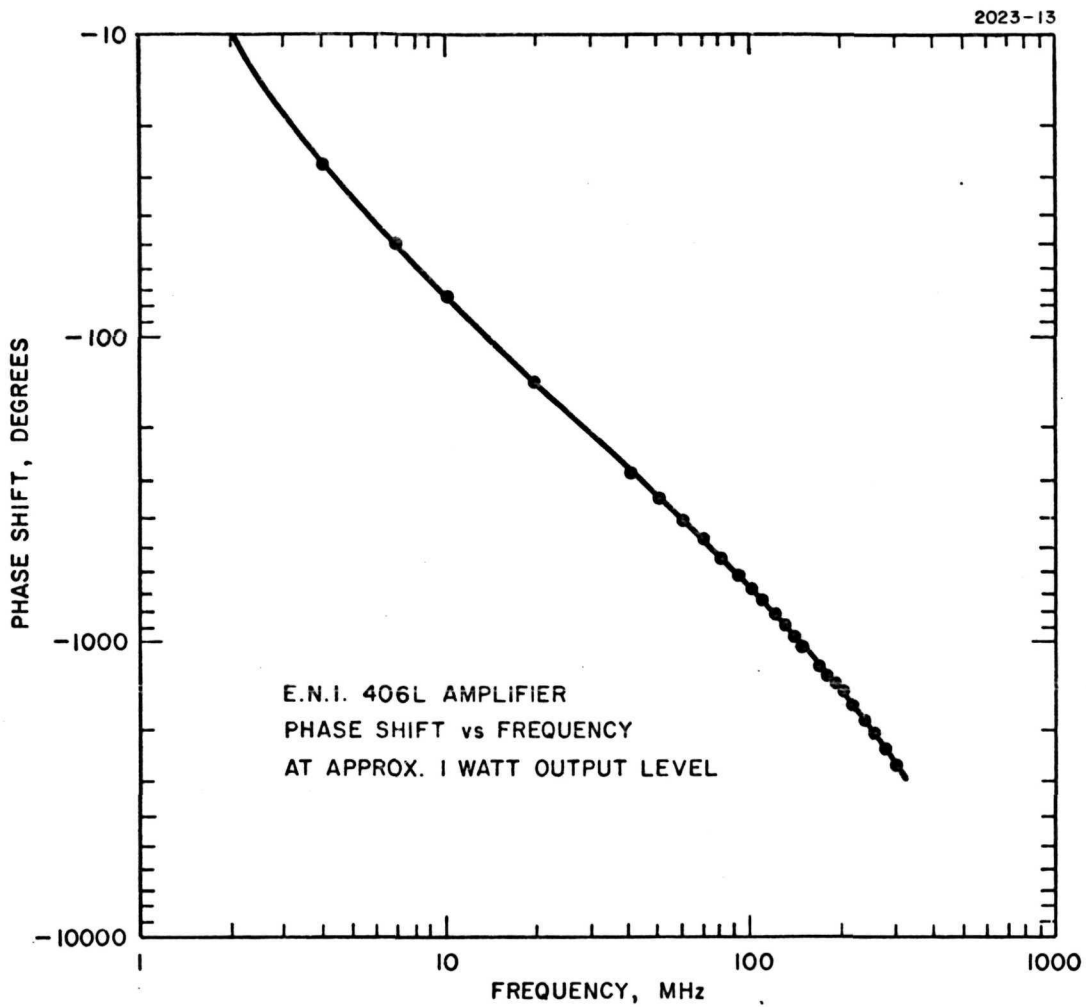


Fig. 5-8. Phase Shift Versus Frequency.

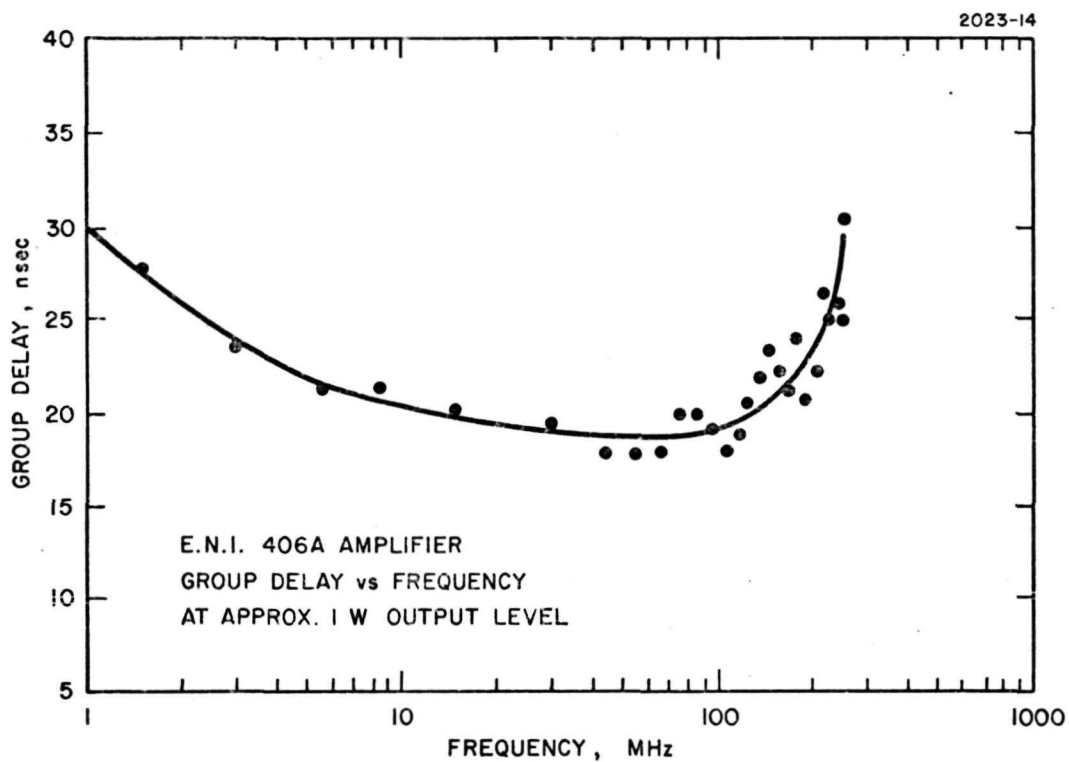


Fig. 5-9. Group Delay Versus Frequency.

5.4 WIDEBAND POWER SPLITTER/COMBINER TECHNIQUES

5.4.1 Core Limitations

The method of obtaining high, wideband rf power by in-phase summation of multiple amplifier outputs in a power combiner rests upon the ability to build wideband, constant group delay power splitters and combiners. These devices usually are cascades of 2:1 or 4:1 impedance ratio transformers bifilar wound on small toroidal cores. Clearly, careful selection of the core material, size, and shape factor are important for obtaining optimum performance. The upper frequency limitations of the core, power handling criteria and inductance criteria are given in detail in Appendix D.

5.4.2 Wideband Transformer Designs

Actual design of power splitters and combiners together with performance data are also presented in Appendix D.

5.5 BREADBOARD AMPLIFIER DESIGN AND PERFORMANCE DATA

The requirements for the modulator driver power were determined from Section 2.2 and Section 5.1, and the design goals for the breadboard amplifier were reviewed in Section 5.1. In achieving high performance from a transistor amplifier, a tradeoff must be made between the output voltage and the bandwidth of the device. A bandwidth was chosen sufficient to accommodate the fastest commercial

logic family, high-speed, emitter-coupled logic, such as Motorola's MECL III. The most significant performance characteristics of any amplifier that handles these signals are the rise and fall times and pulse droop. Typically, a 300 MB/sec data rate, previously stated as the basic system goal for wideband data transmission for a laser space relay link, requires a 1 nsec risetime in the driver. The lower frequency limit set by the 300 MB/sec data format is that 50 nsec of continuous high or low states must pass before pulse equalization to give a return to parity. For continuous pulse lengths longer than 50 nsec, 10% pulse droop at the modulator can be tolerated. In terms of rf bandwidth, the driver represents a broadband amplifier with a 3 dB bandpass of from 300 kHz to 350 MHz.

The modulator load is nominally 6 pF. At higher frequencies, the CdTe crystal becomes slightly lossy, but even at 350 MHz the real part of the load impedance is not significant.

The change in potential across the crystal must be 100 V to achieve the desired coupling modulation. The present design achieves this by modulating opposite sides of the load ± 25 V in opposite phase for a net potential of 50 V and -50V in the high and low states respectively.

A further goal for the driver is that the efficiency $\geq 33\%$. This is dictated by the tight power budget in a space application.

5.5.1 Efficiency and Bandwidth Considerations

The design of the breadboard amplifier was aimed at meeting the two primary performance requirements of improved efficiency and bandwidth. The approach to the improvement of efficiency was to operate the amplifier in a nonlinear class of operation. Class A transistor amplifiers have working efficiencies of 8 to 10%, particularly in wideband operation. For the amplification of binary digital information, the transistor can be operated as a switch; this mode is an overdriven class C and is sometimes called class D. Efficiencies of

50 to 60% are achievable in bandwidths of less than an octave, whereas in an application where bandwidth spans several octaves, 30 to 40% efficiency is the practical limit.

The difficulty of driving a transformer with a switch type device is that when the transistor is not conducting, the transformer sees a very high impedance and is susceptible to excessive ringing. This can be eliminated by using PNP/NPN matched pairs of transistors such that when one is not conducting the other is conducting, providing a continuous low impedance to the transformer primary. In the present case, however, there is no PNP counterpart to the 2N5635, so that two 2N5635's are used in a conventional push-pull combination.

Since the power splitter/combiner techniques offer a method of adding the power from a number of driver stages, the power performance of the individual transistor stages is not a critical matter. However, since the gain bandwidth of the transistor is fixed, the optimum efficiency is obtained when the bandwidth of the transistor stage is adjusted to match the bandwidth limitations of the transformers. Under these conditions, maximum gain per stage is achieved and maximum efficiency is achieved.

The bandwidth and risetime limitations of the amplifier clearly are determined by the transformers. Furthermore, the over-all power output of the amplifier is also limited by the core. Curiously, the core is under maximum load at the low end of the amplifier frequency range, and handles only a small amount of energy at the high end. This is because of the technique of bifilar winding of the transformers, and permits the use of physically small ferrite beads as a core material, permitting maximum upper cutoff frequency. The design of the transformers is given in detail in Appendix D.

5.5.2 Circuit Configuration

The configuration of the driver is shown in Fig. 5-10. The pre-driver accepts a 0 and 1.0 V logic signal from a signal source of 50 Ω . The pre-driver has a low impedance output of 50 Ω and drives a transmission line transformer with complementary outputs. The two complementary signals are then amplified in two identical driver stages. The driver output voltage, 50 V peak-to-peak about 0 V average, is applied to opposite sides of the modulator crystal.

The schematic of the pre-driver and power splitter are shown in Fig. 5-11. The common-emitter first stage drives the second stage, which is operated as a current mode amplifier to give a low impedance output. The feedback ratio of this stage has been adjusted for 5 V output swing with 1 V input to the pre-driver. Both stages are biased by active biasing networks. This simplifies biasing when the amplifier stages have little or no emitter resistance and ensures the proper bias current with changes in temperature and variations in sample-to-sample 2N3866 characteristics.

The power splitter that follows the pre-driver produces two signals, complementary and half the voltage of the pre-driver output. Further information on the individual transformer designs follows the summary of breadboard parameters.

The driver stages (one was breadboarded) are shown in Fig. 5-12. Each consists of a pair of 2N5635 RF power transistors. The transistor selection was based on the need for a 1.0 nsec risetime. The 2N5635 is a 470 MHz transistor and has a pulse performance of a nanosecond risetime. Higher frequency transistors have been used at UHF frequencies, but their use is usually not recommended. The basis for this is in the layout of the multiple emitters of the microwave transistors. At microwave frequencies, the skin depth is the order of the thickness of the deposited emitter stripes. This effect helps equalize the currents between the emitters. At UHF the skin depth is larger and the currents may now be unbalanced and cause hot-spot partial failures.

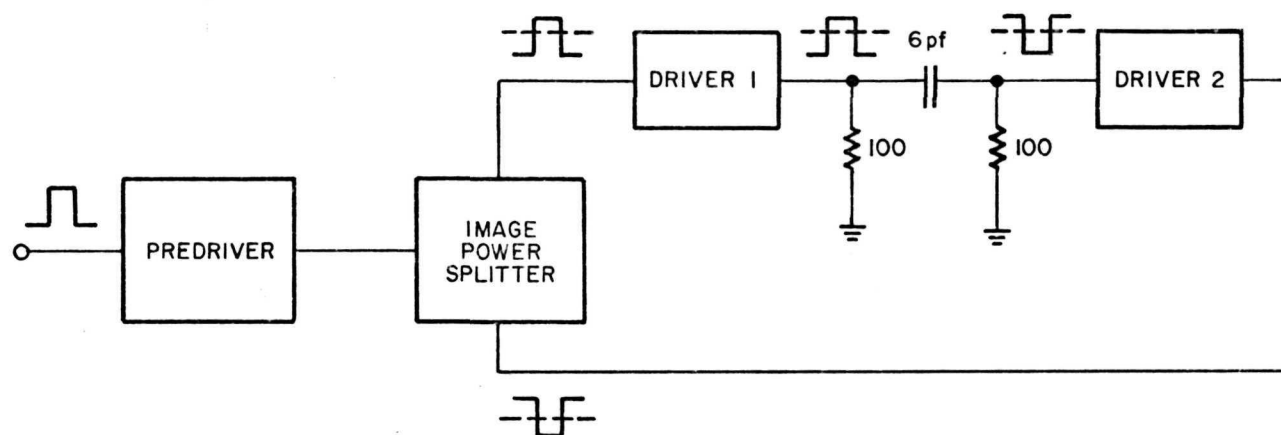
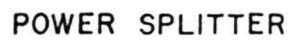


Fig. 5-10. Block Diagram of Balanced Driver Using Two Power Amplifier Stages.



109

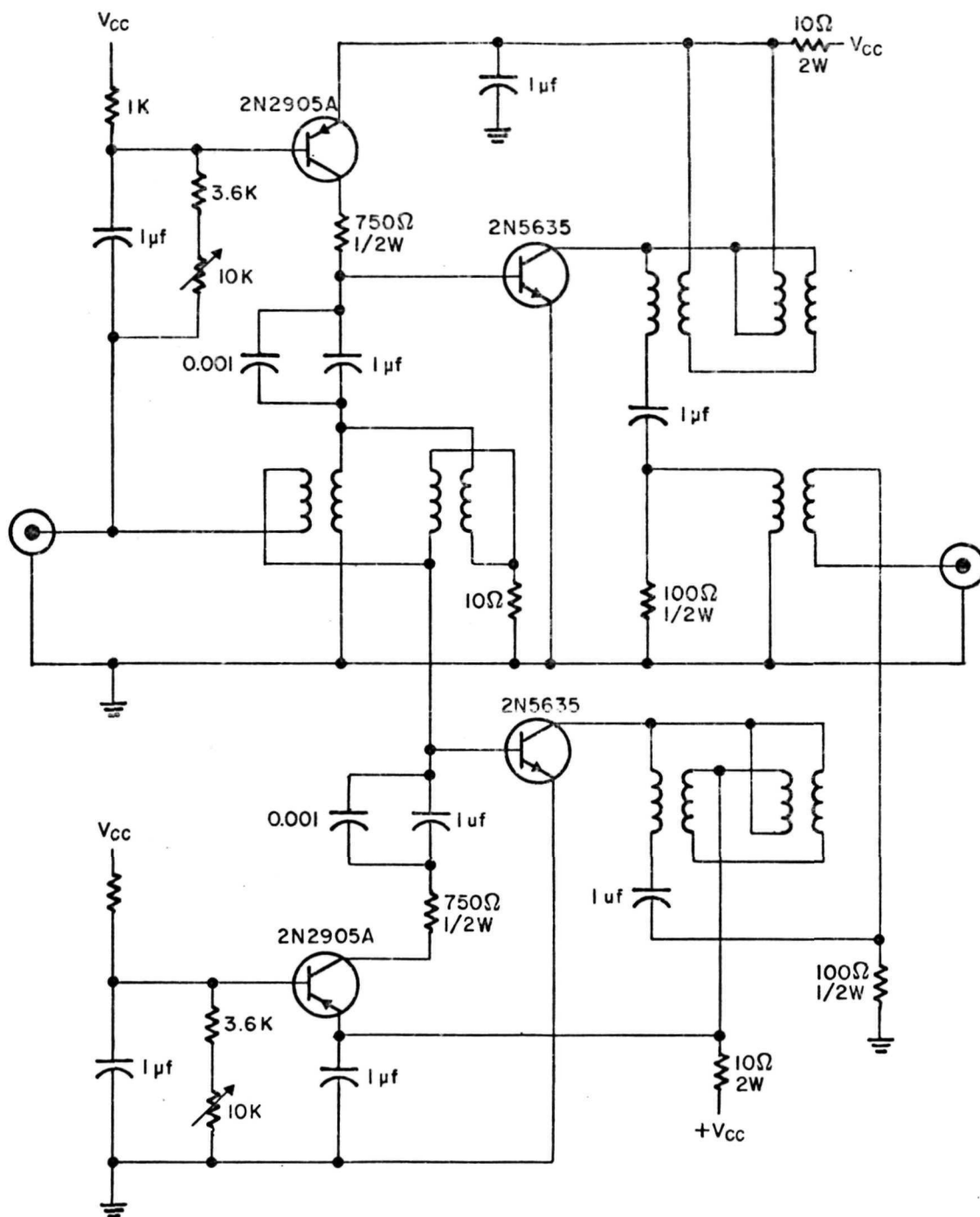


Fig. 5-12. Circuit Diagram of Power Amplifier.

One failure causes a domino-effect string of failures. Imbalances occur, for example, with variations in the emitter characteristics or the thickness of the emitter stripes. To overcome this, most UHF and lower frequency transistors have emitter ballasting (small emitter resistors in each leg) to equalize currents. UHF transistors are therefore much safer when the designer is attempting a broadband match and cannot be especially restrictive in decoupling and bypassing.

The transistors are rated at 2.5 W output with 1 amp maximum collector current. With the capacitive load, each of the four transistors supplying the drive must supply 0.75 A and approximately 2.25 W average power. The 2N5635 meets this requirement with some margin for combining and transformer losses. The saturation voltage of the device is 4 V, leaving an ample swing for the output voltage.

The driver, Figure 5-12, consists of a power splitter, the transistors, a 9 to 1 step-up transformer, and an output summer. The transformers are discussed in the transformer section of this report. In addition to the RF components, an active bias circuit is used with each output transistor. This is basically the same circuit as used in the pre-driver.

The active bias circuitry was added after the breadboard showed some touchiness in normal class C self-biased operation. With just a return at the base, the driver showed distortion of the output waveform when the digital input varied in amplitude or varied greatly in pulse width. Since the circuits leading to the driver are linear, clipping would be necessary before the driver if the instability were not remedied. The active biasing sets the transistor current at the average for normal operation. As the digital drive is applied, the biasing circuitry has virtually no contribution to the bias current and only corrects for errors in duty cycle and input level.

5.5.3 Design of Broadband Transformers

Broadband transmission line transformers were used to match input and output impedances of the driver. A differential

transformer was used to absorb the mismatch from impedance level changes due to frequency and signal level variations.

Many factors must be taken into account to obtain the desired response from broadband transformers. The transmission line mode transformer ensures minimum leakage reactance over large bandwidths. In conventional transformers, interwinding capacitance limits the response at high frequencies. Transmission line transformers combine this distributed capacitance with distributed series inductance and yield reactance free operation over a broadband of frequencies.

The upper frequency cutoff is raised by making the line length as small as possible. A rule of thumb is to limit the line length to an $1/8$ wavelength or less at the highest frequency of interest.

Transmission line transformers have a low frequency cutoff. This can be corrected in two ways: (1) by increasing the line length (degrading the high frequency response), or (2) by using a ferrite core permeability, therefore increasing low frequency response and not affecting high frequency characteristics.

5.5.3.1 Transformer Data

A. Four-to-one Stepdown Transmission Line Transformer (see Figure 5-13):

1. Properties

- (a) Designed for impedances of 50 ohms stepping down to 12.5 ohms
- (b) Six bifilar turns
- (c) Non-inverting output

2. Performance

- (a) Risetime = 1 nsec
- (b) Droop of 10% over 50 nsec
- (c) Falltime = 1 nsec

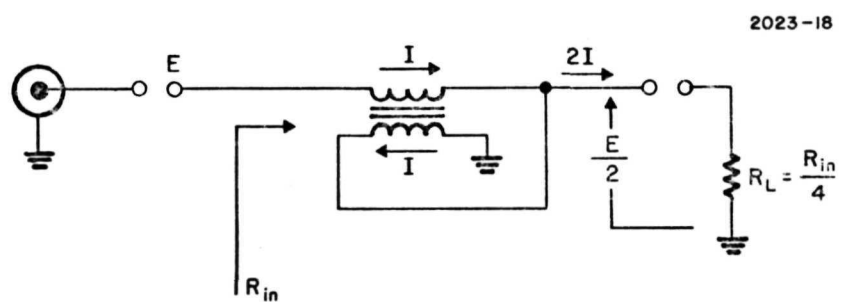


Fig. 5-13. Four-To-One Stepdown Transmission Line Transformer.

3. Materials

- (a) Core type (Indiana General)
Part number - CF101
Permeability = 400 (initially)
- (b) Wire size, No. 30 enameled.

B. One-to-nine Stepup Transmission Line
Transformer (see Fig. 5-14)

1. Properties

- (a) Designed for impedance levels of approximately 3 ohms stepping up to 27 ohms
- (b) Eight turns and four turns (see Fig. 5-14)

Explanation:

For a given magnetic field, the top transmission line in Fig. 5-14 must carry twice the voltage as the bottom line.

- (c) Non-inverting output

2. Performance

- (a) Risetime = 1 nsec
- (b) Droop of 20% over 70 nsec
- (c) Falltime = 1 nsec

3. Materials

- (a) Ferrite bead: Ferroxcube 3B
 - (1) Permeability = 900
 - (2) Wire size = 38 enameled.

C. Hybrid Power Divider (see Figure 5-15)

1. Properties

- (a) Designed for impedance of 12.5 ohms stepping down to 6.25 ohms
- (b) Outputs out of phase
- (c) Two turns per bead

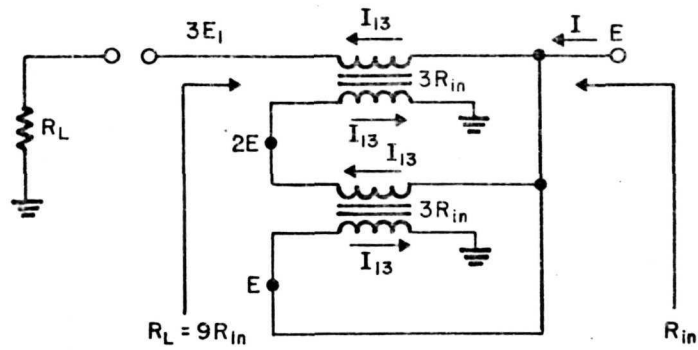


Fig. 5-14. One-To-Nine Stepup Transmission Line Transformer.

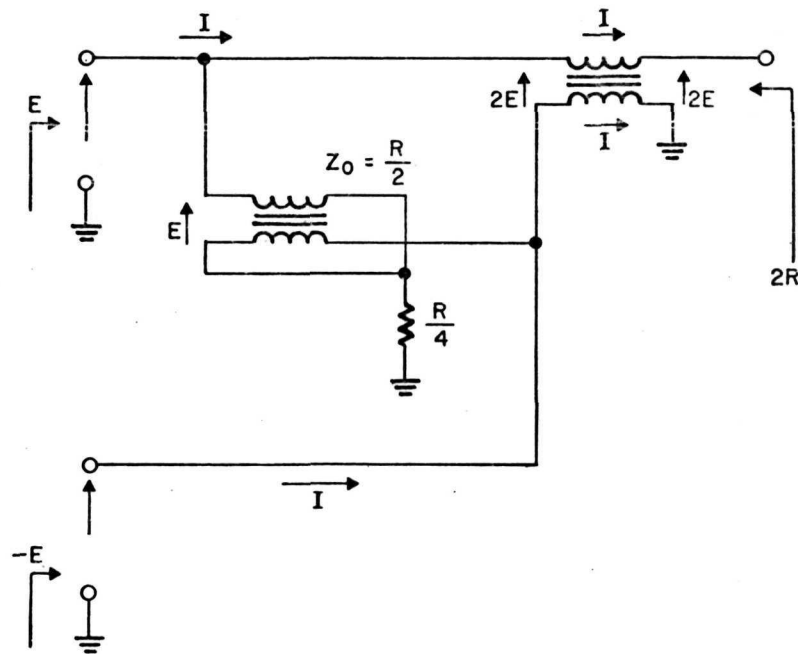


Fig. 5-15. Hybrid Power Divider.

- (d) Mismatching center section reduces wave distortion by dissipating all power reflected due to a mismatch in load impedances.

2. Performance

- (a) Risetime = 1 nsec
- (b) 25% droop over 50 nsec
- (c) Falltime = 1 nsec

3. Materials

- (a) Ferrite beads: Ferroxcube 3B
 - (1) Permeability = 400 (initially)
 - (2) Wire size = No. 30 enameled.

5.5.4 Breadboard Amplifier Tests

When the amplifier is driving a capacitive load, the available power is determined by the energy per bit that is required to charge the capacitor, times the bit rate. The power delivered to the modulator is then

$$P = 1/2 CV^2 \cdot B$$

where C is the 6 pF capacitance of the modulator,

V is the peak-to-peak voltage delivered by the driver,

B is the bit rate

The breadboard driver amplifier section tested was half of the total bridge amplifier, and had the following performance:

Voltage output (1 driver)	45 V _{pp}
Risetime	2.0 nsec
Pulse droop (50 nsec pulse)	20%
Power delivered to effective 12 pF load	5 W

Power input to amplifier		
100 mA 15 V to pre-driver	1.5 W	
500 mA 28 V to driver	14 W	
Efficiency	32.5%	

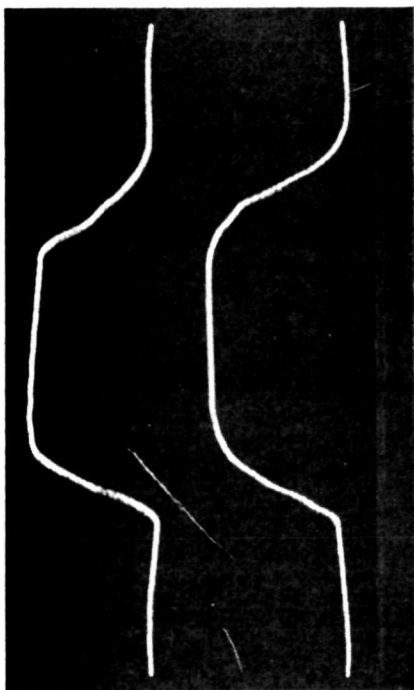
Estimated performance of the bridge driver shown in Fig. 5-10 is given as follows:

Peak-to-peak voltage output	100 V
Risetime	2.0 nsec
Power delivered to 6 pF load	10 W
Power input to amplifier (total)	29.5 W
Efficiency	34%

Figure 5-16 shows the waveform of a 10-nsec pulse and a 20-MHz square wave used as a source for the driver stage. The output voltage in these photos has a peak-to-peak value of 80~90 V with a 10 pF load.

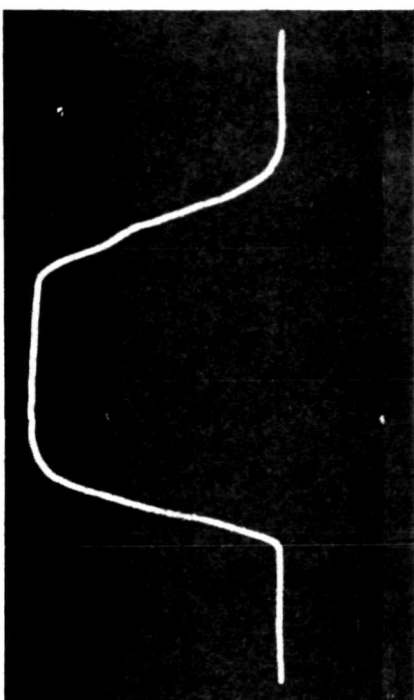
The pre-driver and driver amplifier configuration is shown in Figure 5-17. The pre-driver is shown at the right of the photo and the single driver stage is shown at the left. Two output connectors are shown, one for monitoring waveform of output and the other for the modulator load.

2172-5



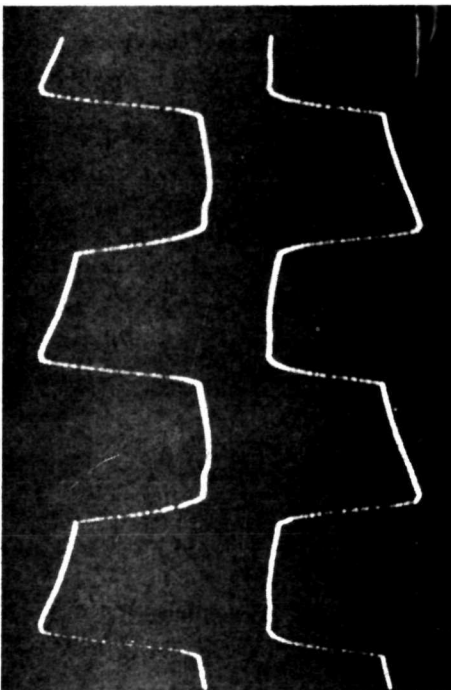
COLLECTOR A (TOP) B (BOTTOM) 40V PEAK TO PEAK

2172-6



COMBINED (A-B) 80V PEAK TO PEAK

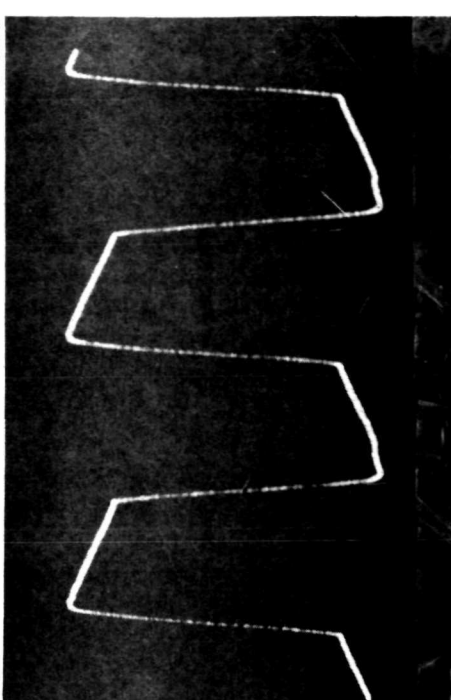
2172-7



COLLECTOR A (TOP) AND B (BOTTOM) 45V PEAK TO PEAK

RISE TIME ≈ 2 nSPULSE DROOP IN 50 nS $\approx 20\%$

2172-8



COMBINED (A-B) 90V PEAK TO PEAK

Fig. 5-16. Waveform of Driver With a 10 ns Pulse (Top) and 20 MHz Square Wave (Bottom) Used as Signal Source.

M9163

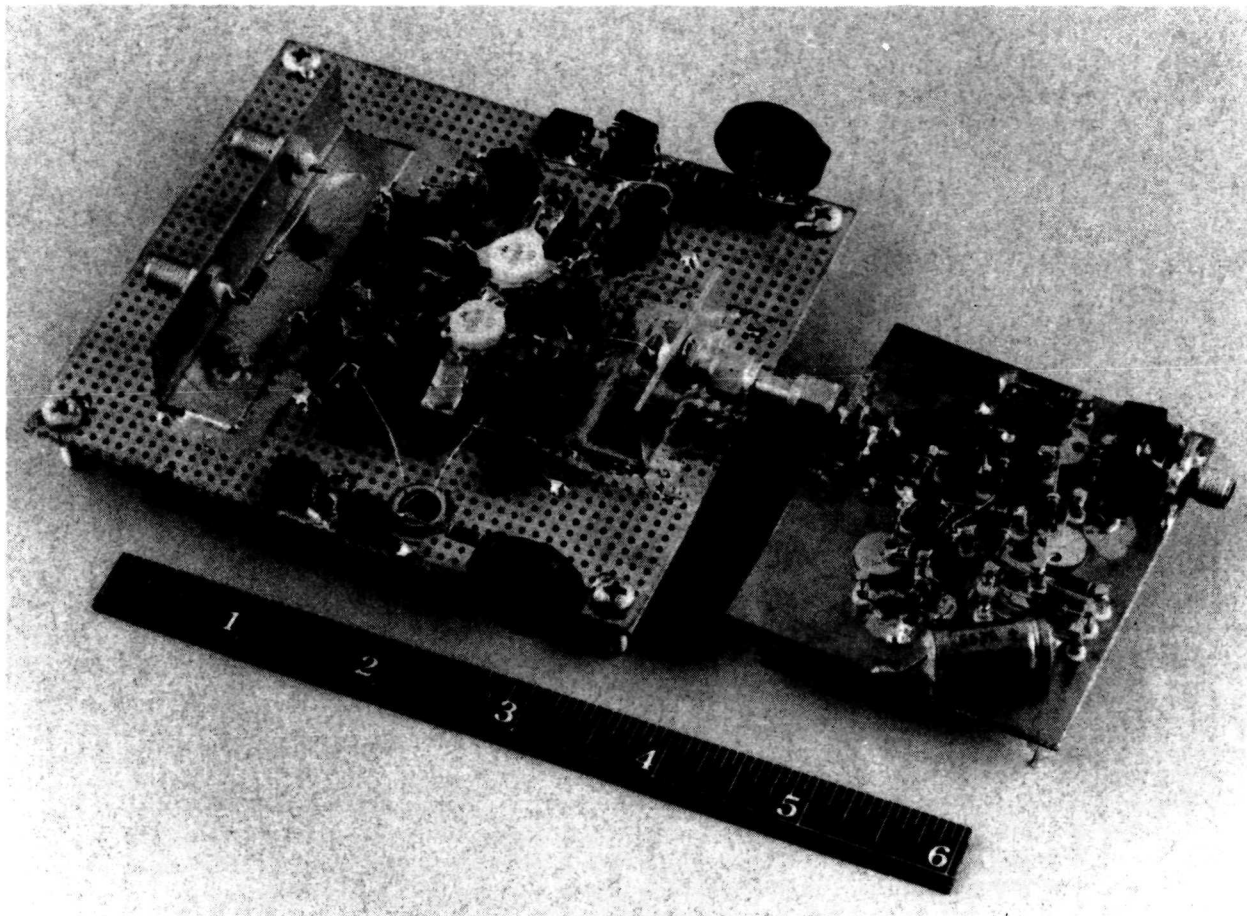


Fig. 5-17. Pre-Driver and Driver Configuration.

"Page missing from available version"

SECTION 6

V-BAND MODULATOR EXPERIMENT

The purpose of this task is to conduct an experiment using cadmium telluride as the modulating material and using V-band energy (50 to 55 GHz) to provide the modulating voltage. This experiment would then demonstrate the feasibility of generating a local oscillator signal that is tunable by varying the frequency of the V-band driver. During the performance of these tests, the V-band modulator rod was broken in handling and the tunable local oscillator experiment could not be completed. However, another rod was fabricated from residual material and two important tests were conducted on this rod; the first was to use the rod inside the laser cavity having a circulating power of about 40 W, and the second was a measurement of modulation retardation when the modulator was driven with a V-band source. The success of the first experiment illustrates that the modulator material losses and coating losses are sufficiently low that to permit the device to be included inside a laser cavity. The success of the second verifies that the performance predicted by the analysis is achievable. These factors can be used to predict an impressive 0.8 mW of tunable LO power with a V-band driving power of 100 mW.

The tunable local oscillator is necessary to track the Doppler shift when operating with a low altitude satellite. The local oscillator laser is operated on an adjacent transition to the received signal transition. Since the transitions are spaced approximately 53 GHz apart, one of the sidebands from the modulation will fall near the adjacent transition and can be controlled in frequency to provide a tunable local oscillator signal. The output signal of the local oscillator consists of an upper and lower sideband with no carrier. The appropriate sideband is then selected with an optical filter and used as the local oscillator signal.

6.1 V-BAND MODULATOR CONFIGURATION

The V-Band modulator configuration uses a millimeter waveguide fully loaded with electro-optical material (cadmium telluride).

Three constraints are imposed: (1) a close velocity match must be achieved between the optical velocity and the V-band phase velocity, (2) the maximum allowable modulator length is limited by diffraction and crystal length, and (3) the available driver power at 53 GHz is limited to a range of a few hundred milliwatts by current IMPATT driver technology.

To achieve the ideal velocity match for an optical refractive index of $n_0 = 2.6$ for cadmium telluride and a dielectric permittivity of $\epsilon = 10$, the waveguide aperture, a , is 1.7 mm.

The amount of required local oscillator power varies depending on the type of photoelectric mixer used and the bandwidth of the coherent optical receiver. Another consideration is the maximum amount of local oscillator that can be tolerated by the mixer. For the purposes of this calculation, a local oscillator power level of 1 mW is assumed. The coupling coefficient is, from Section 2.1,

$$C_m = k\Gamma_m^2$$

The microwave power $P_{\mu w}$ in a waveguide is related to the maximum field strength E_m by the relation

$$P_{\mu w} = \frac{a \cdot b E_m^2}{4Z(f)}$$

where a and b are the guide dimensions and $Z(f)$ is the impedance of the guide filled with dielectric. The field-distance product in the waveguide required to produce the necessary retardation is

$$E_m \cdot \ell = \frac{V}{\pi} \Gamma_m$$

Finally, the modulated output power is

$$P = k\Gamma_m^2 P_c$$

which is the power in both upper and lower first-order sidebands. The usable power for the oscillator purposes is 1/2 this amount. Thus, the

usable local oscillator power may be expressed as a function of laser circulating power and microwave driving power $P_{\mu W}$

$$P_{LO} = \frac{2kZ(f)\ell^2\pi^2}{a \cdot bV_{\pi}^2} P_{\mu W} P_c$$

This equation is plotted in Fig. 6-1 for a modulator rod length of 3 cm for a value of 1 mW local oscillator power required.

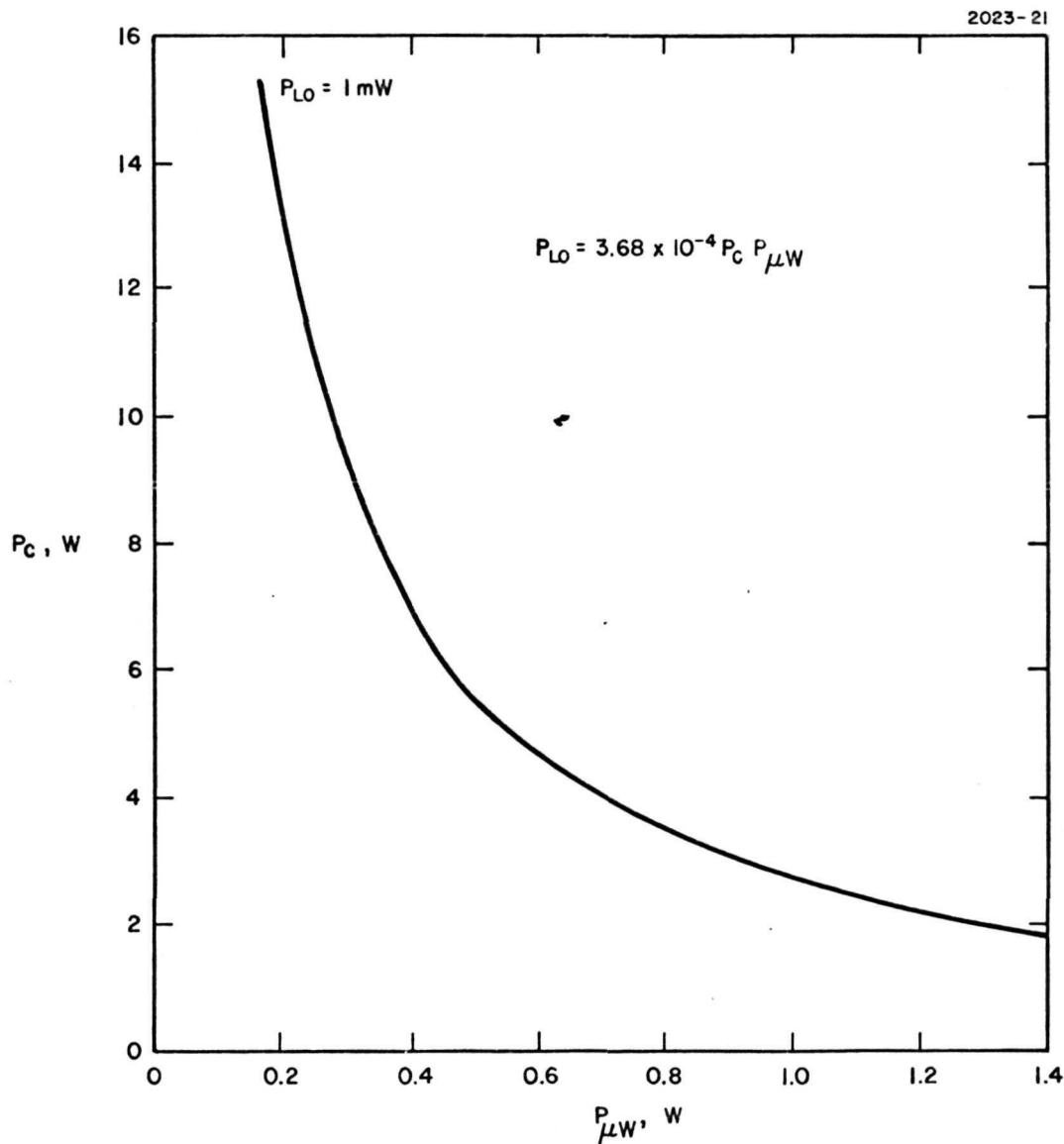


Fig. 6-1. V-Band Power ($P_{\mu W}$) Versus Laser Circulating Power for 1 mW of 1-Sideband Modulated Output Power. (V-Band Cavity Not Resonated).

The configuration of the V-band modulator as it is used as a coupling modulator is shown in Fig. 6-2. The test fixture (Fig. 6-3) is a waveguide beyond cutoff, unless the modulator rod is in place. Thus, the conventional V-band waveguide couples energy from the source to the modulator rod. A tuning stub is necessary to match out the inductive susceptance formed at the junction of the conventional and the filled waveguide. The microwave power enters the waveguide, it is reflected at the end of the rod (the guide is beyond cutoff in this region), and it is coupled back out of the structure. Thus the Q of the cavity formed by the dielectric filled section of waveguide is unity.

If it is necessary to drive the modulator from a lower power microwave source, then it may become necessary to resonate the microwave structure to obtain field enhancement. This can be achieved by adding susceptance at the junction of the conventional and filled waveguides and by adjusting the phase to obtain a cavity resonance at the desired millimeter wave frequency. However, the price for this enhancement of the electric field is reduced bandwidth of the device and severe complications for maintaining the cavity at the desired frequency.

The modulator may be used external to the cavity with a 1 W V-band source and a 3 W laser source. When used as an intracavity element, a modulator driver power of 0.2 W is required for a laser circulating power of 13 W.

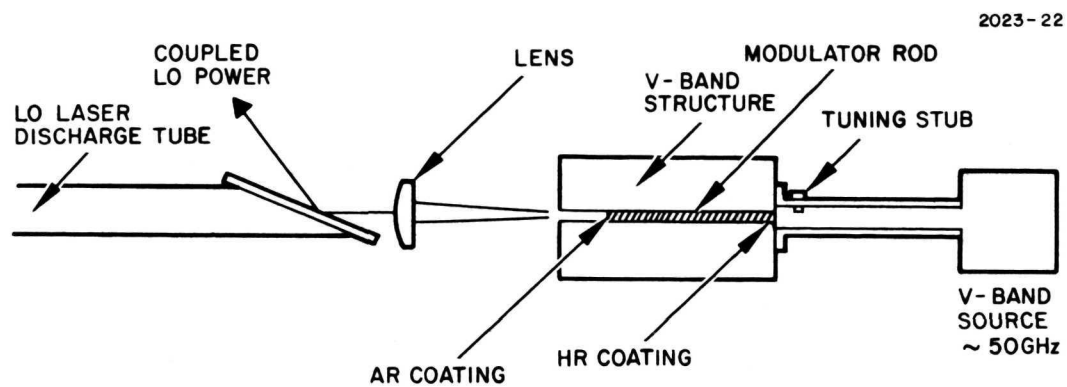


Fig. 6-2. Configuration of V-Band Modulator Experiment.

M9631

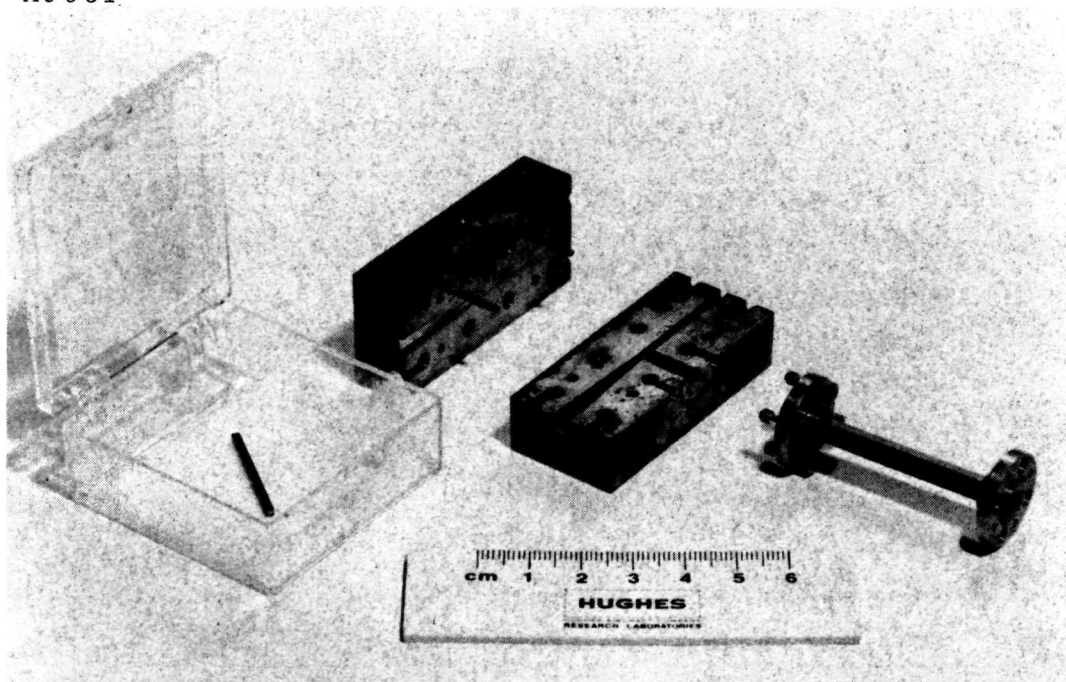


Fig. 6-3. V-Band Modulator Test Fixture and Rod.

The satisfactory performance of the V-band modulator in a waveguide requires that the dielectric loss properties of the material at the frequency of 53 GHz are within reason. For a resonant cavity structure, should field enhancement be required, the dielectric loss properties must be extremely low. V-band dielectric loss measurements were made using both cadmium telluride and gallium arsenide. A single crystal of CdTe taken from boule 176 was found to have a Q of 615, which is equivalent to a dielectric loss tangent of 0.0016. The microwave resonance characteristics of the waveguide structure over a frequency range from 51 through 59 GHz are given in Fig. 6-4; those for a 52.2 to 53.3 are shown in Fig. 6-5. The tip of the resonance curve nearest 53 GHz is shown in Fig. 6-6, indicating a bandwidth of about 75 MHz.

The first modulator crystal installed in the V-band modulator structure has a slightly larger dielectric loss tangent. Although the crystal was cut from the same boule as above (boule 176) its maximum Q was 560 and its loss tangent is $\sim 10^{-3}$. This measurement indicates that there is considerable variation in the V-band dielectric loss properties of cadmium telluride, even in samples from the same boule.

The rod selected for the V-band modulator measurements, however, has sufficiently low loss tangent not to cause significant dissipation.

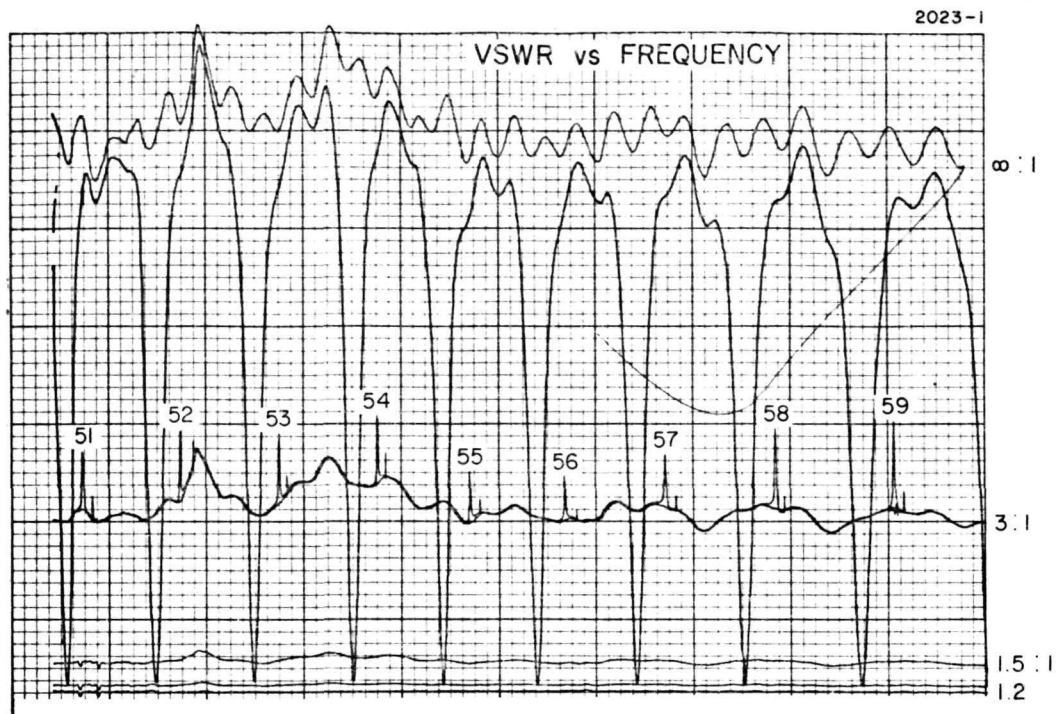


Fig. 6-4. V-Band VSWR Versus Frequency.

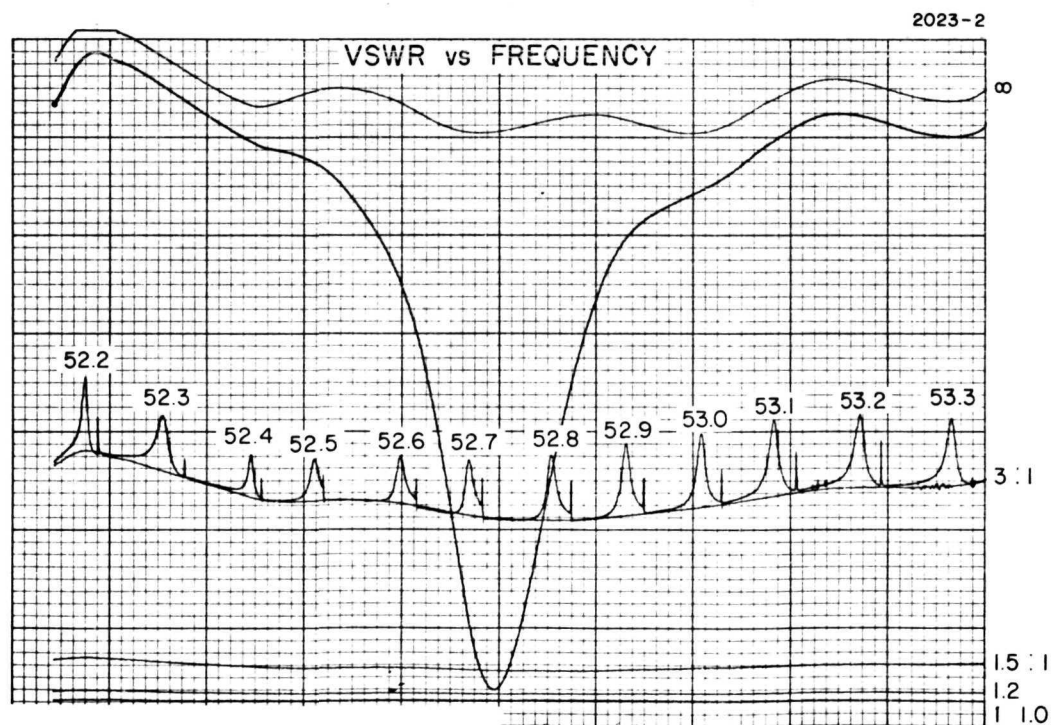


Fig. 6-5. V-Band VSWR Versus Frequency.

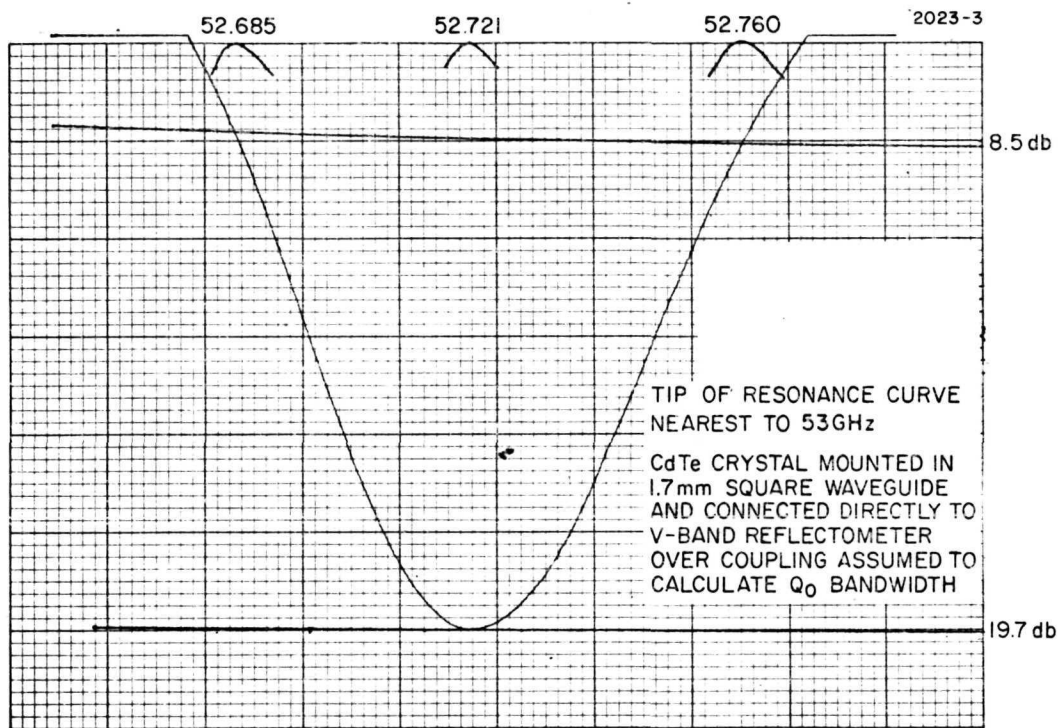


Fig. 6-6. V-Band Reflection Versus Frequency (Tip of Resonance Curve Nearest to 53 GHz).

6.3 V-BAND MODULATOR TESTS

The rod used for the V-band experiments is identified as the V-band rod, having a length of 2.8 cm and a square cross section of 1.7 x 1.7 mm. This rod is fitted precisely into the waveguide structure such that the waveguide is completely dielectric filled in the region of the modulator material.

The amount of local oscillator power required in an optical heterodyne communication system is on the order of 1 mW. The testing of the V-band modulator device was to be oriented toward identifying the sideband optical energy and measuring its level. Simple power measurements such as are used for the data modulator tests were made by merely modulating the V-band source with a 1000 Hz and to measure the 1000 Hz component of the output power (6.3.2). The ideal experimental setup is, however, considerably more complicated, requiring two lasers, one to serve as the signal and the other the local oscillator, a wideband detector, an optical spectrum analyzer to identify the transition of the transmitter laser and the local oscillator laser, a grating to separate the leakage from the local oscillator laser and a complete V-band millimeter wave test facility. An ideal experimental setup is illustrated in Fig. 6-7. For the purposes of this experiment, the following frequencies are used:

Transmitter	P_{18}	28,359,800 MHz *
Local Oscillator	P_{20}	28,306,251 MHz
Difference freq.		53,549 MHz

The V-band driving source is tunable around the center driving frequency of 53,549 MHz.

6.3.1 Laser Performance With Modulator in Cavity

The performance of the laser with the modulator rod and lens in the cavity behaves the same as for data modulator rods No. 4, 5, and 6.

*Shiffner, G., "Calculation of Accurate CO₂ Laser Transition Frequencies and their Standard Deviations," Opto-Electronics, August 1972.

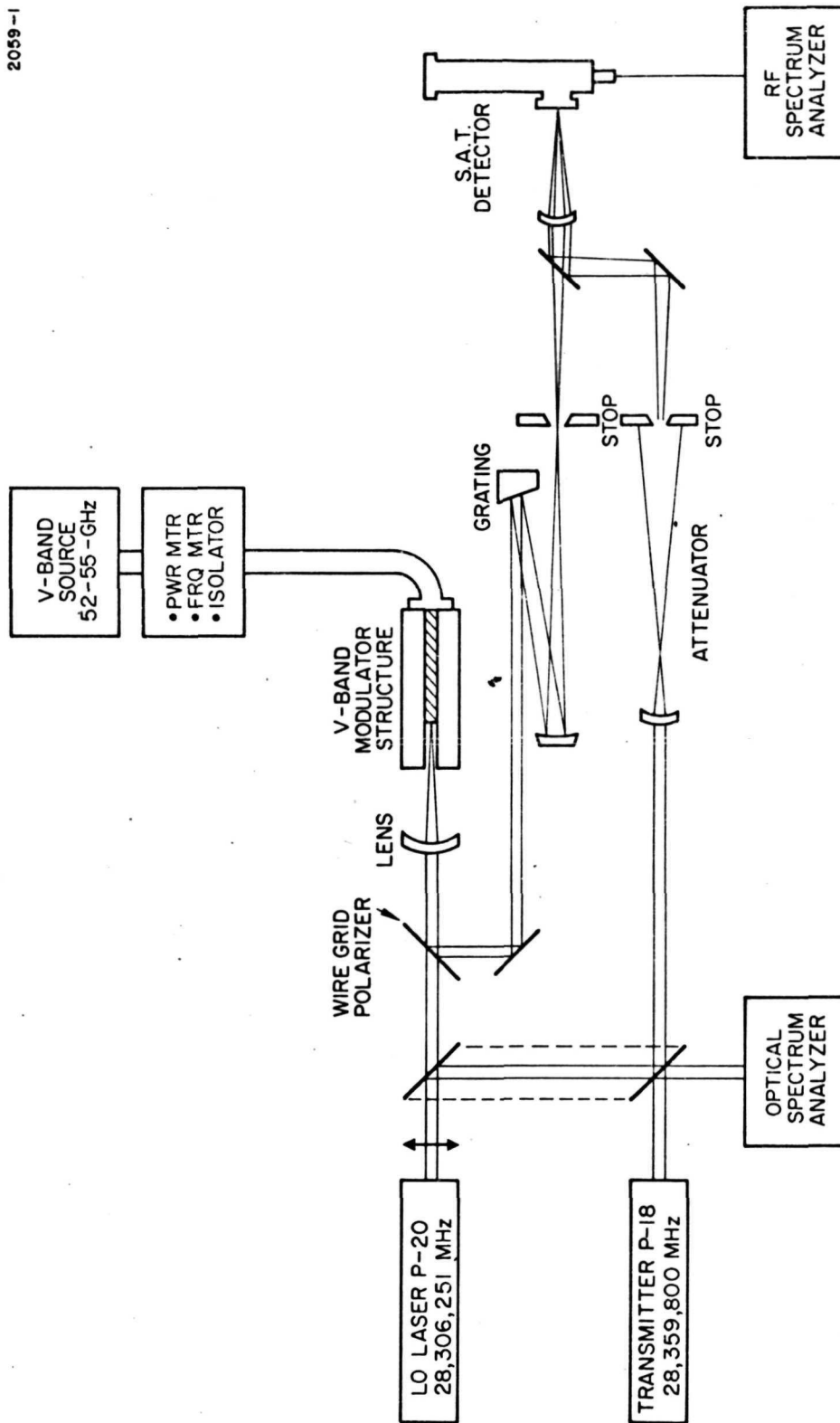


Fig. 6-7. Ideal V-Band Modulator Experiment Test Setup.

6.3.2 Measurement of Modulator Retardation

Verification of modulator retardation as a function of applied millimeter wave power was made external to the laser cavity. Using the experimental conditions described in Fig. 6-7, the ratio of modulated (one sideband only) power to incident power can be written

$$\frac{P}{P_i} = 1/2 \left(\frac{\pi}{V_\pi} \right)^2 (E_m \cdot l)^2 = 0.39 P_{\mu w} \times 10^{-3} .$$

For a P_i of 1.0 W, and a millimeter wave power of 1 W, the modulated power was 0.2 mW.

Theoretical:	$\frac{P_{\text{modulated (1 SB)}}/P_{\text{incident}}}{3.9 \times 10^{-4} P_{\mu w}}$	$\frac{\text{Effective } \Gamma_m}{0.028 \sqrt{P_{\mu w}}}$
	$\sim 2 \times 10^{-4} P_{\mu w}$	$\sim 0.02 \sqrt{P_{\mu w}}$

The experimental results are found to be within a factor of 2 of the theoretically predicted values. The technique of measurement, that of modulating the V-band source with a 1000 Hz square wave and to measure the 1000 Hz component of the detected signal, is unfortunately not an accurate method. It is sufficient, however, to verify that the V-band retardation of the cadmium telluride modulator is very close to that expected.

6.3.3 Conclusion

Because of breaking the original V-band rod and the difficulty in remaking another from residual material, the complete tunable LO experiment could not be completed during the program. However, the operation of the modulator rod in the CO₂ laser cavity and the verification of the V-band retardation with a 1000 Hz modulated V-band signal, has given verification that the concept is a valid one. Because

of these results, the predicted performance of such a modulator can be stated with assurance.

Assembling the V-band modulator in a CO_2 laser cavity with optimum mirror coatings should permit circulating power as high as 50 W in the laser cavity. Under these conditions, a tunable local oscillator power of 10 mW can be provided with 1 W of mm wave driving power. Further enhancement can obviously be obtained through the use of resonant mm-wave cavities to enhance the electric field in the cavity.

SECTION 7

COMMUNICATION DEMONSTRATION TESTS

The vast improvement offered by coherent detection over direct detection of $10\text{ }\mu\text{m}$ signals makes the use of this wavelength feasible in a satellite communication system. The bandwidth required of the Laser Space Relay Communication System is significantly greater than that achieved previously with optical intracavity FM systems (see Appendix A), and the technique of intracavity coupling modulation is the most direct way of achieving these bandwidths. It has been pointed out in detail in Section 2 that the most effective use of this technique is through the use of DSBSC coupling modulation and coherent or homodyne detection.

Modulator performance tests consisting of retardation measurements and frequency response measurements have been reported in Section 2. These tests verify that the device itself is performing in the prescribed way; however, they do not show that the system concept is correct. To prove the system concept of DSBSC modulation and coherent detection, wideband data must be used to drive a coupling modulator, and coherent detection must be used to detect this signal. The full implementation of the coherent system is clearly beyond the state of the art and beyond the scope of this program. A homodyne receiver, phase locking and phase detection of a $10\text{ }\mu\text{m}$ optical signal have not been achieved. The ultimate development of these techniques clearly is necessary.

The tools necessary for the demonstration of coherent detection in the laboratory are available, however. Recent completion of the development of $10.6\text{ }\mu\text{m}$ acousto-optic modulators for beam scanning experiments^{*} gives us a tool to generate an offset local oscillator. Further, the availability of solid-state voltage controlled oscillator (VCO) equipment with fast tunability allows us to electronically track the laser signal, producing phase locking of high quality.

^{*}Air Force Contract No. F33615-71-C-1736

7.1 COMMUNICATION TESTS USING DIRECT DETECTION

The test setup for communication tests using direct detection is shown in Fig. 7-1. As mentioned in Section 2, direct detection requires that some carrier is transmitted along with the signal sidebands. For these tests, the carrier was provided by a leakage vestigial carrier of 20 mW. Thus, the level of modulation during these tests produced a sideband power of about 10 mW. Modulator rod No. 4 was used, with a driving voltage from 10 to 15 V.

7.1.1 Swept Frequency Tests

The purpose of the swept frequency tests is to ascertain the frequency response of the components and of the system. The raw data were taken in the format shown in Fig. 7-2(a) and (b). The scope display was photographed for the output of the sweep generator directly into the scope and through the entire system. Comparing these two traces gives the frequency response of the system, including the ENI driver, coupling modulator, SAT-type C-2 detector, and Avantek amplifier. A plot of this frequency response data is given in Fig. 7-3.

A complete trace of the system frequency response using the SAT-type C-2 detector (No. 985) as compared with that of the SAT-type A-2 (No. 667) is shown in Fig. 7-4(a) and (b). These traces were taken on the Tektronix 7904 oscilloscope that has a 500 MHz baseband frequency response.

7.1.2 Digital Waveform Tests

Using a 240 MBit/sec pseudo-random word generator as a signal source, digital information was transmitted through the system. This signal waveform first was measured directly as the voltage on the modulator after amplification by the ENI amplifier. This is shown as Fig. 7-5(a). After passage through the system and detection on the

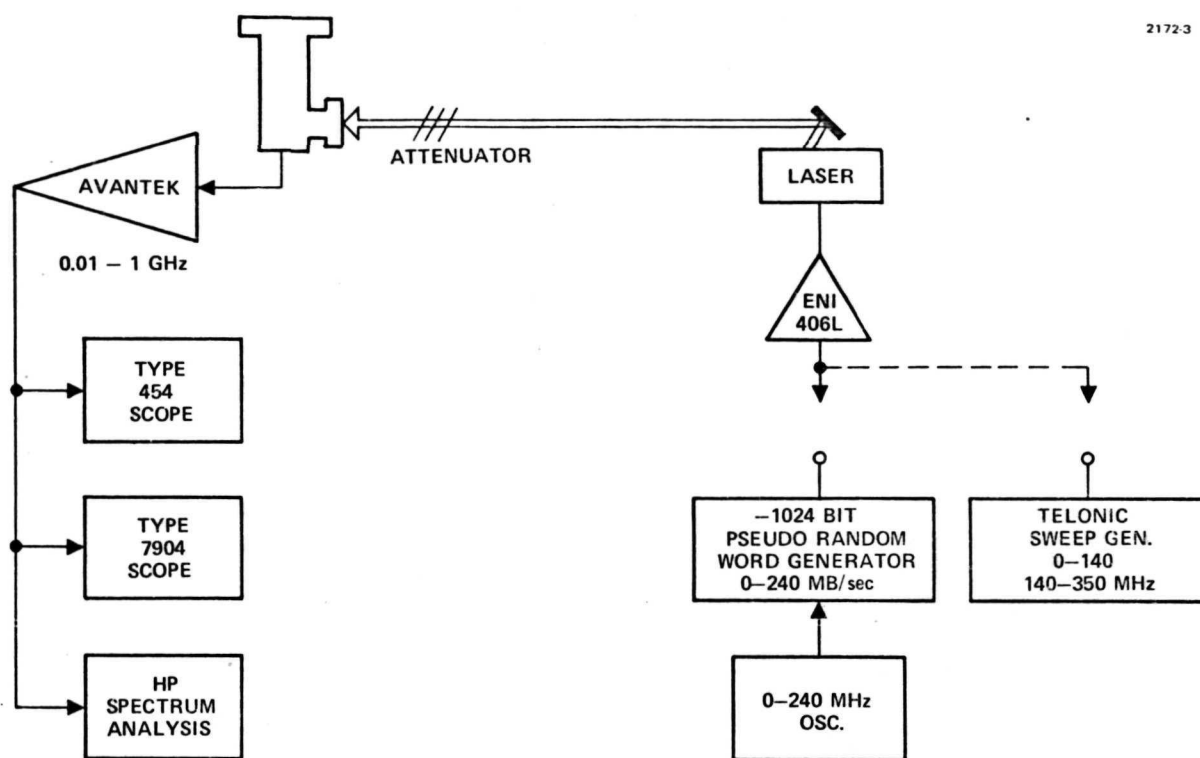
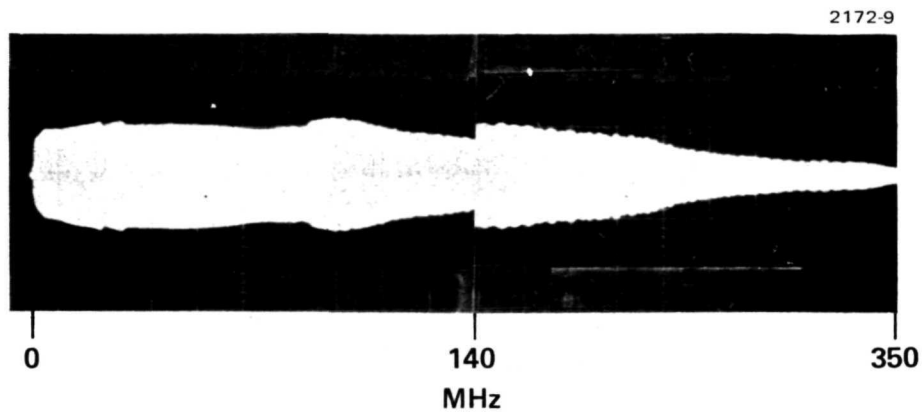
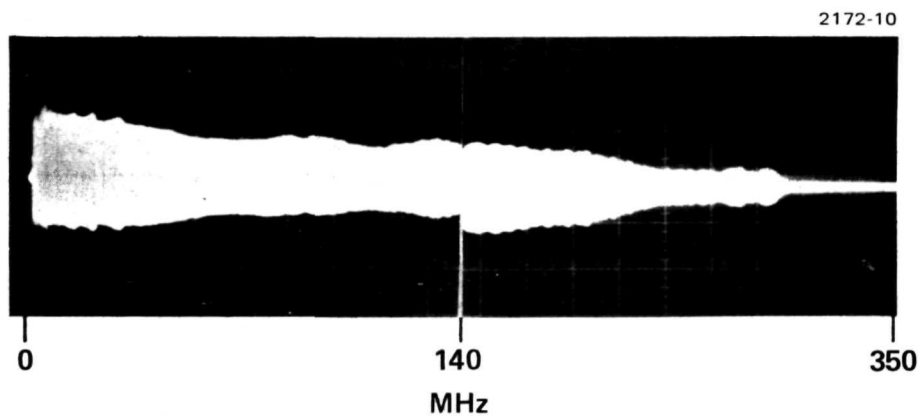


Fig. 7-1. Setup for Communication Tests Using Direct Detection.



(a) SWEEP GENERATOR + AVANTEK + SCOPE



(b) ENTIRE SYSTEM (ENI DRIVER, LASER
MODULATOR, SAT DETECTOR, AVANTEK
AMPLIFIER AND 454 SCOPE)

Fig. 7-2. Swept Frequency Response, Raw Data Format.

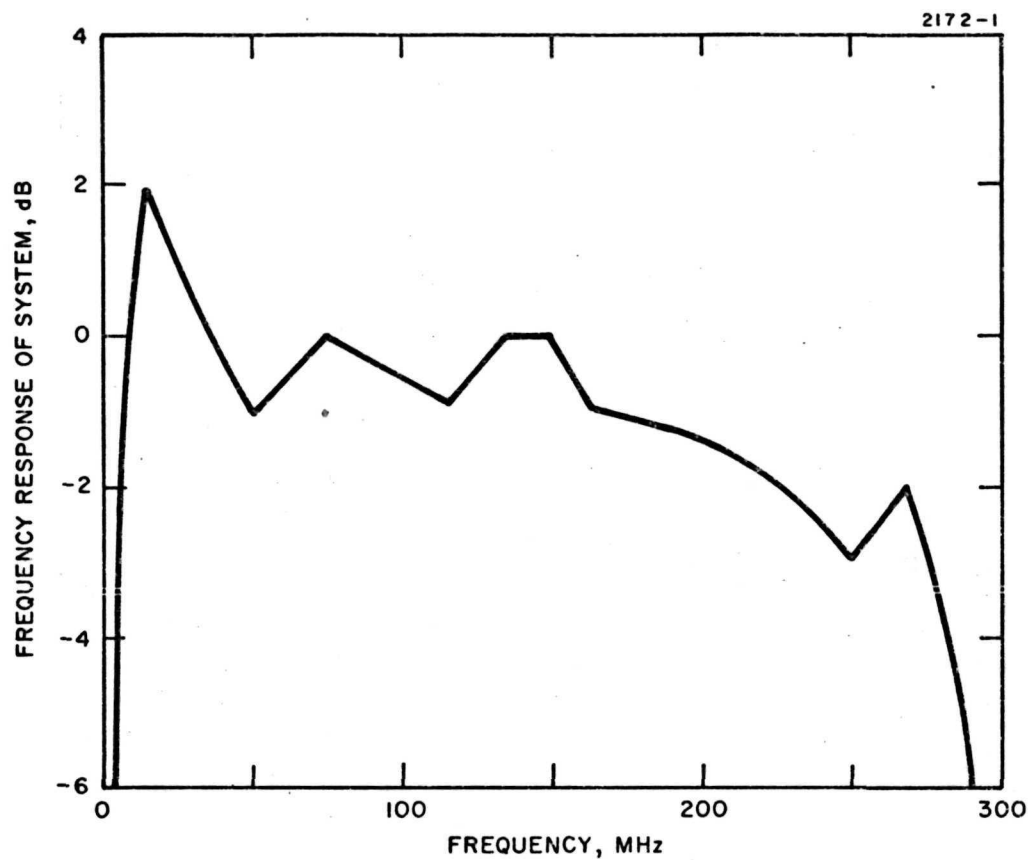
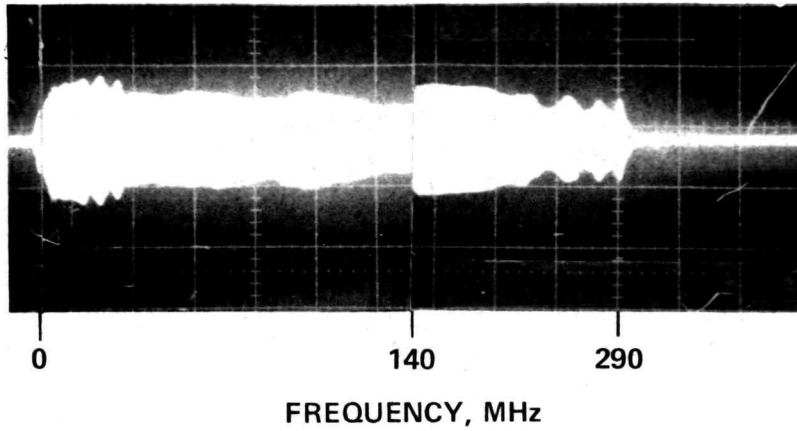


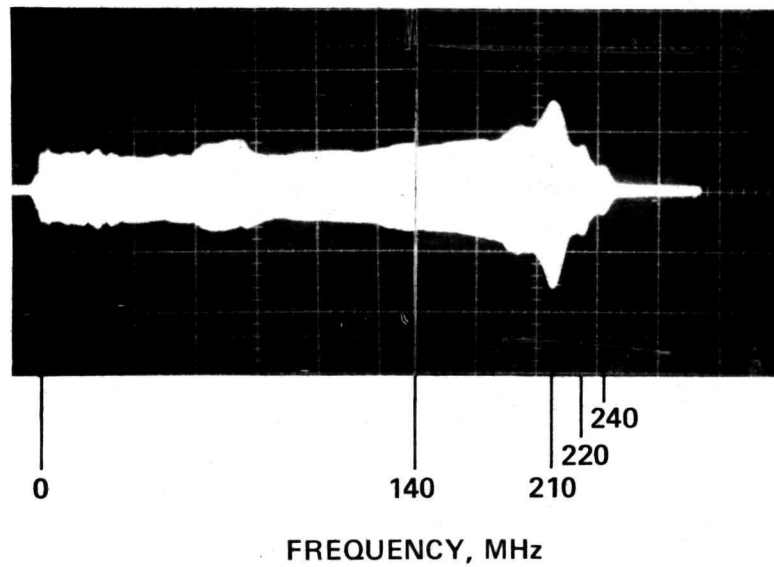
Fig. 7-3. Frequency Response of System: ENI Driver, Coupling Modulator, SAT Detector and Avanter Amplifier.

2172-11



(a) ENTIRE SYSTEM WITH SAT NO. 985 DETECTOR (C-2)

2172-12



(b) ENTIRE SYSTEM WITH SAT NO. 667 DETECTOR (A-2)

Fig. 7-4. Swept Frequency Response Using 7904 Oscilloscope With 500 MHz Response.

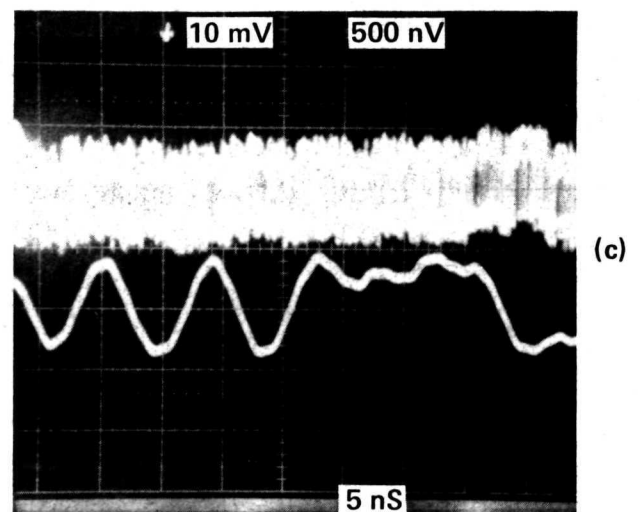
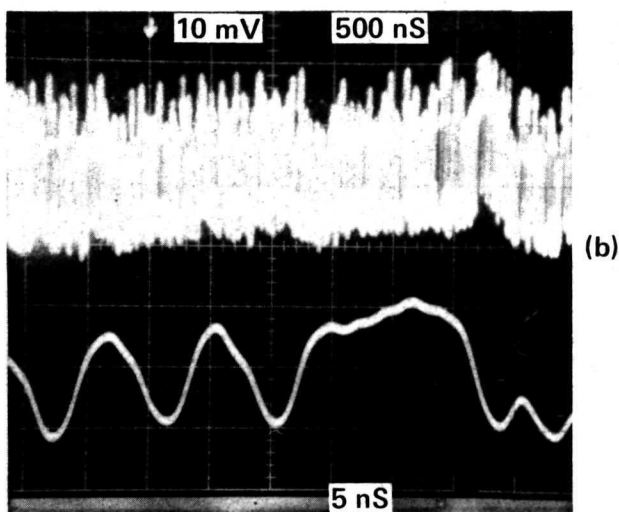
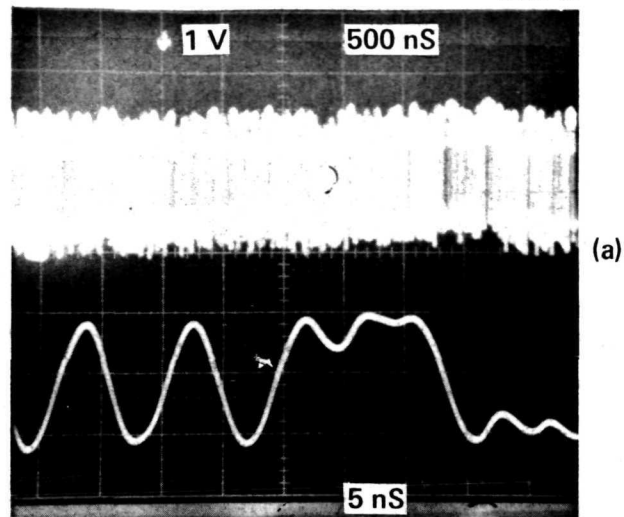


Fig. 7-5. Signal Waveform 240 MB/sec, 1024 Bit PSW, 7904 Scope.
 (a) Through ENI, (b) Through System, SAT Det No. 985
 (Type C-2), (c) Through System SAT Det No. 667 (Type
 A-2).

Note: Top trace of each photo is entire 1024 word (5 μ sec in length).
 Lower trace is a 10-bit sample of the beginning of the word.

SAT-type C-2 detector, the signal waveform is as shown in Fig. 7-5(b). Finally, after passing through the system and detection on SAT-type A-2 detector, the waveform appears as in Fig. 7-5(c).

The top trace in each photograph is the entire 1024-bit pseudo-random word. The bright spot near the left of the top trace is the portion (10 bit sample) of the word that is expanded in the bottom trace of each photo.

It can be seen from these signal waveforms that the system risetime is on the order of 3 nsec and that it is limited by the driver amplifier. The maximum bit rate that can be handled by the system without a penalty of either greater signal-to-noise ratio or loss of information is about 330 MB/sec, allowing 1 bit for each 3 nsec.

7.1.3 Eye Pattern Tests⁹

Since the pseudo-random word length is 1024 bits, eye pattern tests provide a suitable means for determining the quality of the channel for the transmission of digital information. The technique requires that the oscilloscope horizontal trace is triggered by the clock rather than the word-sync from the data generator. The results are given in Fig. 7-6(a) for the waveform directly from the data generator, Fig. 7-6(b) for the waveform after passing through the ENI amplifier, and Fig. 7-6(c) for the waveform after passing through the entire system and with a 20 dB signal-to-noise ratio. It can be seen that the eye pattern shows clear decision (black region) areas for the signal after passing through the system. It is estimated that this waveform corresponds to a bit-error-rate of better than 10^{-6} .

7.1.4 Baseband Spectrum of Digital Information

The spectrum of the digital signal is shown in Figure 7-7(a). The first minimum coincides with the clock frequency of 240 MHz and the second minimum coincides with the second harmonic of the clock at 480 MHz.

2172-14

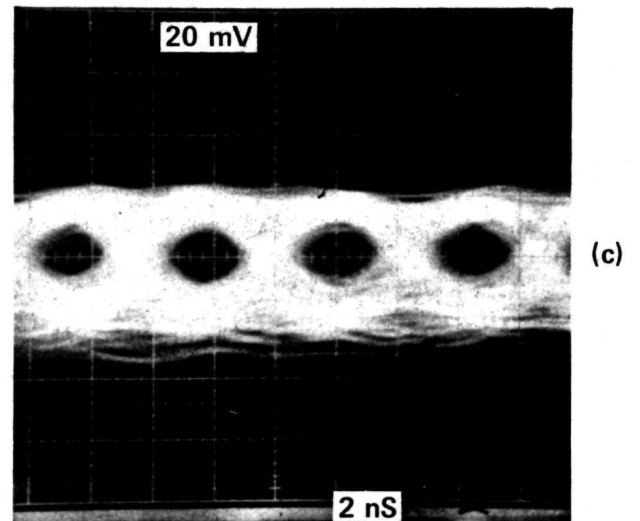
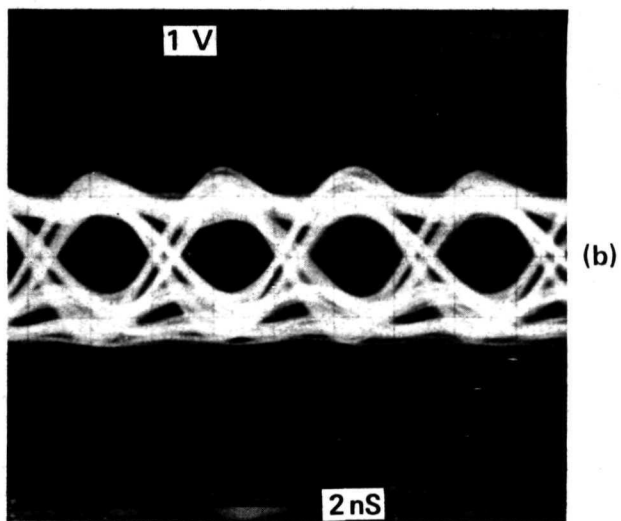
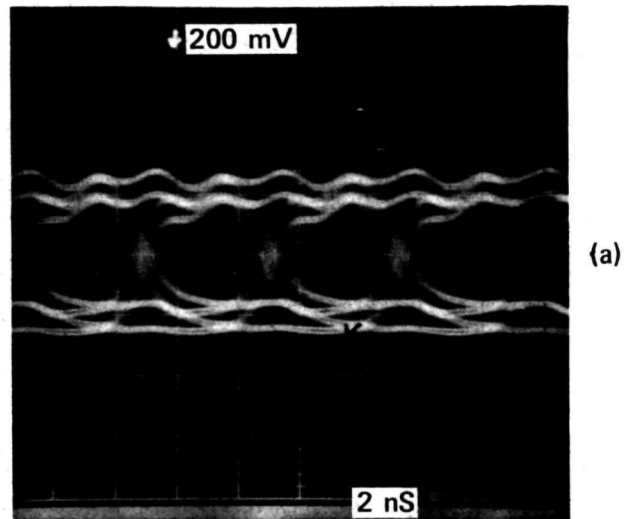


Fig. 7-6. Eye Patterns for 240 MB/sec Signal.

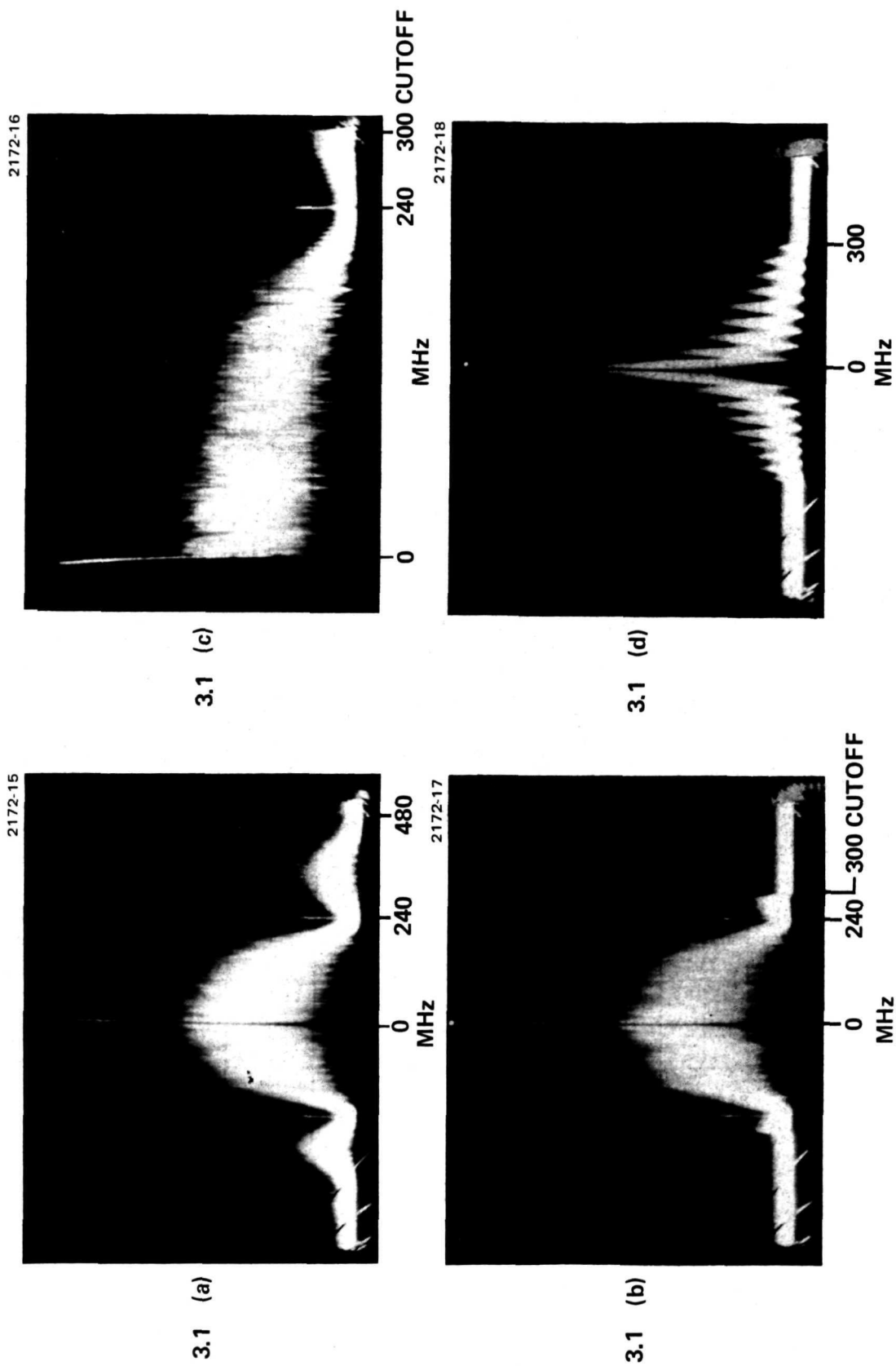


Fig. 7-7. Baseband Spectrum of Digital Signal.

After passing through the system, it can be seen that the spectrum is limited by the ENI driver at about 290 MHz as shown in Fig. 7-7(b) and again expanded in Fig. 7-7(c).

Figure 7-7(d) shows the data spectrum for a clock frequency of 20 MHz. In this case, the first ten harmonics of the signal are clearly visible on the spectrum analyzer.

These traces are shown with a logarithmic amplitude scale and correspond to about 10 dB per vertical division. The primary lobe, therefore, is about 30 dB greater than the secondary lobe. The amount of bandwidth required to pass 99% of the signal energy appears to be about 200 MHz (for the 240 Mbit/sec signal shown). Using this same rationale, the 290 MHz passband of the present system can handle a maximum data rate of 350 MBit/sec. This estimate corresponds reasonably well with the number of 330 MBit/sec determined from the rise-time measurements of Subsection 7.1.2.

7.2 COMMUNICATION TESTS USING COHERENT DETECTION

The DSBSC modulation format for digital signals is akin to the concept of phase shift keying, long favored in communications. Typical phase detection is achieved with phase-locked carrier injection. The coherent optical receiver offers two methods by which this may be achieved. The heterodyne method is up-conversion of the signal spectrum to some convenient i. f. frequency and then injecting an rf carrier at the appropriate i. f. frequency. The homodyne method is phase locking the laser local oscillator directly to the incoming optical signal. The tests described in this section are aimed at studying digital communications using both types of coherent detection. The test setup for these tests is shown in Fig. 7-8. The heterodyne carrier is provided by an acousto-optic frequency translator which shifts the frequency of the modulated beam by 300 MHz. The offset carrier, when mixed with the signal, provides a signal spectrum centered at 300 MHz. For the homodyne tests, the acousto-optic modulator is turned off, and the carrier is added to the modulated signal at the detector.

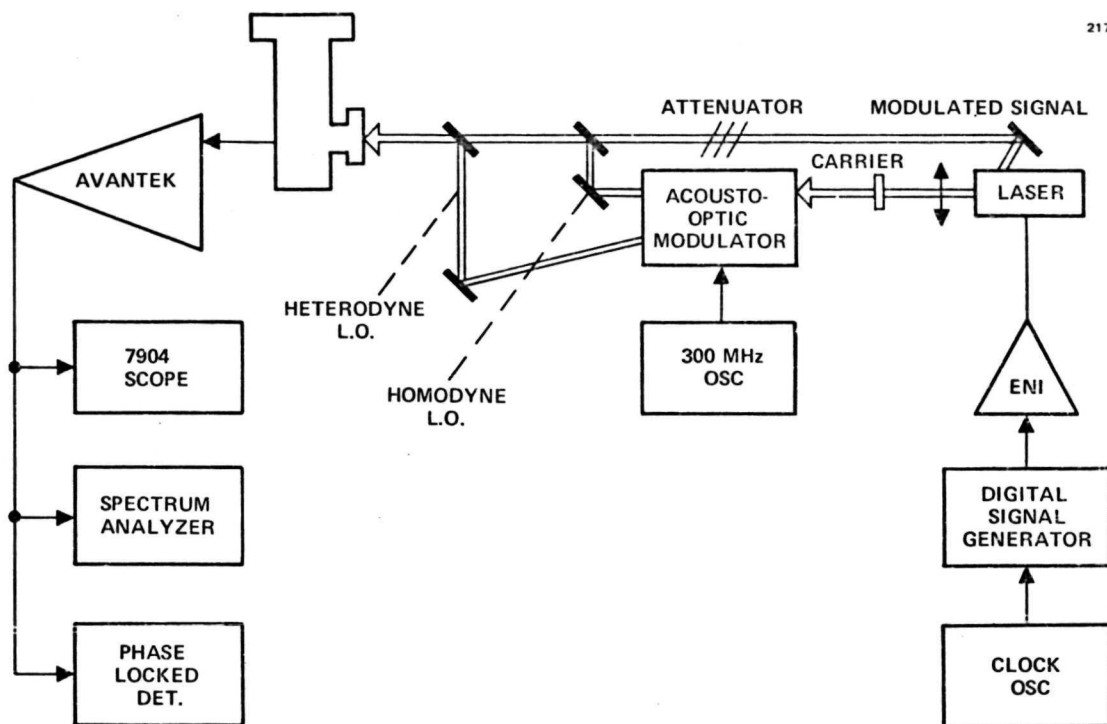


Fig. 7-8. Test Setup for Communication Tests Using Coherent Detection.

7.2.1 Homodyne Tests

The homodyne method depends upon directly phase locking one optical signal to another, i. e., the local oscillator laser to the incoming signal. In these laboratory experiments, we are using the carrier from the same laser, thus there is no problem of phase locking the local oscillator and the signal. The relative phase of the carrier can be varied by change in the path length of the local oscillator beam.

The advantage of the homodyne method is that very efficient use is made of the detector bandwidth. In fact, because of the foldover of the sidebands in phase detection, the optical detector can be 100% utilized to detect information on the incoming signal. Furthermore, the signal-to-noise ratio is increased by a factor of two over heterodyne detection because the noise bandwidth of the receiver is only half that of the heterodyne method.

In the homodyne tests we are concerned mainly about preservation of the signal waveform when the phase of the injected carrier is shifted slightly due to noise or jitter on the local oscillator. To examine this possibility, various amounts and phases of homodyne local oscillator were added to the modulated signal. The results are shown in Fig. 7-9. Figure 7-9(a) shows the waveform directly detected without any local oscillator. The vestigial carrier in this case is about 5 mW. The phasor diagram related to this waveform is shown at the left of the photograph showing the vestigial carrier only and the modulation vectors. Figure 7-9(b) demonstrates what happens when the local oscillator is added in phase with the carrier in true homodyne detection. Notice that the amplitude of the signal is increased by a factor of four times. Figure 7-9(c) shows the signal waveform when the local oscillator is exactly out of phase with the vestigial carrier. The only demodulated signal is due to the modulation vectors and is made up entirely of even harmonics. Figure 7-9(d) illustrates what happens when the strength of the local oscillator is increased to oppose and override the vestigial carrier. It is seen that the polarity of the digital signal is reversed as expected.

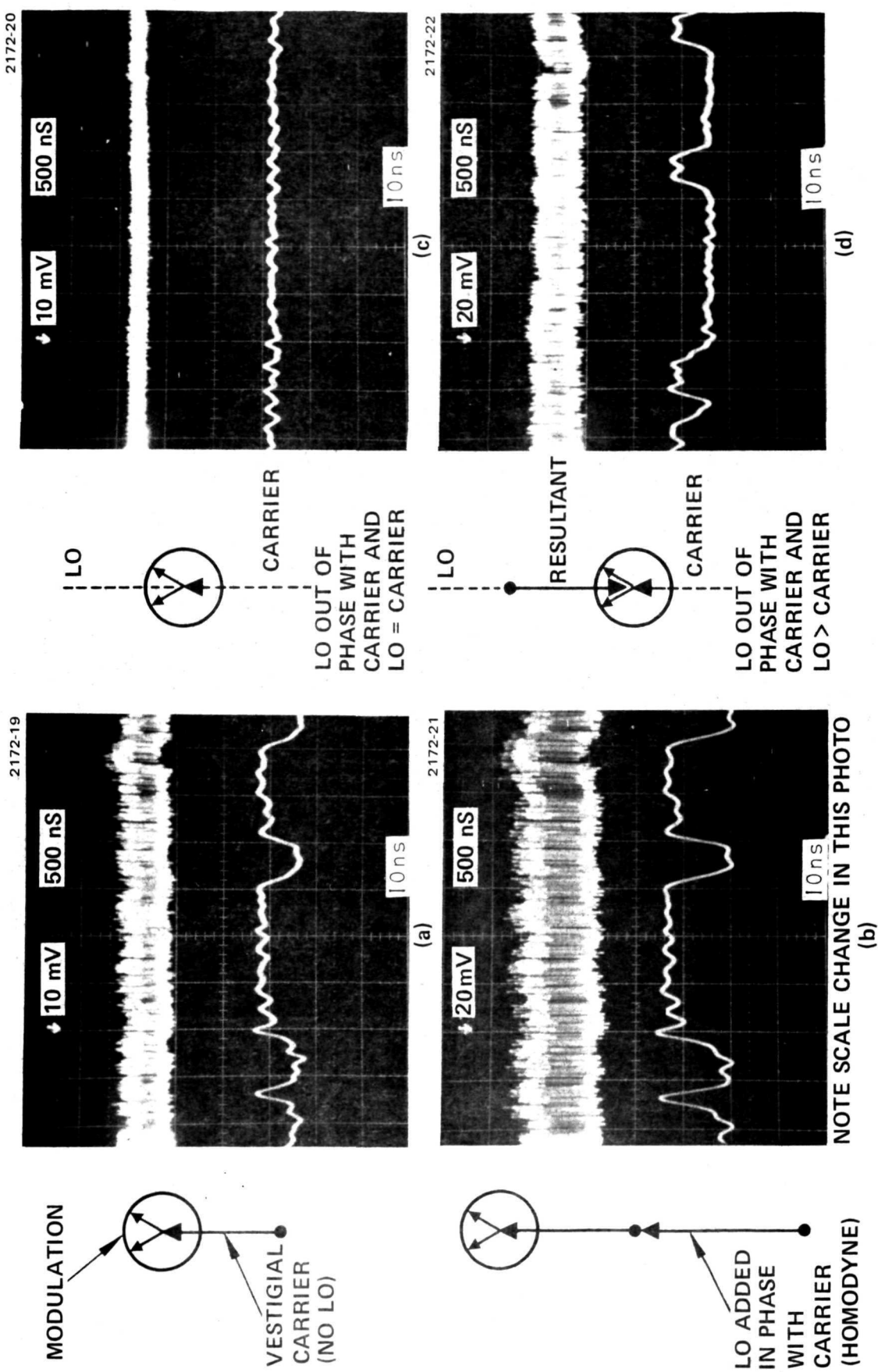


Fig. 7-9. Homodyne Tests.

The conclusions of these homodyne tests is that no serious distortion of the signal results, provided the phase does not reverse. Detection and demodulation of the digital signal will depend on locking the phase of the local oscillator reasonably well to the vestigial carrier, but general (slow) phase drift and jitter will change only the amplitude of the demodulated digital signal. AGC circuitry and limiters can be used to reshape the waveform to relieve the requirements on the phase-locked oscillator.

7.2.2 Heterodyne Tests

One of the most difficult problems in performing heterodyne tests using an acousto-optic modulator is that radio frequency interference (rfi) from the rf driver for the acousto-optic modulator is directly coupled into the receiver. Through careful matching of the driver and the acousto-optic device, this rfi was reduced to a negligible value. Figure 7-10(a) shows the output of the spectrum analyzer showing no rfi leakage at 300 MHz.

Figure 7-10(b) shows the two mixed carriers, the vestigial carrier and the laser local oscillator. Figure 7-10(c) shows this carrier with two modulated sidebands provided by a 3 MHz tone driving the data modulator. Figure 7-10(d) shows these sidebands when the frequency of the tone is 30 MHz. Note that the upper sideband amplitude has fallen off. This is due primarily to the roll-off characteristics of the SAT detector, which was operated at a current of 0.3 mA during these tests.

The 300 MHz carrier as seen directly on the oscilloscope is shown in Fig. 7-11(a). The modulation spectrum of a 10 MB/sec digital signal is shown on the carrier in Fig. 7-11(b). A higher frequency spectrum, such as a 240 MBit/sec signal appears to result in overlap of the baseband spectrum and causes a confused spectrum. This is the reason for choosing a lower data rate digital signal for these tests.

Figure 7-11 shows the 300 MHz RF envelope (lower trace) which clearly shows the phase transitions corresponding to the demodulated digital signal (top trace).

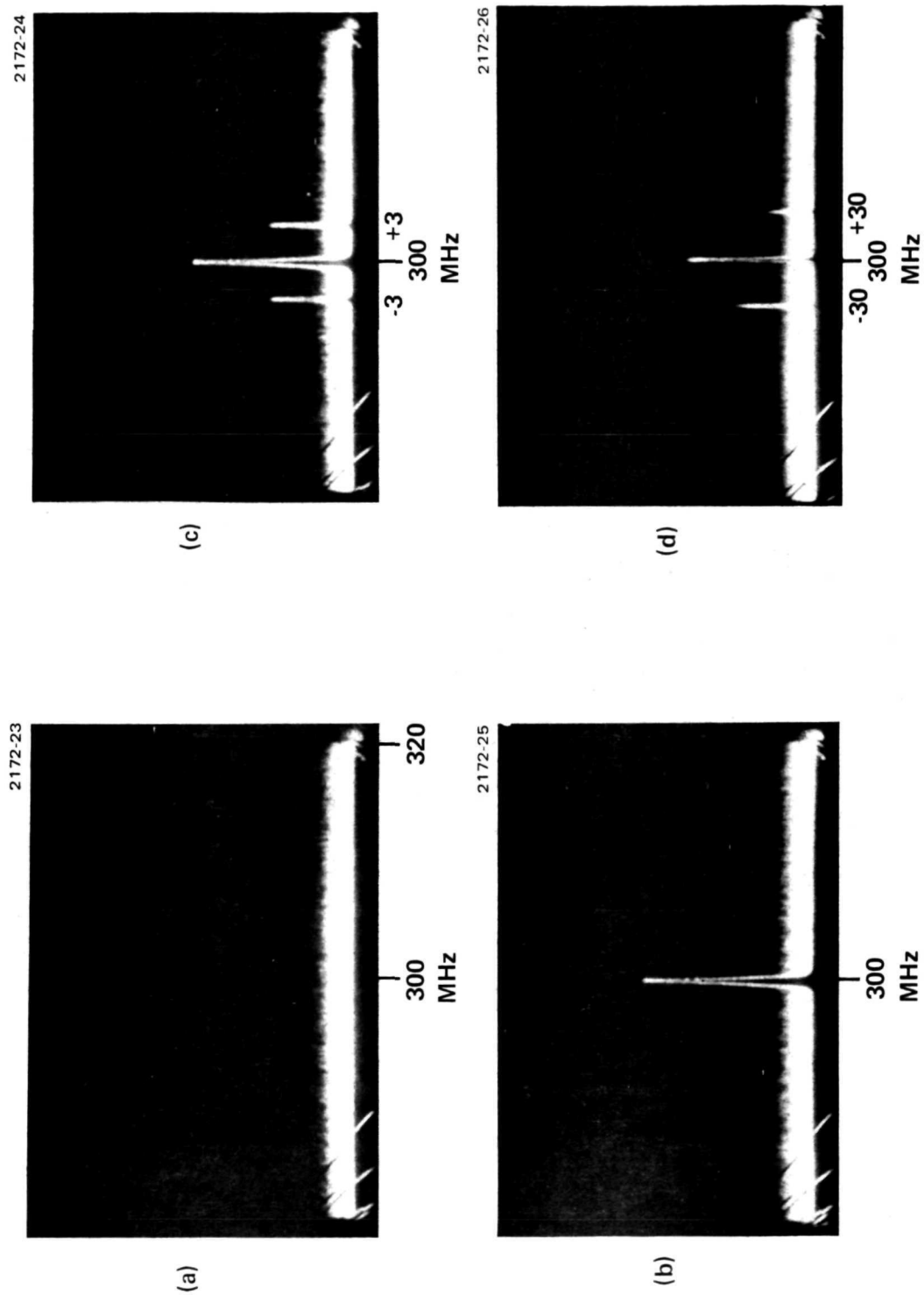


Fig. 7-10. Heterodyne Spectrum at 300 MHz.

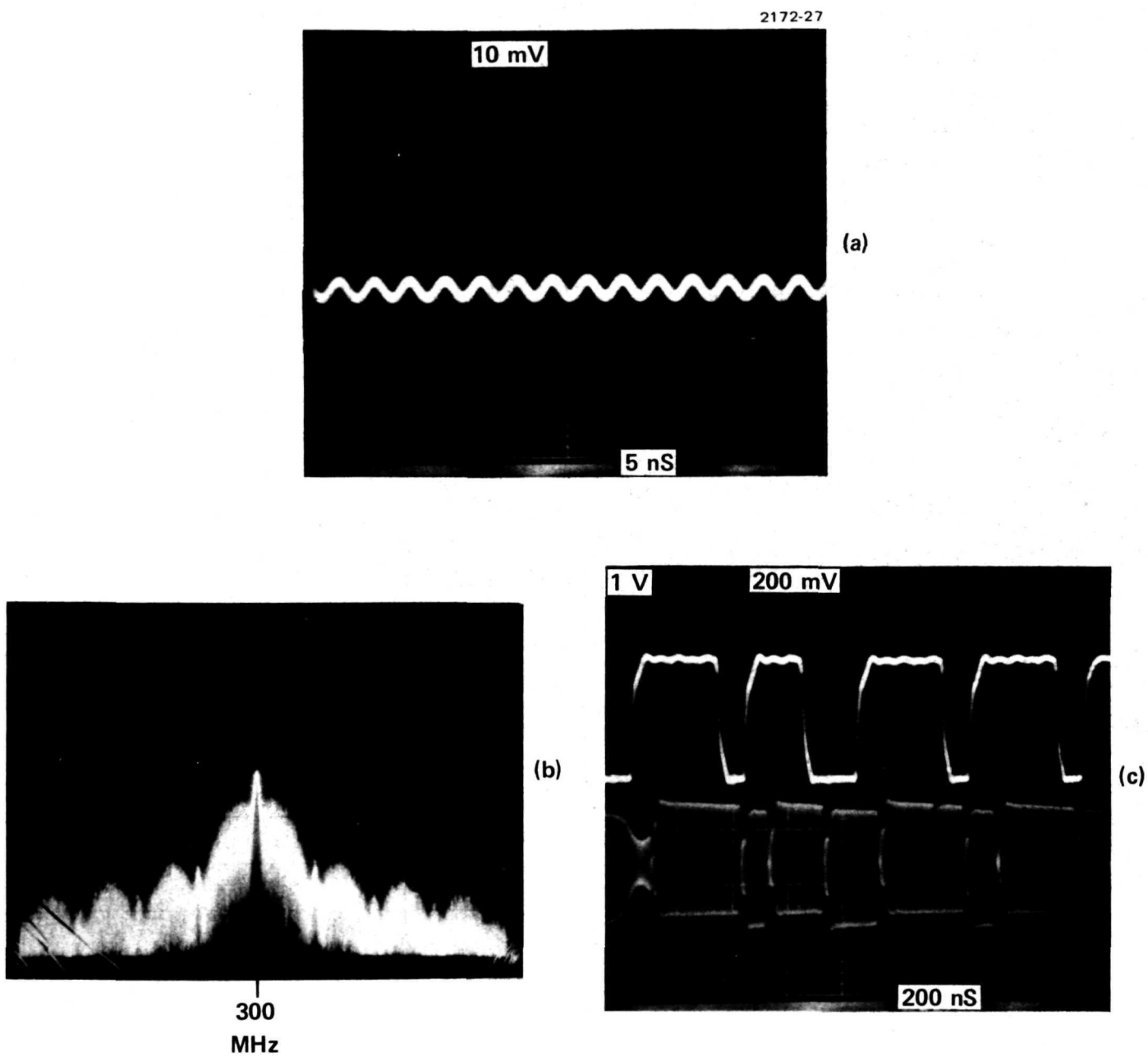


Fig. 7-11. Heterodyne Tests.

"Page missing from available version"

REFERENCES

1. I. P. Kaminow and E. H. Turner, "Electro-optic Light Modulators," *Proc. IEEE* 54, No. 10, Oct. 1966, pp. 1374-90.
2. G. D. Boyd and H. Kogelnik, "Generalized Confocal Resonator Theory," *Bell System Tech. J.*, Jul. 1962, pp. 1347-69.
3. D. de Nobel, *Philips Res. Rpt.* 14, 361 (1959).
4. N. R. Kyle, *J. Electrochem. Soc.* 118, 1790-1797 (1971).
5. L. R. Shiozawa, J. M. Jost, and D. A. Roberts, The Application of Physical Vapor Deposition to Semiconductor Materials for Use as High Power Infrared Windows, Quarterly Progress Report No. 4, 30 June 1972, Contract F33615-71-C-1777, Air Force Material Laboratory, WPAFB.
6. Cox, J. Thomas, and Hass George (1964), "Antireflection coatings for optical and infrared optical materials," Physics of Thin Films 2 (Academic Press).
7. Macleod, H. A., (1969) Thin Film Optical Filters, American Elsevier Publishing Company, Inc., New York.
8. Smith, S. O. and Seeley J. S. (1968) "Multilayer filters for the region 0.8 to 100 microns," "Final Scientific Report, Contract AF61(052)-833.
9. S. Brand and C. W. Carter, *AIEE Transactions*, 80, Part I, Communications and Electronics, pp. 652-661.

RELATED BIBLIOGRAPHY

1. N. McAvoy, J. Osmundson, and G. Schiffner, "Broadband CO₂ laser coupling modulation," *Applied Optics* 11, 473 (1972).
2. D. R. Hall, C. J. Peruso, E. H. Johnson, G. Schiffner, J. H. McElroy, and N. McAvoy, "Multichannel Television Coupling Modulation Experiments at 10.6 μ m," Internal NASA publication, NASA Goddard Space Flight Center, Greenbelt, Md.
3. V. B. Baglikov and V. N. Parygin, "Asynchronous Modulation of Gas Laser Coupling," *Radio Engineering and Electronic Physics*, 16, No. 8, (1971).

4. V. B. Baglikov and V. N. Parygin, "Unlocked Internal Modulation of a Multifrequency Gas Laser," Radio Engineering and Electronic Physics 16, No. 3 (1971).
5. V. B. Baglikov and V. N. Parygin, "Coupling Modulation of a High Gain Gas Laser," Radio Engineering and Electronic Physics 16, No. 11, (1971).
6. A. Yariv, "Electro-Optic Frequency Modulation in Optical Resonators," Proc. IEEE, Vol. 52, No. 6, June 1964.
7. F. R. Nash and P. W. Smith, "Broadband Optical Coupling Modulation," JQE, Vol. QE 4, No. 1, January, 1968.
8. M. B. White and W. D. Gerber, "Intracavity Polarization Modulation of a Nearly Isotropic CO₂ Laser," JQE, Vol. 5, No. 6, June, 1969.
9. W. M. Doyle and W. D. Gerber, "Frequency Discrimination Characteristics of an Elliptically Polarized Dual-Polarization Gas Laser," JQE, Vol. 4, No. 11, November 1968.
10. M. B. White and W. D. Gerber, "Frequency Modulation of a Self-Mode-Locked Dual-Polarization CO₂ Laser," JQE, Vol. 7, No. 12, Dec. 1971.

APPENDIX A

Reprinted by permission from
IEEE JOURNAL OF QUANTUM ELECTRONICS
Vol. QE-8, No. 2, February 1972
Copyright © 1972, by the Institute of Electrical and Electronics Engineers, Inc.
PRINTED IN THE U.S.A

Intracavity CdTe Modulators for CO₂ Lasers

JAMES E. KIEFER, MEMBER, IEEE, THOMAS A. NUSSMEIER, AND FRANK E. GOODWIN, MEMBER, IEEE

Abstract—The use of cadmium telluride as an electrooptic material for intracavity modulation of CO₂ lasers is described. Included are the predicted and measured effects of CdTe intracavity modulators on laser performance. Coupling and frequency modulation are discussed and experimental results compared with theoretically predicted performance for both techniques. Limitations on the frequency response of the two types of modulation are determined.

I. INTRODUCTION

LASER SYSTEMS designers continually ask for increased modulator bandwidth and sensitivity and, at the same time, decreased driving power. The burden is thus on the modulator designer who must continually search for more efficient techniques and better

materials. In this paper the results of work at Hughes Research Laboratories in the area of electrooptic modulation at 10.6 μ will be discussed. In particular, intracavity modulating techniques including coupling and frequency modulation using the infrared electrooptic material cadmium telluride will be described.

By operating the modulator inside the laser cavity a significant reduction in driving power may be realized compared with that required for the same modulator operated external to the laser. This reduction is due primarily to the fact that the modulator operates on the higher optical power available within the cavity. The advantage is somewhat offset however, by certain bandwidth limitations that will be discussed later and by the high sensitivity of the laser power output to optical loss within the cavity. In particular, it has been found that the output of the CO₂ laser is affected to a significant degree by only a very small increase in internal loss.

Manuscript received July 7, 1971; revised September 8, 1971.
The authors are with Hughes Research Laboratories, Malibu, Calif. 90265.

II. CdTe MODULATORS

The semiconductor CdTe has proven to be a very useful electrooptic material for intracavity modulation at $10.6\ \mu$ due to its low bulk optical absorption and high electrooptic coefficient. The use of the material for infrared modulation was reported earlier [1]. Some of the important characteristics of CdTe relating to its use as a modulator material are summarized as follows.

Clamped (high-frequency) electrooptic characteristic

$$n_0^3 r_{41}: 10 \pm 1 \times 10^{-11} \text{ m/V.}$$

$$V_\pi \cdot l/d (10.6\ \mu): 53 \text{ kV.}$$

$$\text{Dielectric constant } \epsilon/\epsilon_0: 10.$$

$$\text{Resistivity: } > 10^7 \Omega \cdot \text{cm.}$$

$$\text{Tan } \delta (1 \text{ GHz}): < 10^{-2}.$$

$$\text{Refractive index } n_0: 2.67.$$

$$\text{Transmission range: } 1\text{--}30\ \mu.$$

$$\text{Optical absorption coefficient: } 0.001\text{--}0.005 \text{ cm}^{-1}.$$

For this application, the most important parameters are the half-wave voltage, which is about half that of GaAs (its closest rival for $10.6\text{-}\mu$ modulation), and the optical absorption coefficient, which is 2–10 times less than that of the best GaAs reported.

Two CdTe modulators that have been developed at Hughes Research Laboratories are shown in Figs. 1 and 2. The first of these is used in coupling and Q-switching experiments. The crystal is a 2-cm-long by 5-mm-square cross section; the faces are antireflection (AR) coated and the total transmission is better than 96 percent. Fig. 2 shows the modulator used in our FM experiments. The crystal was cut with Brewster-angle faces and the transmission is better than 98 percent. The effective length and cross section are 1 cm and 5 mm^2 , respectively.

III. LASER PERFORMANCE

Fig. 3 is a photograph of the CO_2 laser and one of the CdTe modulators used in these experiments. The discharge tube is of all metal-ceramic construction using BeO bore sections, a self-heated nickel cathode, Kovar anodes, and GaAs Brewster windows. (CdTe windows are used in later models of the laser.) The active discharge region is approximately 30 cm long by 5 mm in diameter. Heat is removed conductively to a water-cooled manifold that also acts as a mechanical support. The tube is designed to operate in a hemiconfocal cavity 50 cm long with a TEM_{00} diffraction loss of about 2 percent. The modulators were placed in the cavity near the flat mirror where the optical mode diameter is a minimum. For coupling experiments the GaAs Brewster window nearest the modulator was used to reflect the coupled energy from the cavity. The curved mirror used to form the optical cavity was a gold-coated silica substrate mounted on a circular bimorph to provide electrical adjustment of the cavity length. The experimental apparatus was mounted on a 1-m optical bench that allowed cavity length adjustments from 40 to 90 cm.

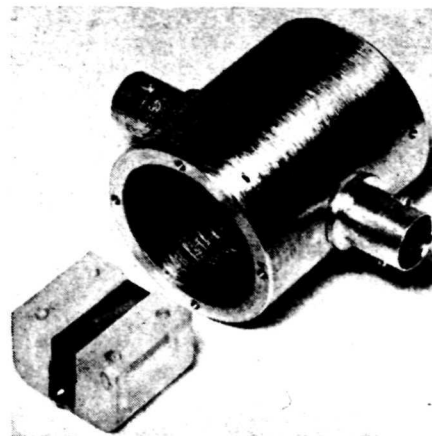


Fig. 1. CdTe modulator—antireflection-coated faces.

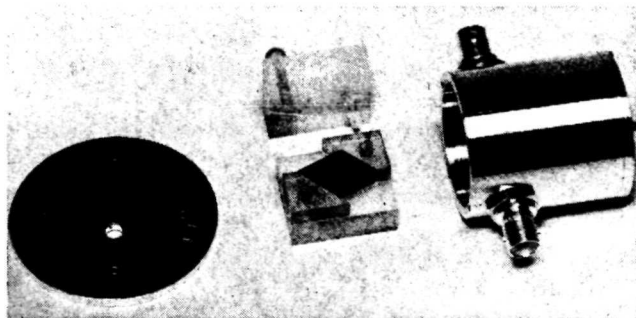


Fig. 2. CdTe modulator—Brewster-angle faces.

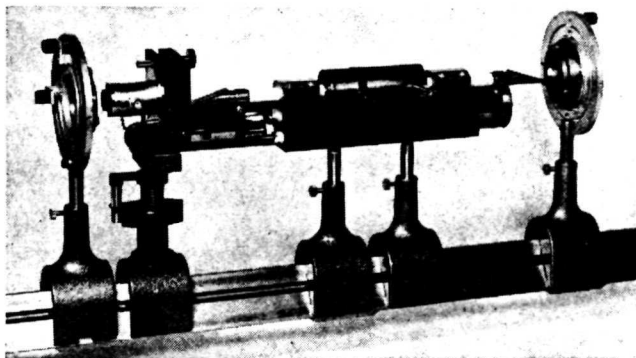


Fig. 3. Metal-ceramic CO_2 laser with intracavity CdTe modulator.

In an effort to predict laser performance as a function of modulator and coupling losses, an expression previously developed [2] [3] for the intracavity power incident on the modulator is used

$$P = \frac{\pi A I_s (1 - \alpha_c)^{1/2} [g_0 L + \frac{1}{2} \ln (1 - \alpha_c)(1 - \alpha_f)]}{2[(1 - \alpha_c)^{1/2} + (1 - \alpha_f)^{1/2}][1 - (1 - \alpha_c)^{1/2}(1 - \alpha_f)^{1/2}]}, \quad (1)$$

where A is the cross-sectional area of the tube bore, I_s is the saturation intensity, α_c and α_f are the total effective losses at the curved mirror end and flat mirror end of the cavity, respectively, and $g_0 L$ is the tube gain. α_c is taken as the sum of the diffraction loss and the curved mirror loss and $\alpha_f = 2\alpha_m + \alpha_2 + c_o + c_m$ where α_m is the modulator loss, α_2 is the flat mirror loss, c_m is the

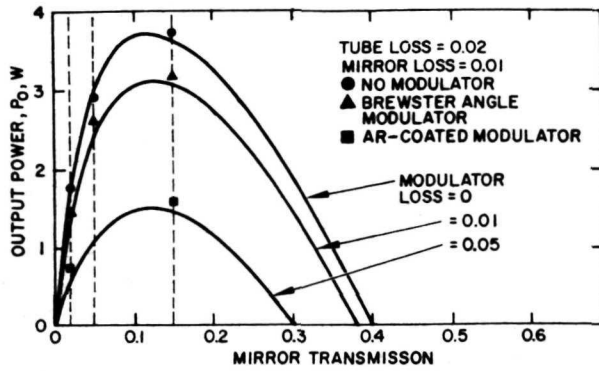


Fig. 4. Laser output power versus mirror coupling for internal modulator loss equal to 0, 0.01, and 0.05.

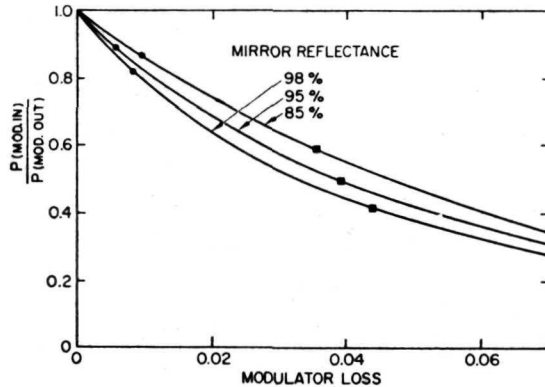


Fig. 5. Effect of internal modulator loss on laser output.

modulator coupling, and c_o is the output mirror coupling. The power output taken through the flat mirror P_o is then

$$P_o = (1 - \alpha_m - \alpha_2)Pc_o \quad (2)$$

and the coupled power P_c (for coupling modulation) is

$$P_c = (1 - 2\alpha_m - \alpha_2 - c_o)Pc_m \quad (3)$$

All measurements taken during this study were made with a constant tube current of 10 mA, which gave $I_s = 280$ W/cm² and $g_o L = 0.29$ for this tube. The laser output power P_o is plotted in Fig. 4 as a function of output mirror coupling c_o for three values of modulator loss. Also included on this curve are experimental points taken with no modulator, the Brewster-angle modulator, and an AR coated modulator in the cavity. α_2 was taken to be 0.01. Fig. 5 is a plot of the ratio of the output power of the laser with the modulator in the cavity to that without the modulator as a function of modulation loss for three values of output mirror transmission. Experimental data were taken with two modulators and the results are plotted on the curves. The implied loss from these measurements can be compared to transmission loss measurements made on the same two modulators. The modulator with the lower loss was the one with Brewster-angle faces and thus its loss is representative of the true bulk absorption of the material. The externally measured

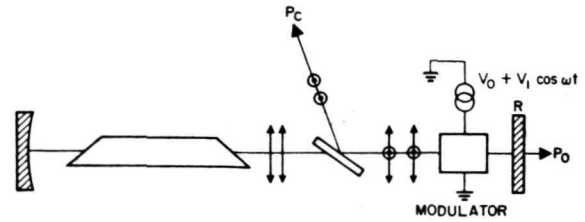


Fig. 6. Coupling modulation.

loss was less than 2 percent (limited by measurement accuracy), whereas that deduced from the intracavity measurement was 0.6–0.9 percent. The second modulator had antireflective coated faces, and the externally measured loss was 4–5 percent while the intracavity value was 3.6–4.4 percent.

IV. COUPLING MODULATION

Coupling modulation was first proposed and demonstrated by Gurs and Muller [4] in 1963 and it has since been examined by a number of groups, primarily with He-Ne lasers [5], [6], [7]. An experimental 3.39- μ communication system using coupling modulation has been developed at this laboratory [8].

The general technique of coupling modulation is illustrated in Fig. 6. The required components for coupling modulation are the modulator, a polarization coupler, and a laser in which the internal circulating energy is constrained to be linearly polarized. The polarization coupler (for example, a Brewster's angle plate) separates orthogonally polarized components of light. In our experiments we used one window of the laser tube as the coupler. By applying voltage to the modulator, an orthogonally polarized component of the circulating energy is generated that is then coupled out of the cavity. The magnitude of the component varies with the voltage applied to the modulated output. Experimentally the coupled power P_c was measured as the modulated output and the internal circulating power was sampled by monitoring the output P_o passing the partially transmitting flat mirror.

The coupling coefficient for the modulator is given by

$$\begin{aligned} c_m &= \sin^2 \Gamma(t) \\ &= \frac{1}{2}[1 - \cos 2\Gamma(t)] \end{aligned} \quad (4)$$

where Γ is the induced phase retardation for a single pass through the modulator crystal. From electrooptic theory

$$\Gamma = 2\pi n_o^3 r_{41} V / \lambda d \quad (5)$$

where l and d are the length and thickness of the electrooptic crystal, $n_o^3 r_{41}$ is the electrooptic characteristic of the material, V is the applied voltage, and λ is the optical wavelength. The modulation $\Gamma(t)$ is assumed to have dc and sinusoidal components. Thus,

$$c_m = \frac{1}{2}[1 - \cos 2(\Gamma_o + \Gamma_m \sin \omega_m t)]. \quad (6)$$

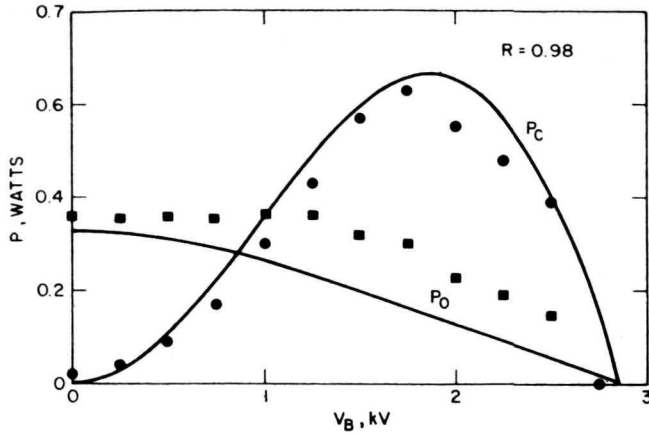


Fig. 7. Coupled output power versus dc bias voltage applied to modulator.

This may be expanded to provide frequency components,

$$\begin{aligned}
 c_m = & \frac{1}{2}[1 - \cos(2\Gamma_0)J_0(2\Gamma_m)] \\
 & + \sin(2\Gamma_0)J_1(2\Gamma_m)\sin(\omega t) \\
 & - \cos(2\Gamma_0)J_2(2\Gamma_m)\cos(2\omega_m t) \\
 & + \sin(2\Gamma_0)J_3(2\Gamma_m)\sin(3\omega_m t) \dots
 \end{aligned} \quad (7)$$

The average power coupled from the laser is proportional to the first term, which is dependent upon both Γ_0 , the dc retardation, and Γ_m , the peak ac retardation. For small Γ_m ,

$$c_m \simeq \frac{1}{2}[1 - \cos(2\Gamma_0)(1 - \Gamma_m^2)]. \quad (8)$$

The power coupled from the laser is then

$$P_c \simeq kc_m P_s \quad (9)$$

where P_s is the circulating power in the laser and k is the polarizer coupling coefficient, which is about 0.8 for the GaAs window coupler.

A. DC Measurements

By using (2), (3), and (4) it is possible to predict the behavior of the laser as a function of dc bias voltage V_B applied to the modulator. Fig. 7 is a plot of both coupled power P_c and sampled circulating power P_s for 0.98 output mirror coupling. The figure also includes experimental data taken from measurements made using the antireflection coated CdTe modulator in the coupling configuration.

B. Low-Frequency Coupling Modulation

In practice the response of a coupling modulator may be separated into two distinct frequency regimes. The lower frequency regime where the stored energy of the laser may follow the modulating signal is inherently nonlinear and unstable. Overly simplified, this results from a combination of two effects: 1) the tendency of the modulated output to follow both the modulating signal and the stored energy, which also is changing with

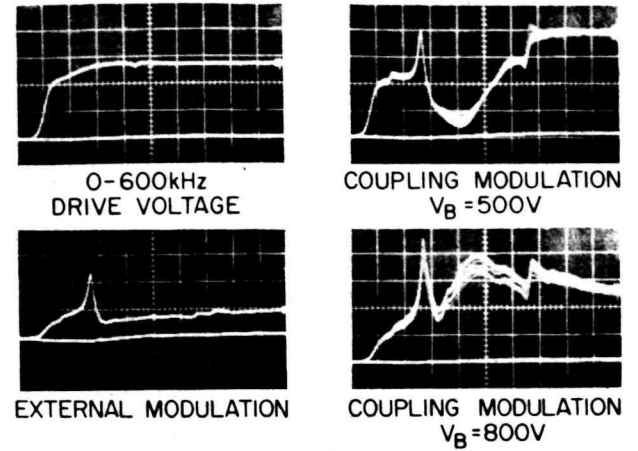


Fig. 8. Coupled output power versus frequency with a 0-600 kHz (60 kHz/div) swept frequency signal (shown in the first trace) applied to the modulator. Operation is shown for this modulator located outside the laser cavity (second trace) and inside the cavity for two values of dc bias voltage. The sharp peak at about 150 kHz is caused by an acoustic resonance of the modulator crystal.

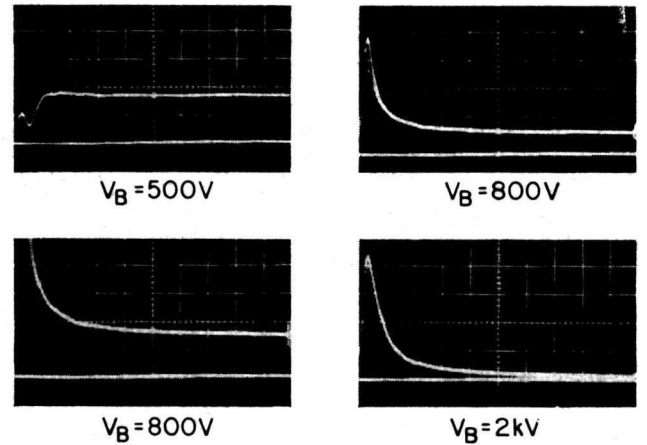


Fig. 9. Coupled output power versus modulating frequency for several values of dc bias. Sweep range is 0-5 MHz (0.5 MHz/div).

the modulating signal, and 2) the excitation of naturally occurring resonances associated with pumping and relaxation rates of the laser medium by the time varying loss of the coupling process. An analysis of the performance in this frequency domain is beyond the scope of this paper but is treated in detail elsewhere [9]. Typically, this regime extends to about 1 MHz. To illustrate the low-frequency response, swept frequency measurements were made in the low-frequency transition area and are presented in Figs. 8 and 9. These measurements were made using a sweep generator and power amplifier to drive the modulator. The detector was followed by a wide-band (10 kHz to 200 MHz) amplifier and a second detector to monitor the laser output level. The total energy in this frequency band was displayed synchronously with the sweep generator and includes all harmonic distortion components.

The response curves in Fig. 8 were taken over the 0-600-kHz frequency band to show the effects of dc bias. The first curve illustrates the 80-kHz low-frequency

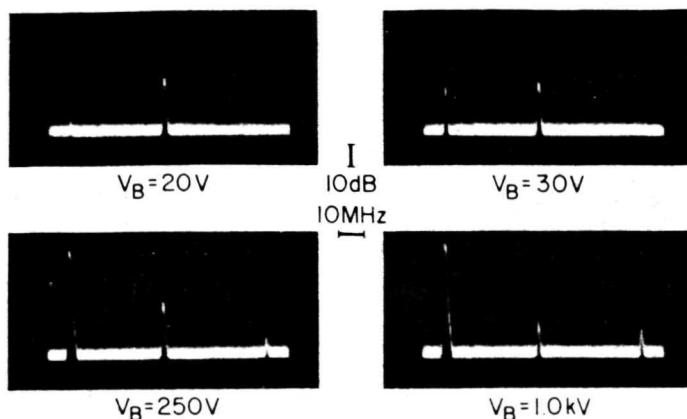


Fig. 10. Coupling modulation frequency spectrum for single-frequency modulation ($f_m \sim 45$ MHz). Frequency range displayed is approximately 40–140 MHz.

cutoff of the driver amplifier. The second curve was taken with the modulator external to the cavity. The sharp peak at about 150 kHz is an acoustic resonance caused by the undamped crystal. The remaining two curves show the null and peak response at 250 kHz for two different bias levels. Fig. 9 is a series of measurements made over a frequency range of 0–5 MHz. The ac modulator driver voltage was maintained constant while the dc bias voltage was varied. The response with 500-V bias shows a pronounced dip in the region of 250 kHz; the response at this frequency increased dramatically as the bias level was increased. Of major significance, however, is the flat response at higher frequencies. This shows that the useful low-frequency response of coupling modulation can be as low as 1 MHz. The region around the resonance effect is primarily of academic interest; useful modulation will necessarily avoid low frequencies.

C. High-Frequency Coupling Modulation

In contrast to the low-frequency response, coupling modulation in the high frequency region is stable and the performance may be readily analyzed. This regime is where practical application of coupling modulation will be implemented. Coupling measurements of frequency response and harmonic amplitude were made during this study using direct detection. A wide-band copper-doped germanium detector, a spectrum analyzer, and a sampling oscilloscope were used for all measurements. Fig. 10 shows four spectrum analyzer displays to illustrate the variation in harmonic content as a function of bias voltage. The first display shows the modulator bias adjusted to null the fundamental, the required bias being very low. This implies both good alignment of the crystal and high quality (very low residual or strain birefringence). As the bias is increased, the fundamental rapidly becomes predominant, the second harmonic remaining essentially constant.

The relative harmonic component amplitudes can be predicted from (7). Fig. 11 shows the predicted components for the particular ac drive voltage (35 V peak) and the particular crystal parameters used. The relative

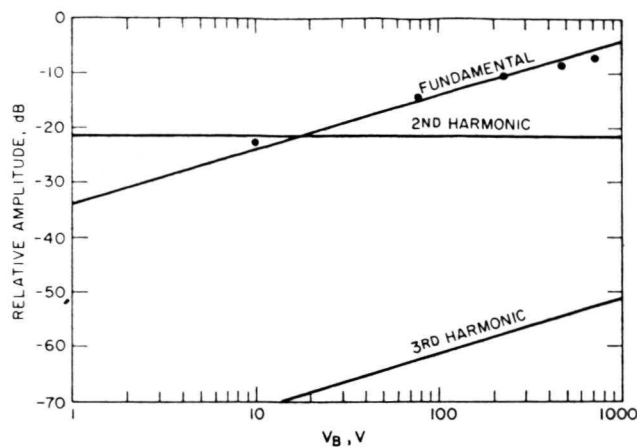


Fig. 11. Predicted harmonic amplitudes versus dc bias voltage for single-frequency coupling modulation. Experimental points are shown for $f_m \sim 45$ MHz.

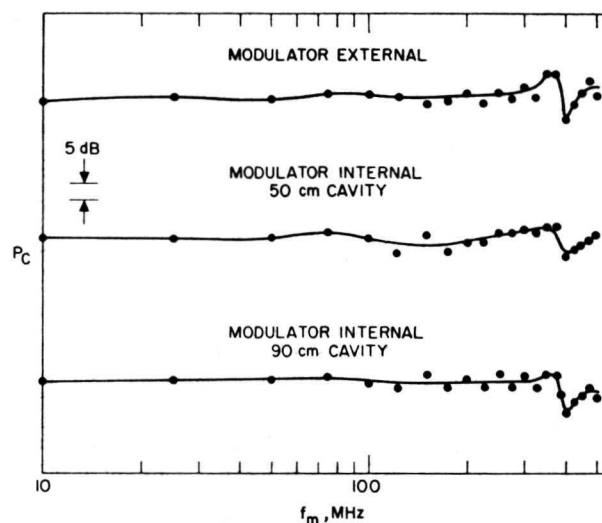


Fig. 12. CdTe coupling modulation, 10–500 MHz frequency response.

amplitudes of the fundamental and second harmonic were measured from the spectrum analyzer display, corrected for the square-law characteristic of the detector, corrected for the 20-V bias offset due to residual birefringence, and plotted on Fig. 11 using the second-harmonic amplitude as a reference. Agreement with predicted values is good. The third-harmonic amplitude prediction is about 48 dB below that of the fundamental. The amplifier used to drive the modulator is specified to have third-harmonic distortion products typically 30 dB below the fundamental. Thus the third-harmonic components visible in Fig. 10 are all due to amplifier distortion.

In theory, the upper-frequency response of coupling modulation is restricted only to the modulator characteristics with possible exceptions near cavity resonances ($c/2L$). For the modulator used in these measurements, optical transit time would limit frequency response to about 10 GHz. For these measurements, we were limited in upper-frequency response by the modulator driver to 500 MHz. Fig. 12 shows the measured fundamental

amplitude as a function of frequency from 10 to 500 MHz. The response is shown for operation of the same modulator both external and internal to the laser cavity and for two different cavity lengths. The response perturbation at 400 MHz was caused by a modulator circuit resonance. The second-harmonic amplitude was also measured over the same frequency band and found to follow the same curve, verifying the electrical resonance at 400 MHz. No limitations to the upper-frequency response were found.

During the course of the high-frequency coupling measurements, particular attention was given to the regions near the $c/2L$ intermode spacing frequencies. Two cavity lengths were used, 50 and 90 cm, corresponding, respectively, to $c/2L$ frequencies of about 300 and 165 MHz. The laser operated in a single longitudinal mode, but it has been reported [5], [7] that in some cases energy could be coupled to nonoscillating or so-called cold modes with a resulting response distortion. A spectrum analyzer was used to determine any perturbations in amplitude or harmonic content and the detected signal was monitored with a sampling oscilloscope to observe any waveform changes. No effects directly attributable to cavity modes were observed for either cavity length leading us to conclude that to first order there will be no upper limitations on modulation bandwidth imposed by the CO₂ laser, provided the cavity is sufficiently short to prevent $c/2L$ from occurring where there is significant laser gain. Subsequent analysis using a treatment by Kaminow [5] has indicated that response distortion at the $c/2L$ frequencies should be low. This analysis relates the energy coupled into the nonoscillating or "cold" cavity modes to the gain and loss at the frequency of the cold modes. This analysis shows that unless the cold mode is on the verge of oscillation, distortion will be low. Since the linewidth of the measured CO₂ laser is much smaller than the $c/2L$ spacing, the cold modes are well below threshold and no distortion should be measured.

V. FREQUENCY MODULATION

Frequency modulation of a laser using an internal modulator, which was first described by Yariv [10], is the most direct form of internal modulation, requiring a minimum of additional components. The frequency of the laser oscillator is changed when a voltage applied to the crystal changes the optical length of the laser cavity by a change in the refractive index of the crystal. The laser will oscillate at a frequency ν such that $\nu = jc/2L$, where j is the appropriate cavity harmonic given by $2L/\lambda$ and L is the optical length of the cavity. The frequency change with length is $d\nu/dL = -jc/2L^2$, or $-c/\lambda L$. If $L \gg \Delta L$, the change in frequency, $\Delta\nu$ can be approximated by $-c \Delta L/\lambda L$. For internal frequency modulation the induced phase retardation as defined by (5) is reduced by a factor of 2. Thus the change in optical length of the crystal is

$$\Delta L = \Gamma\lambda/4\pi. \quad (10)$$

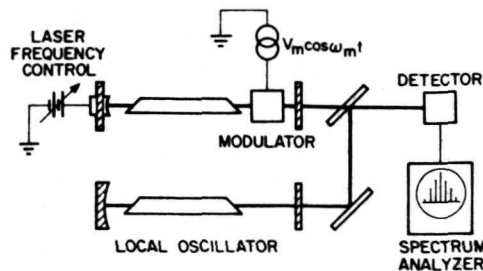


Fig. 13. Experimental arrangement for intracavity frequency modulation experiments.

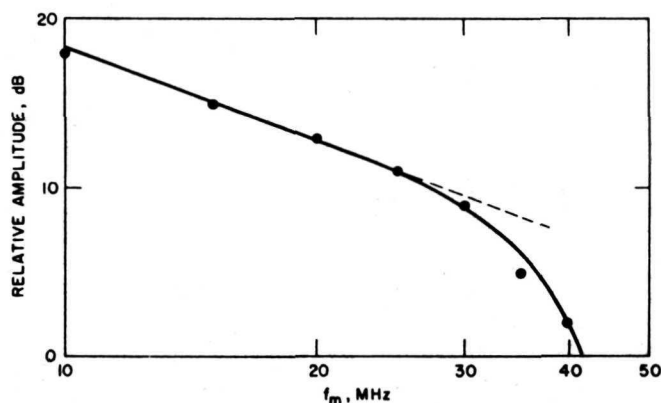


Fig. 14. CdTe intracavity frequency modulation, sideband amplitude.

The frequency change due to an applied voltage is

$$\Delta\nu = cn_0^3 r IV / 2\lambda L \text{ Hz.} \quad (11)$$

FM measurements were made with a modulator driver adjusted to deliver a peak ac voltage of 35 V to the modulator. The peak phase change corresponding to this voltage is 2.5×10^{-3} radians for a peak frequency deviation of 240 kHz. Fig. 13 is a diagram showing the experimental setup for these measurements. The laser and Brewster angle modulator were mounted on an optical bench to allow changes in cavity configuration. The signal from the modulated laser was combined with a signal from a passively stabilized laser on an uncoated BaF₂ beamsplitter and detected on a compensated copper-doped germanium detector with a bandwidth in excess of 500 MHz. The output of the detector was monitored with a calibrated spectrum analyzer. The frequency and transition of the test laser were manually controlled by means of a bimorph-mounted cavity mirror. The measured sideband amplitudes are plotted in Fig. 14.

The modulation index for the FM measurement was much less than one. For this case, only the first sidebands are of significant amplitude. The amplitude of the first sideband is proportional to $J_1(m)$ where m is the ratio of the peak deviation to the modulating frequency, $m = f_d/f_m$. For these measurements, $m \ll 1$, and $J_1(m) \simeq m/2$. The amplitudes of the sidebands are thus proportional to $1/f_m$ and the power in the sidebands as measured by the spectrum analyzer is proportional to $1/f_m^2$, assuming no bandwidth-limiting elements. This

corresponds to a slope of -2 in Fig. 14 since the plot is logarithmic. The measured response is seen to follow a slope of -2 out to about 30 MHz with response to about 40 MHz. At 40 MHz the sidebands were not significantly above the spectrum analyzer noise level, thus the error in plotting this point is large.

Under certain conditions, the bandwidth of intracavity modulation is limited by cavity Q [11], [12]. The Q of a laser cavity is $Q = 2\pi L/\lambda\alpha$, where α is the total round-trip cavity loss. The $\frac{1}{2}$ power response of the cavity resonance is about ν/Q where ν is the oscillating frequency. For the measured configuration, cavity loss was about 0.14 for a $\frac{1}{2}$ -power bandwidth of 13 MHz and a response limitation of 6.5 MHz. The fact that the measured response extends out to at least 30 MHz implies that for low deviation FM the cavity Q does not limit the bandwidth.

The proposition that cavity Q should limit the bandwidth implies that in the presence of a change in cavity length, the stored energy at one frequency must decay and build up again at the new frequency. According to Yariv [10], this is not the case for internal frequency modulation. Under steady-state conditions a standing wave is established in the cavity that fulfills the boundary conditions imposed by the end mirrors and transverse bounds. A change in the cavity length will cause the field distribution to change to conform to the new cavity length; this new distribution will occur at a different wavelength and hence a different frequency. The change in stored energy that accompanies this frequency change will be very slight, thus the cavity Q , which limits the rate of change of stored energy, should not limit the bandwidth of internal FM. Fig. 14 indicates the validity of this argument since no frequency-dependent response was observed.

This program was undertaken primarily for coupling measurements, hence laser frequency stability and FM measurements received secondary consideration. The results shown in this section indicate that more careful measurements using a stabilized laser and higher frequency deviations are necessary for a complete understanding of the bandwidth limitations for internal FM. These measurements are planned for the future.

VI. SUMMARY AND CONCLUSIONS

CdTe has been shown to be a very useful material for internal modulation of CO₂ lasers. The low optical loss of the material allows it to be used within the laser cavity with a relatively small degradation of the laser performance. Coupling modulation is potentially the most useful form of modulation of CO₂ lasers for wideband communication systems. The usefulness of this technique is confined to the frequency regime above 1 MHz, however. Intracavity frequency modulation was shown to have a higher frequency response than that predicted by simple theory. A more detailed analysis and improved measurements are planned to confirm this performance.

ACKNOWLEDGMENT

The authors wish to thank A. Yariv, T. R. O'Meara, and W. B. Bridges for several helpful discussions. The CdTe and the antireflection coatings were provided by the Chemical Physics Department, Hughes Research Laboratories.

REFERENCES

- [1] J. E. Kiefer and A. Yariv, "Electrooptic characteristics of CdTe at 3.39 and 10.6 microns," *Appl. Phys. Lett.*, vol. 15, p. 26, 1969.
- [2] W. W. Rigrod, "Gain saturation and output power of optical masers," *J. Appl. Phys.*, vol. 34, p. 2602, 1963.
- [3] Aerojet General Corp., Azusa, Calif., Contract Rep. 4033, NAS 5-21072.
- [4] K. Gurs and R. Muller, "Internal modulation of optical masers," *Phys. Lett.*, vol. 5, p. 179, 1963.
- [5] I. P. Kaminow, "Internal modulation of optical masers (bandwidth limitations)," *Appl. Opt.*, vol. 4, p. 123, 1965.
- [6] M. DiDomenico, "Small-signal analysis of internal (coupling-type) modulation of lasers," *J. Appl. Phys.*, vol. 35, pp. 2870-2876, 1964.
- [7] F. R. Nash and P. W. Smith, "Broad-band optical coupling modulation," *IEEE J. Quantum Electron.*, vol. QE-4, pp. 26-34, Jan. 1968.
- [8] F. E. Goodwin, "A review of operational laser communication systems," *Proc. IEEE*, vol. 58, pp. 1746-1752, Oct. 1970.
- [9] A. Yariv, T. A. Nussmeier, and J. E. Kiefer, "Anomalous frequency response of intracavity laser modulators," unpublished.
- [10] A. Yariv, "Electro-optic frequency modulation in optical resonators," *Proc. IEEE (Corresp.)*, vol. 52, p. 719, June 1964.
- [11] D. W. Jackson, W. H. Huntley, Jr., and A. D. Rugari, "Comments on 'bandwidth limitations of in-cavity laser modulation,'" *Proc. IEEE (Corresp.)*, vol. 53, p. 616, June 1965.
- [12] F. E. Goodwin, "A 3.39-micron infrared optical heterodyne communication system," *IEEE J. Quantum Electron.*, vol. QE-3, pp. 524-531, Nov. 1967.

APPENDIX B
FREQUENCY RESPONSE OF INTRACAVITY
LASER COUPLING MODULATION

A. Yariv, T. A. Nussmeier, and J. E. Kiefer

ABSTRACT

A resonant energy coupling between the atomic system and the oscillating optical mode leads to severe output distortion in intracavity laser coupling modulation. This anomalous behavior, which places a lower limit on the modulation frequency, is investigated in a case of a CO₂ laser and compared with theoretical predictions.

I. INTRODUCTION

The advantages of intracavity coupling modulation as a means of efficient broadband laser modulation are now well established. (1-5) These are due primarily to the fact that the modulator operates on the internal circulating power of the laser and thus requires significantly less driving power than for similar performance with the modulator located outside the laser cavity. Furthermore, there are no fundamental limitations on high frequency performance other than those imposed by the modulator structure itself. At low frequencies, however, an internal modulator will invariably interfere with the interaction process between the atomic system and the optical resonant mode. This may lead under certain conditions to strong fluctuations in the internal power and hence to modulation distortion. A proper design of internally modulated lasers requires an understanding of this phenomenon and its parametric dependences.

In this paper we present an analysis of this effect as well as the results of a series of experiments that are used to check the

theory and illustrate the practical problems encountered in this type of modulation.

II. THEORY

The main features of the internal coupling modulator are shown in Fig. 1. In each roundtrip an electro-optic crystal placed inside the laser resonator transfers a fraction equal to $\sin^2 \Gamma$ of the internal circulating power from the dominant polarization (in the plane of the figure) to the orthogonal polarization state. Γ is the single pass electro-optic retardation, which can be written as

$$\Gamma(t) = \frac{V_o}{V_\pi} \pi + \frac{V_1}{V_\pi} \pi \cos \omega t \equiv \Gamma_o + \Gamma_1 \cos \omega t \quad (1)$$

where V_π is the half-wave voltage of the electro-optic crystal. The orthogonally polarized wave is assumed to be coupled completely out of the optical resonator by means of a polarizer as, for example, the high index Brewster angle window shown in Fig. 1. The coupled beam constitutes the useful power output of the laser. The form of Eq. 1 makes no allowance for the frequency dependence of the modulation element itself since Γ_1 is taken to be proportional to the modulation voltage V_1 . This places an upper limit on the modulation frequency, which for most cases will be determined by the transit time through the crystal.

The combination of an electro-optic crystal and internal polarization coupler thus is equivalent to a mirror with an instantaneous transmission.

$$T(t) = \sin^2 \Gamma \approx \Gamma_o^2 + 2\Gamma_o \Gamma_1 \cos \omega t + \Gamma_1^2 \cos^2 \omega t \quad (2)$$

where we allowed for a double traverse of the crystal and assumed $\Gamma(t) \ll 1$, a condition which is obeyed in practical situations in order to avoid excessive loading of the laser.

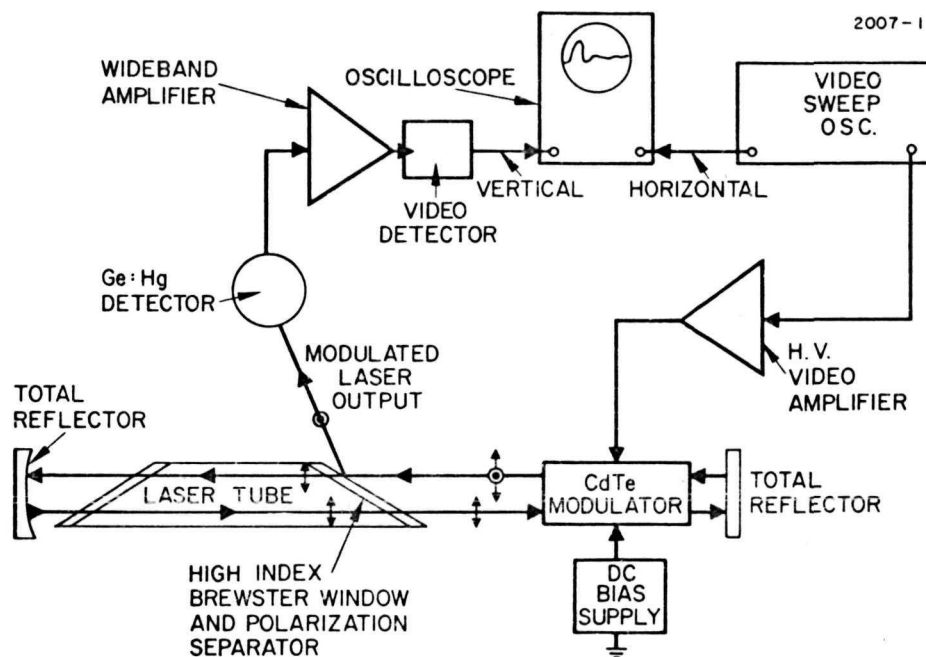


Fig. 1. Experimental Arrangement for Coupling Modulation Measurements.

An alternative point of view, and one which will be used in the following, is to represent the modulator-polarizer combination by an effective photon decay rate

$$\frac{1}{t_c(t)} = \frac{cT(t)}{L} \cong \frac{c\Gamma_o^2}{L} + \frac{2c\Gamma_o\Gamma_1}{L} \cos\omega t + \frac{c\Gamma_1^2}{L} \cos(2\omega t) \quad (3)$$

where c is the velocity of light and L is the length of the resonator. In the following we limit the discussion to the case $\Gamma_o \gg \Gamma_1$ and neglect the last term in (3). The inclusion of this term when Γ_o and Γ_1 are comparable does not change significantly any of the results reached below.

Our first task is to solve for the total stored energy in the optical resonator in the presence of the time varying losses represented by (3). We start with the rate equations for the total number of photons in the resonator q and the (total) atomic inversion N .

$$\frac{dN}{dt} = R - BqN - \frac{N}{\tau} \quad (4)$$

$$\frac{dq}{dt} = BqN - \frac{q}{t_c} \quad (5)$$

where R is the pumping rate (atoms/sec) into the upper laser level, τ^{-1} is the inversion relaxation rate, and B is a constant proportional to the spontaneous transition rate such that BqN is equal to the rate of induced transitions. The steady state solutions of (4) and (5) for the case of constant photon losses ($\frac{1}{t_c} = \frac{1}{t_{co}}$) are

$$N_o = \frac{1}{Bt_{co}}, \quad q_o = \frac{RBt_{co} - 1/\tau}{B} = \frac{1}{B\tau} (r-1), \quad r = RBt_{co}\tau \quad (6)$$

Eq. (6) has physical significance only for $r \geq 1$. At threshold $r = 1$, and for finite power output ($q > 0$), $r > 1$. The parameter r thus is the factor by which the pumping rate exceeds its threshold value.

In considering the case of internal coupling modulation, we replace t_c^{-1} in (5) by

$$\frac{1}{t_c(t)} = \frac{1}{t_{co}} + \alpha(t) \quad (7)$$

where $\alpha(t) \ll t_{co}^{-1}$ represents the time dependent part of the losses due to the modulation voltage as in (3). We write the solutions of (4) and (5) in this case as

$$N = N_o + N_1(t), \quad N_1 \ll N_o \quad (8)$$

$$q = q_o + q_1(t), \quad q_1 \ll q_o$$

where N_o and q_o are the steady state solutions ($\alpha = 0$) as given by (6). Substituting (7) and (8) in the rate equations (4) and (5) and using (6) to eliminate the steady state variables leads to

$$\frac{dN_1}{dt} = -\frac{r}{\tau} N_1 - \frac{q_1}{t_{co}} \quad (9)$$

$$\frac{dq_1}{dt} = \frac{1}{\tau} (r-1) N_1 - \frac{(r-1)}{B\tau} \alpha(t) \quad (10)$$

In obtaining the last pair of equations, we discarded second-order terms involving the factors $q_1 N_1$ and $q_1 \alpha$. From (9) and (10) we obtain

$$\frac{d^2 q_1}{dt^2} + \frac{r}{\tau} \frac{dq_1}{dt} + \frac{(r-1)}{\tau t_{co}} q_1 = -\frac{(r-1)}{B\tau} \frac{d\alpha}{dt} - \frac{r(r-1)}{B\tau^2} \alpha \quad (11)$$

The left side of this equation is formally identical to that of a damped harmonic oscillator. The right side represents the driving force due

to the loss of modulation α . For the case of harmonic modulation, we take α in the form

$$\alpha(t) = \frac{\alpha_1}{2} (e^{i\omega t} + e^{-i\omega t}) \quad (12)$$

and

$$q_1 = \frac{Q_1}{2} (e^{i\omega t} + e^{-i\omega t}) \quad (13)$$

where, using (3)

$$\alpha_1 = \frac{2c\Gamma_o\Gamma_1}{L} \quad (14)$$

Substitution of (12) and (13) in (11) leads to

$$Q_1 = \frac{\frac{i\omega(r-1)}{B} + \frac{r(r-1)}{B^2}}{(\omega - \omega_m - i\beta)(\omega + \omega_m - i\beta)} \alpha_1 \quad (15)$$

where,

$$\omega_m \equiv \sqrt{\frac{1}{t_{co}\tau} (r-1) - \left(\frac{r}{2\tau}\right)^2} \quad (16)$$

$$\beta \equiv \frac{r}{2\tau} \quad (17)$$

From Eq. (15) it follows that at modulation frequencies $\omega \approx \omega_m$ the laser stored energy can oscillate strongly while at $\omega - \omega_m \gg \beta$, Q_1 is small and $q(t) \rightarrow q_o$. This oscillation, in turn, will lead to a distortion of the power coupled out of the laser resonator. This problem is considered next.

The instantaneous fraction of the internal power coupled by the modulator-polarizer combination was given in (2) as

$$T(t) = \sin^2 \Gamma(t) \approx \Gamma_o^2 + 2\Gamma_o\Gamma_1 \cos \omega t, \Gamma_1^2 < \Gamma_o^2 \quad (18)$$

The number of photons coupled per second thus is

$$P(t) = \frac{c}{L} q(t) T(t) = \frac{c}{L} \left(q_o + \frac{Q_1}{2} e^{i\omega t} + \frac{Q_1^*}{2} e^{-i\omega t} \right) \left(\Gamma_o^2 + \Gamma_o \Gamma_1 e^{i\omega t} + \Gamma_o \Gamma_1 e^{-i\omega t} \right).$$

Singling out the terms with $\exp(i\omega t)$ time dependence gives

$$P^{(\omega)}(t) = \frac{c}{L} \left(q_o \Gamma_o \Gamma_1 e^{i\omega t} + \frac{Q_1}{2} \Gamma_o^2 e^{i\omega t} + \text{complex conjugate} \right) \quad (19)$$

for the component of the output power modulated at the signal frequency. The first term on the right side of (19) represents the useful undistorted output since according to (1) it is proportional to the modulation voltage amplitude $V_1 = \Gamma_1 V_\pi / \pi$. The second term that is proportional to $Q_1 \Gamma_o^2$ represents a distortion of the output since, as shown in Eq. (15), Q_1 depends on the modulation frequency ω . The distorted component is expected to be appreciable at modulation frequencies near ω_m where, according to (15) Q_1 goes through a maximum.

To obtain a better estimate of the expected distortion, we use (6), (14) and (15) to write the last equation as

$$P^{(\omega)}(t) = \left(\frac{c}{L} \right) \frac{\Gamma_o \Gamma_1 (r - 1)}{B\tau} \left[1 + \frac{i\omega + \frac{r}{\tau} \Gamma_o^2 \left(\frac{c}{L} \right)}{2(\omega - \omega_m - i\beta)(\omega + \omega_m - i\beta)} \right] e^{i\omega t} + \text{complex conjugate} \quad (20)$$

The second term in the square brackets in (20) undergoes a rapid phase variation near $\omega = \omega_m$ so that a plot of $P^{(\omega)}(t)$ versus ω may be expected to display a structure near ω_m , which is due to the interference of the amplitudes represented by the two terms within the brackets.

III. THE EXPERIMENT AND EXPERIMENTAL RESULTS

The experimental arrangement used for low frequency coupling measurements is shown schematically in Fig. 1. The laser discharge tube is of metal-ceramic construction with an active region 30 cm long by 5 mm diameter. Power input is 33 watts, and heat is removed conductively to a water-cooled base and support structure. The tube is designed to operate in a hemi-confocal cavity 50 cm long with a TEM_{00} diffraction loss of about 2 percent. In this configuration, an output power of 3.6 watts is obtained using an 85 percent reflective output mirror. For this experiment, the laser is operated with fully reflective mirrors whose spacing can be varied between 40 and 90 cm. The output power is coupled from the optical cavity via the GaAs Brewster window nearest the modulator. The modulator is a [110] oriented CdTe crystal 2 cm long by 5 mm square with antireflection coated faces that reduce the reflective insertion loss to less than 4 percent. The halfwave voltage (unclamped) for the modulator is 12 kV at $10.6\ \mu\text{m}$. Fig. 2 is a photograph of the laser with the modulator installed in the optical cavity.

The modulator circuit is arranged to allow both ac and dc signals to be applied simultaneously and independently, thus providing separate control of the parameters Γ_0 and Γ_1 . The video driver amplifier is capable of 600 volts peak-to-peak over a 4 MHz bandwidth, and the dc voltage is limited to 2 kV to prevent dielectric breakdown. The corresponding (maximum) retardations are $\Gamma_0 = 0.52$ rad and $\Gamma_1 = 0.15$ rad. A video sweep generator was used to drive the amplifier and the horizontal input to an oscilloscope; the coupled output from the laser was detected, amplified, envelope detected, and displayed vertically.

The most important result of the theoretical analysis is Eq. (20) for the frequency dependence of the modulated power output.

M7915

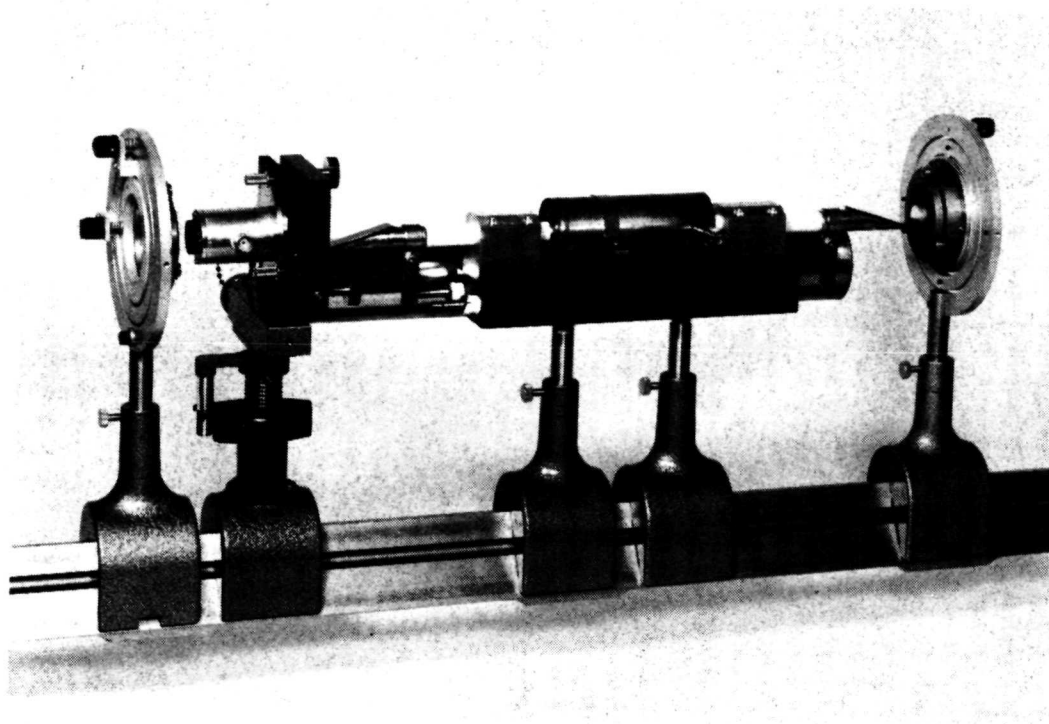


Fig. 2. Metal-Ceramic Laser and Modulator Test Setup.

In our experiment, as discussed below, ω_m exceeds r/τ by nearly two orders of magnitude, so that for frequencies $\omega > 0.1 \omega_m$ we can approximate (20) by

$$p(\omega) = \left(\frac{c}{L}\right) \frac{\Gamma_o \Gamma_l (r-1)}{B} \left[1 - \frac{i\omega \Gamma_o^2 \left(\frac{c}{L}\right)}{2(i + \omega_m - \omega)(\omega + \omega_m)} \right] \quad (21)$$

where $p(\omega)$ is the complex amplitude of $p(\omega)_{(t)}$.

At $\omega = \omega_m$ the modulated component of the power output should have a minimum value of

$$p(\omega_m) = \left(\frac{c}{L}\right) \frac{\Gamma_o \Gamma_l (r-1)}{B\tau} \left[1 - \frac{\omega \Gamma_o^2 \left(\frac{c}{L}\right)}{4\beta \omega_m} \right] \quad (22)$$

The experimentally observed dip in the power output is shown in Figs. 3(a) and 3(b). The minimum of Fig. 3(a) occurs at a value of $f_m \equiv \omega_m/2\pi = 2.1 \times 10^5$ Hz. The theoretical value of f_m was calculated using (16). The collision lifetime τ was obtained by using published⁽⁶⁾ collision cross sections for CO₂ molecules with CO₂, H₂, He, N₂ molecules and the appropriate partial pressures (8 Torr, 0.2 Torr, 15 Torr, 4 Torr, respectively) of these constituents in our laser. The results is $\tau = 7 \times 10^{-5}$ sec. The photon lifetime t_{co} appropriate to Fig. 4(a) is $t_{co} \cong \ell/c(1-R) \approx 10^{-8}$ sec. The laser was pumped at twice its threshold value to $r=2$. Using these data in (16) gives

$$(f_m)_{\text{theoretical}} = 1.9 \times 10^5 \text{ Hz}$$

to be compared with the observed value of 2.1×10^5 Hz. As a further check, we compared the measured dependence of the dip frequency f_m on the cavity length to the theoretical prediction of $f_m \propto \ell^{-1/2}$, which results from (16) when $t_{co} \ll \tau$. This should result in a value of

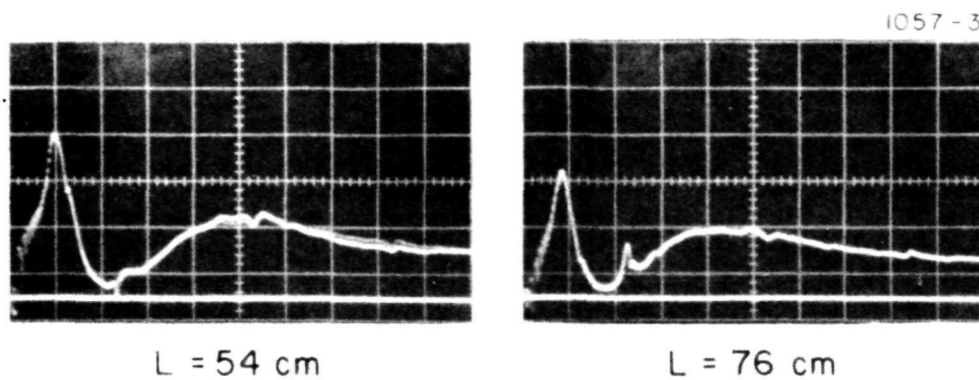


Fig. 3. Laser Output Power vs. Modulation Frequency For Two Cavity Lengths.

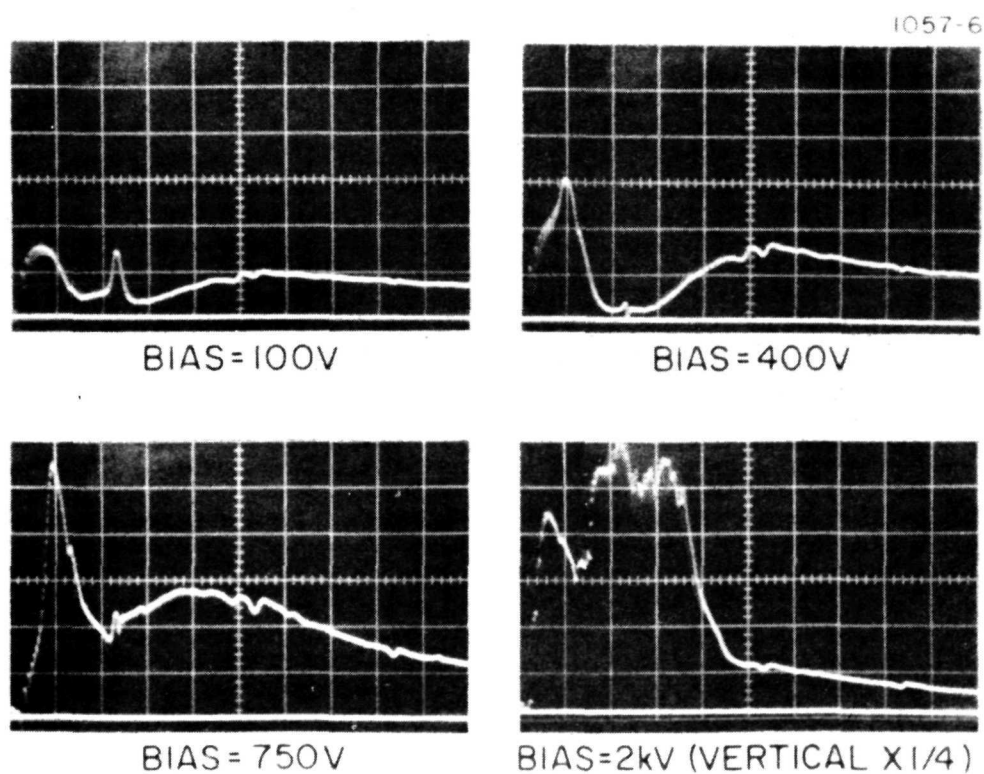


Fig. 4. Laser Output Power vs. Modulation Frequency For Different Amplitudes of the Modulation Signal Amplitude.

f_m in Fig. 3(b) ($L=75$ cm), which is lower by a factor $\sim\sqrt{1.4}$ than the value of Fig. 3(a) ($L=54$ cm). The observed change, from $2.1 \pm 0.1 \times 10^5$ Hz to $1.7 \pm 0.1 \times 10^5$ Hz is consistent with this prediction.

Another feature of the theory that agrees, at least qualitatively, with the analysis, has to do with the dependence on the dip at $\omega=\omega_m$ on the dc retardation bias Γ_0 . According to (22) an increase from zero of Γ_0 should lead to a decrease in the modulated component of the power output $p(\omega_m)$ at the dip frequency. When $\Gamma_0^2 = 4\beta L/c$ the output power is zero. Further increases in Γ_0 cause $p(\omega_m)$ to increase.

This general behavior can be observed in the sequence of Figs. 4(a)-4(d). The output $p(\omega_m)$ becomes zero at a bias of 400 volts and increases progressively with further increases in bias.

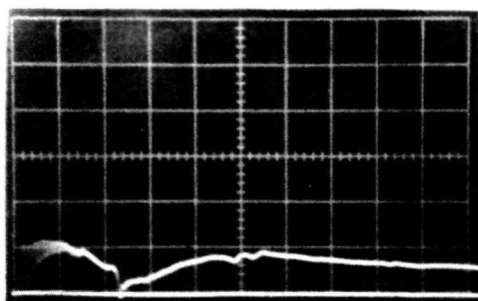
As a last check, we note in the sequence of Fig. 5(a)-5(d) that the dip at $\omega=\omega_m$ is not affected by increasing the rf component of the retardation Γ_1 . Away from ω_m , but still at nearby frequencies, we notice a faster increase in the signal level than the proportional dependence on Γ_1 predicted by (22).

IV. SUMMARY AND CONCLUSIONS

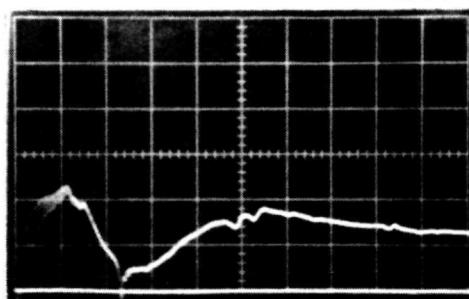
A region of severe distortion has been observed in the otherwise flat frequency response of intracavity laser coupling modulation. This anomalous behavior has been analyzed and explained in terms of a fundamental resonance in which the stored energy oscillates between the inverted atoms and the electromagnetic field.

The effect of this phenomenon is to limit the useful range of the coupling modulator to those frequencies well above that of the distortion region. In practice, it has been found that this useful range extends above 1 MHz.

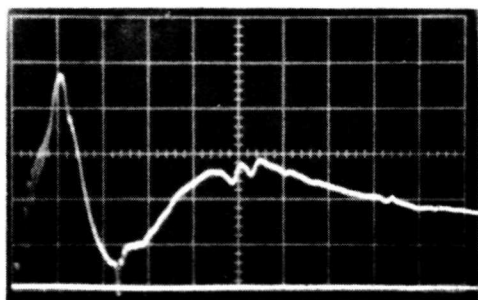
1057-7



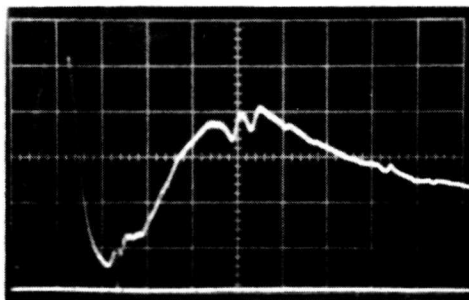
SIGNAL = 300 V P-P



SIGNAL = 400 V P-P



SIGNAL = 500 V P-P



SIGNAL = 600 V P-P

Fig. 5. Laser Output Power vs. Modulation Frequency for Different Amplitudes of the Modulation Signal Amplitude.

REFERENCES

1. K. Gurs and R. Muller, "Internal Modulation of Optical Masers," Phys. Lett., vol. 5, p. 179, 1963.
2. I. P. Kaminow, "Internal Modulation of Optical Masers (Bandwidth Limitations)," Appl. Optics, vol. 4, p. 123, 1965.
3. M. DiDomenico, "Small-Signal Analysis of Internal (Coupling-Type) Modulation of Lasers," J. Appl. Phys., vol. 35, pp. 2870-2876, 1964.
4. F. R. Nash and P. W. Smith, "Broad-Band Optical Coupling Modulation," IEEE J. Quantum Electron., vol. QE-4, pp. 26-34, Jan. 1968.
5. J. E. Kiefer, T. A. Nussmeier, and F. E. Goodwin, "Intracavity CdTe Modulators for CO₂ Lasers," IEEE J. Quantum Electron., vol. QE-8, pp. 173-179.
6. R. L. Taylor, S. Bitterman, "Survey of Vibrational Relaxation Data for Processes Important in the CO₂-N₂ Laser System," Rev. Modern Phys., vol. 41, p. 26, 1969.

APPENDIX C

CALCULATIONS FOR DIRECT AND COHERENT DETECTION TECHNIQUES

The schematic for the basic modulator and detector is shown in Fig. C-1. The output signal of the coupling modulator transmitter is given by

$$\frac{E_o}{\sqrt{2}} [\cos (\omega_c t + \alpha_o + \psi_1) - \cos (\omega_c t + \alpha_o + \psi_3)] , \quad (1)$$

where

E_o = electric field vector of the laser light

ω_c = $2\pi \times$ frequency of the laser light

t = time

α_o = arbitrary phase angle

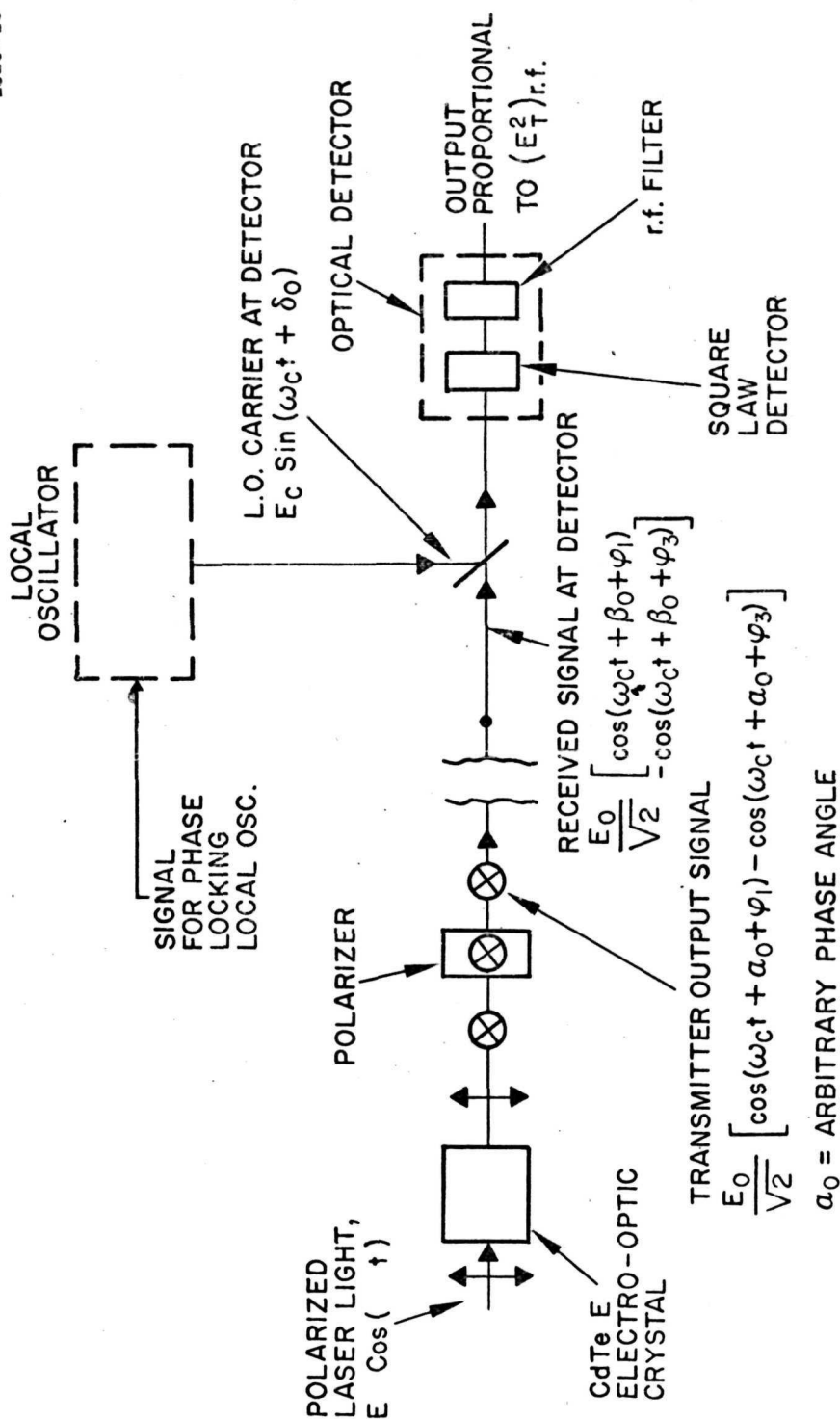
ψ_1 and ψ_3 = phase angles

due to the electro-optic Cd to crystal.

When voltage is applied to the crystal ψ_1 and ψ_2 are not equal:

$$\begin{aligned} \psi_1 &= \frac{2\pi (n_o + \Delta n) L}{\lambda_o} , \\ \psi_3 &= \frac{2\pi (n_o - \Delta n) L}{\lambda_o} , \end{aligned} \quad (2)$$

$$\Delta n = - \frac{n_o^3}{2} \frac{rV}{d}$$



$$E_T = \frac{E_0}{\sqrt{2}} [\cos(\omega_c t + \beta_0 + \varphi_1) - \cos(\omega_c t + \beta_0 + \varphi_2)]$$

$$+ E \sin(\omega_c t + \delta_0)$$

$$= \sqrt{2} E_0' \sin(\omega_c t + \beta_0 + G) \sin(\Gamma_0 + \Gamma_m \sin \omega_m t)$$

$$+ E_c \sin(\omega_c t + \delta_0)$$

Fig. C-1. Idealized Schematic for Modulation and Detection Analysis.

where

n_o = refractive index at laser frequency with no electric field on the crystal

Δn = change of refractive index with applied voltage

λ_o = vacuum wavelength of laser light

L = length of crystal along light propagation direction

r = electro-optic coefficient

d = width of crystal which that voltage is applied across

$V = V_o + V_m \sin \omega_m t$, voltage applied to e.o. crystal,

V_o = d.c. bias,

V_m = modulation voltage amplitude,

ω_m = $2\pi \times$ frequency of modulation

Also we note (for use below) that

$$\psi_3 - \psi_1 = - \frac{4\pi \Delta n L}{\lambda_o} \quad (3)$$

or

$$\psi_3 - \psi_1 = \frac{2\pi L n_o^3 r}{\lambda_o d} (V_o + V_m \sin \omega_m t) \quad (4)$$

Define for convenience

$$\Gamma \equiv \Gamma_o + \Gamma_m \sin \omega_m t = \psi_3 - \psi_1 ; \quad (5)$$

then

$$\Gamma_o = \frac{2\pi n_o^3 r}{\lambda_o} \frac{L}{d} V_o \quad (6)$$

$$\Gamma_m = \frac{2\pi n_o^3 r}{\lambda_o} \frac{L}{d} v_m . \quad (7)$$

We further note that

$$\psi_3 + \psi_1 = \frac{4\pi n_o L}{\lambda_o} \quad (8)$$

is a constant; we define

$$G \equiv \frac{\psi_3 + \psi_1}{2} = \frac{2\pi n_o L}{\lambda_o} \quad (9)$$

After transmission through space, the signal at the optical detector of the receiver is attenuated in amplitude and the phase angle is changed; the signal at the detector is written as

$$\frac{E_o'}{\sqrt{2}} [\cos (\omega_c t + \beta_o + \psi_1) - \cos (\omega_c t + \beta_o + \psi_2)] , \quad (10)$$

where E_o' is the attenuated amplitude, and β_o is the altered phase angle.

The local oscillator at the receiver injects a carrier at the detector; the carrier is characterized by

$$E_c \sin (\omega_c t + \delta_o) , \quad (11)$$

where

E_c = electric field vector of local oscillator at detector

δ_o = arbitrary phase angle at detector.

The local oscillator is locked in phase to the received carrier (vestigial in the case of suppressed carrier transmission); this phase locking technique is discussed further in Section .

The total electric field amplitude E_T intercepted at the optical detector is the sum of the expressions (10) and (11):

$$E_T = \frac{E_o'}{\sqrt{2}} [\cos(\omega_c t + \beta_o + \psi_1) - \cos(\omega_c t + \beta_o + \psi_2)] + E_c \sin(\omega_c t + \delta_o) \quad (12)$$

By trigonometric substitution, (12) becomes

$$E_T = \sqrt{2} E_o' \sin\left(\frac{\psi_3 - \psi_1}{2}\right) \sin\left(\omega_c t + \beta_o + \frac{\psi_1 + \psi_3}{2}\right) + E_c \sin(\omega_c t + \delta_o). \quad (13)$$

Substituting from (5) and (9) in (13), E_T is expressed as:

$$E_T = \sqrt{2} E_o' \sin(\omega_c t + \beta_o + G) \sin\left(\frac{\Gamma_o}{2} + \frac{\Gamma_m}{2} \sin \omega_m t\right) + E_c \sin(\omega_c t + \delta_o) \quad (14)$$

In the coupling modulation method, the light traverses the crystal twice or a length $2L$ instead of L . Therefore, Γ_o and Γ_m , as defined by expressions (6) and (7), respectively, must be doubled in expression (14) where a single pass through length L was assumed. Therefore, for coupling modulation we change (14) to

$$E_T = \sqrt{2} E_o' \sin(\omega_c t + \beta_o + G) \sin(\Gamma_o + \Gamma_m \sin \omega_m t) + E_c \sin(\omega_c t + \delta_o), \quad (15)$$

where $\frac{\Gamma_o}{2}$ was replaced by Γ_o , $\frac{\Gamma_m}{2}$ by Γ_m . Expression (15) is the total electric field amplitude E_T just before optical detection. Note

that if $\delta_o = \beta_o + G$, the signal and local oscillator are in zero phase angle relationship.

It is of interest to determine the sideband frequency amplitudes of the total electric field as amplitude E_T . This is readily calculated by expanding the first term for E_T of (15) in terms of Bessel functions:

$$\begin{aligned} E_T = & \sqrt{2} E_o' \sin(\omega_c t + \beta_o + G) [\sin(\Gamma_o) \cos(\Gamma_m \sin \omega_m t) \\ & + \cos(\Gamma_o) \sin(\Gamma_m \sin \omega_m t)] \\ & + E_c \sin(\omega_c t + \delta_o) \end{aligned} \quad (16)$$

$$\begin{aligned} E_T = & \sqrt{2} E_o' \sin(\omega_c t + \beta_o + G) \left\{ \sin \Gamma_o [J_o(\Gamma_m) + 2 J_2(\Gamma_m) \cos(2\omega_m t) + \dots] \right. \\ & + \cos(\Gamma_o) [2 J_1(\Gamma_m) \sin(\omega_m t) + 2 J_3(\Gamma_m) \sin(3\omega_m t) + \dots] \\ & + E_c \sin(\omega_c t + \delta_o) \\ = & \sqrt{2} E_o' \sin(\Gamma_o) \cdot J_o(\Gamma_m) \sin(\omega_c t + \beta_o + G) + E_c \sin(\omega_c t + \delta_o) \\ & + \sqrt{2} E_o' \sin(\Gamma_o) \cdot 2 \cdot J_1(\Gamma_m) \cdot \sin(\omega_c t + \beta_o + G) \cdot \sin \omega_m t \\ & + \sqrt{2} E_o' \sin(\Gamma_o) \cdot 2 \cdot J_2(\Gamma_m) \cdot \sin(\omega_c t + \beta_o + G) \cdot \cos 2\omega_m t \quad (17) \\ & + \sqrt{2} E_o' \cos(\Gamma_o) \cdot 2 \cdot J_3(\Gamma_m) \cdot \sin(\omega_c t + \beta_o + G) \sin 3\omega_m t \\ & + \dots \end{aligned}$$

(17) is written in terms of the carrier and sidebands as

$$\begin{aligned}
E_T = & \sqrt{2} E'_0 \sin(\Gamma_0) \cdot J_0(\Gamma_m) (\sin(\omega_c t + \beta_0 + G) + E_c \sin(\omega_c t + \delta_0)) \\
& \quad \quad \quad [\text{signal carrier} + \text{l.o. carrier}] \\
& + \sqrt{2} E'_0 \cos(\Gamma_0) J_1(\Gamma_m) \left\{ \cos[(\omega_c - \omega_m)t + \beta_0 + G] \right. \\
& \quad \quad \quad \left. - \cos[(\omega_c + \omega_m)t + \beta_0 + G] \right\} \\
& \quad \quad \quad [\text{signal sidebands, first harmonic}] \\
& + \sqrt{2} E'_0 \sin(\Gamma_0) \cdot J_2(\Gamma_m) \left\{ \sin[(\omega_c - 2\omega_m)t + \beta_0 + G] \right. \\
& \quad \quad \quad \left. + \sin[(\omega_c + 2\omega_m)t + \beta_0 + G] \right\} \\
& \quad \quad \quad [\text{signal sidebands, second harmonic}] \\
& + \sqrt{2} E'_0 \cos(\Gamma_0) \cdot J_3(\Gamma_m) \left\{ \cos[(\omega_c - 3\omega_m)t + \beta_0 + G] \right. \\
& \quad \quad \quad \left. - \cos[(\omega_c + 3\omega_m)t + \beta_0 + G] \right\} \\
& \quad \quad \quad [\text{signal sidebands, third harmonic}] \\
& + \dots \text{ higher harmonics}
\end{aligned}$$

(18)

Expression (18) describes completely the carrier and sideband amplitudes and phase angles for the signal and the l. o. carrier.

The total electric field E_T is now detected with the optical detector, which is considered to be a square law detector (measures E_T^2) and a frequency filter (output current does not respond at light frequencies) which we will denote by rf. E_T as expressed by (15) is now squared.

$$\begin{aligned}
 E_T^2 = & 2E_o'^2 \sin^2 (\omega_c t + \beta_o + G) \sin^2 (\Gamma_o + \Gamma_m \sin \omega_m t) \\
 & + E_c^2 \sin^2 (\omega_c t + \delta_o) + 2\sqrt{2} E_o' E_c \sin (\omega_c t + \beta_o + G) \\
 & \cdot \sin (\omega_c t + \delta_o) \cdot \sin (\Gamma_o + \Gamma_m \sin \omega_m t).
 \end{aligned}$$

Expanding with trigonometric identities,

$$\begin{aligned}
 E_T^2 = & 2E_o'^2 \frac{1}{2} [1 - \cos 2(\omega_c t + \beta_o + G)] \frac{1}{2} [1 - \cos (2\Gamma_o + 2\Gamma_m \sin \omega_m t)] \\
 & + E_c^2 \frac{1}{2} [1 - \cos 2(\omega_c t + \delta_o)] \\
 & + 2\sqrt{2} E_o' E_c \frac{1}{2} [\cos (\beta_o + G - \delta_o) - \cos (2\omega_c t + \beta_o + G + \delta_o)] \\
 & \sin (\Gamma_o + \Gamma_m \sin \omega_m t)
 \end{aligned} \tag{19}$$

Neglecting the terms at twice the laser light frequencies ($2\omega_c$) in expression (19), the detector electrical output current is now proportional to

$$\begin{aligned}
 (E_T^2)_{\text{rf}} &= \frac{E_o'^2}{2} [1 - \cos(2\Gamma_o + 2\Gamma_m \sin \omega_m t)] + \frac{E_c^2}{2} \\
 &+ \sqrt{2} E_o' E_c \cos(\beta_o + G - \delta_o) \sin(\Gamma_o + \Gamma_m \sin \omega_m t) \\
 &= \frac{E_o'^2}{2} [1 - \cos(2\Gamma_o) \cdot \cos(2\Gamma_m \sin \omega_m t) + \sin(2\Gamma_o) \sin(2\Gamma_m \sin \omega_m t)] \\
 &+ \frac{E_c^2}{2} + \sqrt{2} E_o' E_c \cos(\beta_o + G - \delta_o) [\sin(\Gamma_o) \cos(\Gamma_m \sin \omega_m t) \\
 &\quad + \cos(\Gamma_o) \sin(\Gamma_m \sin \omega_m t)] \\
 &= \frac{E_o'^2}{2} \left\{ 1 - \cos(2\Gamma_o) [J_o(2\Gamma_m) + 2J_2(2\Gamma_m) \cos 2\omega_m t + \dots] \right. \\
 &\quad \left. + \sin(2\Gamma_o) [2J_1(2\Gamma_m) \sin \omega_m t + 2J_3(2\Gamma_m) \sin 3\omega_m t + \dots] \right\} \\
 &+ \frac{E_c^2}{2} + \sqrt{2} E_o' E_c \cos(\beta_o + G - \delta_o) \left\{ \sin(\Gamma_o) [J_o(\Gamma_m) \right. \\
 &\quad \left. + 2J_2(\Gamma_m) \cos \omega_m t] \right. \\
 &\quad \left. + \cos(\Gamma_o) [2J_1(\Gamma_m) \sin \omega_m t + 2J_3(\Gamma_m) \sin 3\omega_m t + \dots] \right\}
 \end{aligned}$$

Separating the dc and harmonic terms,

$$\begin{aligned}
 (E_T^2)_{\text{rf}} = & \left\{ \frac{E_o'^2}{2} [1 - \cos(2\Gamma_o) J_o(2\Gamma_m)] + \frac{E_c^2}{2} + \sqrt{2} E_o' E_c \cos(\beta_o + G - \delta_o) \right. \\
 & \left. \sin(\Gamma_o) J_o(\Gamma_m) \right\} \\
 & + \left\{ E_o'^2 \sin(2\Gamma_o) \cdot J_1(2\Gamma_m) + 2\sqrt{2} E_o' E_c \cos(\beta_o + G - \delta_o) \right. \\
 & \left. \cdot \cos(\Gamma_o) J_1(\Gamma_m) \right\} \sin(\omega_m t) \\
 & + \left\{ -E_o'^2 \cos(2\Gamma_o) \cdot J_2(2\Gamma_m) + 2\sqrt{2} E_o' E_c \cos(\beta_o + G - \delta_o) \right. \\
 & \left. \sin(\Gamma_o) \cdot J_2(\Gamma_m) \right\} \cos(2\omega_m t) \\
 & + \left\{ E_o'^2 \sin(2\Gamma_o) \cdot J_3(2\Gamma_m) + 2\sqrt{2} E_o' E_c \cos(\beta_o + G - \delta_o) \right. \\
 & \left. \cos(\Gamma_o) \cdot J_3(\Gamma_m) \right\} \sin(3\omega_m t) \\
 & + \dots
 \end{aligned} \tag{20}$$

This result gives the low frequency (or rf) harmonic spectrum of the modulation frequency for the general case of coherent detection. We remember that a phase locked local oscillator carrier has been injected to heterodyne with the received signal. A non-zero ($\Gamma_o \neq 0$) dc bias on the electro-optic crystal has been assumed. It will be noted that when the dc bias is set to zero ($\Gamma_o = 0$), the carrier field is zero; in that case sufficient vestigial carrier intensity is assumed to be available for phase locking the local oscillator.

Special cases are now considered:

- A. Coherent Detection. DSBSC local oscillator $E_c \neq 0$. Assume no dc bias on crystal ($\Gamma_o = 0$). Vestigial carrier phase locking is assumed. Then from (20),

$$\begin{aligned}
 (E_T^2)_{rf} = & \left\{ \frac{E_o'^2}{2} [1 - J_o(2\Gamma_m)] + \frac{E_c^2}{2} \right\} + \left| 2\sqrt{2} E_o' E_c \cos(\beta_o + G - \delta_o) \right. \\
 & \left. \cdot J_1(\Gamma_m) \right| \sin \omega_m t \\
 & - \left| E_o'^2 J_2(2\Gamma_m) \right| \cos(2\omega_m t) \\
 & + \left| 2\sqrt{2} E_o'^2 E_c \cos(\beta_o + G - \delta_o) \cdot J_3(\Gamma_m) \right| \sin 3\omega_m t \\
 & + \dots
 \end{aligned}
 \tag{21}$$

- B. Direct Detection. No local oscillator ($E_c = 0$). With dc bias ($\Gamma_o \neq 0$).

$$\begin{aligned}
 (E_T^2)_{rf} = & \left\{ \frac{E_o'^2}{2} [1 - \cos(2\Gamma_o) \cdot J_o(2\Gamma_m)] \right\} \\
 & + \left| E_o'^2 \sin(2\Gamma_o) \cdot J_1(2\Gamma_m) \right| \sin(\omega_m t) \\
 & - \left| E_o'^2 \cos(2\Gamma_o) \cdot J_2(2\Gamma_m) \right| \cos(2\omega_m t) \\
 & + \left| E_o'^2 \sin(2\Gamma_o) J_3(2\Gamma_m) \right| \sin(3\omega_m t) + \dots
 \end{aligned}
 \tag{22}$$

C. Direct Detection. No local oscillator ($E_c = 0$). No dc bias ($\Gamma_o = 0$).

$$(E_T^2)_{rf} = \left\{ \frac{E_o'^2}{2} [-J_o(2\Gamma_m)] \right\} - \left\{ E_o' J_2(2\Gamma_m) \right\} \cos(2\omega_m t) + \dots \quad (23)$$

The carrier and sideband amplitude and phase angle spectrum of expression (18) is tabulated in Table C-I for convenience.

The harmonic output of the optical detector for coherent (heterodyne) and direct detection are listed in Table C-II; the listings correspond to expressions (20), (21), (22) and (23). In Table C-II the phase angle between the signal and the local oscillator carrier ($\beta_o + G - \delta_o$) [see expression (15)] has been replaced by Δ defined as $\Delta \equiv (\beta_o + G - \delta_o)$.

TABLE C-I
Carrier and Sideband Amplitude and Phase Angle Spectrum

Frequency of Carrier and Sidebands	Frequency Spectrum (Amplitude) Carrier and Sidebands of Signal Plus Local Oscillator Carrier ($E_c \neq 0$), with dc on e.o. Crystal ($\Gamma_o \neq 0$). Arbitrary Phase, L.O. to Signal	Frequency Spectrum (Amplitude) with No dc Bias ($\Gamma_o = 0$) and with No L.O. Carrier ($E_c = 0$)
ω_c	$\sqrt{2} E'_o \sin(\Gamma_o) \cdot J_0(\Gamma_m) \sin(\omega_c t + \beta_o + G) + E'_c \sin(\omega_c t + \delta_o)$	0
$\omega_c - \omega_m$	$\sqrt{2} E'_o \cos(\Gamma_o) \cdot J_1(\Gamma_m) \cdot \cos[(\omega_c - \omega_m)t + \beta_o + G]$	$\sqrt{2} E'_o \cdot J_1(\Gamma_m) \cdot \cos[(\omega_c - \omega_m)t + \beta_o + G]$
$\omega_c + \omega_m$	$-\sqrt{2} E'_o \cos(\Gamma_o) \cdot J_1(\Gamma_m) \cdot \cos[(\omega_c + \omega_m)t + \beta_o + G]$	$-\sqrt{2} E'_o \cdot J_1(\Gamma_m) \cdot \cos[(\omega_c + \omega_m)t + \beta_o + G]$
$\omega_c - 2\omega_m$	$\sqrt{2} E'_o \sin(\Gamma_o) \cdot J_2(\Gamma_m) \cdot \sin[(\omega_c - 2\omega_m)t + \beta_o + G]$	0
$\omega_c + 2\omega_m$	$\sqrt{2} E'_o \sin(\Gamma_o) \cdot J_2(\Gamma_m) \cdot \sin[(\omega_c + 2\omega_m)t + \beta_o + G]$	0
$\omega_c - 3\omega_m$	$\sqrt{2} E'_o \cos(\Gamma_o) \cdot J_3(\Gamma_m) \cdot \cos[(\omega_c - 3\omega_m)t + \beta_o + G]$	$\sqrt{2} E'_o \cdot J_3(\Gamma_m) \cdot \cos[(\omega_c - 3\omega_m)t + \beta_o + G]$
$\omega_c + 3\omega_m$	$-\sqrt{2} E'_o \cos(\Gamma_o) \cdot J_3(\Gamma_m) \cdot \cos[(\omega_c + 3\omega_m)t + \beta_o + G]$	$-\sqrt{2} E'_o \cdot J_3(\Gamma_m) \cdot \cos[(\omega_c + 3\omega_m)t + \beta_o + G]$
...	...	

T789

TABLE C-II

Harmonic Output of Optical Detector for Coherent and Direct Detection (Four Cases)

Detected Power Output Frequency	rf Power Output of Optical Detector with dc Bias on e.o. Crystal ($\Gamma_0 \neq 0$) Coherent Detection: with Local Oscillator ($E_c \neq 0$)	rf Power Output, Optical Det. with No dc Bias ($\Gamma_0 = 0$) Coherent Detection: with L.O. ($E_c \neq 0$) DSBSC	rf Power Output, Optical Det. with dc Bias ($\Gamma_0 \neq 0$) Direct Detection: No L.O. ($E_c = 0$)	rf Power Output with No dc Bias ($\Gamma_0 = 0$) Direct Detection: No L.O. ($E_c = 0$)
dc	$\frac{E_o^2}{2} [1 - \cos(2\Gamma_0) \cdot J_0(2\Gamma_m)] + \frac{E_c^2}{2} + \sqrt{2} E_o E_c \cos(\Delta) \cdot \sin(\Gamma_0) \cdot J_0(\Gamma_m)$	$\frac{E_o^2}{2} [1 - J_0^2(2\Gamma_m)] + \frac{E_c^2}{2}$	$\frac{E_o^2}{2} [1 - \cos(2\Gamma_0) \cdot J_0(2\Gamma_m)]$	$\frac{E_o^2}{2} [1 - J_0(2\Gamma_m)]$
ω_m	$[E_o^2 \sin(2\Gamma_0) \cdot J_1(2\Gamma_m) + 2\sqrt{2} E_o E_c \cos(\Delta) \cdot \cos(\Gamma_0) \cdot J_1(\Gamma_m)] \sin(\omega_m t)$	$2\sqrt{2} E_o E_c \cos(\Delta) \cdot J_1(\Gamma_m) \cdot \sin(\omega_m t)$	$E_o^2 \sin(2\Gamma_0) \cdot J_1(2\Gamma_m) \cdot \sin(\omega_m t)$	0
$2\omega_m$	$[-E_o^2 \cos(2\Gamma_0) \cdot J_2(2\Gamma_m) + 2\sqrt{2} E_o E_c \cos(\Delta) \cdot \sin(\Gamma_0) \cdot J_2(\Gamma_m)] \cos(2\omega_m t)$	$-E_o^2 \cdot J_2(2\Gamma_m) \cos(2\omega_m t)$	$-E_o^2 \cos(2\Gamma_0) \cdot J_2(2\Gamma_m) \cos(2\omega_m t)$	$-E_o^2 \cdot J_2(2\Gamma_m) \cos(2\omega_m t)$
$3\omega_m$	$[E_o^2 \sin(2\Gamma_0) \cdot J_3(2\Gamma_m) + 2\sqrt{2} E_o E_c \cos(\Delta) \cdot \cos(\Gamma_0) \cdot J_3(\Gamma_m)] \sin(3\omega_m t)$	$2\sqrt{2} E_o E_c \cos(\Delta) \cdot J_3(\Gamma_m) \sin(3\omega_m t)$	$E_o^2 \cdot \sin(2\Gamma_0) \cdot J_3(2\Gamma_m) \cdot \sin(3\omega_m t)$	0
...	...			

 $\Delta \approx \beta_0 + G - \delta_0$ is the phase angle between the received signal and the L.O. carrier at the optical detector

APPENDIX D

WIDEBAND POWER SPLITTER/COMBINER TECHNIQUES

1. CORE LIMITATIONS

The method of obtaining high, wideband rf power by in-phase summation of multiple amplifier outputs in a power combiner rests on the ability to build wideband, constant group delay power splitters and combiners. These devices usually are cascades of 2:1 or 4:1 impedance ratio transformers bifilar wound on small toroidal cores. Clearly, careful selection of the core material, size, and shape factor are essential. The following series of arguments and partial derivations establishes criteria for selecting a core for a particular design.

a. Core Upper Frequency Limit

The first criterion is the required upper frequency range of the core material. Wideband or transmission line transformers are usually wound in a bifilar fashion so that at low frequencies coupling is effected by the core and at high frequencies close coupling is effected by the bifilar winding technique. This method allows frequency ranges from a few tens of kiloHertz to hundreds of megaHertz. The toroidal core material should exhibit its design magnetic properties to a frequency of several megaHertz where the bifilar coupling predominates.

b. Basic Equations

The starting point is a collection of four basic equations:

$$\text{Faraday's induction law} \quad e = -N \frac{d\phi}{dt} \quad (1)$$

$$\text{Ampere's law} \quad \Sigma NI = \int H d\ell \quad (2)$$

The flux density -- magnetic intensity relation

$$B = \mu_o \mu_r H \quad (3)$$

where

μ_o = free space permeability

and

μ_r = relative permeability

and one definition of inductance L

$$e = -L \frac{di}{dt} \quad (4)$$

c. Power Handling Criterion

Assuming sinusoidal excitation, Faraday's induction law (1) may be rearranged and integrated to give

$$B = \frac{E}{2\pi f N A} \quad (5)$$

where

B = core flux density

E = peak voltage of the applied wave

f = sinusoid frequency

N = number of turns on the core

A = cross sectional area of the toroid.

The non-integral form of Ampere's law is

$$NI = H\ell \quad (6)$$

where

ℓ = effective magnetic path length in the core.

Combining (5) and (6), the volt-ampere product that the core will support is

$$EI = \frac{2B^2 \pi f V_e}{\mu_o \mu_r} \quad (7)$$

where

$V_e = A\ell$ the effective core volume.

In industrial magnetic literature, B is usually expressed in gauss and V_e in Cm^3 . Translating (7) from the rationalized MKS system to a hybrid system where E is in rms volts, I in rms A, B in gauss, and V_e in Cm^3 ; we have

$$EI = \frac{5 \times 10^{-8} B^2 f V_e}{\mu_r} \quad (8)$$

after substituting

$$\mu_o = 4\pi \cdot 10^{-7}$$

Rearranging (8), we have the criterion

$$\frac{B^2 V_e}{\mu_r} \geq \frac{2 \times 10^7 EI}{f} \quad (9)$$

for a given desired volt-ampere product and lowest frequency of operation.

B_s is the saturation flux of the material. For example, to support 5 W at 100 KHz, the product

$$\frac{B_s^2 V_e}{\mu_r} \geq 10^3$$

d. Inductance Criterion

The primary inductance of the wideband transformer must be large enough at the lowest frequency of operation to make its reactance greater than the impedance level of the circuit.

$$\omega L \geq R \quad (10)$$

Relation (4) may be integrated assuming sinusoidal excitation to give

$$L = \frac{-E}{\omega I} \quad (11)$$

substituting (3), (5) and (6);

$$L = \frac{\mu_o \mu_r N^2 A}{\ell} \quad (12)$$

and substituting this into (10)

$$\frac{2\pi f \mu_o \mu_r N^2 A}{\ell} \geq R \quad (13)$$

Rearranging,

$$\frac{\mu_r N^2 A}{\ell} \geq \frac{R}{2\pi \mu_o f} = \frac{1.27 \times 10^5 R}{f} \quad (14)$$

in the rationalized MKS system.

With A and ℓ expressed in centimeters,

$$\frac{\mu_r N^2 A}{\ell} \geq \frac{1.27 \times 10^7 R}{f} \quad (15)$$

For example, a 50-ohm system at 100 KHz requires

$$\frac{\mu_r N^2 A}{\ell} \geq 6.35 \times 10^3$$

As a practical note, turns counts $N > 15$ are undesirable as they produce degradation at frequencies above 100 MHz or so for most designs.

e. Summary

Examine eqs. (9) and (15) in view of transformer operation from 100 KHz to 250 MHz or so at a 50-ohm impedance level. As a rule of thumb, $N \leq 10$. Also, as large a saturation flux density B_s as possible is clearly desirable. Relative permeability, μ_r , is a trade between the two criteria. An adequate core volume is needed, but eq. (15) shows the desirability of a short magnetic path length. Thus the optimum core shape has a large cross sectional area and short magnetic path length. This is the reason why the ENI power combiners have toroids with the unusually stout shape factor.

A data sheet search reveals several interesting facts. First, a relatively small ferrite core, say 0.4-in. diameter by 0.25-in. thick, will support 5 VA. And secondly, the powder iron toroids so common in rf work are undesirable for wideband transformer design due to their low relative permeability (typically 10 to 100).

2. BASIC WIDEBAND TRANSFORMER DESIGNS

Figure D-1 shows the design for a 0° hybrid and a 180° hybrid two-way power splitter. These transformers are drawn schematically as transmission lines. Thus in transformer T1 of the 0° hybrid, 1 and 3 are the start ends of a bifilar winding while 2 and 4 are the finish ends. In transformer T2 of the 180° hybrid, wire 5-6 is a continuation of wire 1-2 as far as winding on the core is concerned.

In the 0° hybrid, transformer T1 steps down the impedance from 50 ohms to

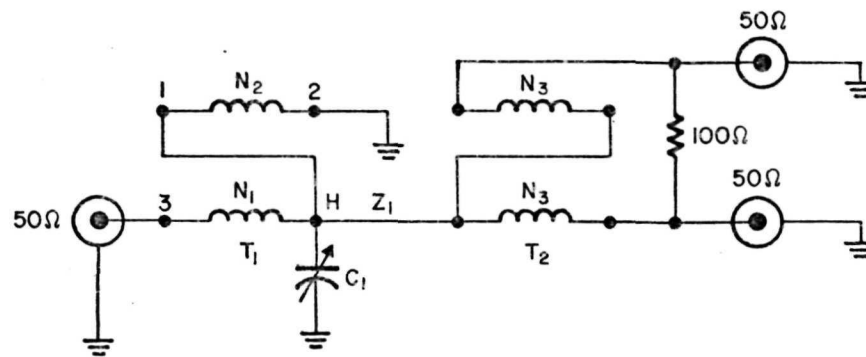
$$Z_1 = \left(\frac{N_2}{N_1 + N_2} \right)^2 \times 50 \Omega \quad (16)$$

If $N_1 = N_2$, it is a standard 4:1 impedance transformer. In the 0° hybrid it is wound as a 2:1. T2 is a 4:1 impedance transformer. The resistor absorbs out of phase power reflected from either output port and gives considerable isolation between the in-phase output ports.

Capacitor C1 is needed to load T1. Without C1, the high frequency response falters. C1 is tuned to an optimum trade between high frequency response and passband flatness.

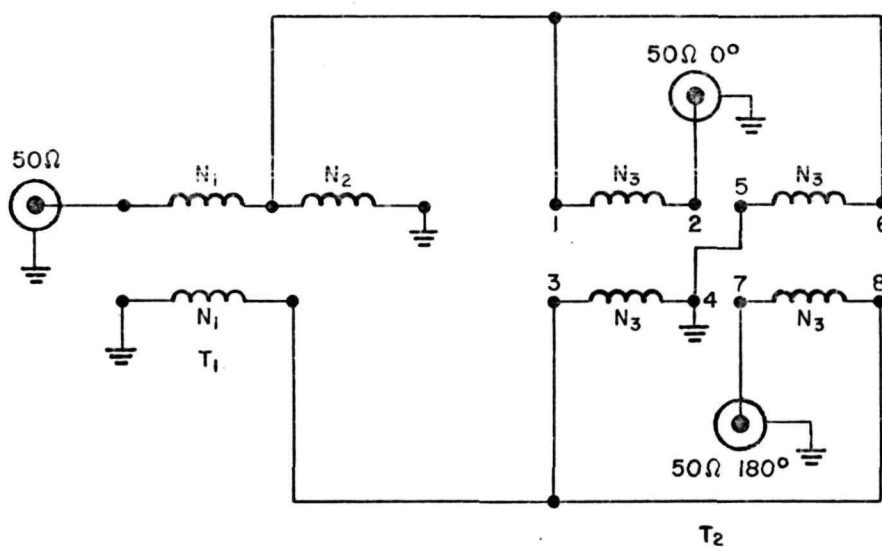
T1 in the 180° hybrid impedance transforms the single-ended 50 ohm input into a floating 25 ohm impedance. T2 is a 4:1 impedance transformer with a floating input and out of phase, single-ended, 50 ohm outputs. This design does not require capacitive loads and as a result generally gives better high frequency response. Since the outputs are out of phase, an isolation resistor cannot be employed. The output port isolation is poorer.

2023-24



0° HYBRID

2023-25



180° HYBRID

Fig. D-1. Two-Way Power Splitters or Combiners.

Figures D-2 and D-3 show hybrids drawn as conventional transformers. Figure D-2 shows a 4-way power splitter comprised of an input impedance transformer and cascaded in-phase 4:1 transformers. T2 requires capacitive loading to obtain upper frequency response. Good port-port isolation is acquired in this design.

Figure D-3 shows a 4-way power splitter consisting of cascaded 180° hybrids. Six cores are required to implement this design compared to 4 cores for the in-phase 4-way splitter shown in Fig. 2.

Although the devices were described above as power splitters, they are bilateral and also can be used as power combiners.

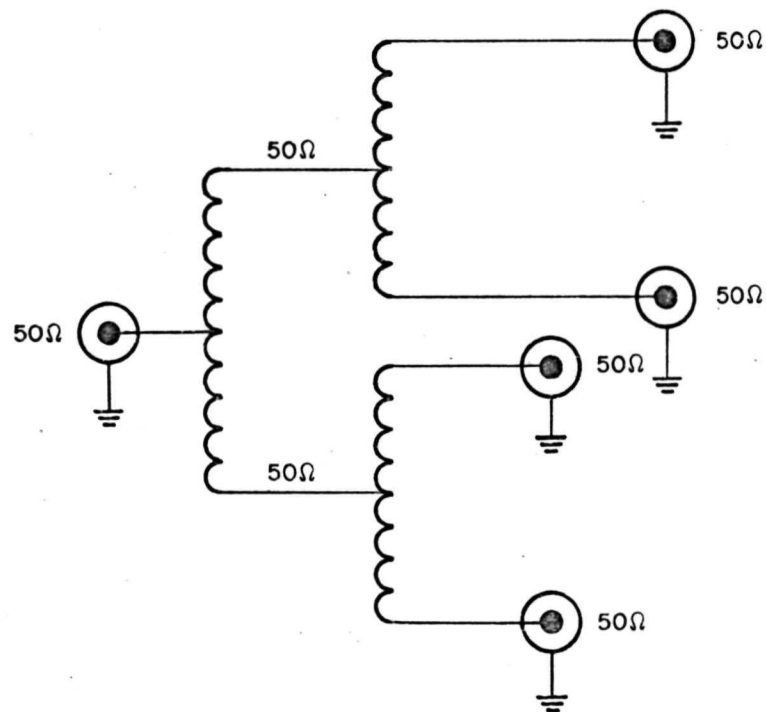
a. Test Results

Figure D-4 shows the frequency response of an in-phase, 4-way power splitter built on Indiana General CF121 cores type H material. This size and material were selected under the ground rules outlined in a previous IDC (Dobratz - 14 September 1971). 3 dB bandwidth is 14 KHz to 250 MHz. Without capacitive tuning, the upper frequency response rolls off as indicated approximately along the dotted line. If the number of bifilar turns is reduced on all three cores from 4 to 2, the response in Fig. D-5 is obtained. The lower 3 dB point has moved to 67 kHz and the upper to 280 MHz. Note that the tuning can now be optimized to give both high frequency response and low passband ripple. In part, the improvement is due to a shorter transmission line length. A general design rule of thumb (see references) is to keep the transmission line length shorter than 0.1 wavelength at the highest frequency of interest.

Phase response for the coupler of Fig. D-4 is shown in Fig. D-6.

Group delay of the two bifilar turn design is shown in Fig. D-7. Group delay change is very nominal up to the upper frequency limit. The group delay characteristics and the steepness of the high frequency response rolloff demonstrate the cost of employing tuning

2023-27



D-9

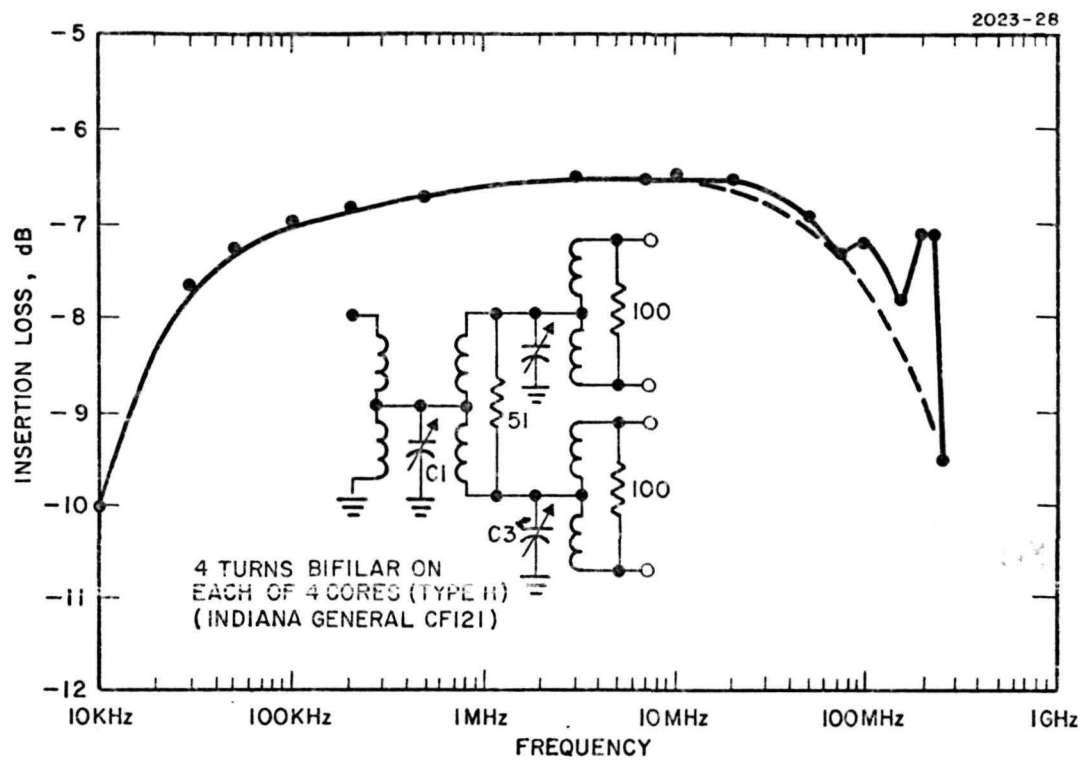


Fig. D-4. Frequency Response of In-Phase 4-Way Power Splitter.

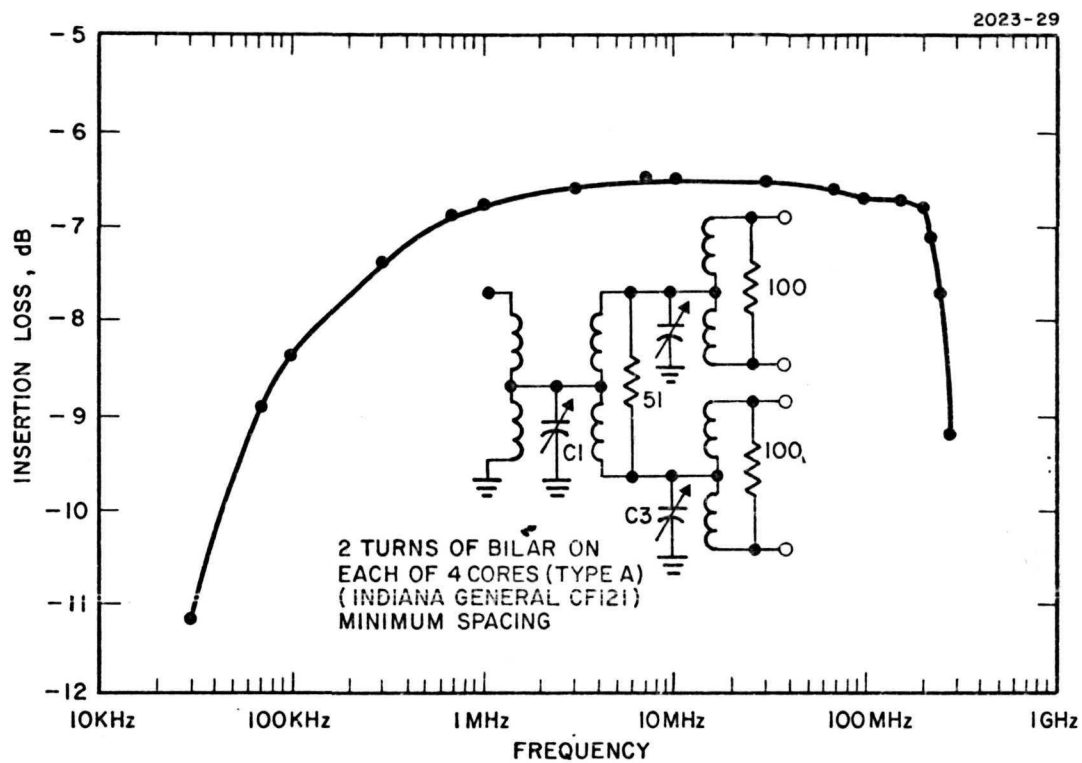


Fig. D-5. Frequency Response of In-Phase 4-Way Power Splitter.

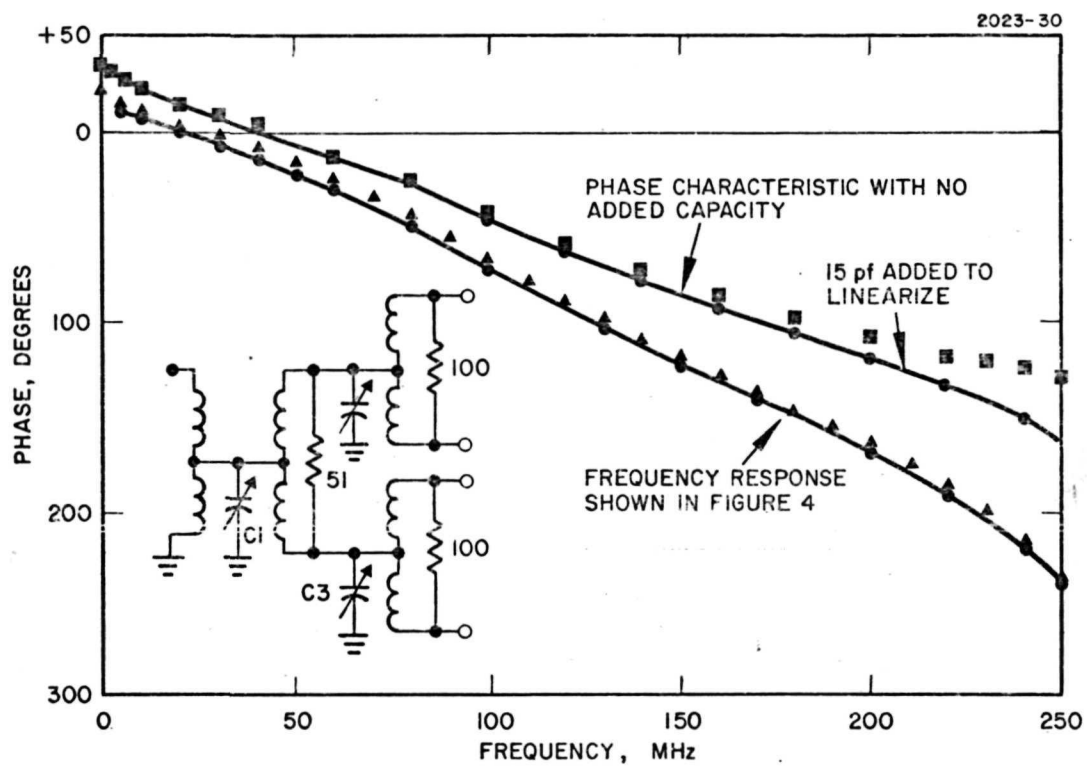


Fig. D-6. Phase Response of the 4-Way Power Splitter Shown in Fig. D-4.

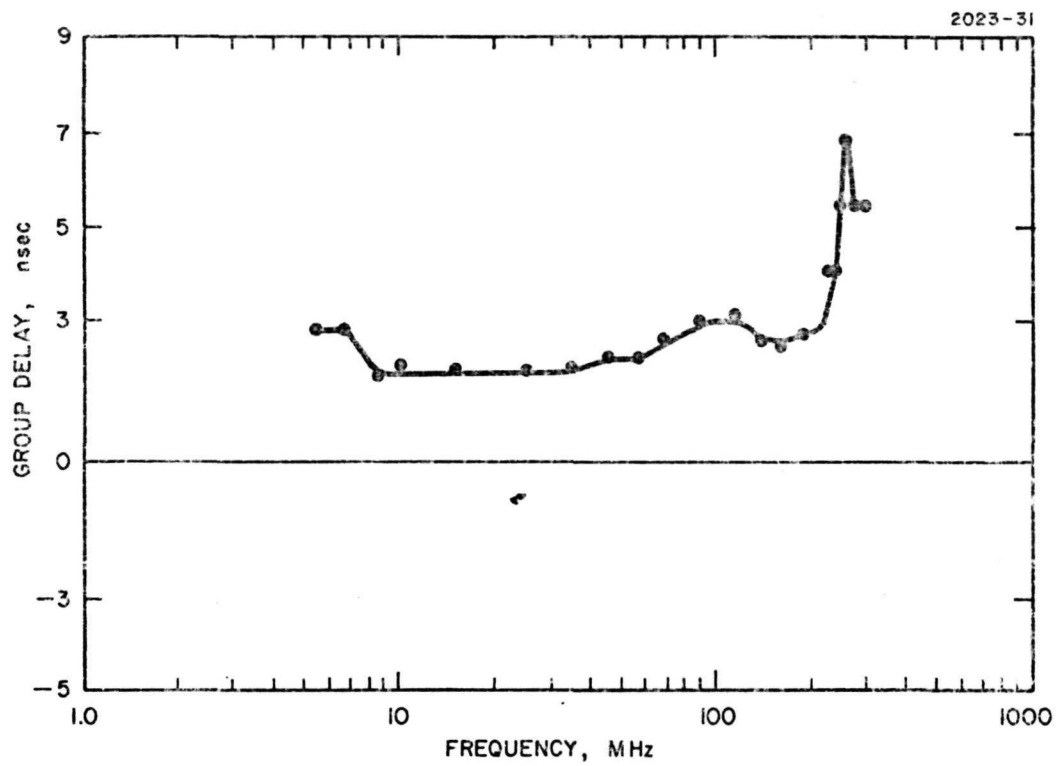


Fig. D-7. Group Delay of 4-Way Power Splitter Shown in Fig. D-5.

capacitors in the in-phase hybrids to flatten frequency response characteristics. These same effects are noted in the ENI 406L amplifier that uses in-phase hybrids tuned with selected fixed capacitors. In particular, the ENI's group delay changed considerably above 100 MHz. This probably is due to the cascaded 0° hybrid's group delay variation.

Some preliminary testing was done on 180° hybrids. These demonstrated (singly) better high frequency response and less passband ripple. To date, a 4-way power splitter has not been constructed of these devices due to program redirection.

b. Conclusions

The amplifier effort is directed toward constructing a digital device with significant square wave response to several hundred MHz. Thus, the power combiner transformers should pass frequencies up to the third harmonic of the digital information fundamental frequency with small group delay shift. Typically, this could be expected to be on the order of 500-600 MHz. Great difficulty has been encountered in extending the 0° hybrid element response beyond 250-300 MHz, and this element appears unfeasible. Initial tests on the 180° hybrid show a higher upper frequency limit. Also, the absence of tuning capacitors should result in a flatter group delay curve at higher frequencies. Thus, designs of a 100 kHz-600 MHz 4-way splitter or combiner should use this hybrid as a basic element.

The Indiana General CF121 core (type H) is identical in unusual form factor to that used in the ENI 406L amplifier and the amplifier frequency response closely matches that of our best 0° hybrid design. We conclude that the CF121 probably is the core used in the ENI 406L. As indicated earlier, the CF121 is very conservatively rated for power handling on the order of 5-10 W. A smaller core can be used with the attendant advantage of reducing transmission line length. This should improve high frequency response.

Both 0° and 180° hybrids were built with Ferroxcube miniature shielding beads. The 0° hybrid demonstrated a 3 dB response from ~40 kHz to 250 MHz. The 180° hybrid covered the range ~40 kHz to 660 MHz. The bead's 3B material had both a lower permeability and a lower loss factor than the CF121 H material core.

BROADBAND TRANSFORMER REFERENCES

1. C. L. Ruthroff, "Some Broad-Band Transformers," Proc. IRE, Vol. 47, August 1959, pp. 1337-1342.
2. O. Pitzalis, Jr., "Broadband Transformer Design for RF Transistor Power Amplifiers," Electronic Components Conference, Washington, 1968 IEEE, pp. 207-216.
3. C. N. Winningstad, "Nanosecond Pulse Transformers," IRE Trans. on Nuclear Science, Vol. NS-6, March 1959, pp. 26-31.
4. R. E. Matick, "Transmission Line Pulse Transformers — Theory and Applications," Proc. IEEE V56 N1, January 1968, pp. 47-62.
5. W. K. Roberts, "A New Wide-Band Balun," Proc. IRE, December 1957, pp. 1628-1631.
6. A. Talkin and J. Cuneo, "Wide Band Balun Transformer," Review of Scientific Instruments, V28 N10, October 1957, pp. 808-815.
7. V. K. Paramonov, Telecommunications, V24 N5, May 1970, pp. 41-46 (English translation).
8. V. K. Paramonov and V. D. Kuznetsov, Telecommunications, V23 N9, September 1969, pp. 48-51 (English translation).
9. E. Lampert, "Theorie des Leitungsübertragers zur Potentialumkehr von Nanosekunden — Impulsen," Arch. elektr. Übertr., V22 N11, Nov. 1968, pp. 537-548.

10. W. Hilberg, "Enige grundsätzliche Betrachtungen zu Breitband-Übertragern," NTZ 1966 No. 9, pp. 527-538.
11. H. Rudenberg, "The Distributed Transformer," internal paper, Research Division, Raytheon Manufacturing Co., Waltham, Mass. (1952).
12. M. Brouant, "Transformateurs A Lignes," C&T, 22A No. 4, 1968, pp. 279-288.
13. O. Pitzalis, Jr., "Practical Design Information for Broad-band Transmission Line Transformers," Proc. IEEE April 1968, pp. 738-739.
14. W. Hilberg, "Die Eignung des Leitungsübertragers für die Impulstedwig," N. T. Z. 1965 No. 4, pp. 219-230.
15. E. Lampert, "Leitungsübertrager mit beliebigem, ganzzahligem Übersetzungsverhältnis," Arch. elektr. Übertr., V.23 N.1, 1969, pp. 49-59.